THESE DE DOCTORAT

Présentée à l'Université de Lille

Par

Junteng WU

Pour obtenir le grade de Docteur de l'Université Lille

Ecole Doctorale : Sciences de la Matière du Rayonnement et de l'Environnement

Discipline : Energétique, thermique, combustion

Theoretical and experimental studies on the hygroscopic properties of soot particles sampled from a kerosene diffusion flame: impact of the aging processes by O_3 and SO_2

Etudes théoriques et expérimentales sur les propriétés hygroscopiques de particules de suie prélevées sur une flamme de diffusion de kérosène : impact des processus de vieillissement de l'O_3 et du SO_2

Soutenue le 26 Avril 2019 devant la commission d'examen

M. LOBO Prem	Senior Researcher, NRCC, Ottawa, Canada	RAPPORTEUR
M. OUF François-Xavier	Chercheur, IRSN, GIF SUR YVETTE CEDEX	RAPPORTEUR
Mme. D'ANNA Barbara	Directrice de Recherche CNRS, LCE, Marseille	EXAMINATEUR
Mme. PIRIM Claire	Maîtresse de Conférences, Université de Lille, Villeneuve d'Ascq	EXAMINATEUR
Mme. DESGROUX Pascale	Directrice de Recherche CNRS, PC2A, Villeneuve d'Ascq	DIRECTRICE DE THESE
M. FACCINETTO Alessandro	Chargé de Recherche CNRS, PC2A, Villeneuve d'Ascq	CO-ENCADRANT DE THESE
M. CAZAUNAU Mathieu	Ingénieur de Recherche CNRS, LISA, Créteil	MEMBRE INVITE

Acknowledgement

In the three years and seven months of my Ph.D., there are too many unforgettable stories. What I learned and the people I met are precious in my life. I'd like to give my appreciation to labex CaPPA who provides an excellent platform to let me learn this great Ph.D. project in laboratory "PhysicoChimie des Processus de Combustion et de l'Atmosphère" of the University of Lille.

First and foremost, I would like to say thank you to my supervisor Dr. Pascale Desgroux. It's really an honor to be one of her Ph.D. students, and maybe the closed one. I appreciate all her contributions of time, ideas and scientific directions to my work. She let me know the complicity of the combustion process and what is soot that I worked with for almost four years. Not only the scientific knowledge, her passional and motivational attitude affected and encouraged me, especially when I met the difficulties in the experimental work.

I'd like to thank my co-supervisor Dr. Alessandro Faccinetto. I've learned a lot of skills and techniques from Alessandro. It was very comfortable to work with him. We build and tested together with the Lille Atmospheric Simulation Chamber (LASC) system. We improved together with the Lille Ice Nucleation Chamber (LINC). He supervised basically all the experiments during my Ph.D. and I can't forget every moment about the discussions and brainstorms on the experimental design. All the knowledge about the mass spectrometer and data treatment that I learned come from him. I could never forget those weeks when we build the peak list of the mass spectra and identified hard the peaks which own several corresponding chemical species. I admire his spirit of exploration. He is always looking forward to the new techniques on recent work to improve understanding. His procedure of statistical analysis on the mass spectra of soot samples is an important part of this manuscript. Out of the work, I enjoy his Italian humor. I loved to spend time with him to exchange the understandings of the different culture and history between China and European countries. I enjoyed every match of the board game and chess with him. The most important, I will never forget the experience that we picked cherries in the campus and the consequence of eating cherries with drinking water.

I'd like to give my appreciation to my co-supervisor Dr. Professor Denis Petitprez as well. He was one of my professors when I studied as a master student. He gave me a lot of help during my Ph.D., especially the bibliography and the knowledge on kinetic reaction. He was always patient to listen to my questions and gave the details as he could. I can't forget the moment we studied where the problem came to our "baby"- CCNc.

Besides my supervisors, I'd like to thank the members of the jury: Dr. Prem Lobo, Dr. François-Xavier Ouf, Dr. Barbara D'Anna, Dr. Claire Pirim and Dr. Mathieu Cazaunau who had accepted to review this manuscript. Thank you very much for all interesting and constructive comments which improved a lot the quality of this manuscript.

I'd like to thank Dr. Sébastien Batut for the help on the framework design, digital communication of the device and the knowledge of using Solidworks. Also, he made a significant contribution to the analysis of soot morphology by TEM technique. I never felt bored when we took thousands of pictures from the sample grid. Without his help, I could not finish the analysis of soot morphology in this work.

Friendly thanks to Dr. Symophorien Grimonprez for teaching me how to use most of the experimental instruments at the beginning of my Ph.D. and for helping me to be familiar with the aging process of soot particles in the simulation chamber.

I want to thank Edouard Pangui and Dr. Michel Maille for the help during the campaign in the CESAM chamber of laboratory LISA of the University of Créteil.

I want to thank Dr. Jérôme Yon for the help and the suggestions on the publication work, especially the knowledge about the morphology of soot.

This work would not have been succeeded without all your help.

I'd like to thank the director of PC2A Dr. Professor Laurent Gasnot for the help on the questions of the administration. Thank you to Marc Ribaucour, Guillaume Vanhove and Abderrahman El Bakali who take care of me during my teaching work. I'd like to thank Sylvie Gosselin and Béatrice Lecrenier for preparing the chemical product and supervise the security. I want to thank Sébastien Germain for the calibration of the instruments. Thank you to Olivier Hombert for the mechanical work on the framework. Thank you to Pascal Demaux for the help on the reparation of the instrument device. Thank you to Sadio Diakhate and Valérie Vilan for the administrative help, especially ask the refunding during the event, conference and the defense. Friendly thanks to Lise Deschutter, Eliane Assy and Coralina Sampaio Mergulhao for preparing the unforgettable party after the defense. I'd like to thank all the people in the laboratory PC2A, especially the members of the Combustion Group and the Atmosphere Group. Thanks to my friends in the laboratory: Hwasup, Quan, Linh Dan, Jinane, Camille, Patrice, Christopher, Florent and Alexandre.

Last but not least, thank you to my family for all the support during these years. Thanks to my parents who always encouraged me without any doubt. Thanks to my parents-in-law for the support at every moment. Thank you to my love, Qun. Without you, I can’t go further like this. You give me strength. I’d like to thank my angel Léna, your coming gave me the direction. I give all the wishes to you and I hope you growth healthily.

List of acronyms

AIDA	aerosol interactions and dynamics of the atmosphere
APS	aerodynamic particle sizer
BC	black carbon
CCN	cloud condensation nuclei
CCNc	cloud condensation nuclei counter
CFDCs	continuous flow diffusion chambers
CFMCs	continuous flow mixing chambers
CPC	condensation particle counter
DMA	differential mobility analyzer
FFT	Fourier transform algorithm
HAB	height above the burner
HCA	hierarchical cluster analysis
HEPA	high-efficiency particulate arrestance
IN	ice nuclei
IPCC	intergovernmental panel on climate change
IUPAC	international union of pure and applied chemistry
LASC	Lille atmospheric simulation chamber
LINC	Lille ice nucleation chamber
MFC	mass flow controller
NCC	nitrogen containing compounds
OCH	oxygen containing hydrocarbons
PAHs	polycyclic aromatic hydrocarbons
PCA	principle component analysis
PCs	principal components
PINC	portable ice nucleation chamber
PM	particle matter
RF	radiative forcing
RH	relative humidity
SCC	sulfur containing compounds
SDCs	static diffusion chambers

SIMS	secondary ion mass spectroscopy
SMPS	scanning mobility particle sizer
SS	supersaturation
TEM	transmission electron microscopy
ToF	time of flight
UV	ultraviolet
VOCs	volatile organic compounds

Table of Contents

Chapter I Introduction

1. Impact of the atmospheric aerosols on the climate change

1.1. Atmospheric aerosols

Atmospheric aerosols are suspensions of solid or liquid particles in the atmosphere having size in the range from nanometers to micrometers. The concentration and the chemical composition of atmospheric aerosols vary significantly with time and location, and strongly depend on the emission source and the ensemble of physical and chemical modifications the particles undergo during their lifetime in the atmosphere.

Atmospheric aerosols can be generated in a wide variety of sources and are typically classified based on their natural or anthropogenic origin. Natural atmospheric aerosols include sea salt, mineral dusts, volcanic ashes, dust from soil erosion, soot and ashes from forest fires and biogenic particles, while anthropogenic atmospheric aerosols include industrial emissions, emissions from the agriculture and from the combustion of fossil fuels and biomass. According to different pathways of the formation, the aerosols can also be classified as primary aerosols and secondary aerosols. Primary aerosols are emitted directly in the atmosphere, for example combustion emissions and volcanic ashes. Secondary aerosols are formed from the gas phase during the so-called nucleation processes (gas-to-particle transition). Estimations on the aerosol mass are available as shown in Figure I-1-1 (Andreae and Rosenfeld 2008; Durant et al. 2010), and demonstrate that 98% of the aerosols are of natural origin (12100 Tgy^{-1}) and only 2% are of anthropogenic productions (300 Tgy^{-1}). This large percentage of natural aerosols is dominated by sea salts and mineral dust. Anthropogenic aerosols are dominated by industry dust and black carbon.

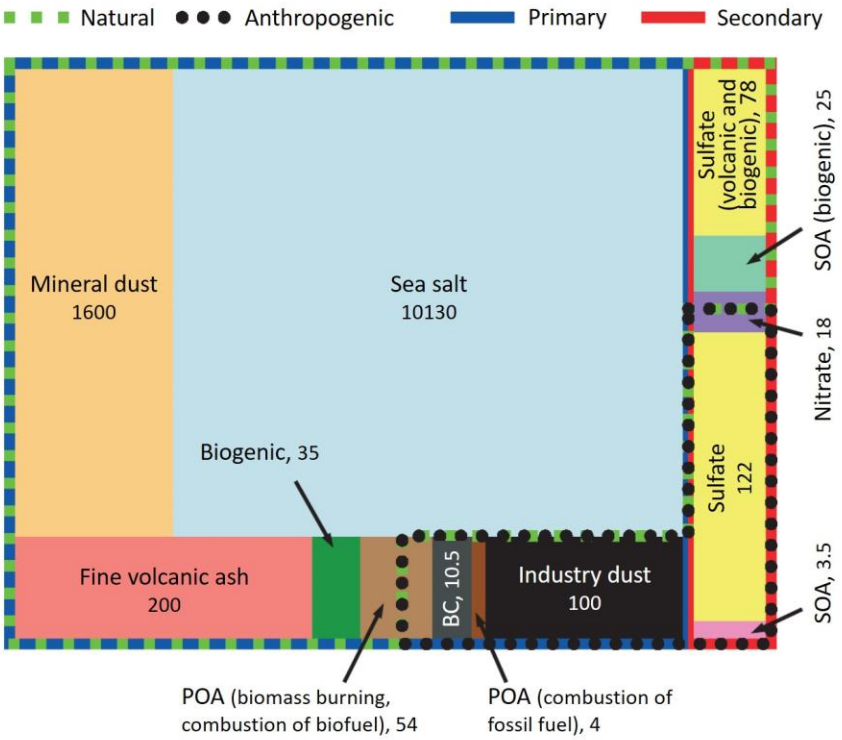

Figure I-1-1 Primary and secondary atmospheric particle matter (PM), expressed in teragram per year (1 Tg = 10^9 kg) and shown as a fraction of the area of a rectangle. POA = primary organic aerosol; SOA = secondary organic aerosol; BC = black carbon.

1.2. Contributions of the atmospheric aerosols to the radiative forcing

According to the Intergovernmental Panel on Climate Change (IPCC), "*radiative forcing is a measure of the influence a factor has in altering the balance of incoming and outgoing energy expressed in Watts per square meter (Wm^{-2}) in the Earth-atmosphere system and is an index of the importance of the factor as a potential climate change mechanism*". In simple terms, the radiative forcing (RF) is the net energy per unit area as measured at the top of the tropopause. It is one of the indicators commonly used to understand the energy flux of Earth-atmosphere system and to understand the global climate change.

Atmospheric aerosols play a role on the climate change by directly or indirectly influencing the radiative budget of the Earth-atmosphere system or the planetary albedo that is defined as the ratio between outgoing and incoming energy. Direct effects concern the absorption and the diffusion of the solar radiation (Yu et al. 2006) that both reduce the flux of solar radiation to Earth surface, thus cool down the Earth-atmosphere system. This interaction depends on the physical and chemical properties of aerosols. Indirect effects are due to the interaction between aerosols and clouds, in particular the presence of aerosols can trigger the formation of persistent clouds, and thus affecting the local coverage, via heterogeneous nucleation. This work focuses on the indirect effect of carbonaceous atmospheric aerosols. Figure I-1-2 shows the schematic of the aerosol indirect effects. Generally, clouds reflect part of the solar radiation back to space thus cool down the Earth-atmosphere system. Interactions between aerosols and clouds change the albedo, thus influence the radiative budget. On condition that the content of liquid water in clouds is constant, aerosols increase the cloud droplet number concentration due to their potential role as cloud condensation nuclei (CCN), thus increase the total surface of droplets in clouds. The increase of the total droplets surface decreases the albedo of clouds, which causes the warming on Earth surface (Lohmann and Feichter 2005). This interaction of aerosols on clouds is the “first” indirect effect. On condition that the relative humidity clouds is sufficient, the liquid water content can increase due to the role of aerosols as CCN, thus increase the coverage, height and the lifetime of clouds which are related to the albedo of clouds. This interaction of aerosols on clouds is the “second” indirect effect. Indirect effects occur on clouds situated at different altitude. Specifically, contrails and cirrus-like clouds formed by aerosols as ice nuclei (IN) occurring in high troposphere are considered to increase the RF of climate (Burkhardt and Kärcher 2011).

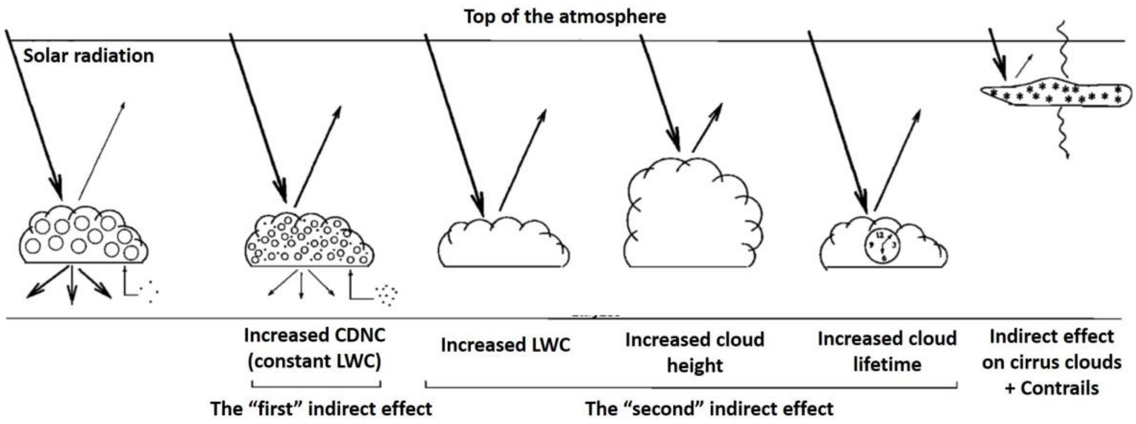

Figure I-1-2 Schematic of the aerosol indirect effects (Haywood and Boucher 2000)**. CDNC means cloud droplet number concentration, and LWC is the means liquid water content.**

The estimated contributions (Stocker et al. 2013) to the RF of climate change due to greenhouse gases, short lived gas and aerosols are presented in Figure I-1-3. Many researches demonstrate that greenhouse gases such as CO_2 and CH_4 have large positive contributions to the RF (Ehhalt et al. 2001). Short lived gas such as CO, non-methane volatile organic compounds and NO_x contribute to the RF as well. Aerosols and clouds give significant contributions to the RF as well. Inorganic aerosols (sulfate, nitrate, sea salts, mineral dust, etc.) have negative RF. However black carbon aerosols are estimated as +0.65 [+0.25 to +1.15] Wm^{-2}, which is around one-third of the global mean radiative forcing of CO_2 (Boucher et al. 2013; Bond et al. 2013). The RF due to aerosol-radiation interactions and aerosol-cloud interactions are generally considered to be negative. However, the RF of clouds (contrails for example) formed by black carbon aerosols due to the indirect effects is positive and also reported in other works (Kärcher et al. 2007; Wong and Miake-Lye 2010; Kapadia et al. 2016). Aerosols have significant contributions on the RF of the climate change due to their direct and indirect effects. It is important to notice that many of the estimated contributions to the RF are affected by large uncertainties. In particular, both direct and indirect effect of black carbon aerosols are still poorly understood due to the complexity of their emission sources, transportation and the interactions with clouds (Blake and Kato 1995; Govardhan et al. 2017; Penner et al. 2018). It is therefore necessary to complete the understanding of the contributions on the RF, thus reduce the uncertainty of the RF due to black carbon aerosols.

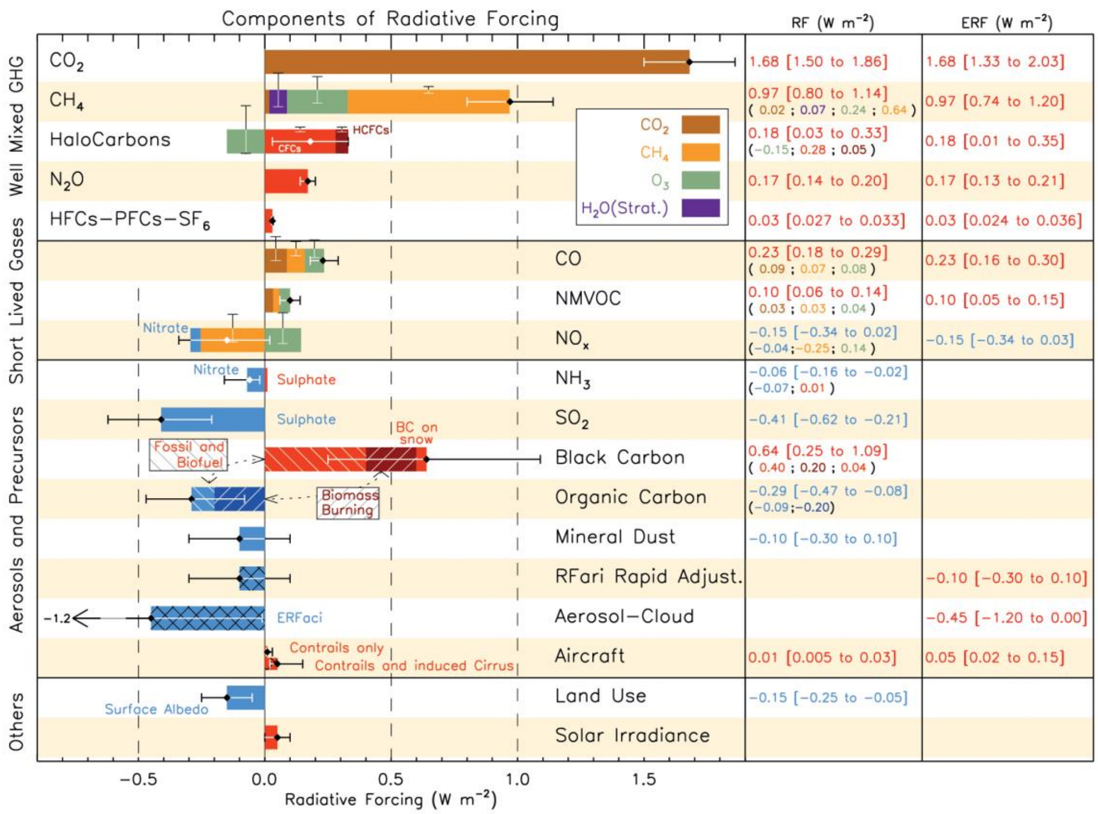

Figure I-1-3 Radiative forcing (RF) during the Industrial Era shown by emitted components from 1750 to 2011 (Stocker et al. 2013)**. The horizontal bars indicate the overall uncertainty, while the vertical bars are for the individual components (vertical bar lengths proportional to the relative**

uncertainty, with a total length equal to the bar width for a ± 50% uncertainty). CFCs = chlorofluorocarbons, HCFCs = hydrochlorofluorocarbons, HFCs = hydrofluorocarbons, PFCs = perfluorocarbons, NMVOC = Non-Methane Volatile Organic Compounds, BC = black carbon.

2. Role of soot particles on the heterogeneous nucleation of atmospheric water and ice

In aerosol community, the term "black carbon" is defined as carbonaceous components having strong light-absorbing properties, while less absorbing carbonaceous aerosol often refer to "organic carbon". Among the different names describing black carbon, the term "soot" is probably the most common (Bond and Bergstrom. 2006). Soot is formed in the incomplete combustion process. Compared to other inorganic aerosols (such as sulfate, nitrate, sea salts, mineral dust, etc.), soot has more complex morphology and complex but chemical composition essentially dominated by of carbon, hydrogen and oxygen, which bring the difficulty and necessity of the understanding its role on the RF.

2.1. Origin and characteristics of soot

The combustion of carbon containing materials exist both in nature and is widely used as a source of power in anthropogenic activities. In ideal conditions, the combustion of hydrocarbons leads to the formation of carbon dioxide and water only following the balanced chemical equation:

$$C_xH_y + (x + y/4)\ O_2 \rightarrow x\ CO_2 + y/2\ H_2O$$

However, in practice combustion is often incomplete and releases other products such as carbon monoxide, unburned hydrocarbons and soot particles.

Soot formation is a very complex process, which particularly depend on the combustion conditions, the fuel, the fuel-to-air ratio, the pressure and the temperature. Figure I-2-1 shows a general schematic of soot formation in the turbulent diffusion flame in which four steps can be identified: formation of soot precursors, nucleation of soot particles, surface growth/coagulation and soot oxidation. A more detailed description of the soot formation can be found in the literature (D'anna, Mazzotti, and Kent 2004; H. Wang 2011; Karataş and Gülder 2012). It is now well agreed that polycyclic aromatic hydrocarbons (PAHs) take an important part in this process

(Richter and Howard 2000) and PAHs are often designated as soot precursors. The mechanism HACA (Hydrogen Abstraction Condensation Acetylene) proposed by Frenklach (Frenklach et al. 1985) is well established to explain the formation of many PAHs in flames. Being PAHs thermodynamically stable compounds, they are often found adsorbed on the surface of the soot particles within the flame or in the exhausts and contribute significantly to the soot particle reactivity once in the atmosphere.

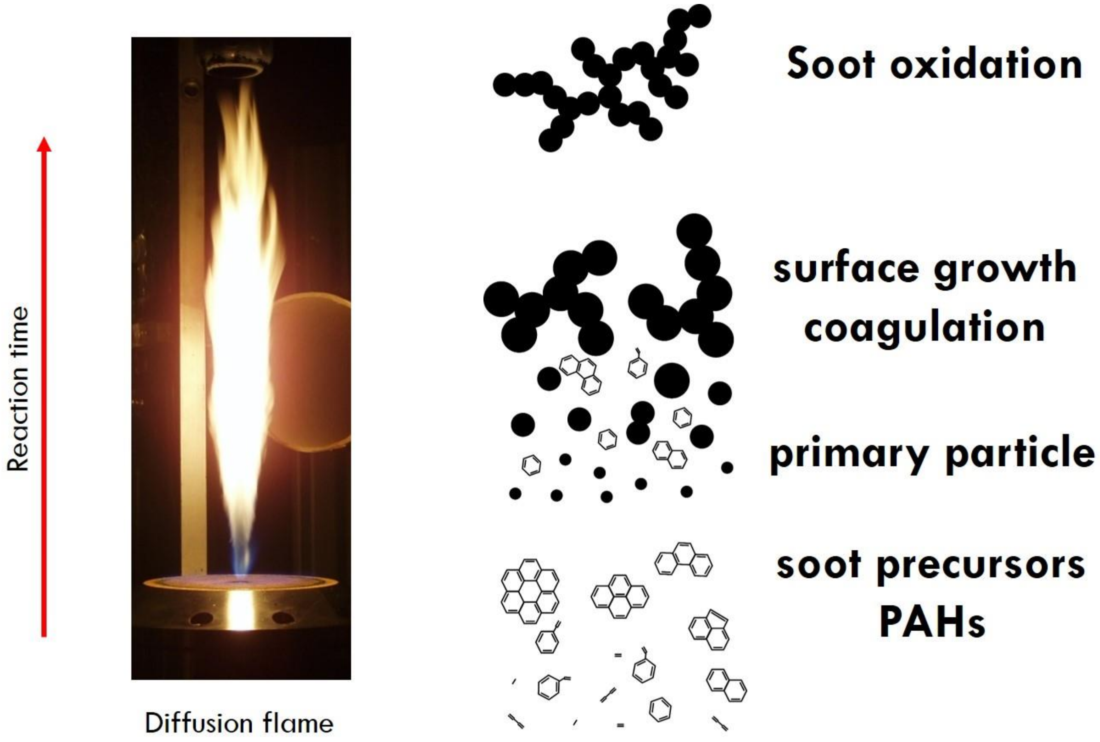

Figure I-2-1 Schematic representation of soot formation and evolution in a diffusion flame.

The transformation from molecular precursors to the first soot nuclei (~2 nm) is still poorly understood and subject of much research (Desgroux et al. 2017). Once the first soot particles are formed, coagulation occurs together with heterogeneous reactions between the nascent soot particles and gas phase species resulting in the increment of their size (surface growth) and of the total volume of the particles. Finally, primary soot particles merge and form complex aggregates.

2.1.1. The morphology of soot

In mathematics, fractal is a subset of a Euclidean space for which its small scale similar patterns increase by doing self-similarity (Mandelbrot 1982). Fractals contain the similar patterns at increasingly small scales and this self similarity is infinite. The morphology of soot aggregates is scale invariant over a relatively small range, therefore fractal-like instead of fractal is the term generally used to describe it (Sorensen 2011; Eggersdorfer and Pratsinis 2014). The morphology of soot particles generally described by the following equation:

$$N_{pp} = k_f \left(\frac{\mathrm{D}_g}{d_{pp}}\right)^{\mathrm{D}_f} \qquad \text{Equation I-2-1}$$

where N_{pp} is the number of the primary particles, d_{pp} is the primary particle diameter, D_g is the gyration diameter, D_f is the fractal dimension which varies from 1 to 3 and k_f is the prefactor.

In the literature, D_f of soot aggregates is estimated by three techniques: angular light scattering (Köylü et al. 1995a; Sorensen et al. 1992), scanning electron microscopy (Colbeck et al. 1997) and transmission electron microscopy (Köylü and Faeth 1992; Cai et al. 1995; Hu et al. 2003). Theoretically, D_f of an aggregate can vary from 1 to 3, where $\mathrm{D}_f = 1$ means the linear configuration and $\mathrm{D}_f = 3$ means the spherical configuration. Figure I-2-2 shows simulated aggregates with different D_f from 1.5 to 3.

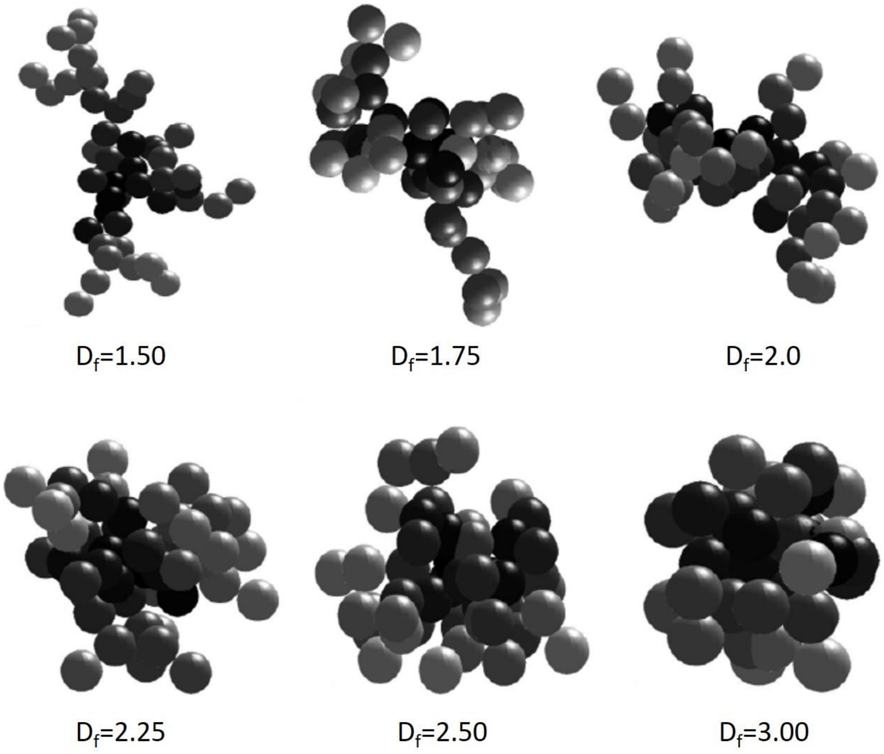

Figure I-2-2 Morphology of aggregates with different D_f (OUF 2006)**.**

2.1.2. Evolution of soot characteristics with combustion environment

The molecular precursors participating to soot formation and found adsorbed on soot particles can be as small as PAHs containing 3-7 aromatic cycles (14-24 carbon atoms, 150-300 u), or as large as tens of aromatic cycles and hundreds of carbon atoms (Faccinetto et al. 2011). The former is comparatively rich in hydrogen and therefore tend to be very reactive, while the latter are richer in carbon and tend to be more inert. Figure I-2-3 shows the evolution of the mass

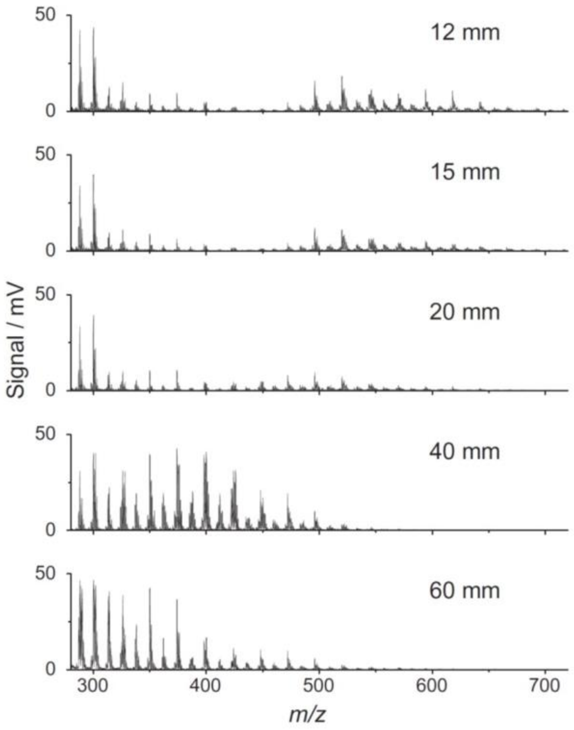

Figure I-2-3 Mass spectra of soot sampled from low pressure methane flame at HAB from 12 to 60 mm. (Faccinetto et al. 2011)

spectra of PAHs adsorbed on soot surface as function of their residence time in the flame (i.e. as function of the height above the burner HAB). It illustrates the fact that soot is not a unique entity from the chemical point of view but on the contrary can span a large variety of chemical coverage and of H/C ratios.

For instance, Figure I-2-4 presents the variation of the H/C ratio of soot particles collected at short residence time (so-called young soot) or long residence time (so-called mature soot) in flames of different fuels. The longer the residence time, the lower the H/C ratio. Also the H/C ratio is strongly dependent on the structure of the fuel (cyclic or aliphatic).

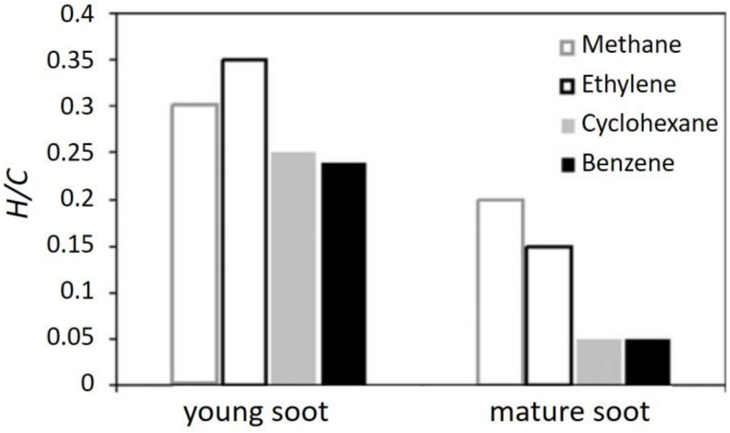

Figure I-2-4 H/C atomic ratio of young and mature soot issued from methane, ethylene, cyclohexane and benzene combustion. (Alfè et al. 2009)

The maturity of soot affects the morphology of soot particles as well. Mature soot particles are well organized in onion-like structures consisting of shell nanostructures while young soot particles appear much more amorphous as shown on TEM images of young soot and mature soot presented in Figure I-2-5. Also, mature soot primary particles often constitute longer and complex aggregates in comparison with young soot particles.

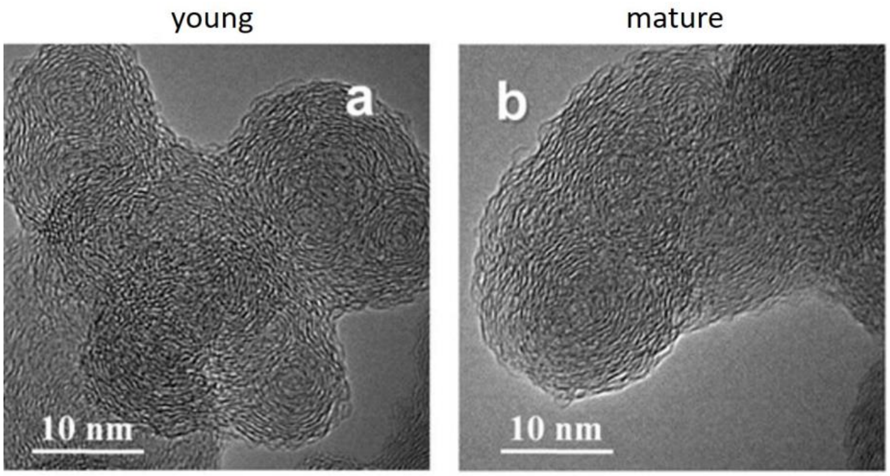

Figure I-2-5 TEM images of young (a) and mature (b) ethylene and benzene soot. (Alfè et al. 2009)

This variability of morphology and chemical composition of soot with the combustion conditions (residence time, fuel, etc.) may impact their reactivity in the atmosphere and their propensity to form CCN or IN.

2.2. Hygroscopic properties of soot as CCNs and INs

Figure I-2-6 shows the classical thermodynamics (p, T) phase diagram of bulk pure water. Crossing the lines that represent thermodynamic equilibrium conditions (green in the figure) trigger a phase transition. However, for especially slow phase transitions, the stability of the original phase can be extended in a (p, T) thermodynamics region in which that phase would not be otherwise stable. This so-called metastable phase in practice allows crossing the equilibrium line without changing the original phase. For example, metastable phases include relative humidity $RH > 100\%$ (water vapor supersaturated conditions), and liquid water at $T < 0°\mathrm{C}$ (supercooled liquid water). Metastable conditions like water vapor supersaturation are very common in clouds. In fact, in the classical nucleation theory aerosol particles facilitate the phase transition by reducing the free energy barrier to the formation of the droplet/particle surface, and for instance reduce the supersaturation SS ($SS = RH - 1$) required for the formation of water droplets (Pruppacher and Klett 2012). Soot particles are considered as well to trigger the cloud condensation nucleation (CCN in red region) of vapor to liquid transition and ice nucleation (IN in blue region) of vapor and liquid to solid transition (Hoose and Mohler 2012).

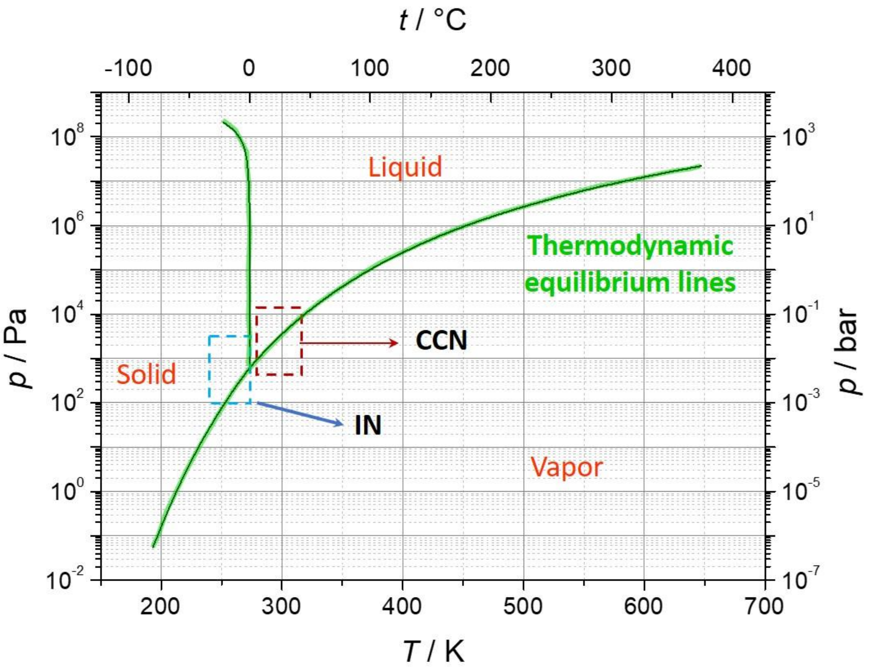

Figure I-2-6 Water phase diagram. CCN = cloud condensation nucleation, IN = ice nucleation.

2.2.1. Fresh and aged soot as cloud condensation nuclei (CCN)

Freshly emitted soot particles are generally considered as poor IN or CCN (Hoose and Mohler 2012). The activation of aerosols is generally described by using the activated fraction (F_a) which is defined as the ratio of the water droplets number to the total particles number. F_a is an important indicator to know the activation of soot particles on the formation of water droplets. The studies of the hygroscopic properties of soot as CCNs are shown in Table I-2-1. All studies on fresh soot as CCNs demonstrate that F_a of soot is basically zero even at SS=15%.

Table I-2-1 Activated fraction (F_a) of fresh soot as cloud condensation nuclei in supersaturation.

Author	Nature of fuel	SS (%)	Activated fraction (F_a)
(Tritscher et al. 2011)	Diesel	1.35%	0
(Wittbom et al. 2014)	Diesel	2%	<1%
(Zuberi et al. 2005)	methane and n-hexane soot	15%	0
(Lambe et al. 2015)	Ethylene	1.8%	0
(S. Grimonprez 2016)	Diesel, kerosene (Jet A1) and commercial pure carbon	1.6%	<0.1%

(Maskey et al. 2017)	Pure carbon powder	0.5%	<0.1%

Nevertheless, many works (Table I-2-2) show the change of the hygroscopic properties of soot after the exposure of soot to oxidizing conditions that include O_3 (Kotzick et al. 1997; Wittbom et al. 2014; Grimonprez et al. 2018), NO_3^- (Zuberi et al. 2005), OH^- (Zuberi et al. 2005; Lambe et al. 2015), or organic hydrocarbon species (Wittbom et al. 2014; Lambe et al. 2015). UV radiation (Tritscher et al. 2011; Lambe et al. 2015) also may have a strong impact. Atmospheric aging experiments in the laboratory are performed in reactors and simulation chambers. Hygroscopic properties of soot are generally determined at supersaturation conditions provided by condensation nuclei counters (VSCNC or CCNc in Table I-2-2). H-TDMA is used to study the water uptake of soot in undersaturated conditions. Kotzick et al. reported that exposure to O_3 decreases the SS to activate soot particles, and half of soot particles are activated to form water droplets at SS=14.6% (Kotzick et al. 1997). The same effects have been found for OH^-, UV radiation and organic HC. Particularly, after aging with OH^-, half of soot particles are activated at SS as low as 0.35%.

Table I-2-2 Works of the impact of atmosphere aging with O_3, NO_3^-, OH^-, UV radiation and organic hydrocarbons on hygroscopic properties of soot.

Author	**Experiments**	**Nature of soot**	**Reactive**	**Experimental setup**	**Soot particle diameter**	**SS at F_a=0.5 (%)**
(Kotzick et al. 1997)	Laminar flow reactor (1.3 L)	GfG 1000 (Palas GmbH, Karlsruhe)	O_3	VSCNC*	d_m=100 nm	14.6
(Zuberi et al. 2005)	Flow tube	Methane and n-hexane	O_3 H_2O OH UV (254 nm) HNO_3	FCOM**	d_{TEM}=440 nm	2
(Tritscher et al. 2011)	Simulation chamber (27 m^3)	Diesel motor (EURO 2) Diesel motor (EURO 3)	UV (290 nm and 400 nm)	CCNc H-TDMA***	d_m=300 nm	0.5
(Wittbom et al. 2014)	Simulation	Diesel motor (EURO 2)	Toluene xylene O_3 UV (354 nm)	CCNc	d_m=150 nm	0.8

	chamber (6 m^3)	CAST (propane)				
(Lambe et al. 2015)	Flow reactor	Premixed flat burner flame of ethylene	H_2SO_4 α-pinene m-xylene O_3 OH UV (254 nm)	CCNc	d_m=220 nm	O_3: 1.5 OH^-: 0.35
(Symphorien Grimonprez et al. 2018)	Simulation chamber (50 L)	Diffusion flame of kerosene and diesel	O_3	CCNc	d_m=150 nm 300 nm 400 nm	1.4

*VSCNC: Variable supersaturation condensation nucleus counter

**FCOM: Flow-cell optical microscopy

***H-TDMA: Hygroscopic Tandem Differential Mobility Analyzer

2.2.2. Current study on the ice nucleation of soot

Many experiments have been performed to understand the ice nucleation of soot in atmospheric simulation chambers. The detailed descriptions are concluded by Hoose (Hoose and Mohler 2012). The ice nucleation concerns the deposition nucleation and freezing nucleation. In deposition nucleation, ice is formed directly from an environment supersaturated with respect to ice but not supercooled water. In freezing nucleation, ice is formed from an environment supersaturated with respect to both ice and supercooled water. Thus, ice could be either formed by the water droplets formed by aerosols which act as CCN (immersion freezing and condensation freezing) or formed by the supercooled water in contacted with a particle (contact freezing). Table I-2-3 shows part of the experiments on the study of deposition nucleation (Hoose and Mohler 2012). Soot particle diameter in the deposition nucleation is generally from nm to µm. The residence time varies from 10 s to 20 minutes. The activated fraction of soot particles on the formation of ice ranges from 10^{-8} to 0.5. From more recent research on the ice nucleation of soot particles, large uncertainty still exists on the ice nucleation of soot particles.

Table I-2-3 Laboratory experiments on the ice nucleation with soot particles (Hoose and Mohler 2012)**.**

Author	Soot source	Soot diameter	F_a	Residence time
(Gorbunov et al. 2001)	benzene/toluene combustion generator	0.02 to 2 µm	10^{-8} to 0.5	20 mins

(Kanji et al. 2006)	n-hexane flame	0.5 to 5 μm	10^{-5}	40 to 60 s
(Crawford et al. 2011)	CAST propane	300 nm	0.001 and 0.01	24 to 86 s
(Friedman et al. 2011)	CAST propane	100 to 400 nm	0.01	12 s
(Kulkarni et al. 2016)	Diesel generator	200 nm	0,1	12 s
(Mahrt et al. 2018)	Mini-CAST propane Lamp black soot	400 nm	0.01 to 0.2	16 s

3. Motivation

Soot particles are emitted in the atmosphere from a wide variety of combustion sources that range from engine and industry emissions to biomass burning. The residence time of the particles in the atmosphere strongly depends on their size and can be as long as thousands of hours for submicron particles. During this time, the particles are subjected to a potentially huge variety of different interactions with the atmospheric environment that often result in dramatic modifications of their physical and chemical properties (*atmospheric aging*). For instance, among these processes, the adsorption of organic species from the gas phase, the internal mixing with other atmospheric aerosols and the oxidation of the particle surface or of the species they adsorbed can all potentially turn hydrophobic, freshly emitted soot particles in efficient CCN and IN given enough time.

In order to understand the effect of the atmospheric aging on the hygroscopic properties of soot, in this work a series of ideal condition experiments are coordinated in which the main parameters believed to play an important role on the activation process are isolated and investigated one by one, compared before and after aging in controlled conditions in atmospheric simulation chamber, and related to the hygroscopic properties of the analyzed particles. These parameters are the particle size distribution, morphology and surface chemical composition.

The particle size distribution and morphology of soot particles generated in a well-controlled laboratory jet diffusion flame supplied with kerosene are estimated from the electrical mobility diameter and electron microscopy images, respectively. The classical thermodynamics κ-Köhler theory is modified to include parameters representative of the particle size distribution and morphology like the geometric deviation and the fractal dimension, and the calculated activation curves are compared to the experimental data to validate the model.

The surface analysis of fresh and aged particles provides a list of the chemical compounds initially adsorbed on the particles surface, and of those formed after the atmospheric aging. The activation of soot particles in conditions that simulate the troposphere is the subject of a large number of experimental investigations that aim to understand the link between hygroscopic properties and chemical composition of the soot particles. In particular, this work focuses on the interaction of fresh soot particles with three important atmospheric species, OH^-, O_3 and SO_2.

Finally, advances in the development of the continuous flow diffusion chamber *Lille ice nucleation chamber* (LINC) are presented that aim to understand the role of soot particles as IN.

A brief summary of the topics discussed in each chapter is provided below.

Chapter 2 describes the experimental setup and protocol used for studying the hygroscopic properties of soot under controlled conditions of temperature, pressure and relative humidity in two simulation chambers: the *Lille atmospheric simulation chamber* (LASC) in laboratory PC2A and the *experimental multiphasic atmospheric simulation chamber* (CESAM) in laboratory LISA. The activated fraction of aerosols is measured in the range of 0-2% of SS at room temperature with a commercial cloud condensation nucleation counter.

Chapter 3 is devoted to the theory of the heterogeneous nucleation of water droplets: κ-Köhler theory. The thermodynamics of pure water and the heterogeneous nucleation of water droplets are described using the tools of classical thermodynamics. A modified κ-Köhler model is developed that takes into account the size distribution and morphology of fractal-like aerosol particles and presented in this chapter. The model is able to reproduce a large data set of activation curves that present F_a as function of SS, observed experimentally on ammonium sulfate aerosols and on soot oxidized by OH^-.

In Chapter 4, we investigate the evolution of the hygroscopic properties of soot exposed to O_3 and SO_2 as a function of the reaction time. Experiments are performed in the LASC and in the CESAM. Because experiments can be as long as 400 min, a thorough investigation of the morphology of soot particles as a function of time using electron microscopy has been performed in parallel. Operating conditions have been found that limit the particle coagulation, while ensuring the minimum particle concentration required for measurements in the CCNc. Finally, κ of soot particles is obtained for a wide range of exposure to OH^-, O_3 and SO_2.

Chapter 5 gives the chemical composition information of fresh and aged soot particles sampled during experiments in the LASC and in the CESAM in order to understand the role of the surface chemistry on the hygroscopic properties of soot. The chemical analysis of soot is performed using secondary ions mass spectrometry. In order to extract useful information from the treated mass spectra, principal component analysis and hieratical cluster analysis are performed in parallel. This strategy highlights some chemical modifications on soot surface during the aging processes.

Finally, Chapter 6 describes the latest advancements in the development of the LINC for investigating the role of soot particles as IN. Chapter 6 presents the configuration of this facility and shows the preliminary tests on the ammonium sulfate aerosols in deposition nucleation mode.

Chapter II Experimental description

1. Introduction

In this chapter we present the experimental devices used in this Ph.D. for studying the hygroscopic properties of soot and salt aerosol particles. Figure II-1-1 shows a global view of the experimental facility that contains basically three main parts: the aerosol generation system, the atmospheric simulation chamber, and the measurement system. The aerosols can be either characterized online (bypassing the simulation chamber) or injected into the simulation chamber to study the evolution of the chemical and physical properties of aerosols in the controlled atmospheric conditions.

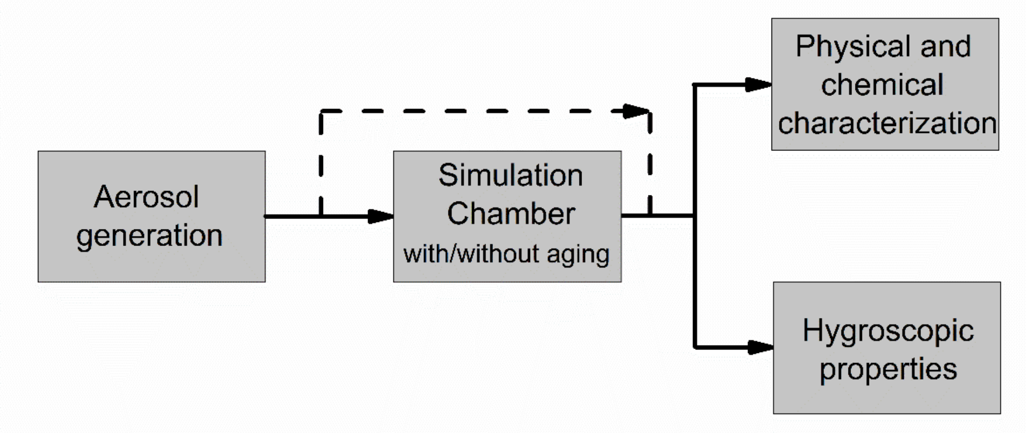

Figure II-1-1 Global view of the experimental set-up for studying soot aerosols and salt aerosols.

Salt aerosols and soot aerosols are generated by atomization (Annex C) and a laboratory diffusion flame (section II-2.2), respectively. The experimental study of ammonium sulfate aerosols is performed in the *Lille atmospheric simulation chamber* (LASC) with a volume of 124 L at PC2A and this work is presented in chapter 3. The study of the atmospheric aging of soot particles is carried out on two scales, in the already mentioned atmospheric chamber LASC at PC2A and in the *experimental multiphasic atmospheric simulation chamber* (CESAM) of 4.2 m^3 at the Laboratoire Interuniversitaire des Systèmes Atmosphériques (LISA). This work on the study of atmospheric aging is presented in Chapter 4. In this chapter, the generation condition of soot aerosols is examined and selected for the study of the atmospheric aging. Then the two simulation chambers and their accessories are described.

2. Aerosol generation

2.1. Ammonium sulfate aerosol generation

In this thesis, ammonium sulfate aerosol is used for calibrating the dilution ratio of the microprobe used in sampling system (section II-2.2.2), verifying the self-consistency of the model of aerosol activation (chapter 3), and calibrating the Lille Ice Nucleation Chamber (chapter 6). From literature, a dry aerosol is required for studying the hygroscopic properties (M. D. Petters and Kreidenweis 2007). Ammonium sulfate aerosol is generated by atomization in a TSI 3076 model atomizer, then dried by the diffusion dryer system shown in Figure II-2-1. Ammonium sulfate aerosols coming from the atomizer is still wet. The impactor stops the largest droplet and the diffusion dryer containing silica gel ensures aerosols passing to a dry environment. In practice, the relative humidity measured after this generation set-up is lower than 1%.

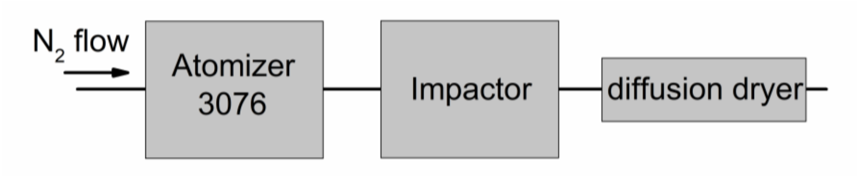

Figure II-2-1 Ammonium sulfate generation set-up.

According to the manual of the atomizer 3076, both the inlet flow rate and the concentration of the solution influence the total concentration and the size distribution of the aerosols (LIU and LEE 1975). Figure II-2-2 shows an example of the size distribution generated by the atomizer with the concentration of the ammonium sulfate solution of 0.1 gL^{-1}. The atomizer works with the nitrogen inlet flowrate between 1.5 $Lmin^{-1}$ and 3 $Lmin^{-1}$. The size mobility distribution of the ammonium sulfate aerosols is recorded by SMPS (Annex A) and follows a lognormal distribution. Increasing the flow rate, the total concentration of the ammonium sulfate particles in the aerosol increases, but the mode of the distribution is basically constant.

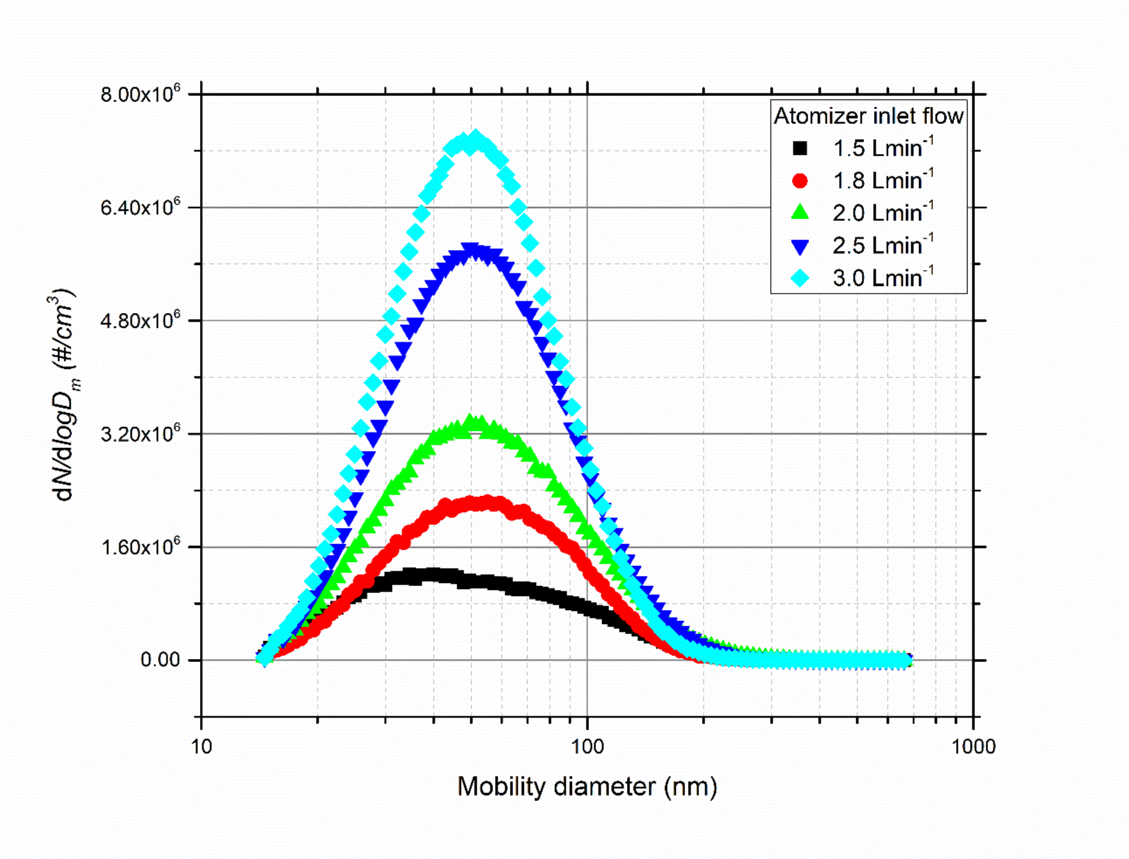

Figure II-2-2 Size mobility distribution of the ammonium sulfate aerosols generated by the atomization system. The black, red, green, blue and cyan solid dots represent the size mobility distribution with the nitrogen inlet flow rate of 1.5, 1.8, 2.0, 2.5 and 3.0 Lmin^{-1}, respectively.

2.2. Soot generation form a kerosene diffusion flame

In this work, all studied soot particles are extracted from a turbulent diffusion flame supplied by kerosene (Jet A1). This diffusion flame is piloted by a flat flame supplied by CH_4/air. Soot particles are extracted by a sampling system based on a quartz microprobe and nitrogen dilution flow. The dimension of soot particles generated depends on the height above the burner (HAB) and dilution ratio.

2.2.1. Description of the burner

The diffusion flame is stabilized on a commercial modified McKenna burner which is well described by Romain Lemaire (Lemaire, Maugendre, et al. 2009). In Figure II-2-3, on the top of the burner, a water cooled porous sintered plug with a diameter of 60 mm supports the pilot

CH_4/Air flame (equivalence $\mathrm{ratio} = 0.96$) at the atmospheric condition. In the center of the burner, a coaxial orifice with a diameter of 6.35 mm allows the insertion of a fuel injector.

In this work, a commercial Direct High Efficiency Nebulizer-170-AA-0.2 is used to generate the liquid fuel spray. The inner diameter of the capillary is 104 μm and its thickness is 15 μm. On the top of the capillary part, a low-speed liquid jet is injected at the central axis of a high-speed coaxial nitrogen jet, the liquid break-up and the droplet atomization phases can be divided into spray.

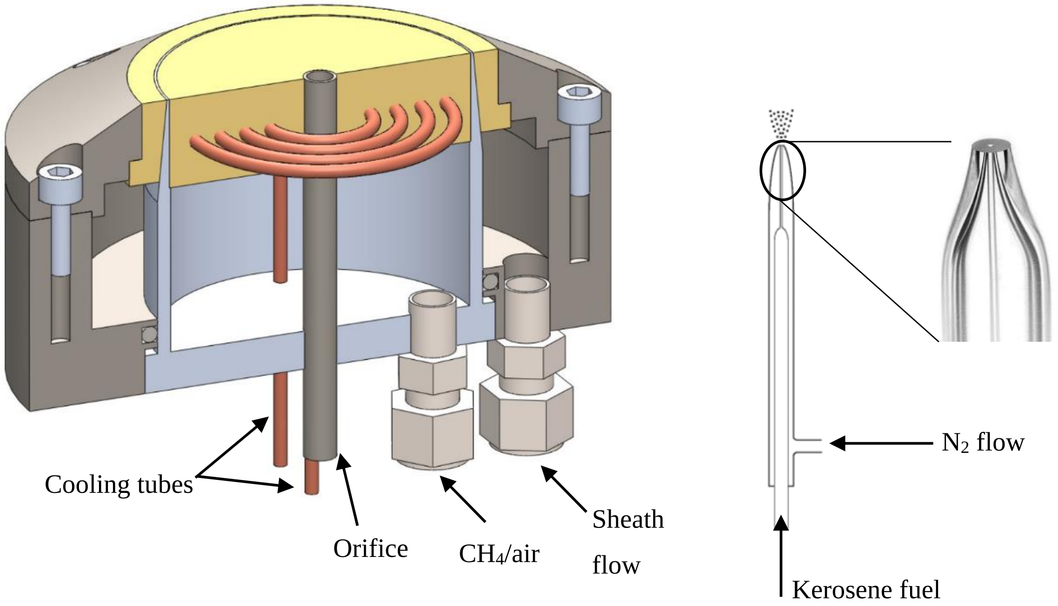

Figure II-2-3 Configuration of the modified McKenna burner and the model 170-AA nebulizer.

2.2.2. Sampling system for soot particles

The sampling system is based on a dilution quartz microprobe which contains two coaxial tubes presented in Figure II-2-4. On the tip of the outer tube, an orifice with a diameter of 130 μm is obtained by erosion with emery paper. Dilution gas enters between the tubes from the side port and exits from the inner tube from the back port. The inner tube section and the section between two tubes are the same for avoiding the differential pressure caused by gas flow change. Once the pressure at the exit of inner tube decreases, the differential pressure between the atmosphere and the microprobe forces gas and soot aerosols to enter the tip of the microprobe, then to be diluted by dilution gas.

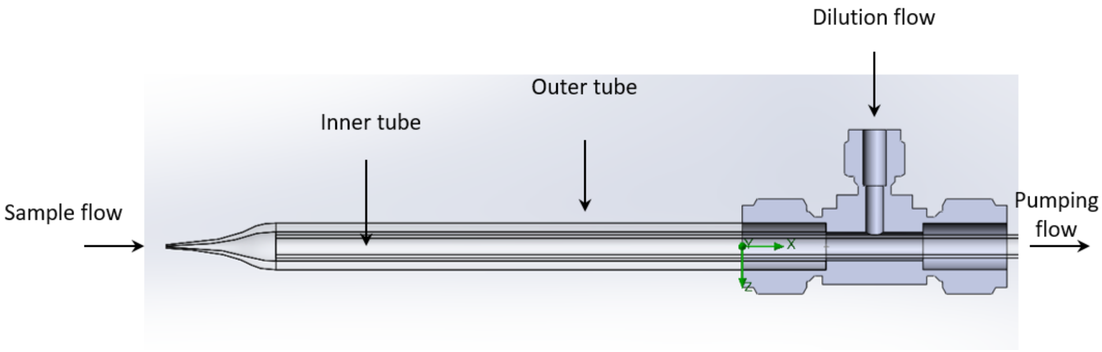

Figure II-2-4 Configuration of the sampling microprobe.

The dilution during sampling limits the condensation of water vapor and the coagulation of particles. The dilution factor is defined as function:

$$Q = \frac{[aerosol]_b}{[aerosol]_a} \qquad \text{Equation II-2-1}$$

where Q is the dilution factor, $[aerosol]_{bd}$ is the aerosol concentration before entering the microprobe and $[aerosol]_{ad}$ is the soot concentration after the dilution.

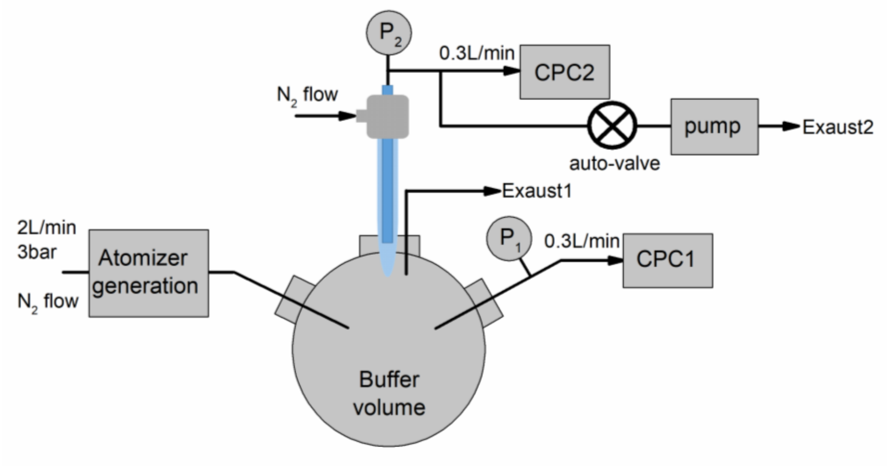

Figure II-2-5 Calibration set-up of the dilution factor used in the sampling microprobe.

In order to know the dilution factor, the microprobe is calibrated by ammonium sulfate aerosol with using the calibration configuration presented in Figure II-2-5. Atomizer TSI provides the ammonium sulfate aerosol with a stable concentration and measured by two condensation particle counters (CPC presented in Annex B) to know aerosol concentration before and after the dilution. The automatic valve (Leybold Vaccum, type MOVE 1250) and the pressure gauge (Pfeiffer 1000 torr) make it possible to regulate the pressure in real time and thus to maintain a stable and precise differential pressure Δp between before (p_1) and after (p_2) the microprobe. Figure II-2-6 shows the concentration of ammonium sulfate recorded by the two CPCs. The blue and black dots represent $[aerosol]_b$ and $[aerosol]_a$, respectively. During the calibration of the microprobe, $[aerosol]_b$ is kept stable around 2×10^5 cm^{-3}. $[aerosol]_a$ is initially stable around 1000 cm^{-3}, then decreases due to the change of the Δp . When Δp is stable, we take the average of $[aerosol]_b$ and $[aerosol]_a$ during the last 90 s before changing Δp to determine the dilution ratio experimentally.

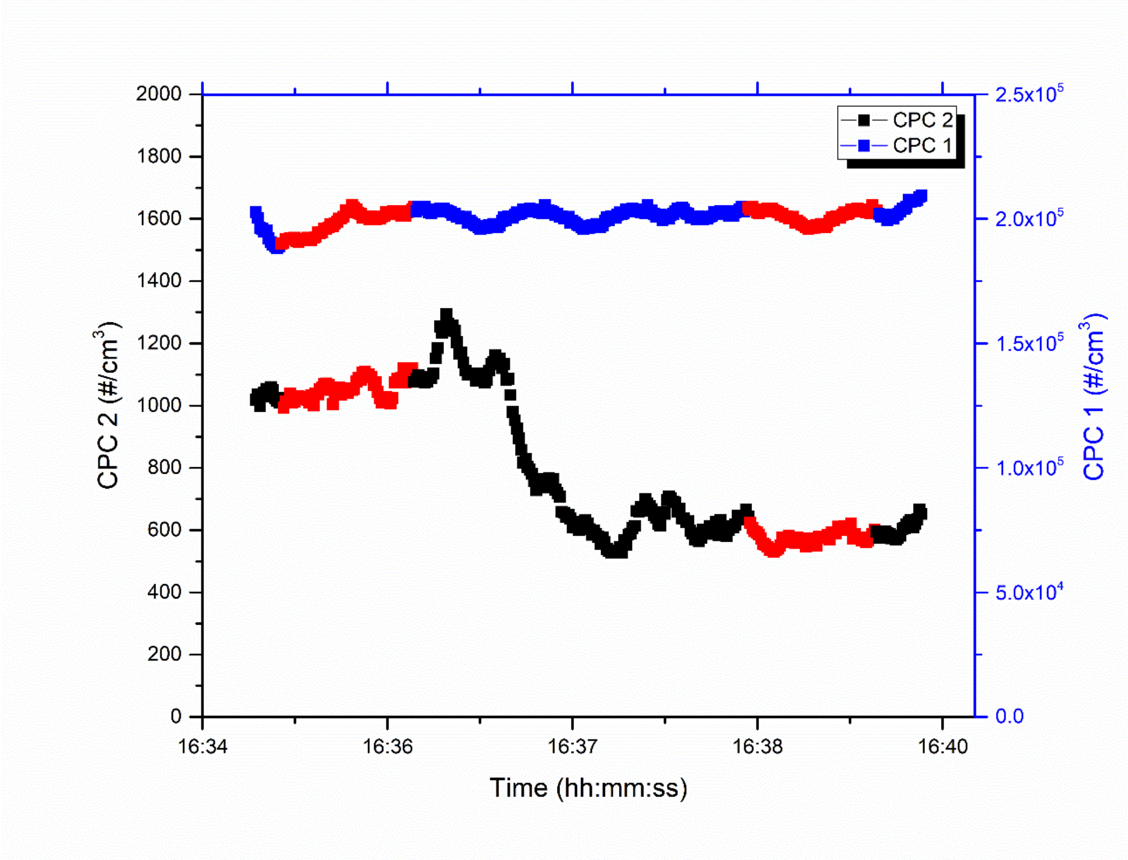

Figure II-2-6 Recording of the concentration of the ammonium sulfate by the two CPCs.

Appling the previous method, the dilution ratio is examined with the different nitrogen dilution flowrate: 2, 6 and 15 Lmin^{-1}. The CPCs record the concentration of ammonium sulfate as a function of the differential pressure Δp from 0 to 100 mbar. The dilution ratio of this microprobe is presented in Figure II-2-7. With 15 Lmin^{-1}, Q can be as high as 2500 with a stable Δp. With the same Δp, the higher dilution flowrate, the higher the dilution ratio.

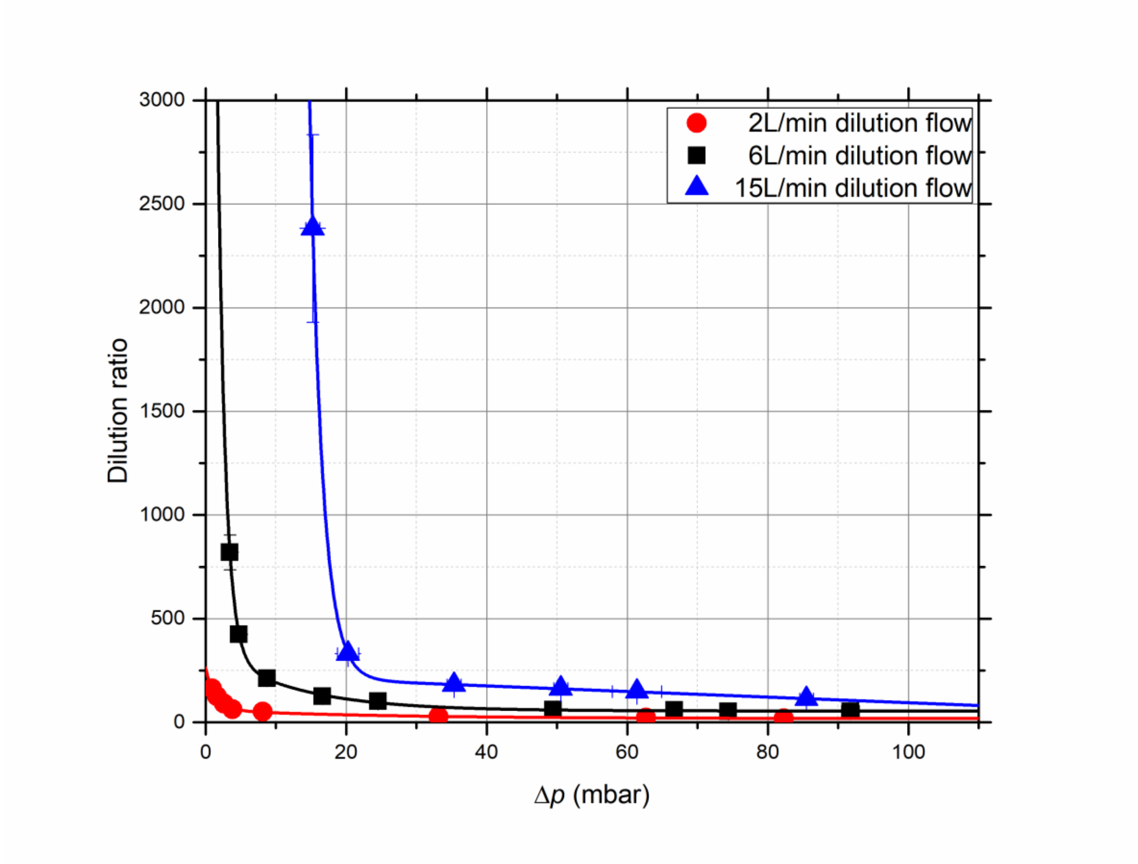

Figure II-2-7 Dilution ratio of the sampling microprobe against differential pressure for different dilution flows. Red, black and blue solid dots represent the dilution ratio with the dilution flowrate of 2, 6 and 15 Lmin^{-1}, respectively. The lines represent the exponential fits of the dilution ratio data.

2.2.3. Size mobility distribution profile in the diffusion flame

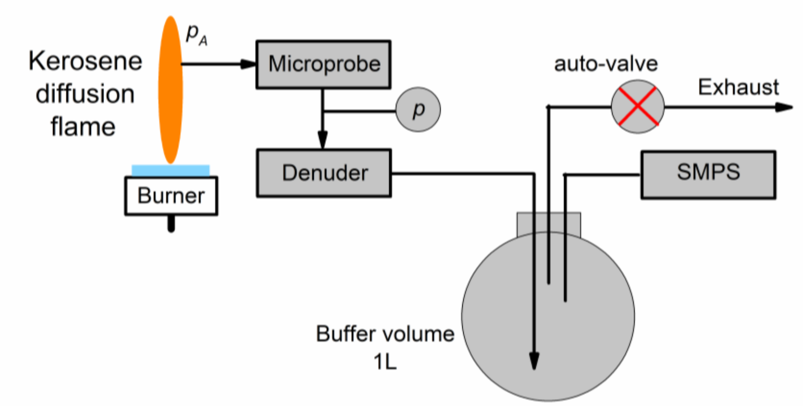

Figure II-2-8 Configuration of the set-up to characterize the size mobility distribution of soot particles in the flame.

The size mobility distribution of soot particles in the diffusion flame is characterized online by using the set-up shown in Figure II-2-8. The soot particles are extracted by microprobe with Δp controlled by auto-valve. The denuder after the microprobe lower the partial pressure of the condensable gas. Then, soot particles are injected into a buffer volume required to stabilize the concentration prior SMPS measurements.

The left panel in Figure II-2-9 represents the size mobility distribution of soot particles at HAB = 120mm with the dilution parameters of $Q_{N_2} = 6$ Lmin^{-1} and $\Delta p = 4$ mbar. The size mobility distribution follows a lognormal distribution and the peak represents the mode of the distribution. The effect of the coagulation or agglomeration on the size mobility distribution is unknown. To minimize sampling artifacts, we sampled the different flames at the same HAB several times by changing Δp during the sampling, then compared the resulting size distributions. The relationship between mode and Δp is shown in the right panel of Figure II-2-9. Black dots represent the mode and the red dash line is the guideline. With increasing Δp, the mode increases. The leftward shift of the mode stops around Δp ~ 3-4 mbar, i.e. we assume that at this Δp, the amount of particles sampled from the flame is too low to trigger coagulation or agglomeration. On one hand, the mobility size distribution of the soot particles extracted after the probe with Δp ~ 3-4 mbar is considered as the measurement "in situ". On the other hand, with playing Δp, the mode of the size distribution changes artificially. This artificial change of the mode is determined and applied in chapter 4 for studying the hygroscopic properties of soot in the simulation chamber.

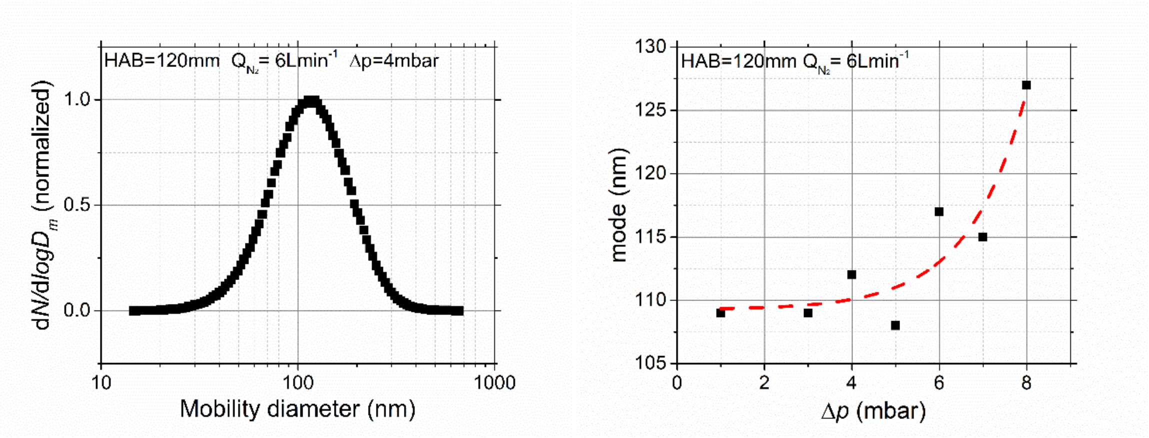

Figure II-2-9 Size mobility distribution of soot particles at HAB = 120 mm (left figure) and the mode of the distribution against Δp (right figure).

According to the calibration result of the sampling microprobe in Figure II-2-7, the dilution ratio is around 700 at the condition that Q_{N_2} = 6 Lmin^{-1} and Δp = 3 mbar. With dilution ratio of 700, the size mobility distribution of soot particles is characterized at different HABs in the flame. Figure II-2-10 shows the mode against HAB. The young soot at lower HAB corresponds to the smaller mobility diameter, and the mature soot at higher HAB corresponds to the larger mobility diameter. At HAB=130mm, the mobility diameter of the soot shows a local maximum.

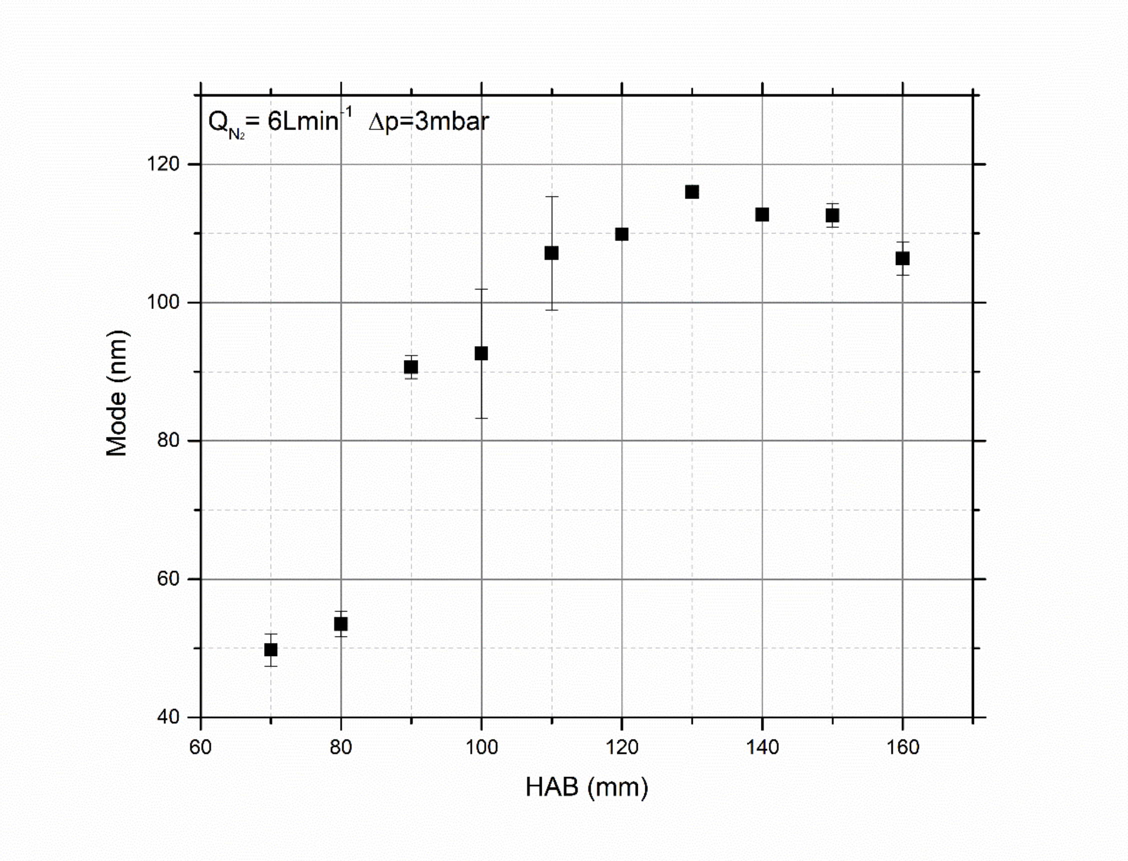

Figure II-2-10 Mode of the size mobility distribution of soot particles against HAB in the diffusion flame.

3. Simulation chamber

Simulation chambers are designed for studying the chemical and physical properties of gas species and/or aerosols in conditions that reproduce the atmospheric environment. Two types of the simulation chamber exist according to their size: outdoor smog chambers and indoor smog chambers. The outdoor smog chambers such as EUPHORE (Bloss et al. 2005) benefit the large volume and the solar light. However, outdoor chambers are necessarily operated at atmospheric pressure. Indoor chambers are generally smaller. They can be made of Teflon (King et al. 2010), Pyrex, quartz or stainless steel (Kirkby et al. 2011). In this section, two indoor simulation chambers and their associated instruments used in this work are presented.

3.1. Lille atmospheric simulation chamber (LASC)

The configuration of LASC located in the laboratory PC2A is shown in Figure II-3-1. It contains a main body and two caps made in Pyrex. The caps are clamped on the top and the bottom of the main body, respectively. On the top cap, four peripheral ports equipped with 1/4 inches stainless steel tubes are connected to the N_2 injection, O_3 injection, aerosol injection, safety valve and pressure gauge. N3S grade nitrogen (purity of 99.999%) was used for filling the chamber and compensating the pressure during the experiment. The ozone is generated by a commercial ozone generator (UVP 97-0067-01). The safety valve prevents the chamber pressure from increasing above 1.5 bar. The pressure is monitored by a commercial pressure gauge (PFEIFFER VACCUM, CMR 361, 0.1 to 1100 mbar). The central port equipped with a long 1/4 inches stainless steel tube extracts the aerosol and gas from the center of the chamber to analyse instruments. In this work, a commercial ozone analyzer (Thermo Environmental Instruments, Model 49C) is permanently installed for monitoring the concentration of ozone in the chamber. On the bottom cap, the fan fixed on the bottom improves the mixing of aerosol and gas in the chamber. The peripheral port equipped with a KF16 connector is connected to the sample collection system such as TEM collection and ToF-SIMS collection. The central port equipped with a KF25 connector is connected to the pump (PFEIFFER VACUUM, model ACP 15) in order to empty the chamber. The LASC is examined with a leak test by isolating the chamber at the pressure of chamber around 0.5 mbar during 3 weeks, and the leak rate is smaller than 10^{-6} $Lmbar^{-1}$.

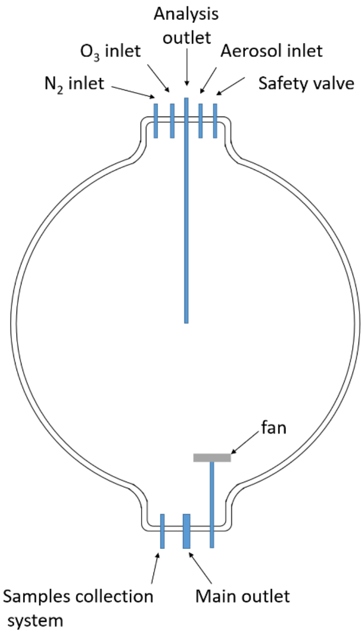

Figure II-3-1 The configuration of LASC in PC2A.

3.1.1. The volume of the LASC

The volume of the LASC was measured as follows: the leak rate is negligible, and we consider an ideal gas condition during the measurement. Initially, the chamber is filled with N_2. According to the ideal gas law, the state of the chamber can be described as:

$$p_b(0)V_b = n_g(0)RT_b \quad \text{Equation II-3-1}$$

where $p_b(0)$ is the initial pressure inside the chamber, V_b is the inner volume of the chamber to be determined, $n_g(0)$ is the initial amount of substance of gas in moles, R is the ideal gas constant and T_b is the ambient temperature of the chamber. Starting from this state, we set the flow rate of the pure nitrogen as a constant value Q_{inlet}. Consequently, the pressure increases and this change can be described as a differential function of Equation II-3-1:

$$\frac{\mathrm{d}p_b(t)}{\mathrm{d}t}V_b = \frac{\mathrm{d}n_g(t)}{\mathrm{d}t}RT_b \quad \text{Equation II-3-2}$$

with

$$\frac{\mathrm{d}n_g(t)}{\mathrm{d}t} = \frac{p_0 Q_{\mathrm{inlet}}}{RT_0} \quad \text{Equation II-3-3}$$

where p_0 and T_0 are the pressure and the temperature in standard condition (273K, 1atm) used for the calibration of mass flow controller (MFC). By combining Equation II-3-2 and Equation II-3-3, the inner volume of the chamber can be obtained as:

$$V_b = \frac{p_0 Q_{\mathrm{inlet}}}{\frac{\mathrm{d}p_b(t)}{\mathrm{d}t}} \frac{T_b}{T_0}$$

Equation II-3-4

With a constant T_b, the inner volume of the chamber is related on Q_{inlet} and $\frac{\mathrm{d}p_b(t)}{\mathrm{d}t}$. We performed five measurements with different Q_{inlet} as shown in the Figure II-3-2. The pressure of the chamber is recorded every 30 s. Three tests starting from the pressure around 630 mbar correspond to Q_{inlet} with 2, 3 and 4 Lmin^{-1}. Meanwhile, two tests starting from the pressure around 200 mbar correspond to Q_{inlet} with 5 and 10 Lmin^{-1}. For five tests, pressure is linearly related to time, and the slope represents $\frac{\mathrm{d}p_b}{\mathrm{d}t}$. The inner volume estimated by fives tests are concluded in Table II-3-1.

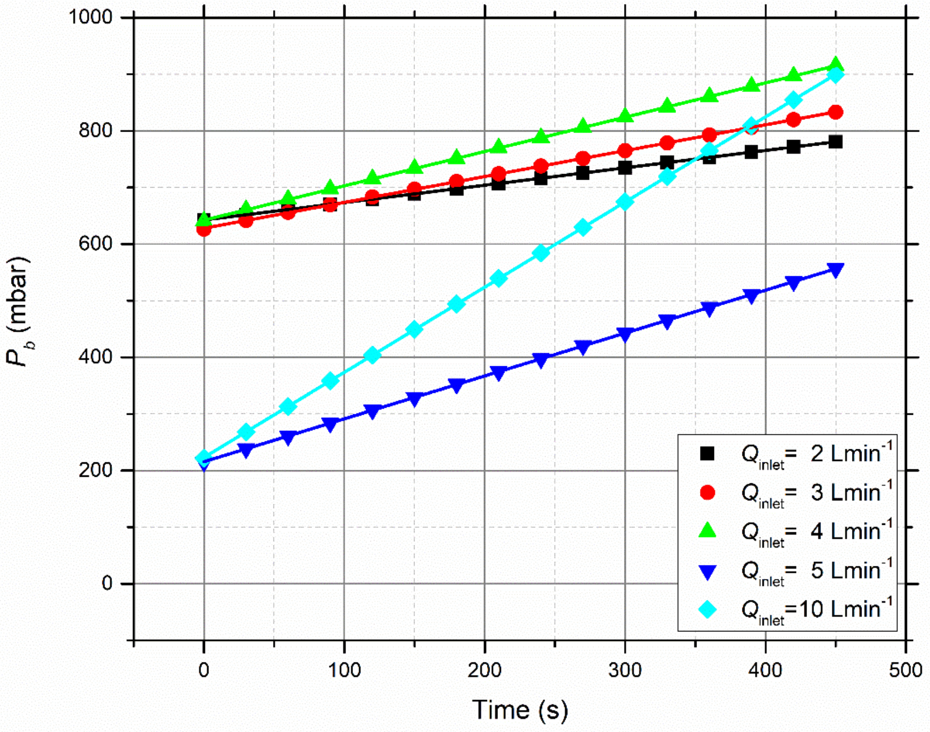

Figure II-3-2 p_b vs t. Black, red, green, blue and cyan dots represent the pressure of the chamber with Q_{inlet} of 2, 3, 4, 5 and 10 Lmin^{-1}, respectively. The lines represent the linear fits of the data.

Table II-3-1 The estimation of the inner volume of the giant glass chamber.

Q_{inlet} (Lmin^{-1})	2	3	4	5	10	Average
Volume (L)	124.8	124.2	124.0	123.5	123.5	124.0±0.5

3.1.2. Ozone generation

The ozone used in the LASC is generated by a continuous flow ozone generator (UVP, model 97-0067-01). It provides a stable radiation source with the wavelength of 185 nm, which photolyzes the oxygen into two oxygen atoms. Each oxygen atom then quickly combines with an oxygen molecule to form an ozone molecule.

$$O_2 \xrightarrow{hv} 2O$$

$$O_2 + O \longrightarrow O_3$$

The ozone generator was calibrated by using air and pure oxygen with different flow rate as shown in Figure II-3-3. In order to increase the initial ozone concentration, hence decrease the injection time, the pure oxygen is used during the work. The ozone generator can provide an initial ozone concentration as high as 4.5 ppm with oxygen flow rate of 1 Lmin^{-1}.

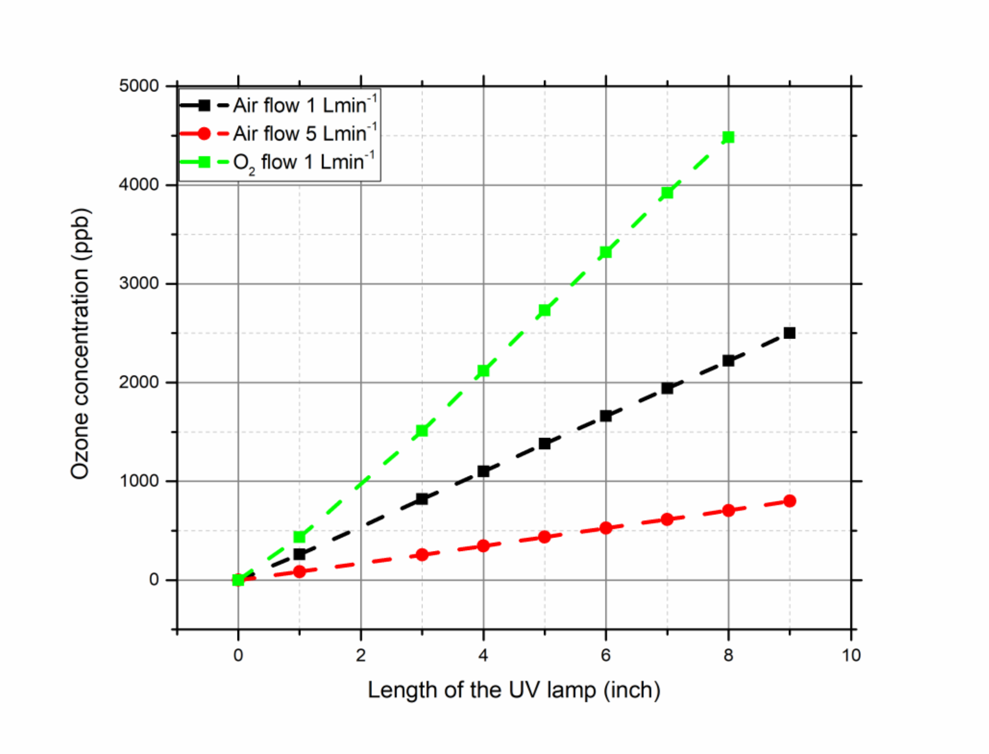

Figure II-3-3 Initial ozone concentration generated by ozone generator against the length of the UV lamp. Black, red solid dots represent the ozone concentration using air with a flow rate of 1 and 5 Lmin^{-1}, respectively. The green dots represent the ozone concentration using pure oxygen with a flow rate of 1 Lmin^{-1}. The dash lines are the guide lines.

3.2. Experimental multiphasic atmospheric simulation chamber (CESAM)

A scheme of the CESAM atmospheric simulation chamber (Wang et al. 2011) is shown in Figure II-3-4. It is a national instrument of the INSU Institute of the CNRS located on the Campus of the University of Créteil.

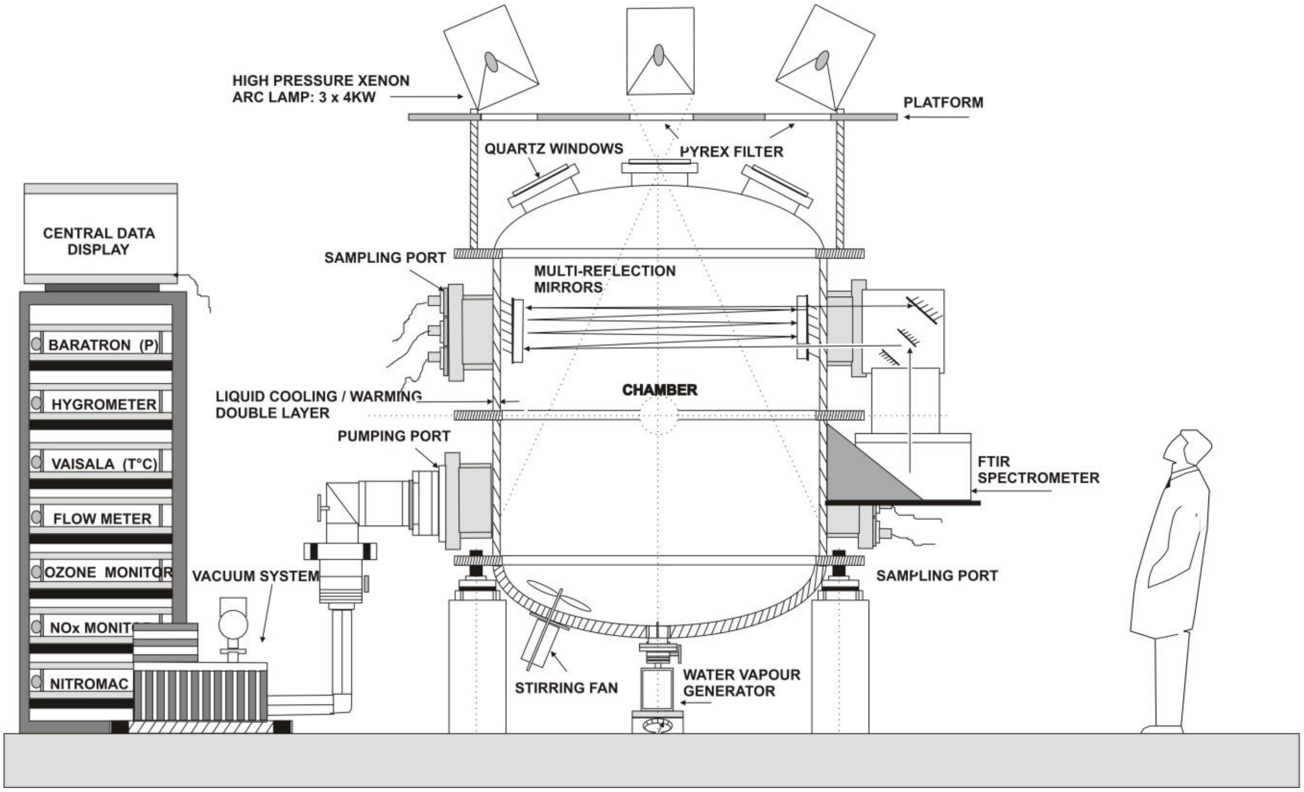

Figure II-3-4 Configuration of the CESAM chamber of laboratory LISA. (Wang et al. 2011)

The CESAM chamber is a stainless-steel atmospheric simulation chamber with a volume of 4.2 m^3 that can be operated over a range of pressure from 10^{-4} mbar to 2000 mbar. The reactor body is made of double layers which allow circulating a warm or cold fluid to control the reactor temperature. A 4-wing stainless steel fan of 50 cm diameter is installed at the bottom of the chamber to improve the mixing. The maximum operational rate can arrive as high as 300 rpm. A cooker is installed on the bottom of the chamber and connected to the port for providing the water vapor. On the side of the chamber, several ports are available for the aerosol generation, the sample collections and other experimental instruments. On the top of the chamber, three high power xenon arc lamps to provide irradiation in the UV are installed. These lamps emit artificial light whose spectrum is close to the solar radiation at noon on the region of Bordeaux in 21st June (Wang et al. 2011). A series of Pyrex windows/filters can be installed on the top of the chamber to adjust the UV spectrum. The lifetime of submicron aerosols in CESAM can be as high as four days. This aspect provides the controlled conditions required for studying the aging processes of aerosols.

CESAM is equipped with a series of analyzers to study the gas phase and the particulate phase. A series of sensors installed permanently inside the chamber to monitor the thermal state of the chamber such as absolute pressure, the temperature and the relative humidity. For the measurement of most common gaseous species, the concentration of O_3, NO_x, SO_2 and CO are measured by commercial instruments APOA-370 from Horiba, APNA-370 from Horiba, Environment SA and AirMOVOC, respectively. Besides, a Fourier Transform Infra-Red spectrometer (FT-IR) interfaced with a multiple path cell is installed for tracing the gas measurements. During the campaign in CESAM, a Proton-transfer-reaction mass spectrometry (PTR-MS) was connected to the chamber in order to follow the concentration of OH^-. For the measurements of aerosol particles, a SMPS comprising a DMA (TSI, model 3080) coupled with a CPC (TSI, model 3010) is used to monitor the sub-micrometer particle number concentration and size mobility distribution.

During the campaign in CESAM, O_3, SO_2 and OH^- are provided as the oxidant reacting with soot aerosol. Ozone generation is provided by a commercial SPA dielectric ozone generator (MBT 802N, Messtechnik GmbH, Stahnsdorf, Germany). O_3 is introduced into the CESAM chamber by performing several short injections with extremely high ozone concentration in order to obtain a concentration of ozone in the chamber of 1.2 ppm precisely and rapidly. SO_2 is introduced by a syringe from one sampling port with a calculated volume to arrive a concentration of 40 ppb in the chamber.

A procedure is performed to generate and measure the concentration of the OH^- in the CESAM atmospheric chamber. The OH^- is produced in this study with the following mechanism:

$$O_3 + hv \rightarrow O(\,^1D) + O_2$$

$$O(\,^1D) + H_2O \rightarrow 2OH$$

The concentration of the OH^- is measured with a tracer whose reaction constant is known. Butanol D_9 is chosen as the tracer. The reaction follows a pseudo-first-order kinetics with rate constant k_{OH}(Butanol D_9) = 3.4×10^{-12} cm^3s^{-1} (Barmet et al. 2012). The Butanol D_9 (40 ppb) is injected into the atmospheric chamber with a relative humidity of 20% and a concentration of 1.2 ppm of ozone. The photolysis of ozone is carried out with the lamps. The concentration of Butanol D_9 is measured by PTR-MS. Knowing the reaction rate k_{OH} and the concentration of the tracer, the concentration of the OH radical is determined.

4. Protocol to measure the activated fraction of aerosol

In general, for studying the hygroscopic properties of aerosol, a DMA associated with an electronic classifier (Annex A) is required to select aerosol with a known mobility size. The concentration of selected aerosol $\mathrm{N_{particle}}$ is recorded by UCPC 3776 (Annex B) and the number of the water droplet $\mathrm{N_{droplet}}$ formed by aerosol particles is recorded by the cloud condensation nuclei counter (CCNc presented in Annex D) in parallel. The activated fraction is defined as:

$$F_a = \frac{N_{droplet}}{N_{particle}} \qquad \text{Equation II-4-1}$$

The activated fraction is evaluated to represent the activation of the selected aerosol in the supersaturated condition SS. In practice, $\mathrm{N}_{particle}$ and $\mathrm{N}_{droplet}$ are taken as the average of concentration during the last 30 s before changing SS. Figure II-4-1 gives an example of the activation fraction measurement. Due to the dilution in the simulation chamber, the concentration decreases. The red and blue solid dots in the left figure represent the concentration in $\mathrm{cm^{-3}}$ of the aerosol particles and water droplet, respectively. The solid line in black represents SS in the column of CCNc. The solid dots in green represent the data for calculating F_a by using Equation II-4-1. The right figure shows the activation curve on function of SS.

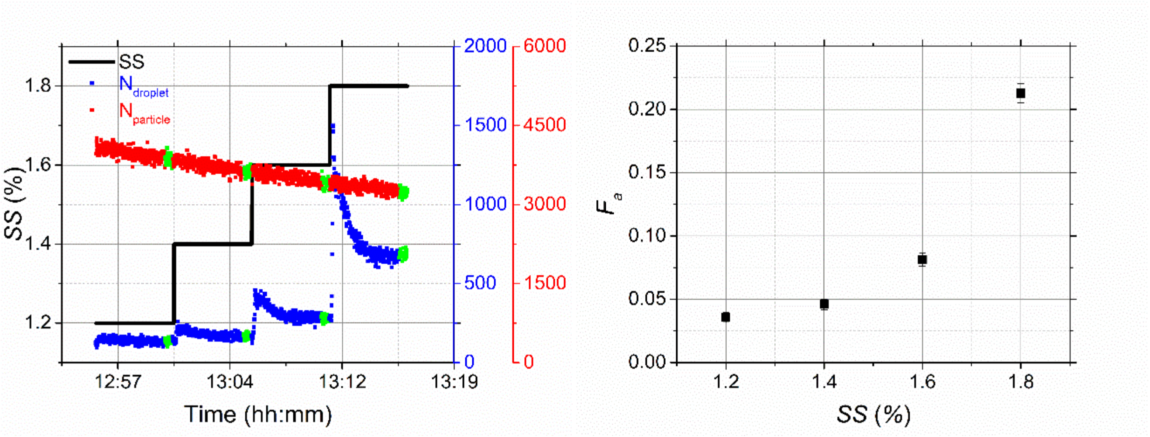

Figure II-4-1 An example to show how to calculate F_a in practice.

Chapter III Model for estimating κ of aerosol

1. Introduction

The first documented idea that clouds are made of water "bubbles" dates back to the 17th century and was originated by Otto von Guericke (1602-1686) (Pruppacher and Klett 1978). The bubble idea prevailed for more than a century until Waller (1816-1870) reported in 1846 that fog particles did not burst on the impact that goes against the bubble idea. Finally, Assmann (1845-1918) ended this dispute by observing cloud droplets under the microscopy in 1884. Before that, Aitken (1839-1919) observed in 1880 that cloud droplets can be formed by water vapor only with the help of dust particles that act as nuclei. A few years later, Wilson (1869-1959) showed a more quantitative observation on the cloud droplets formation by dust particles. This result was contained in the earlier theoretical work of Lord Kelvin (1824-1907), who showed that the equilibrium vapor pressure over a curved liquid surface may be substantially larger than that over a plane surface of the same liquid. Once people knew that dust particles have a significant effect on the formation of droplets, scientists began to study the nature of these dust particles. Köhler (1888-1982) pointed out that the presence of large numbers of hygroscopic particles generally should prevent large supersaturation from occurring in clouds. And he was the first to propose a mathematical description for the variation of vapor pressure over the curved surface of an aqueous solution droplet. Nowadays, almost one century since Köhler's original approach to the cloud droplet nucleation problem, his outstanding studies still represent the fundamental theory of modern condensation research.

To the present day, Köhler theory is still widely used for understanding the role of particles as cloud condensation nuclei (CCNs). The classical Köhler equation is described by water vapor supersaturation, water droplet diameter and solute material volume equivalent diameter. However, many particles naturally present in the atmosphere are formed not only by a single component, but rather by a mix of organic and inorganic components that exist in the same particle (Murphy et al. 1998) and have different solubility in water. Therefore, a hygroscopicity parameter κ is introduced in the modern version of Köhler equation for presenting a quantitative measure of aerosol water uptake characteristics and CCN activity (M. D. Petters and Kreidenweis 2007). This parameter description is called κ-Köhler theory. κ-Köhler theory describes well the soluble particles and we are interested to understand its function on soot particles.

Chapter 3 Model for estimating κ of aerosol

This chapter introduces the understandings of κ-Köhler theory and the discusses of its ubiquitous used approximation when $\kappa > 0.2$ (Petters and Kreidenweis 2007; Tang et al. 2015; Lambe et al. 2015). The effect of the particle morphology on the activation is studied both theoretically and experimentally. An original model taking into accounts the size distribution of aerosol is introduced in this chapter and also presented in (Wu et al. 2019). This model is validated by comparing the experimental results and model-based simulation. Finally, a more complex case, soot aerosol particles, is introduced to the model by taking into account the morphology of soot.

2. κ-Köhler theory

2.1. Thermodynamic equilibrium general relation

The general relation that describes the thermodynamic equilibrium of two phases separated by a curved interface was obtained in a very elegant way (Dufour and Defay 1963) and recalled under the following hypotheses (Pruppacher and Klett 1978):

- Each phase contains the component *i*, and mass transfer is allowed between two phases;
- Chemical reactions are not allowed in this system.

The chemical potential of the component *i* in either of the bulk phases is described as:

$$\mu_i(p,T,a_i) = \mu_{i,0}(p,T) + RT\ln a_i \qquad \text{Equation III-2-1}$$

where μ_i is the chemical potential of species *i* in the system, $\mu_{i,0}$ is the chemical potential of pure species *i*, p is the pressure, T is the temperature, R is the gas constant and a_i is the chemical activity of the species *i* in the system. By following the mathematic development (Pruppacher and Klett 1978), the total derivative of $\frac{\mu_i}{T}$ leads to the following equation:

$$\mathrm{d}\left(\frac{\mu_i}{T}\right) = -\frac{h_{i,0}}{T^2}\mathrm{d}T + \frac{v_{i,0}}{T}\mathrm{d}p + R\,\mathrm{d}\ln a_i \qquad \text{Equation III-2-2}$$

where $h_{i,0}$ is the partial molar enthalpy of pure species *i* and $v_{i,0}$ is the partial molar volume of pure species *i*. Here we suppose a system made of two phases: an aqueous droplet $(^s)$ that can be considered as an ideal solution in an environment of humid air $(^v)$. In equilibrium conditions we have $\mu^s = \mu^v$ to express the equilibrium of the chemical potential of H_2O (*i*) in liquid phase and gas phase. Consequently, we can write:

$$\mathrm{d}\left(\frac{\mu^s}{T}\right) = \mathrm{d}\left(\frac{\mu^v}{T}\right) \qquad \text{Equation III-2-3}$$

By combining Equation III-2-2 and Equation III-2-3, we obtain:

$$-\frac{h_0^s - h_0^v}{T^2}\mathrm{d}T + \frac{v_0^v}{T}\mathrm{d}p^v - \frac{v_0^s}{T}\mathrm{d}p^s + R\,\mathrm{d}\ln\frac{a^v}{a^s} = 0 \qquad \text{Equation III-2-4}$$

A relation between the pressures on the two sides of the interface can be easily obtained from the condition for mechanical equilibrium $p\mathrm{d}V = \sigma\mathrm{d}A$, where σ is the surface tension and $\mathrm{d}A$

is the surface element. Considering that the curved interface is a sphere with diameter d, we note the surface tension between the aqueous droplet and the humid air as $\sigma^{s/v}$. The differential pressure between the two phases is:

$$p^s - p^v = \frac{4\sigma^{s/v}}{d} \qquad \text{Equation III-2-5}$$

The difference of enthalpy between two phases is noted as $H_0^{s/v} = h_0^v - h_0^s$. Then Equation III-2-4 can be written as:

$$-\frac{H_0^{s/v}}{T^2}\mathrm{d}T + \frac{(v_0^v - v_0^s)}{T}\mathrm{d}p^v - \frac{4v_0^s}{T}\mathrm{d}\left(\frac{\sigma^{s/v}}{d}\right) + R\,\mathrm{d}\ln\frac{a^v}{a^s} = 0 \qquad \text{Equation III-2-6}$$

2.2. Kelvin equation

We suppose that the absorption of gases from the air is negligible and the temperature and the pressure of the environment are constant. The first two terms of Equation III-2-6 are negligible. At the condition that the aqueous droplet is pure water, we have $a^s = 1$. Consequently, Equation III-2-6 reduces to:

$$-\frac{4v_0^s}{T}\mathrm{d}\left(\frac{\sigma^{s/v}}{d}\right) + R\,\mathrm{d}\ln a^v = 0 \qquad \text{Equation III-2-7}$$

In humid air environment, assuming ideal gas behavior, we have $\frac{n}{p} = \frac{n_W}{e_W} = \frac{1}{RT}$, where n is the total molar mass per unit volume, n_w is the water molar mass per unit volume and e_w is the partial pressure of water vapor. Thus, the activity of water vapor in humid air is noted as $a^v = n_w/n = e_w/p$. After integrating between ∞ and *d*, we obtain:

$$\ln\frac{e_{D,w}}{e_{\infty,w}} = \frac{4v_0^s\sigma^{s/v}}{RTd} = \frac{4M_w\sigma^{s/v}}{RT\rho_w d} \qquad \text{Equation III-2-8}$$

or alternatively:

$$S = \frac{e_{D,w}}{e_{\infty,w}} = \exp\left(\frac{4M_w\sigma^{s/v}}{RT\rho_w d}\right) \qquad \text{Equation III-2-9}$$

where ρ_w is the density of water, M_w is the molar mass of water, d is the diameter of the droplet and $\sigma^{s/v}$ is the surface tension of solution droplet and humid air. This specific case of Equation

III-2-6 is called Kelvin equation and expresses the saturation S which is the ratio between the water vapor pressure of the droplet and the vapor pressure of water over a flat surface.

2.3. κ-Köhler theory

At the condition that the aqueous droplet is an ideal solution, we have $a^s \neq 1$. We also suppose that (1) the absorption of gas in the air is negligible; (2) the temperature T, the pressure p of the environment and solution salt mass m_s are constant. Consequently, Equation III-2-6 reduces to:

$$-\frac{4v_0^s}{T}\,\mathrm{d}\left(\frac{\sigma^{s/v}}{d}\right) + R\,\mathrm{d}\ln\frac{a^v}{a^s} = 0 \qquad \text{Equation III-2-10}$$

We also assume that the gas behavior is ideal. After integrating between ∞ and d, we obtain:

$$\ln\frac{e_{D,w}}{e_{\infty,w}} = \ln a^s + \frac{4M_w\sigma^{s/v}}{RT\rho_w d} \qquad \text{Equation III-2-11}$$

or alternatively the Köhler equation:

$$S = \frac{e_{D,w}}{e_{\infty,w}} = a^s \exp\left(\frac{4M_w\sigma^{s/v}}{RT\rho_w d}\right) \qquad \text{Equation III-2-12}$$

where S is the saturation. The Köhler equation describes two phenomena during the formation of water droplets. For a flat surface of an aqueous salt solution, Equation III-2-12 reduces to $\frac{e_{D,w}}{e_{\infty,w}} = a^s$ that corresponds to Raoult's law which denotes the equilibrium vapor pressure over the flat surface. For $a^s = 1$, Equation III-2-12 reduces to the Kelvin equation which denotes the equilibrium between pure water drop and humid air.

Several ways to approximate the water activity exist (McDonald 1953; Low 1969; Mason 1971; Petters and Kreidenweis 2007). And in a solution that contains one component, the "hygroscopicity" parameter κ is defined through its effect on the water activity of the solution (M. D. Petters and Kreidenweis 2007):

$$a^s = \frac{V_w}{V_w + \kappa V_s} \qquad \text{Equation III-2-13}$$

where V_w is the volume of pure water in the solution and V_s is the volume of the solute in the solution. And for a multicomponent system (multi solutes + water) at equilibrium, based on the

ZSR relation (Zdanovskii 1936; Stokes and Robinson 1966), the total volume of the water is the sum of the water contents of the individual component, i.e. $V_w = \sum_i V_{wi}$, where V_{wi} is the volume of water corresponding to the component *i*. For each individual solution, the water activity corresponding to component *i* follows Equation III-2-13:

$$\frac{1}{a_i^s} = 1 + \kappa_i \frac{V_{si}}{V_{wi}} \qquad \text{Equation III-2-14}$$

where V_{si} is the volume of the component *i*, a_i^s is the water activity in the solution and κ_i is the "hygroscopicity" of component *i*. At equilibrium, $a^s = a_i^s$. V_w can be described as:

$$V_w = \frac{a^s}{1-a^s} \sum_i \kappa_i V_{si} \qquad \text{Equation III-2-15}$$

The total volume of the system (water and solute) is

$$V_T = \sum_i V_{si} + \sum_i V_{wi} = V_s + V_w \qquad \text{Equation III-2-16}$$

By defining a volume fraction of a component *i* as $\varepsilon_i = V_{si}/V_s$, Equation III-2-15 becomes

$$V_w = V_T - V_s = \frac{a^s}{1-a^s} V_s \sum_i \varepsilon_i \kappa_i \qquad \text{Equation III-2-17}$$

where V_T, V_w and V_s correspond to the total volume, the volume of water and the volume of solute, respectively. Consequently, for this multicomponent system, the water activity is evaluated as:

$$a^s = \frac{V_w}{V_w + \sum_i \varepsilon_i \kappa_i V_s} \qquad \text{Equation III-2-18}$$

The volumes can be converted to their volume equivalent diameters as considering the solute particles and droplets are approximated with spheres:

$$d_p^3 = \frac{6V_s}{\pi} \qquad d^3 = \frac{6V_T}{\pi} \qquad \text{Equation III-2-19}$$

Then, applying Equation III-2-17 and Equation III-2-19 in Equation III-2-12, the so-called "κ-Köhler theory" is introduced as:

$$S(d, d_p, \kappa) = a^s \exp\left(\frac{4M_w \sigma^{s/v}}{RT\rho_w d}\right) = \frac{d^3 - d_p^3}{d^3 - d_p^3(1-\kappa)} \exp\left(\frac{4M_w \sigma^{s/v}}{RT\rho_w d}\right) \qquad \text{Equation III-2-20}$$

where S is the saturation, d_p is the volume equivalent diameter of the dry particle, d is the diameter of the droplet solution, $\sigma^{s/v}$ is the surface tension of solution droplet in humid air and κ represents the "hygroscopicity" of the particle with a following a simple mixing rule $\kappa = \sum_i \varepsilon_i \kappa_i$. By defining the supersaturation $SS = S - 1$, the critical supersaturation that initiates the droplet formation of a dry particle is:

$$SS_c = max\left[\frac{d^3 - d_p^3}{d^3 - d_p^3(1-\kappa)}\exp\left(\frac{4M_w\sigma^{s/v}}{RT\rho_w d}\right) - 1\right] \qquad \text{Equation III-2-21}$$

Figure III-2-1 shows an example of Köhler curves for ammonium sulfate particles as condensation nuclei of different sizes. The coordinate of the maximum of each curve represents the critical supersaturation SS_c and the critical droplet diameter d_c. Two interpretations of the curves in Figure III-2-1 are possible depending on the droplet diameter. If $d \geq d_c$ (right descending branch of the curve), assuming that a small perturbation causes a few molecules of water to be added to the droplet, at this slightly larger new diameter, the equilibrium supersaturation is lower than that in the environment. Hence, water molecules will continue to flow to the droplet that will grow ever larger. Conversely, a small evaporation will produce the droplet with a slightly smaller diameter. The equilibrium supersaturation is higher than that in the environment, and the droplet will continue to evaporate. Consequently, the solution droplet is in unstable equilibrium with its environment. Else, if $d < d_c$ (left ascending branch of the curve), assuming that a small perturbation causes a few molecules of water condensed on the droplet, the diameter of the droplet slightly increases. The equilibrium supersaturation of this new droplet is higher than that in the environment, hence, some water will be evaporated until the droplet returns back to the size which corresponds to the supersaturation of the environment. Conversely, a small evaporation will minimize the droplet size. The equilibrium supersaturation is lower than that in the environment, hence, some water molecules will condense on the droplet until the droplet returns back to the size which corresponds to the supersaturation of the environment. Consequently, the solution droplet is in stable equilibrium.

Furthermore, the particle diameter d_p has an important influence on the curves as well. In Figure III-2-1, the critical supersaturation is higher when the diameter of ammonium sulfate particle is smaller. In other words", a higher supersaturation environment is required in order to activate the smaller particle to form the droplet.

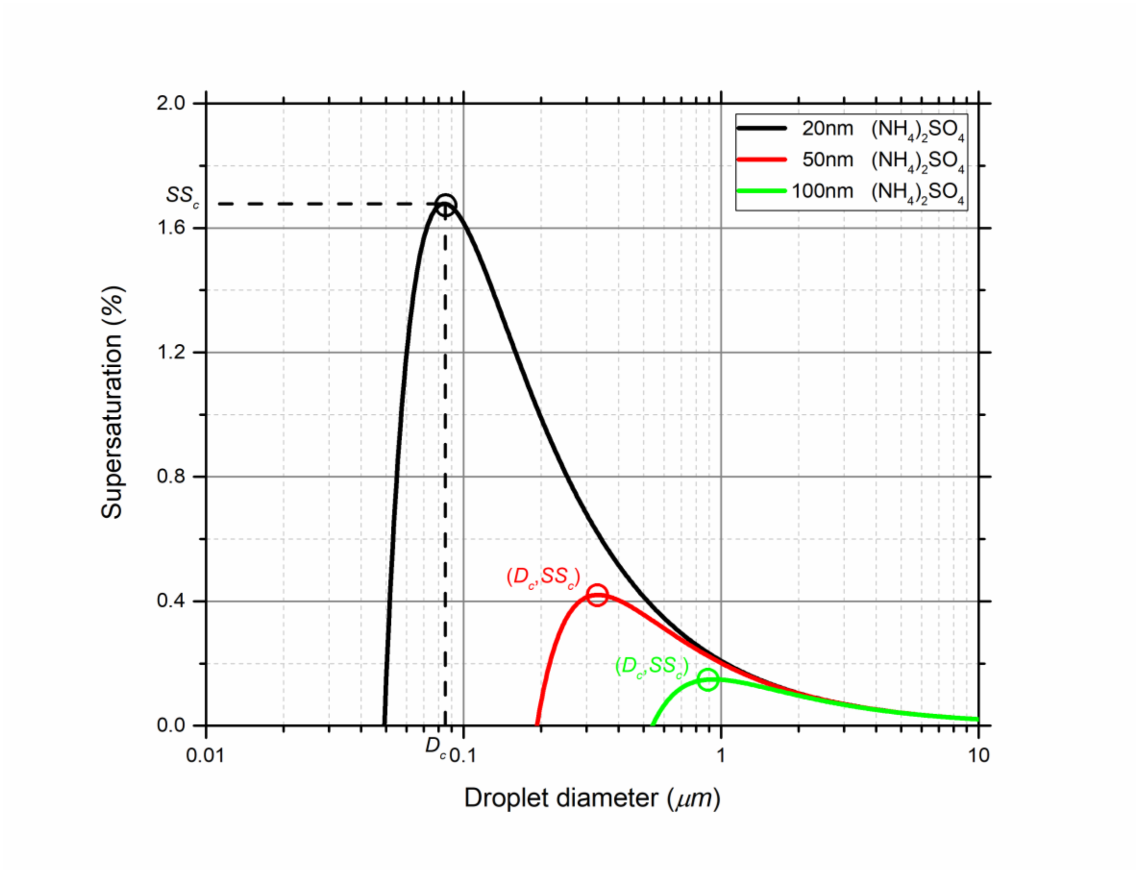

Figure III-2-1 Köhler curves for ammonium sulfate particles from Equation III-2-21. Black, red and green curves represent the Köhler curve of dry ammonium particle (κ = 0.61) with 20nm, 50nm and 100nm respectively ($\sigma^{s/v}$ = 0.072 Jm^{-2} M_w = 0.018 kgmol^{-1}) and T = 20°C).

2.4. Analytical approximation of κ-Köhler theory

To avoid numerical calculation, an analytical approximated form of κ-Köhler equation can be obtained when κ ≥ 0.2 (M. D. Petters and Kreidenweis 2007). This is for instance the case of sodium chloride that is the most hygroscopic species typically found in atmospheric aerosols (κ~1.4):

$$\kappa = \frac{4A^3}{27 d_p^3 \ln^2(1 + SS_c)} \qquad \text{Equation III-2-22}$$

with

$$A = \frac{4\sigma^{s/v} M_w}{RT\rho_w} \qquad \text{Equation III-2-23}$$

where $\sigma^{s/v} = 0.072$ Jm^{-2} and $T = 20$°C are commonly used for calculations (M. D. Petters and Kreidenweis 2007).

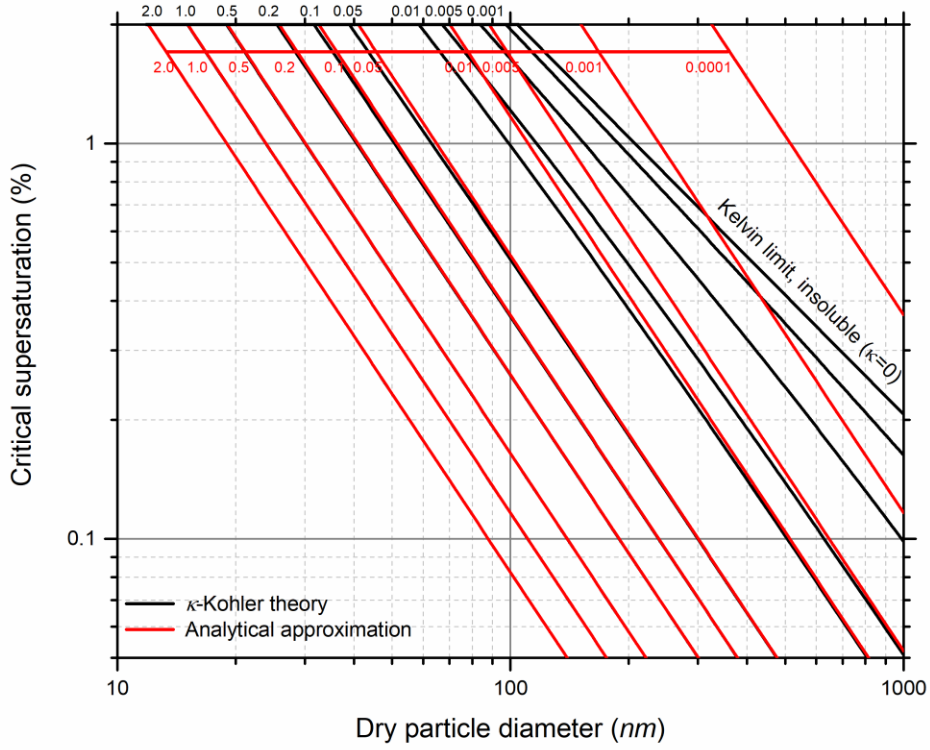

Figure III-2-2 Critical supersaturation SS_c against dry particle diameter d_p with overlaid κ isolines. The black curves represent $SS_c - d_p$ relation from κ-Köhler equation (Equation III-2-21), and the red curves represent $SS_c - d_p$ relation from the analytical approximation (Equation III-2-22).

Figure III-2-2 shows the comparison of κ-Köhler equation and analytical approximation at several given κ in the region $0.05 \leq SS_c \leq 2$. When $\kappa \geq 0.2$, the analytical approximation closely follows the non-approximated κ-Köhler obtained by numerical calculations. In other words, when $\kappa < 0.2$, the approximation is significantly far from κ-Köhler numerical calculation. Particularly, the approximation expression cannot describe the Kelvin equation transformed by κ-Köhler equation in the limit of completely insoluble particles ($\kappa = 0$).

3. Model for aerosol particles activated fraction on function of SS $(F_a - SS)$

To study the hygroscopic properties of aerosol in the atmosphere, a very convenient variable to measure is the so-called activated fraction F_a (varies from 0 to 1) that can be easily related to the critical supersaturation SS_c. Experimentally, $F_a - SS$ curves obtained from cloud condensation nuclei counter (CCNc in annex 3) are used for estimating SS_c, thus κ according to κ-Köhler theory. In the literature, often sigmoid curves (Sullivan et al. 2009; Lambe et al. 2015; Tang et al. 2015) or a cumulative Gaussian function (Rose et al. 2008; Paramonov et al. 2013) are used to fit the $F_a - SS$ curve and SS_c is defined as the supersaturation where F_a is 50% from the fitting curve. However, these fitting functions don't contain physical parameters. In this section, in order to understand the physical meanings behind aerosols activation behavior, we developed an original model based on the κ-Köhler theory and the size distribution of aerosols. Furthermore, the numerical and experimental databases with ammonium sulfate aerosol are compared to test the validation of the model.

3.1. Activation of monodisperse and polydisperse aerosol

In conditions of supersaturation with respect to water vapor (RH > 100%), aerosols can potentially be activated to form water droplets. To determine κ, experimental measurements of the activation fraction F_a are commonly realized in laboratory nucleation chambers. F_a of a certain aerosol is defined as:

$$F_a = \frac{N_{droplet}}{N_{particle}} \qquad \text{Equation III-3-1}$$

where the total number of particles used as CCNs and injected in the nucleation chamber is noted as $N_{particle}$, the number of water droplets formed and measured at the nucleation chamber outlet is noted as $N_{droplet}$. For monodisperse aerosols having diameter d_p, once the environment SS

reaches SS_c, all particles are activated to form water droplet. This hypothesis can be written as a step function:

$$\begin{cases} F_a = 1 & SS \geq SS_c \\ F_a = 0 & SS < SS_c \end{cases} \qquad \text{Equation III-3-2}$$

For two aerosols with volume equivalent diameter d_1 and d_2 that contain the same chemical components, i.e. they have the same κ, we suppose that $d_1 \leq d_2$. From Figure III-2-2, it follows that $SS_{1c} \geq SS_{2c}$ ($SS_c \propto 1/d_p$). Supposing that the environment supersaturation $SS = SS_{1c}$, due to Equation III-3-2, all particles with diameter d_1 are activated. Furthermore, all particles with diameter d_2 are also activated due to $SS = SS_{1c} \geq SS_{2c}$. The conclusion we can get is $F_a = 1$ when $d_p \geq d_1$. Symmetrically, we can get the conclusion of $F_a = 0$ when $d_p < d_1$. Therefore, the expression of F_a on function of d_p can be written as a step function too:

$$\begin{cases} F_a = 1 & d_p \geq d_{p,c} \\ F_a = 0 & d_p < d_{p,c} \end{cases} \qquad \text{Equation III-3-3}$$

where $d_{p,c}$ is the critical diameter of a dry particle that corresponds to the initial diameter of aerosol activated at the environment condition that the supersaturation is SS. Combining Equation III-3-2 and Equation III-3-3, the conclusion is that the representations $(d_{p,c}, SS)$ and (d_p, SS_c) are equivalent only when the aerosol is perfectly monodisperse.

However, in practice, laboratory-generated and atmospheric aerosols are polydisperse, and therefore a model taking into account the size distribution is important to predict the behavior of real systems. Let’s consider dry particle aerosols with a hygroscopicity κ and a size distribution described as function $N = N(d_p)$ as shown in Figure III-3-1. $d_{p,c}$ is the critical diameter of dry particles activated at supersaturation SS.

Appling Equation III-3-3, for aerosol shown in Figure III-3-1, the activation fraction at supersaturation SS can be written as:

$$F_a\left(d_{p,c}\right) = \frac{\left(\sum_{d_{p,c}}^{+\infty} N(d_{p,c})\right) \times 1 + \left(\sum_{-\infty}^{d_{p,c}} N\left(d_{p,c}\right)\right) \times 0}{\sum_{-\infty}^{+\infty} N\left(d_{p,c}\right)} \qquad \text{Equation III-3-4}$$

As the environmental supersaturation increases, the critical diameter of dry particles tends to be smaller. Hence, the activated fraction increases as a consequence of the increase of the cumulative function.

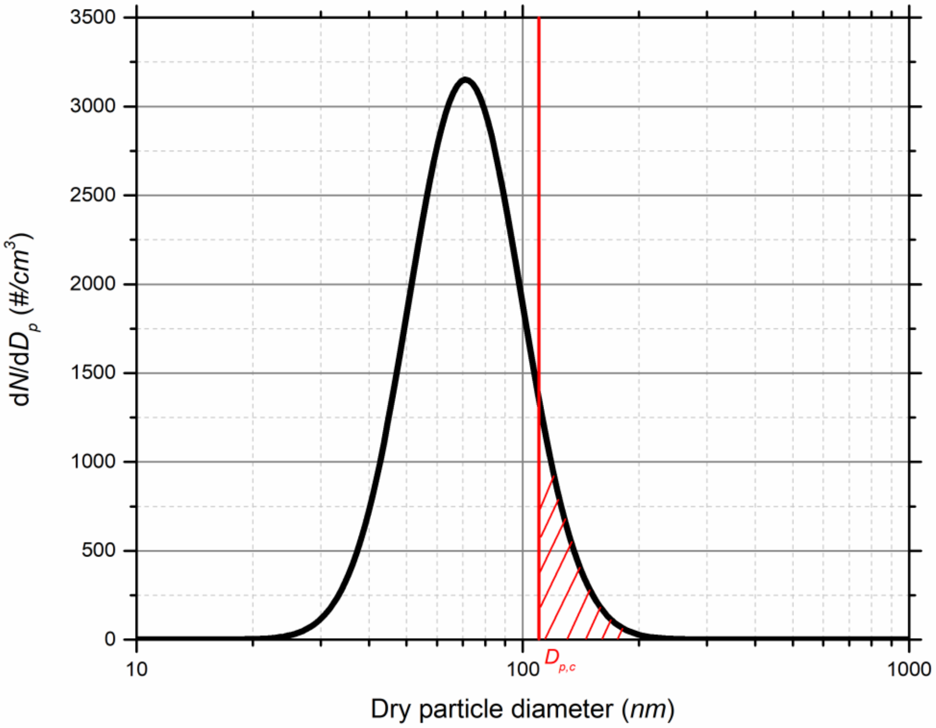

Figure III-3-1 Simulated size distribution of dry particles (black curve). The red line highlights the critical diameter with respect to SS. The area covered by red diagonal line represents the cumulative number for particles having $d_p > d_{p,c}$.

3.2. F_a simulation of aerosol with lognormal distribution

In aerosol science studies, the lognormal distribution is perhaps the most commonly used analytic expression (Heintzenberg 1994). In this work, we improved a model approach which aims to understand the effects from the parameters of size distribution on F_a of the aerosol. We assume that the size distribution of dry particle of the test aerosol follows a lognormal distribution:

$$\mathrm{f}(d_p,\mu,\sigma) = \frac{n_T}{d_p\sigma\sqrt{2\pi}} e^{\frac{-(\ln d_p-\mu)^2}{2\sigma^2}} \qquad \text{Equation III-3-5}$$

where $f(d_p,\mu,\sigma)$ is the probability density function (PDF), n_T is the total concentration of aerosol, μ and σ are the mean and standard deviation of the variable's natural logarithm, respectively. Further, the cumulative distribution function of a lognormal distribution (CDF) is described as:

$$\mathrm{F_X}(d_p,\mu,\sigma) = \int_{-\infty}^{d_p} \mathrm{f}(d_p,\mu,\sigma)\mathrm{d}d_p = \frac{1}{2} + \frac{1}{2}\mathrm{erf}\left[\frac{\ln d_p - \mu}{\sqrt{2}\sigma}\right] \qquad \text{Equation III-3-6}$$

where the error function is defined as:

$$\mathrm{erf}(x) = \frac{2}{\sqrt{\pi}}\int_0^x e^{-t^2}dt \qquad \text{Equation III-3-7}$$

In practice, the position of the mode μ_{mode} and the geometric standard deviation σ_{geo} are easy to obtain from the experimental data:

$$\begin{aligned}\mu_{\mathrm{mode}} &= \exp(\mu - \sigma^2)\\ \sigma_{\mathrm{geo}} &= \exp(\sigma)\end{aligned} \qquad \text{Equation III-3-8}$$

where μ_{mode} represents the maximum of the function on the x-axis, and σ_{geo} is related to the width of the distribution. The larger the geometric standard deviation, the wider the size distribution.

From section III-2, we know that the dry particle diameter has a significant effect on the formation of water droplets. Here we show the effect of σ_{geo} when the mode is constant. Figure III-3-2 shows the size distribution of ideal spherical particles with the same μ_{mode} but different σ_{geo}.

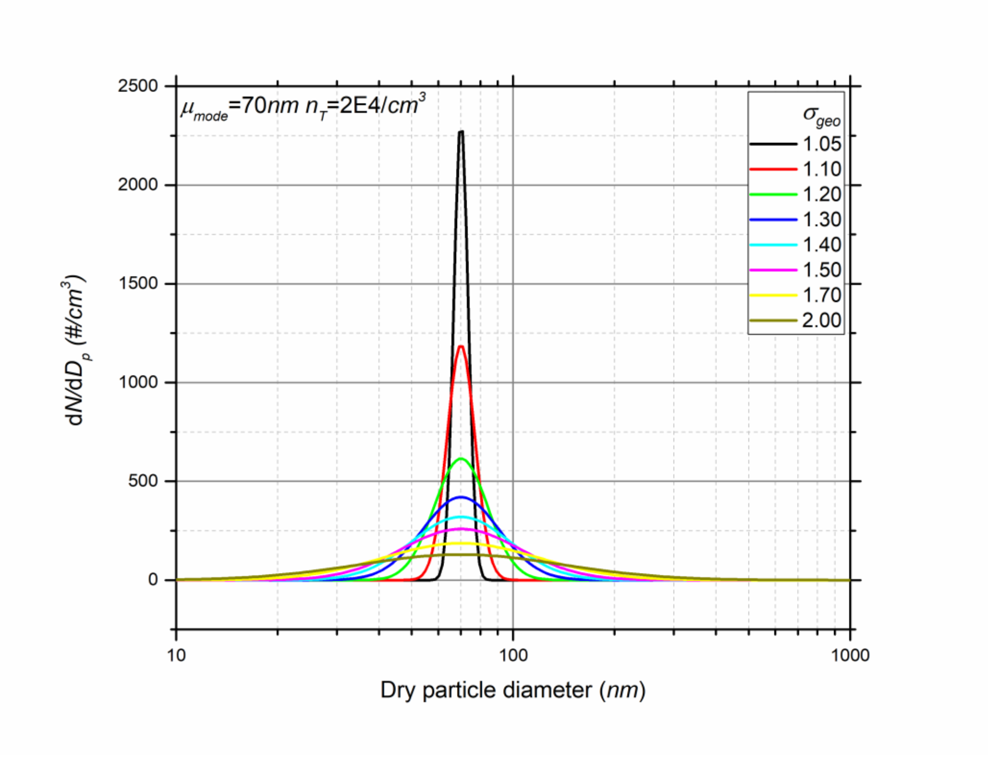

Figure III-3-2 Simulated lognormal size distribution of spherical particles with 8 different geometric standard deviations at μ_{mode} = 70nm and n_T =2×10^4 cm^{-3}.

By combining Equation III-3-4, Equation III-3-5 and Equation III-3-8, the activation fraction of spherical aerosol particles having log-normal size distribution is:

$$F_a\left(d_{p,c}\right)=\frac{1}{2}-\frac{1}{2}\operatorname{erf}\left[\frac{\ln d_{p,c}-\left(\ln \mu_{\text{mode}}+\ln^2 \sigma_{\text{geo}}\right)}{\sqrt{2}\ln \sigma_{\text{geo}}}\right] \qquad \text{Equation III-3-9}$$

3.3. Comparison of F_a between experimental results and simulation results with ammonium sulfate

3.3.1. Application of the model to a real case (ammonium sulfate)

Ammonium sulfate is hygroscopic ($\kappa \sim 0.61 > 0.2$, see section III-2.4), therefore $d_{p,c}$ in Equation III-3-9 can be estimated by using analytical approximation equation of κ-Köhler theory (Equation III-2-22). Then, the activated fraction of ammonium sulfate aerosol particles having lognormal distribution against supersaturation is given by:

$$F_a(SS) = \frac{1}{2} - \frac{1}{2}\operatorname{erf}\left\{\frac{\frac{1}{3}\ln\left[\frac{4A^3}{27\kappa\ln^2(1+SS)}\right] - \left[\ln\mu_{\text{mode}} + \ln^2\sigma_{\text{geo}}\right]}{\sqrt{2}\ln\sigma_{\text{geo}}}\right\} \qquad \text{Equation III-3-10}$$

where Equation III-3-10 is the specific case of Equation III-3-4 for ammonium sulfate aerosol having a lognormal distribution. In order to understand how the activation acts, we apply ammonium sulfate aerosols with 8 size distributions mentioned in Figure III-3-2. Simulation curves of activated fraction against supersaturation SS are shown in Figure III-3-3. If the ammonium sulfate aerosol is perfectly monodisperse, the activation curve is a step function (Equation III-3-2), i.e. $F_a = 1$ once $SS \geq SS_c$, where $SS_c \sim 0.25\%$ in this case. Else, if the ammonium sulfate aerosol is polydisperse and follows a lognormal distribution, the activation curves are different from step functions. With increasing σ_{geo}, activation curves tend to be more and more flat.

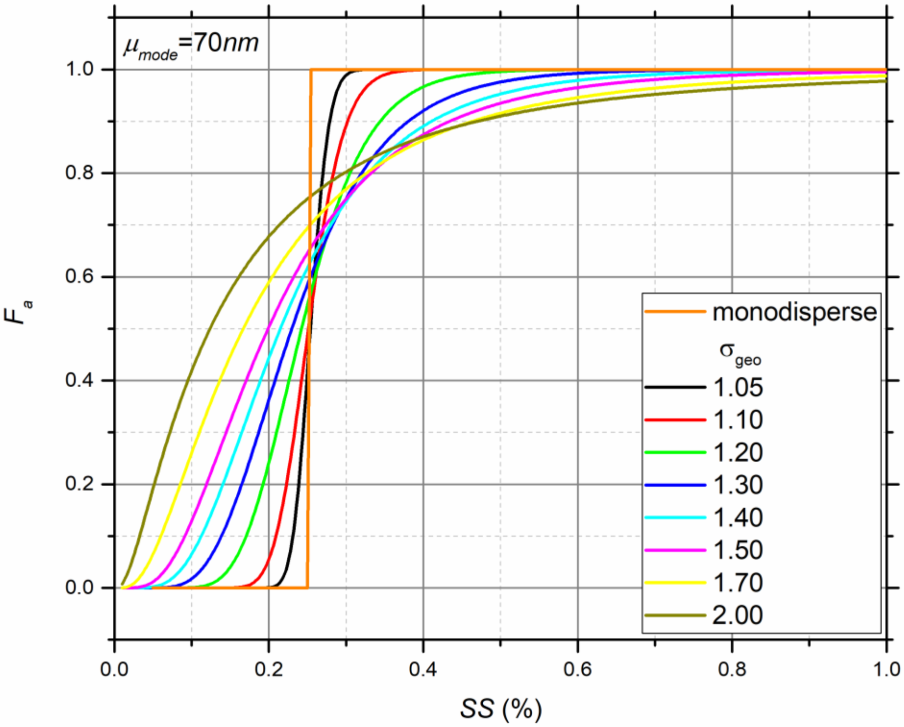

Figure III-3-3 Simulated activated fraction curves of ammonium sulfate against SS. μ_{mode} = 70 nm and κ = 0.61. Curves in black, red, green, blue, cyan, magenta, yellow and dark yellow represent the

calculation by model respecting to the σ_{geo} in 1.05, 1.1, 1.2, 1.3, 1.4, 1.5, 1.7 and 2.0, respectively. The curve in orange represents the theoretical calculation of a perfectly monodisperse aerosol.

3.3.2. Experimental set-up

In order to test the validation of the model proposed in section III-3.3.1, activation experiments are performed on ammonium sulfate aerosols by means of a cloud condensation nuclei counter (CCNc) and a condensation particle counter (CPC 3776) to measure the number of droplets and total number of particles, respectively, according to Equation III-3-1. In order to study the effect of the particle size distribution on F_{a} curve, a differential mobility analyzer (DMA 3081) is applied to select the aerosol particles of a specific size and to provide different σ_{geo}. The experimental set-up is shown in Figure III-3-4 and more details in chapter 2. Ammonium sulfate particles are generated by atomization from a solution with the concentration of 0.1 gL^{-1}, then size selected and injected in the chamber where the relative humidity is invariably lower than 2%. Then, SMPS measures the size distribution in order to estimate μ_{mode} and σ_{geo}. Next, CCNc and CPC record the concentration of water droplets and aerosol particles at different supersaturations in order to plot F_a against SS. The morphology and size distribution of the ammonium sulfate aerosol are compared to transmission electron microscopy measurements in parallel.

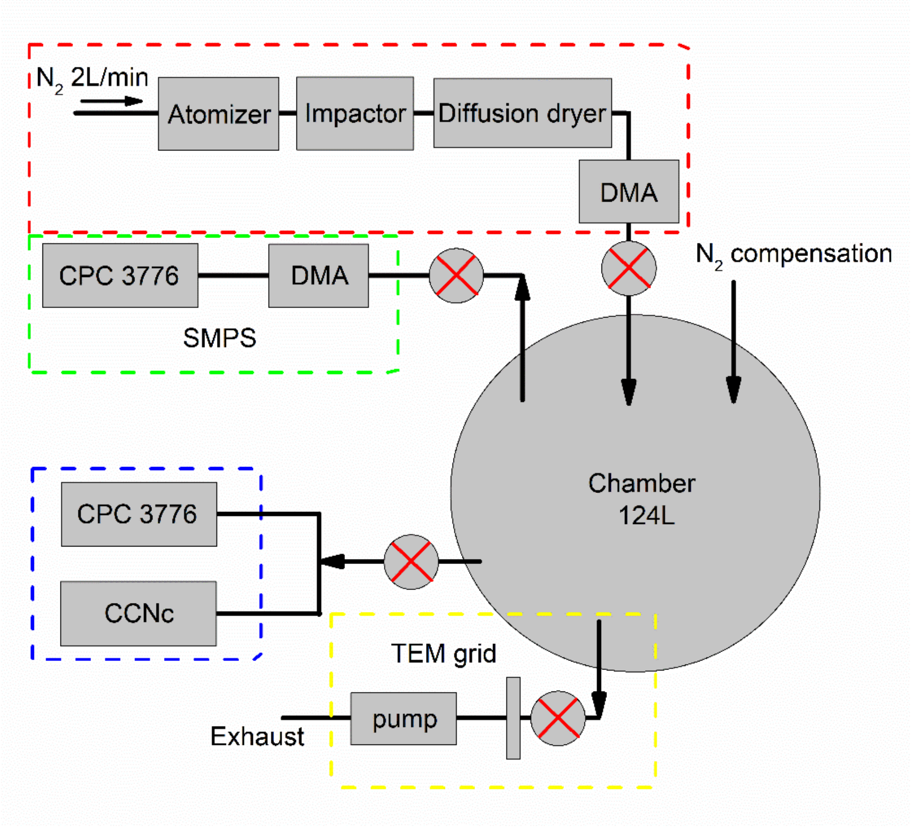

Figure III-3-4 Experiment setup: ammonium sulfate aerosol generation and injection system (red frame); size distribution measurement system (green frame); activation fraction measurements system (blue frame); collection system for TEM grids (yellow frame).

3.3.3. Ammonium sulfate aerosol generation results

Five experiments are performed with this setup and experiment parameters are shown in Table III-3-1. σ_{geo} is modulated by changing the ratio of the sheath flow rate to the sample flow rate in the DMA classifier (selection ratio in Table III-3-1). The total concentration is estimated in software AIM by scanning the size distribution of ammonium sulfate aerosol. μ_{mode} and σ_{geo} are estimated from fittings as shown in Figure III-3-5.

Table III-3-1 Parameters of ammonium sulfate size distribution with five injections. The selection ratio is the ratio between the sheath flow and the sample flow on the electrostatic classifier of SMPS.

The total concentration is recorded from AIM software.μ_{mode} and σ_{geo} are the parameters of the lognormal fitting according to the size distribution recorded from AIM software.

Number	Selection ratio	Total concentration (cm^{-3})	μ_{mode} (nm)	σ_{geo}
1	10	5063	71.0	1.06
2	1	11167	84.6	1.38
3	none	3115	74.6	1.79
4	2	5718	101.6	1.20
5	2	8897	57.3	1.38

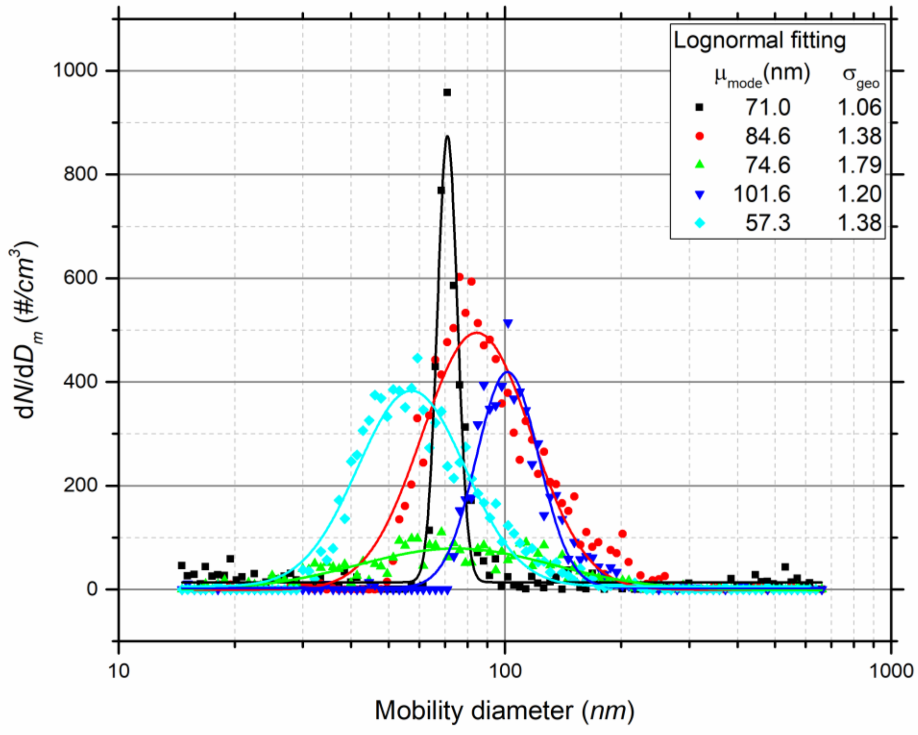

Figure III-3-5 Size distribution of ammonium sulfate aerosol and lognormal fitting curves. Solid dots in black, red, green, blue and cyan represent the size distribution obtained experimentally by SMPS and solid lines represent their lognormal fitting, respectively.

3.3.4. TEM analysis of ammonium sulfate aerosol

Among these 5 experiments, TEM collection has been done for experiments 2, 4 and 5. Figure III-3-7 is an example image of TEM grid that shows size-selected 70nm ammonium sulfate aerosol (experiment 2) on a Lacey carbon mesh. The light gray area that covers most surface of the image represents the background. The mesh structure in dark gray is the Lacey carbon mesh. The dark circles on the border of carbon mesh are the ammonium sulfate particles.

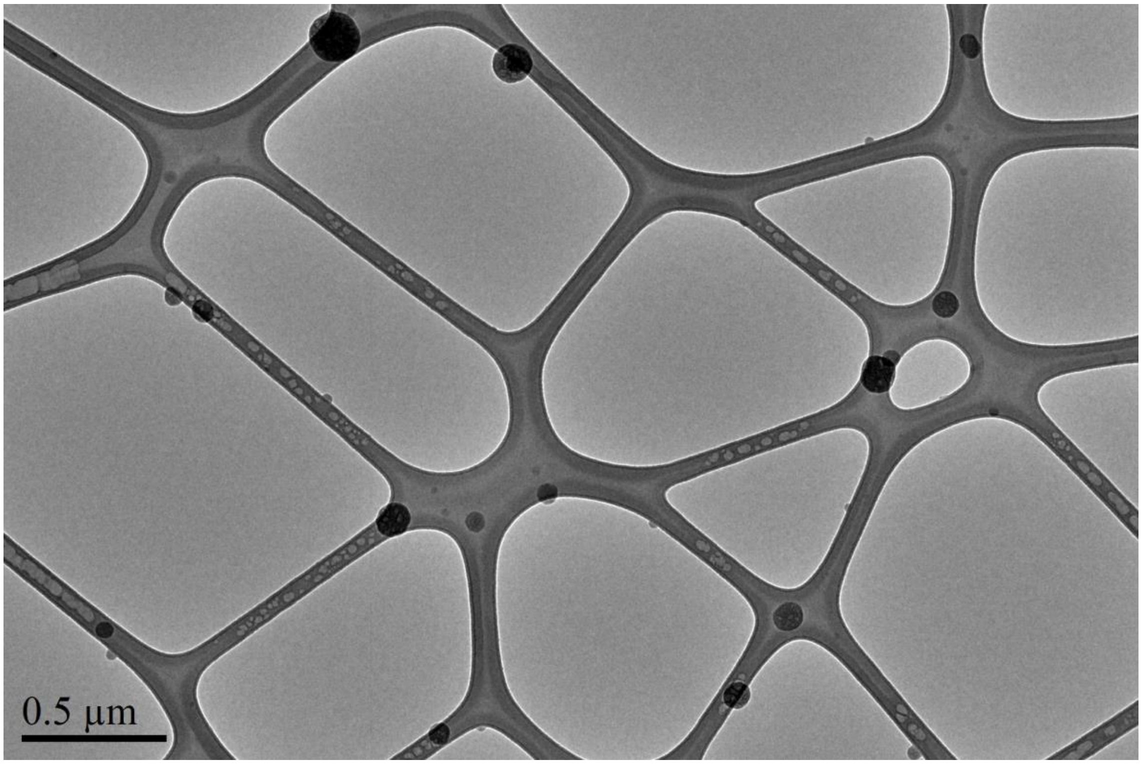

Figure III-3-6 TEM image of 70 nm size selected ammonium sulfate aerosol (black quasi-spherical particles) on a Lacey mesh with 6500 magnification.

Ammonium sulfate is well known for the quasi-spherical particles that can be generated by atomization, and it is often used as a reference material for activation experiments. By means of the free software ImageJ, a series of statistical analysis of the particle's diameter have been done. All particles are selected manually and measured by ImageJ. In the Figure III-3-7, three statistical results (a), (b) and (c) correspond to ammonium sulfate aerosol in experiment 2, 4 and 5, respectively. They follow the lognormal distribution.

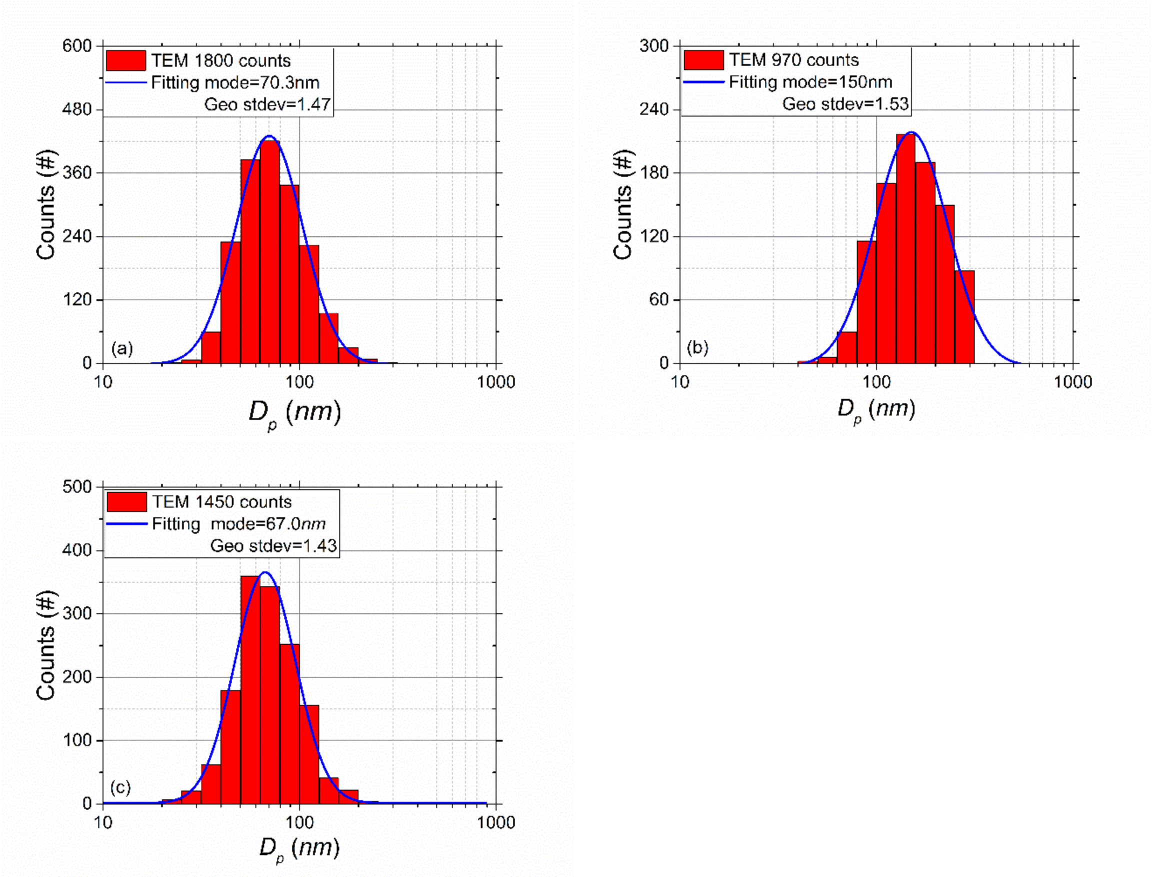

Figure III-3-7 Size distributions of ammonium sulfate particles obtained by manual counting from TEM images. Figure (a), (b) and (c) correspond to ammonium sulfate aerosol with μ_{mode} = 78.3 nm σ_{geo} = 1.34 (experiment 2), μ_{mode} = 101.6 nm σ_{geo} = 1.20 (experiment 4) and μ_{mode} = 52.4 nm σ_{geo} = 1.26 (experiment 5), respectively.

3.3.5. Comparison of $F_a - SS$ between experimental results and simulation results

To test the self-consistency of the model, we used two different ways to input the size distribution of ammonium sulfate. Given the same size distribution obtained experimentally for ammonium sulfate aerosol as explain in section III-3.3.3, we used a numerical approach by summing on the number of each size channel respecting to Equation III-3-4 (size cumulative approach), and alternatively we fit the experimental data with a lognormal function and introduced their parameters in the model respecting to Equation III-3-10 (lognormal approach). The two results are compared in Figure III-3-8 and discussed below.

In Figure III-3-8, CCNc results of five experiments are firstly compared with the size cumulative approach. Globally, CCNc results are well fitted by size cumulative approach.

Especially, the agreement of CCNc results and size cumulative approach for experience 4 and 5 are almost perfect. For experiment 1, both CCNc results and size cumulative approach curve show a sudden increase when SS arrives 0.2%. Furthermore, the size cumulative approach curve represents well the first step (SS <0.2%) of the CCNc results. For experiment 2 and 3, the size cumulative approach curves represent well the difference tendency of the activation curve with different σ_{geo}. For experiment 5, the size cumulative approach curve is as flat as the curve shown by CCNc results.

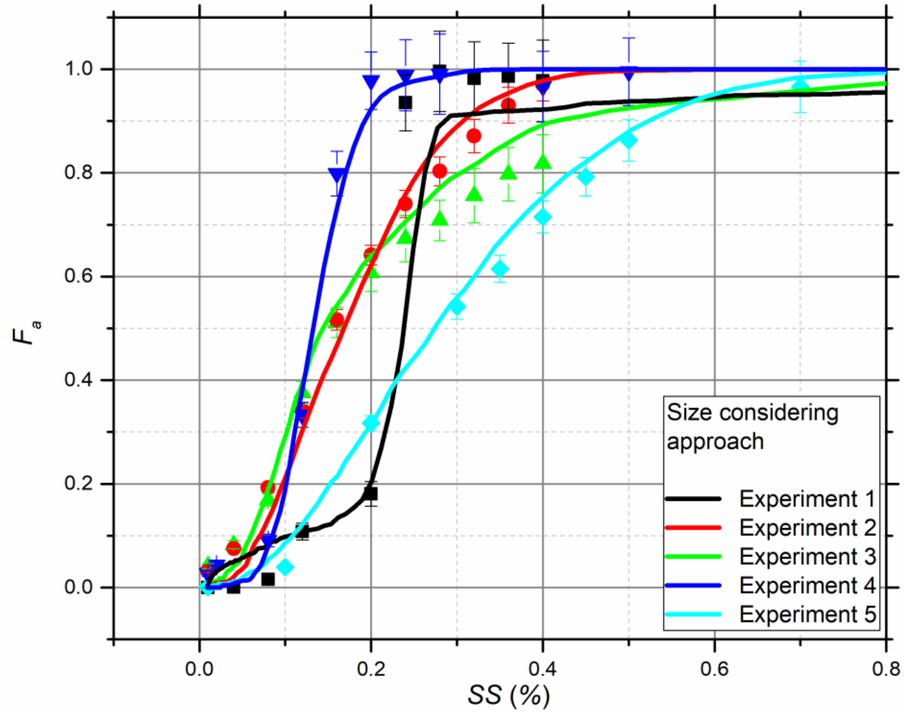

Figure III-3-8 Comparison of F_a vs SS among 5 experimental results and the simulation results of size cumulative approach. Solid dots represent the activation curves estimated by CCNc, solid lines represent the simulation curve respecting the size cumulative approach.

In Figure III-3-9, CCNc results of 5 experiments are compared then with the lognormal approach. Globally, the agreements between CCNc results and lognormal approach are good. Especially for experience 4 and 5, the CCNc results are perfectly fitted by lognormal approach.

According to Figure III-3-8 and Figure III-3-9, we can easily conclude that both the size cumulative approach and the lognormal approach reproduce well the experimental activation curve. The parameters μ_{mode} and σ_{geo} of the size distribution of aerosol have the significant effect on the shape of their activation curves. And this effect has the strong agreement with the simulative study in section III-3.3.1.

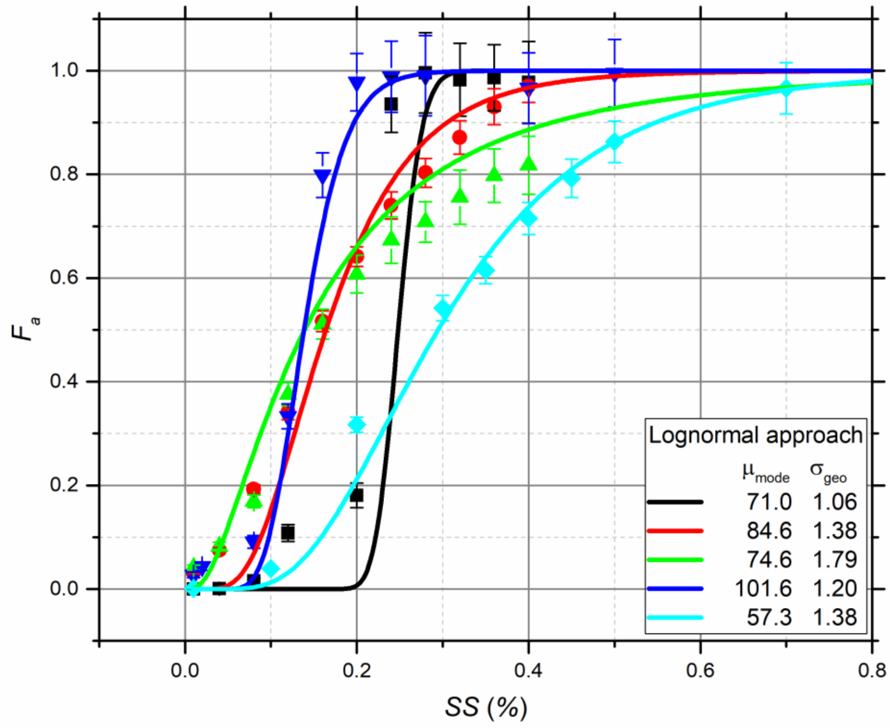

Figure III-3-9 Comparison of F_a vs SS among 5 experimental results and lognormal approach. Solid dots represent the activation curves estimated by CCNc, solid lines represent the simulation curve respecting the lognormal approach.

4. Hygroscopicity estimation of soot particle from its $F_a - SS$ curve

The morphology of soot aggregates is much more complex than ammonium sulfate particles. In order to apply κ-Köhler theory to study soot particles, a volume equivalent diameter which corresponds to the same volume of soot aggregate is ubiquitous used (Tritscher et al. 2011; Wittbom et al. 2014; Lambe et al. 2015). In this section, the morphological parameters such as d_{pp} and D_f (defined in Chapter 1) are taken into account to estimate d_{ve}. Besides, κ of soot particles are basically small than 0.1 (Petzold et al. 2005; Tritscher et al. 2011; Wittbom et al. 2014; Lambe et al. 2015), and they conformably use the analytical approximation of κ-Köhler (Equation III-2-22) which can only describe the relation between κ and SS_c when κ $>$ 0.2. In this section, a model combining soot morphology, κ-Köhler theory and the effect of size distribution (section 3) is examined. As a practical application, we show that the model can be used to extract κ by fitting real $F_a - SS$ curves of soot activated by exposing to OH$^-$, data from S. Grimonprez Ph.D.(S. Grimonprez 2016).

4.1. Determination of the fractal dimension of soot aggregates

The fractal dimension of soot aggregates has already been studied by basically three techniques: angular light scattering (Köylü et al. 1995a; Sorensen et al. 1992), scanning electron microscopy (Colbeck et al. 1997) and transmission electron microscopy (Köylü and Faeth 1992; Cai et al. 1995; Hu et al. 2003). In this work, we choose TEM method to estimate the fractal dimension from aggregate projections to take advantage of the HR-TEM instrument available at the University of Lille.

Figure III-4-1 shows the image of a soot aggregate obtained by TEM. In this picture, the diameter of the particles in the aggregate (primary soot primary particles diameter, d_{pp}), the total surface of the aggregate in the TEM image (projection area surface, A_{2D}) and the maximal length of the aggregate projection in the TEM image (maximal length of aggregate projection, L_{2D}) are all estimated by using the free software ImageJ.

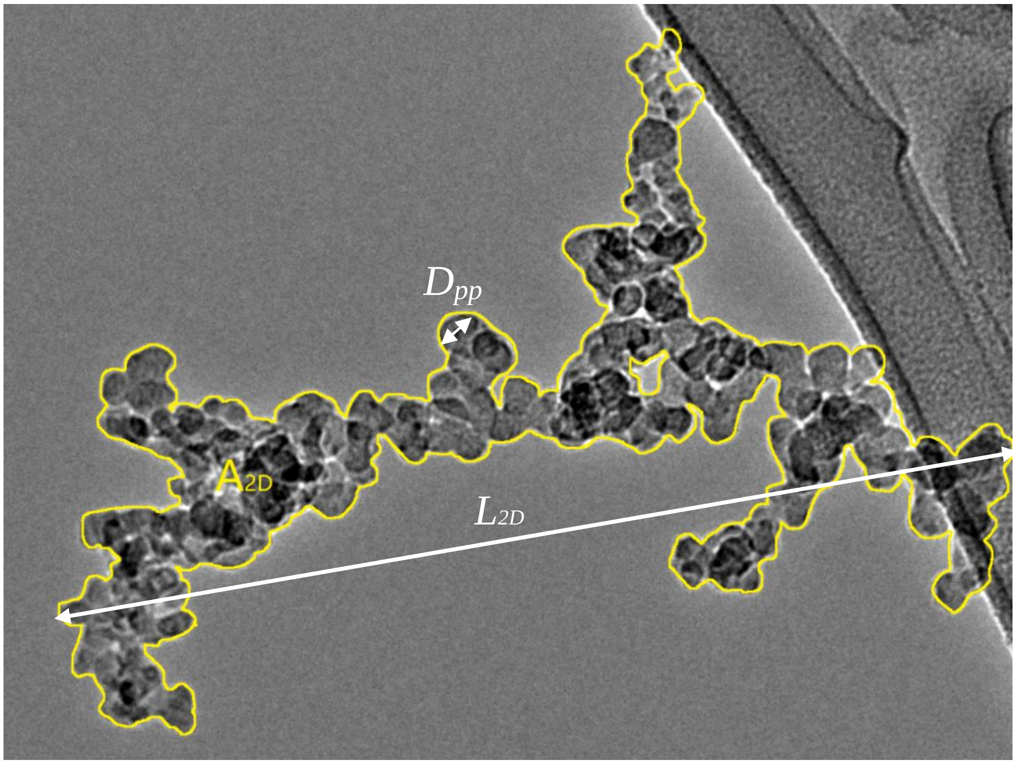

Figure III-4-1 soot aggregate projection on TEM picture

The primary particle size distribution is usually estimated by statistical counting, Figure III-4-2 shows the primary particle diameter distribution of fresh soot at HAB = 130mm obtained by analyzing 100 images.

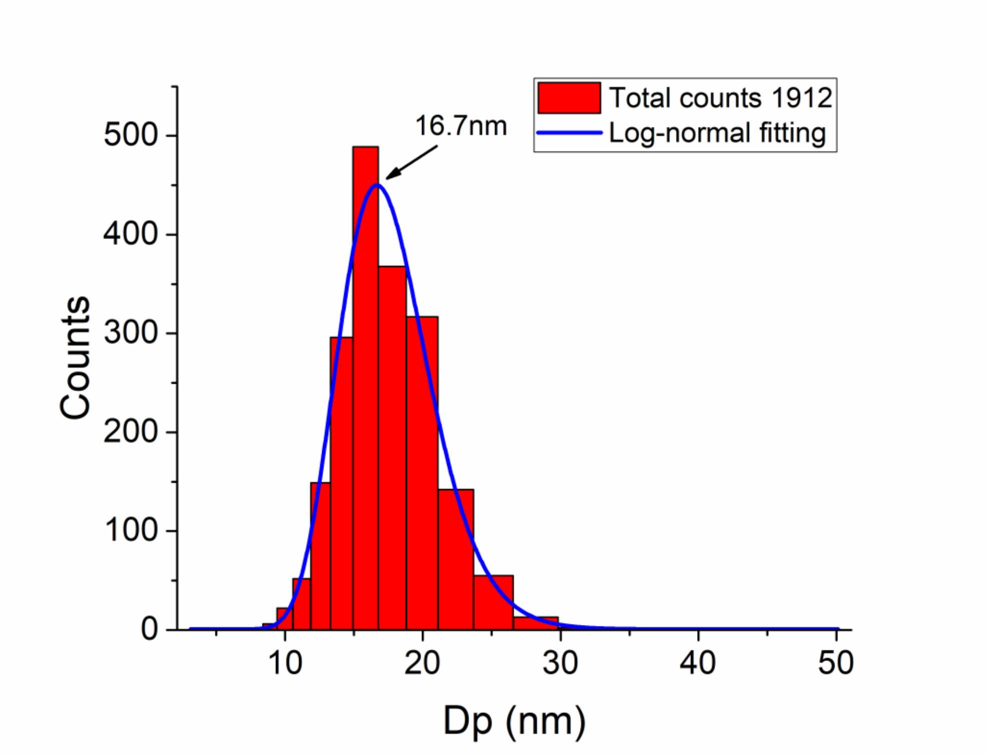

Figure III-4-2 primary particle distribution of fresh soot at HAB = 130 mm. Red bars represent counts in different bins and blue line represents the log-normal fitting corresponding to mode = 16.7 nm and geometry standard deviation = 1.21.

For soot aggregates, the total number of primary particle N_{pp} is exponentially reported by the area surface of the aggregate projection (Medalia and Heckman 1971). Then N_{pp} is evaluated as the relation (Köylü et al. 1995):

$$N_{pp} = k_a\left(\frac{4A_{2D}}{\pi \overline{d_{pp}}^2}\right)^{\alpha} \qquad \text{Equation III-4-1}$$

where $\overline{d_{pp}}$ is the mode of the primary particle diameter, k_a and α are the coefficient and the exponent of the projection area, respectively.

The values of k_a and α are both estimated from numerical calculations on aggregates (Medalia 1967) and experimental determination of soot particles emitted from laboratory flame (Samson et al. 1987; Köylü et al. 1995). By using the previous database, a relation is proposed to determine N_{pp} for $N_{pp} < 1000$ (Meakinet al. 1989).

$$\frac{4A_{2D}}{\pi \overline{d_{pp}}^2} = 0.4784N_{pp} + 0.5218N_{pp}^{0.6789} \qquad \text{Equation III-4-2}$$

According to the definition of fractal dimension D_f given in chapter 1, a method to estimate D_f from 2D images of soot aggregates has been proposed that requires measuring L_{2D} (Cai et al. 1995; Köylü et al. 1995):

$$\ln(N_{pp}) = \ln(k_f) + D_f \ln\left(\frac{L_{2D}}{\overline{d_{pp}}}\right) \qquad \text{Equation III-4-3}$$

In this work, we followed this approach. As an example, Figure III-4-3 shows $\ln(N_{\mathrm{pp}})$ against $\ln(L_{2\mathrm{D}}/\overline{d_{\mathrm{pp}}})$ obtained from the plot of 100 fresh soot aggregates (diffusion flame at HAB = 130mm). The slope of this linear fit corresponds to the fractal dimension D_f with a value of 1.56 and the prefactor coefficient $k_f = 1.26$ which is in the range of 1.23 and 3.49 from the literature (Samson et al. 1987; Köylü et al. 1995; Cai et al. 1995; Sorensen and Feke 1996; Sorensen and Roberts 1997; Tian et al. 2006).

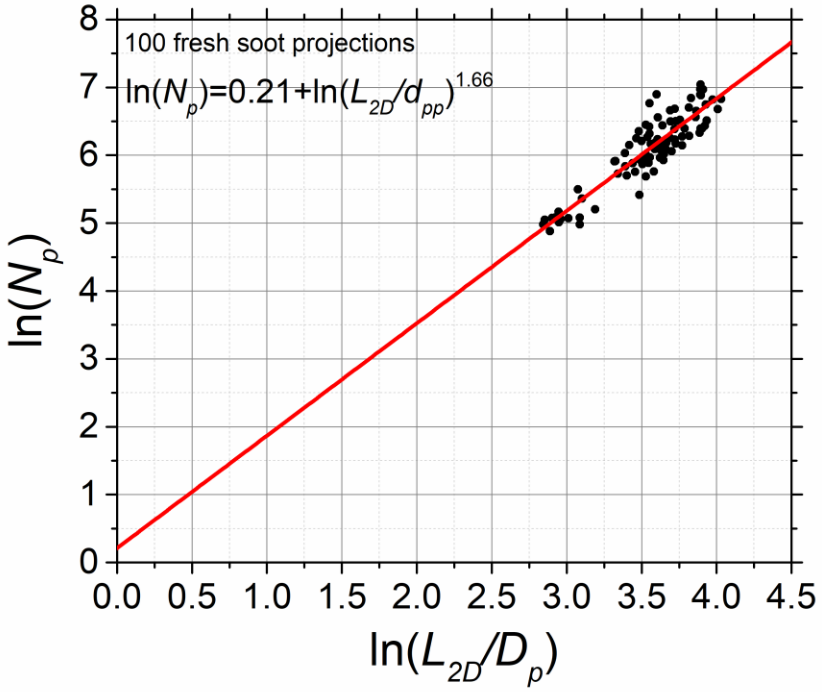

Figure III-4-3 Fractal dimension of fresh soot particles obtained from 100 aggregate projections.

4.2. Relation between volume equivalent diameter and mobility diameter for soot particle

The mobility diameter d_m is a very important parameter to describe the size of soot particle. It can be determined using commercial instruments. In particular, the size distribution of soot aerosol particles in this work is measured by SMPS (annex 1) and a DMA ensures the inject soot particles with a selected size in laboratory. However, according to the κ-Köhler theory (section III-2.3), the dry particle diameter d_p in the theory is the volume equivalent diameter of a particle considered as a sphere. Therefore, in order to introduce d_m estimated in laboratory into the κ-Köhler equation, d_m needs to be converted into d_{ve}. In the simplest case of ammonium sulfate aerosols, we considered $d_m = d_{ve}$ due to the quasi-spherical shape of the particles (section III-3.3.4). However, the fractal morphology of soot aggregates requires using a more complex relation between d_m and d_{ve} with the parameters of soot morphology (section III-4.1).

On the one hand, with the approximation of soot aggregate proposed in section 4.1, d_{ve} of soot aggregate formed by primary particles can be described as:

$$V_{soot} = \frac{\pi}{6} d_{ve}^3 = \sum_{i=1}^{N_{pp}} \frac{\pi}{6} d_{pp,i}^3 \qquad \text{Equation III-4-4}$$

where V_{soot} is the total volume of a certain soot aggregate and $d_{pp,i}$ is the diameter corresponding to the i^{th} primary particle. To simplify the calculation for the soot aggregate, we suppose that soot aggregate is formed by primary particles with a constant diameter d_{pp}. Thus, Equation III-4-4 can be simplified to:

$$d_{ve} = d_{pp} N_{pp}^{\frac{1}{3}} \qquad \text{Equation III-4-5}$$

On the other hand, the mobility diameter d_m (electrical or mechanical) is directly linked to the aerodynamic force acting on the particle:

$$F_{drag} = \frac{3\pi\eta d_m v_r}{C_c(d_m)} \qquad \text{Equation III-4-6}$$

where η represents the kinematic viscosity of the surrounding gas, v_r is the particle relative velocity and C_c is the Cunningham slip factor (Allen and Raabe 1985) defined as:

$$C_c(K_n) = 1 + K_n\left[A + B\exp\left(-\frac{C}{K_n}\right)\right] \qquad \text{Equation III-4-7}$$

where $K_n = 2\lambda_g/d_m$ is the Knudsen number and λ_g represents the mean free path of the surrounding gas. The constants A, B and C are estimated experimentally as 1.142, 0.558 and 0.999 (Allen and Raabe 1985). Yon et al. proposed the approximation that the drag force of an aggregate can be related to the drag force acting on each primary particle which is considered as a sphere (Yon et al. 2015).

$$F_{drag}^{agg} = F_{drag}^{mono} {N_{pp}}^{\frac{\Gamma}{D_f}} \qquad \text{Equation III-4-8}$$

where Γ is experimentally estimated in condition of $1.61 < D_f < 1.79$ (Yon et al. 2015):

$$\Gamma = 1.378\left[\frac{1}{2} + \frac{1}{2}\mathrm{erf}\left(\frac{K_n(d_{pp}) + 4.454}{10.628}\right)\right] \qquad \text{Equation III-4-9}$$

Where K_n is the Knudsen number, d_{pp} is the mass equivalent primary particle diameter which is estimated as $d_{pp} = \left(\sum_i^N \frac{1}{N} d_i^3\right)^{-3}$, where N and d_i are totoal primary particle number and individual primary particle diameter shown in Figure III-4-2.

By combining Equation III-3-5 and Equation III-3-6, relation between d_m and d_{pp} is described as:

$$D_m = \frac{C_c(d_m)}{C_c(d_{pp})}\, d_{pp} {N_{pp}}^{\frac{\Gamma}{D_f}} \qquad \text{Equation III-4-10}$$

Finally, by removing the N_{pp} in Equation III-4-5 and Equation III-4-10, we have:

$$d_{ve}(d_{pp}, D_f, d_m) = d_{pp}\left(\frac{d_m}{d_{pp}}\frac{C_c(d_{pp})}{C_c(d_m)}\right)^{\frac{D_f}{3\Gamma}} \qquad \text{Equation III-4-11}$$

where d_{pp} and D_f can be estimated from the analysis of a large number of TEM images, and d_m can be measured by SMPS.

(a) (b)

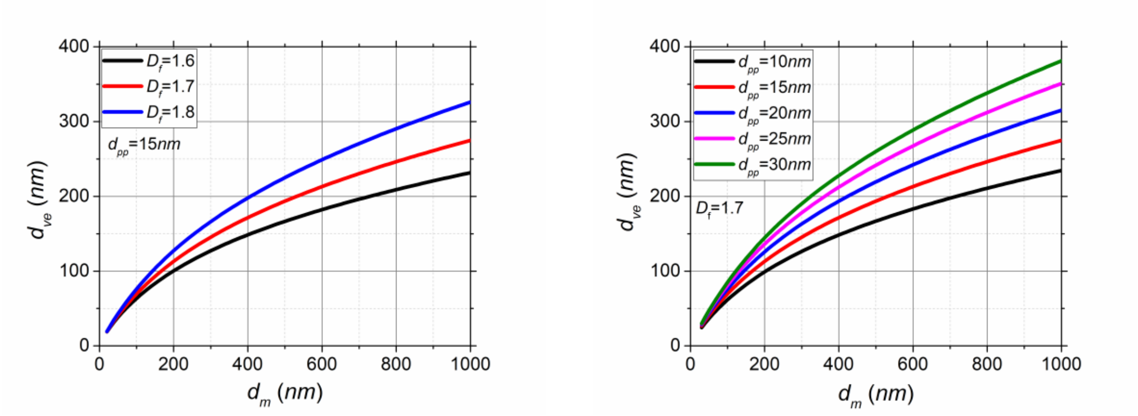

Figure III-4-4 Simulation d_{ve} vs d_m with different morphology. The left figure (a) shows the relation between d_{ve} and d_m on function of D_f at the condition that d_{pp} is 15nm; the right figure (b) shows the relation between d_{ve} and d_m on function of d_{pp} at the condition that D_f is 1.7.

Figure III-4-4 shows the simulated relation between d_{ve} and d_m for aggregates having constant diameter of the primary particle (a), and constant fractal dimension (b). In general, the lower D_f of the particle and the smaller d_{ve}. At the condition that fractal dimension is constant, the smaller the diameter of the primary particle and the smaller d_{ve}.

4.3. Simulation of the activated fraction of soot aggregate

We have a series of soot aggregate having the same morphology with primary particle diameter d_{pp} and fractal dimension D_f. And these aggregates follow a lognormal distribution with total concentration $n_T = 2\times10^4$ cm^{-3}, size distribution mode d_{ve} and geometry standard deviation σ_{geo}^{ve}, where d_{ve} is estimated by the parameters d_m, d_{pp} and D_f (Equation III-4-11). In order to describe the relation between supersaturation and particle diameter, especially when $\kappa < 0.2$, we use Equation III-2-22 to find *SS* corresponding to $d_{p,c}$. By following Equation III-3-9, F_a is described as:

$$F_a\left(d_{p,c}, d_{ve}, \sigma_{\text{geo}}^{ve}\right) = F_a(\max)\left[\frac{1}{2} - \frac{1}{2}\operatorname{erf}\left(\frac{\ln d_{p,c} - \ln d_{ve} - \ln^2 \sigma_{\text{geo}}^{ve}}{\sqrt{2}\ln \sigma_{\text{geo}}^{ve}}\right)\right] \quad \text{Equation III-4-12}$$

$$SS(d_{p,c}) = \max\left\{\frac{d^3 - d_{p,c}^3}{d^3 - d_{p,c}^3(1-\kappa)}\exp\left(\frac{4M_w\sigma_{w/a}}{RT\rho_w d}\right)\right\} - 1$$

where $F_a(\max)$ is the maximum of F_a. In general, $F_a(\max) = 1$, which means that all particles as CCN are formed to the droplets. In order to study the effect of the parameters d_m, D_f, d_{pp}, σ_{geo}^{ve} and κ on $F_a - SS$, we test the model by changing these parameters to explore how the model reacts to different inputs. And five simulated experiments are performed with parameters shown in Table III-4-1.

In simulation 1, a size distribution corresponding to $d_{ve} = 93.1$ nm and $\sigma_{\text{geo}}^{ve} = 1.2$ is applied to Equation III-4-12. κ is applied as a variable from 0 to 0.1. The simulation results show F_a against SS. The double dot curve in black represents the activation curve at κ = 0, and all other curves are above it. With increasing κ, the activation curve shifts to the left, i.e. the soot particles can be activated with a smaller SS. This tendency is consistent with κ-Köhler theory that for particles with a certain size, the larger κ and the smaller SS_c (section II-2).

In simulation 2, we keep d_{pp}, D_f, σ_{geo}^{ve} and κ constant. And d_m is taken as 100, 150 and 200 nm. The simulation results show that with increasing d_m, d_{ve} increases and the activation curve shifts to the left, i.e. the soot particles can be activated with a smaller SS. This tendency is consistent with κ-Köhler theory as well that for particles with a certain κ, the larger d_{ve}, the smaller SS_c (section III-2). The effect of D_f and d_{pp} are studied in simulations 3 and 4, respectively. The simulation results show that the increase of D_f and d_{pp} cause the increase of d_{ve} and the shifting of the activation curve to the left. In summary, the parameters d_m, D_f and d_{pp} affect d_{ve} and this effect is well consistent with Equation III-4-11. Furthermore, d_{ve} affects the shifting of the activation curve.

In simulation 5, we keep d_m, d_{pp}, D_f and κ constant. σ_{geo}^{ve} is taken as 1.1, 1.2 and 1.3. The simulation results show that these three activation curves pass the same point around $(0.6\%,\ 0.6)$. With increasing σ_{geo}^{ve}, the activation curve flattens. In practice, the experimental activation curves of soot particles often have the different shape (Lambe et al. 2015) which potentially due to the size distribution of soot particles analyzed. In our model, the parameters of d_m, d_{pp}, D_f, $\sigma_{\mathrm{geo}}^{ve}$ and κ significantly play the role on the shape of the activation curve.

Table III-4-1 Parameters of soot aggregate, size distribution and $F_a - SS$ simulation results.

Simulation number	Input parameters		Size distribution	$F_a - SS$ simulation results
1	d_m (nm)	**150**	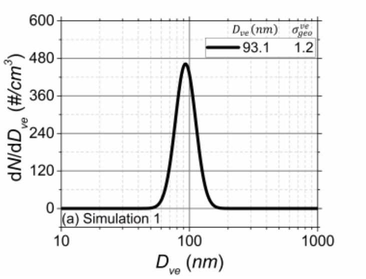	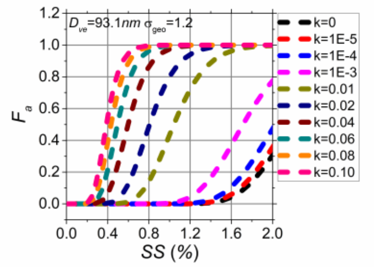
	d_{pp} (nm)	**15**		
	D_f	**1.7**		
	d_{ve} (nm)	**93.1**		
	σ_{geo}^{ve}	**1.2**		
	κ	**0-0.1**		
2	d_m (nm)	**100-200**	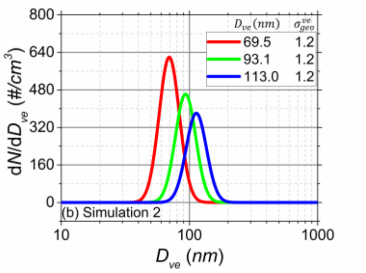	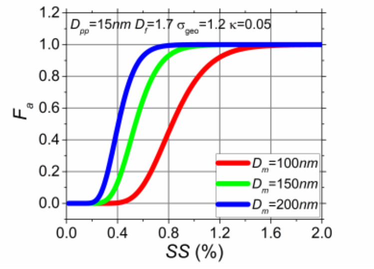
	d_{pp} (nm)	**15**		
	D_f	**1.7**		
	d_{ve} (nm)	**69.5-113**		
	σ_{geo}^{ve}	**1.2**		
	κ	**0.05**		
3	d_m (nm)	**150**	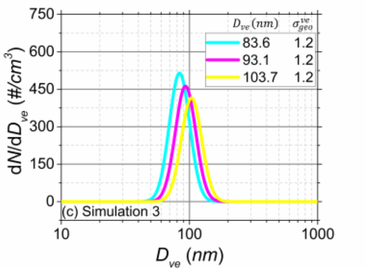	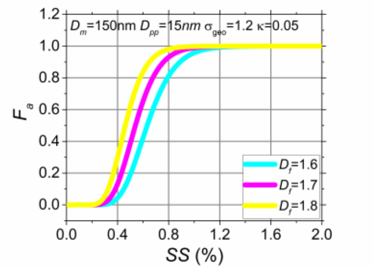
	d_{pp} (nm)	**15**		
	D_f	**1.6-1.8**		
	d_{ve} (nm)	**83.6-103.7**		
	σ_{geo}^{ve}	**1.2**		
	κ	**0.05**		
4	d_m (nm)	**150**	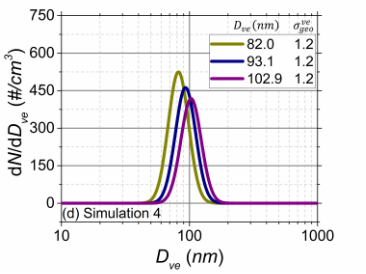	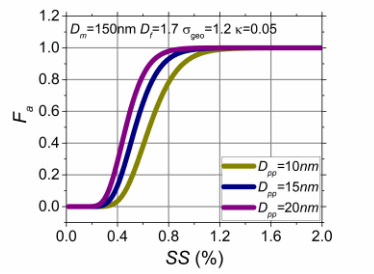
	d_{pp} (nm)	**10-20**		
	D_f	**1.7**		
	d_{ve} (nm)	**82-102.9**		
	σ_{geo}^{ve}	**1.2**		

	κ	**0.05**	
5	d_m (nm)	**150**	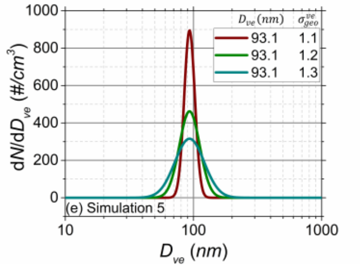 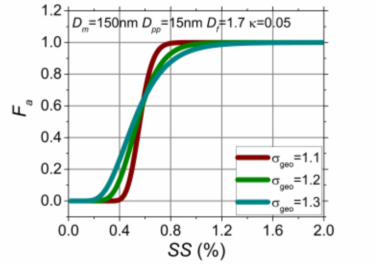
	d_{pp} (nm)	**15**	
	D_f	**1.7**	
	d_{ve} (nm)	**93.1**	
	σ_{geo}^{ve}	**1.1-1.3**	
	κ	**0.05**	

4.4. Estimating κ of soot activated by exposing to OH radicals

A series of experiments for studying the activation of soot aggregates with OH radicals were performed during the Ph.D. of Symphorien Grimonprez (Grimonprez. 2016). Briefly, soot was sampled from two different jet turbulent diffusion flames supplied with kerosene or diesel. The soot aerosols were sampled in-line by means of an extractive microprobe and injected in the CESAM atmospheric simulation chamber (Wang et al. 2011). Here, they were exposed to radical OH (from the reaction of O_3 and water vapor under UV light). The number of droplets and the particle concentration in the CESAM chamber, required to calculate F_a, were measured in parallel by a CCNc and CPC3776 directly sampling the chamber. Soot aggregates particles with mobility diameters of 150 or 300nm were investigated. With increasing the OH exposure, soot particles became more and more hydrophilic. The activation curves at different OH exposure are built for both 150nm selected soot particle from diesel flame and kerosene flame. In order to test the model, we fit these activation curves and then estimated the hygroscopicity at different OH exposure by using parameters introduced in section III-3.3.

During the Ph.D. of Symphorien Grimonprez, the morphology of the fresh soot sampled from kerosene flame at HAB = 130 mm has been determined by TEM measurements. From the literature, for the soot sampled from diesel flame, the primary particle diameter is 16.3 nm and the fractal dimension is 1.8 (Yon et al. 2011). During the aging process, we suppose that the morphology of soot remains constant. Parameters of soot sampled from kerosene flame and diesel flame are shown in Table III-4-2. d_m, d_{pp} and D_f are the morphology of the soot particles analyzed in the activation experiments. d_{ve} is the volume equivalent diameter estimated by the method proposed in section III-4.2. σ_{geo}^{ve} and κ are two variables to be estimated from the experimental activation curves.

Table III-4-2 Morphology parameters of fresh soot sampled from kerosene flame and diesel flame.

Fuel	d_m (nm)	d_{pp} (nm)	D_f	d_{ve} (nm)	σ_{geo}^{ve}	κ
Kerosene	150	16.5	1.7±0.1	96±10	variable	to be estimated
Kerosene	300	16.5	1.7±0.1	96±10	variable	to be estimated
Diesel	150	16.3	1.8±0.1	107±10	variable	to be estimated

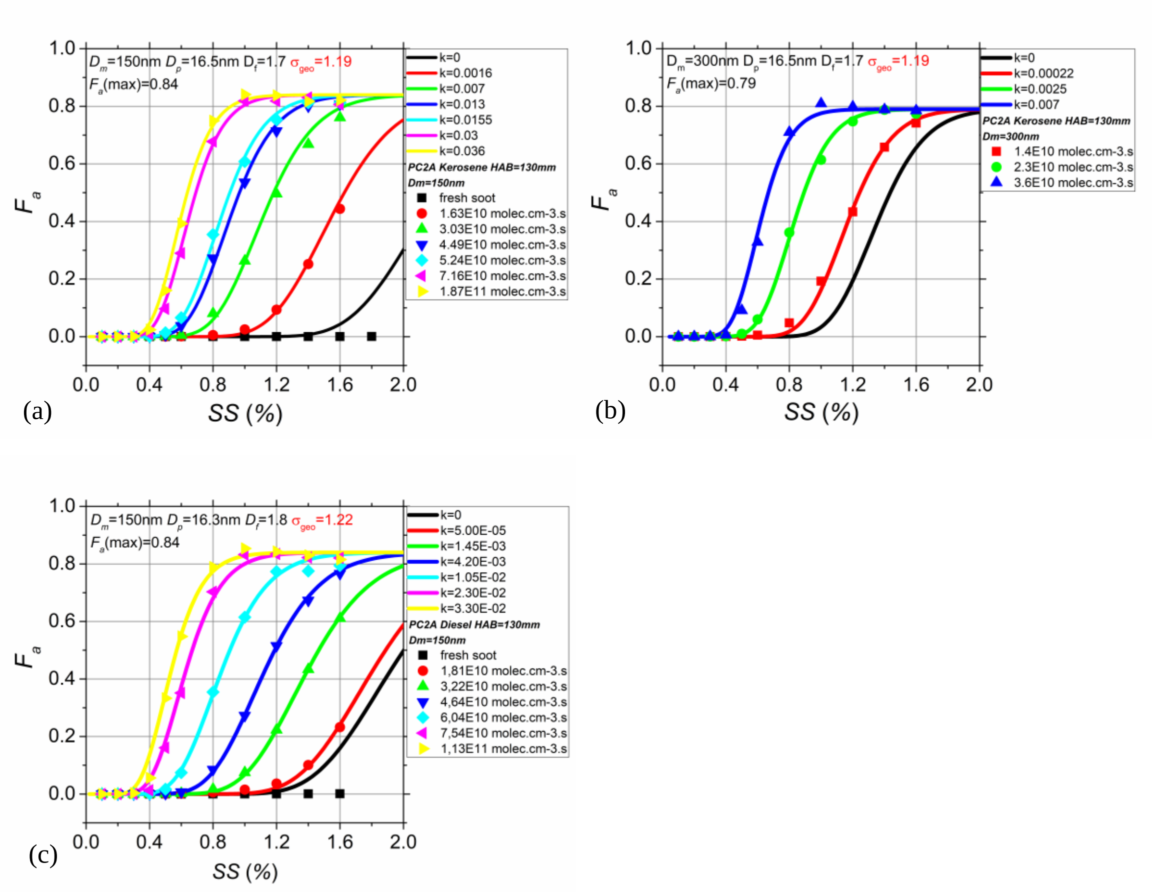

Figure III-4-5 Fittings of F_a vs SS curves of kerosene and diesel soot particles with D_m = 150nm and D_m = 300nm exposed to OH radicals. In the left figure, solid dots represent experimental activated fraction results and solid lines represent simulated fittings by using Equation III-4-12.

Figure III-4-5 shows fittings of F_a vs SS curves of kerosene and diesel soot particles with mobility diameters of 150 and 300 nm respectively. In all the three figures, $F_a(\max)$ is counted as the average of F_a at the plateau of the activation curves. $F_a(\max) < 1$ potentially means that $N_{droplet} < N_{particle}$ when all particles are activated. We still introduce $F_a(\max)$ into accounts in Equation III-4-12 for fitting experimental F_a. In figures (a) and (b), the fittings of experimental F_a are good except for the fresh soot. F_a of fresh soot with $d_m = 150\ \mathrm{nm}$ in two cases are below the limit of the simulation fittings. The same thing happens in figure (c), F_a of fresh diesel soot with $d_m = 150\ \mathrm{nm}$ is below the limit of the simulation fitting. $\sigma_{\mathrm{geo}}^{ve}$ in figure (a), (b) and (c) is between 1.19 and 1.22 which is quite stable in one series of measurements. $\sigma_{\mathrm{geo}}^{ve}$ represents the shape of the size distribution of studied soot. The higher $\sigma_{\mathrm{geo}}^{ve}$, the wider of the size distribution (section III-4.3). In conclusion, by applying the parameters of the morphology of the soot particles, the model represents extremely well the experimental activation curve with a $\sigma_{\mathrm{geo}}^{ve}$ around 1.2, where $\sigma_{\mathrm{geo}}^{ve}$ potentially represents the geometric standard deviation of d_{ve} of soot particles.

We plot the κ estimated from the fitting against the OH^- exposure in Figure III-4-6. For the kerosene soot, κ of soot particles having mobility diameter of 150nm and 300nm have the same tendency against OH^- exposure. A plateau around the value 0.04 seems to be reached for large values of OH exposure. For Diesel soot, a similar behavior is observed (although the range of investigated exposures is smaller) indicating that the hygroscopicity of soot particles is not affected by the different composition of the two liquid fuels. In particular, small sulfur content in kerosene does not increase the hygroscopicity of aged soot particles.

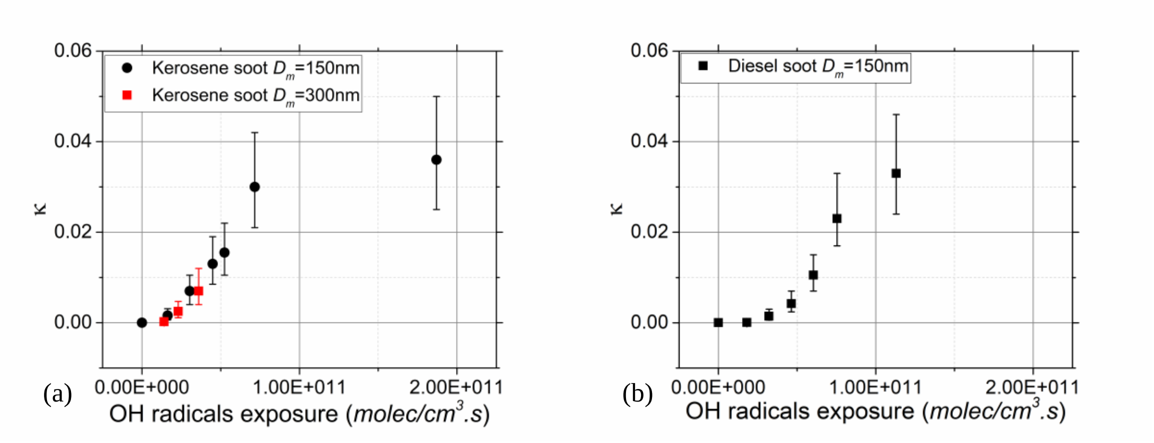

Figure III-4-6 κ of kerosene soot against OH^- exposure. Black solid dots represent κ of kerosene and diesel soot having mobility diameter of 150 nm; red solid dots represent κ of kerosene soot having mobility diameter of 300nm.

5. Conclusions

κ-Köhler theory combines the classical Kohler theory and a single parameter representation of cloud condensation nuclei activity. The analytical approximation of κ-Köhler theory works well with the agreement that a series of soluble component aerosols are measured experimentally with a range of κ from 0.2 to 1.4 (M. D. Petters and Kreidenweis 2007) and does not take into account the aerosol size distribution and morphology. In this work, we propose a generalization of κ-Köhler theory for polydisperse aerosols with complex morphology. Two hypotheses are used in this model:

- The volume equivalent diameter of the particle has the same effect on the behavior of the activation compared to a diameter of a perfect sphere particle.
- For a series of aerosol having the same κ, at certain supersaturation conditions, all aerosols having volume equivalent diameters larger than the critical diameter are activated.

The model is tested on the very well-known and ubiquitous used standard ammonium sulfate aerosols (polydisperse spherical particles), and then on the much more complex real case of soot particle (polydisperse fractal aggregates). The morphology of dry ammonium sulfate particles is obtained from TEM measurements. We find that the model corresponds well with the experimental results for a wide range of sizes and geometric standard deviations. Then, for studying the hygroscopic property of soot particle, we introduce a process of transforming the mobility diameter which is measured in practice to volume equivalent diameter which is applied in the model. This process is based on the analysis of soot aggregate projection from TEM images. And the volume equivalent diameter d_{ve} is related to primary particle diameter d_{pp}, mobility diameter d_m and fractal dimension D_f. Similar to the geometric standard deviation in the case of ammonium sulfate, we introduce a variable σ_{geo}^{ve} as the geometric standard deviation of soot particles. All these soot morphology parameters are studied in this model for understanding the effect on the activation. Essentially, the effect from d_{pp}, d_m and D_f on the activation is due to the effect of d_{ve} on the activation according to κ-Köhler theory. The geometric standard deviation σ_{geo}^{ve} affects the shape of the activation curve. Finally, we apply this model to estimate κ of soot particles exposed to OH^- by the fitting activation curves obtained from experiments. The activation curves are well fitted by model's simulation with κ in the range 0-0.04, and σ_{geo}^{ve} the range 1.19-1.22.

The perspectives are still essential for our model. For example, for soot particles, it exists the activation which is beyond the Kelvin limit ($\kappa = 0$). This could be the improvement of the activation theory for insoluble particles (Sorjamaa and Laaksonen, 2007) or the process of transferring d_m to d_{ve}. More cases of the experimental soot activation curves are analyzed in chapter 4.

Chapter IV Hygroscopicity behavior of soot during aging with O_3 and SO_2

1. Introduction

Freshly emitted soot particles are generally considered as poor CCN in the atmosphere (Andreae and Gelencsér 2006; Stubenrauch and Schumann 2005). In particular, similar results are found from the study of soot particles generated by flame combustion in laboratory (Petzold et al. 2005; Zhang et al. 2008; Khalizov et al. 2009; Tritscher et al. 2011; Wittbom et al. 2014; Lambe et al. 2015). However, after the emission in the atmosphere, the so-called aging that involves processes such as surface oxidation, photochemical reactions and coating by low volatile organic compounds (VOCs) may change the physical and chemical properties of freshly emitted soot particles and turn them into efficient CCNs. In this chapter, we study experimentally the change of the hygroscopic properties of soot particles sampled from kerosene flames in laboratory during a simulated aging process with O_3 and SO_2 that are known to be important atmospheric pollutants both in the lower and upper troposphere where soot are emitted (Chapleski et al. 2016; Streets and Waldhoff 2000). Two campaigns of simulated atmospheric aging processes with O_3 and SO_2 have been performed respectively in the Lille Atmospheric Simulation Chamber (LASC) and in the Experimental Multiphasic Atmospheric Simulation Chamber (CESAM) for studying the hygroscopic properties of kerosene diffusion soot particles in controlled atmospheric conditions of temperature, pressure and relative humidity. In these experiments, the morphology, size distribution and hygroscopicity parameter κ (see the modified κ-Köhler model proposed in chapter 3) are used as important indicators to understand the role of O_3 and SO_2 on the hygroscopic properties of soot. The effect of the reactants on the particle morphology has been studied by comparing fresh and aged soot particles. Soot size distribution with different geometrical standard deviations (σ_{geo}) have been analyzed in the cloud condensation nuclei counter (CCNc) in order to understand the influence of the size distribution on soot activation curves, thus to verify the validity of the model. Finally, κ estimated from soot activation curves by considering the size distribution and the morphology are presented as function of the exposure time of O_3 and SO_2, and compared with well-known dry particles as references in the $SS_c - d_p$ diagram which is commonly used in the literature (M. D. Petters and Kreidenweis 2007).

2. Review in the literature of soot aging studies in laboratories

In the literature, hygroscopic properties of soot particles sampled from soot generators, laboratory flames and engines are studied either in simulation chambers (Tritscher et al. 2011; Wittbom et al. 2014; S. Grimonprez 2016), or in continuous flow reactors (Kotzick et al. 1997; Zuberi et al. 2005; Lambe et al. 2015). Recent studies (Table I-2-2) show the effect of reactants (O_3, OH, UV, mineral acid and VOCs) on hygroscopic properties of "monodisperse" soot particles which are determined either in undersaturation (FCOM, H-TDMA), or in supersaturation (VSCNC, CCNc) conditions. In this chapter, the term "monodisperse" is used to indicate size selected soot particles obtained after filtering with a differential mobility sizer (DMA) set to a given electrode voltage, and typically feature σ_{geo} <1.1. At the DMA outlet, the size selected particles are electrically charged, however this effect is not taken into account in this work, and will probably be the subject of more detailed investigations in the future. Conversely, the term "polydisperse" is used to indicate the whole size distribution without any manipulation that typically feature σ_{geo}>1.5.

As mentioned in chapter 3 about the modified κ-Köhler model, the morphology and size distribution of soot particles are important parameter to understand the hygroscopic properties in the experiments. However, most of the recent studies (Table I-2-2) consider neither the morphology of soot nor the evolution of the morphology of soot during aging processes. The fractal dimension (D_f) is determined experimentally for freshly emitted soot particles and is assumed to be constant during the aging process by Kotzick and Grimonprez (Kotzicker al. 1997; Grimonprez. 2016). The primary particle diameter of freshly emitted soot particles are determined experimentally in the work of Zuberi and Wittbom (Zuberi et al. 2005; Wittbom et al. 2014). In fact, the particle size distribution and morphology might be influenced by physical processes such as particle coagulation or coating on surface or by chemical processes such as particle surface oxidation, both of which occur in soot aging processes. For instance, the increase of the mode of the mobility distribution during aging processes has been reported in the work of Kotzick and Grimonprez for instance (Kotzicker al. 1997; Grimonprez. 2016) soot particles are exposed to O_3, and is potentially induced by the particle coagulation due to the high concentration.

Table IV-2-1 The morphological properties of soot in the aging experiments. Mode increase ratio is defined as $\mu_{mode}^{t}/\mu_{mode}^{0}$, where μ_{mode}^{0} and μ_{mode}^{t} is the mode of the size distribution before and after the aging process.

Author	Experiments	Nature of soot	Reactive	Hygroscopic properties	Initial soot concentration	Coagulation indicators	Morphology indicators
(Kotzick et al. 1997)	Laminar flow reactor (1.3 L)	GfG 1000 (Palas GmbH, Karlsruhe)	O_3	VSCNC*	1-50×10^3 cm^{-3}	Distribution mode increase ratio 1.03	$D_f = 2$ D_m 20-100 nm
(Zuberi et al. 2005)	Flow tube	Methane and n-hexane	O_3 H_2O OH UV (254 nm) HNO_3	FCOM**	Deposition on the cell	Unknown	$\overline{D_{TEM}}$ 440 nm D_{pp} 30-70 nm
(Tritscher et al. 2011)	Simulation chamber (27 m^3)	Diesel motor (EURO 2) Diesel motor (EURO 3)	UV (290 nm and 400 nm)	CCNc H-TDMA***	14-25 μgm^{-3} (4-7×10^3 cm^{-3})	Unknown	D_m 30, 50, 100, 200 and 300 nm
(Wittbom et al. 2014)	Simulation chamber (6 m^3)	Diesel motor (EURO 2) CAST (propane)	Toluene xylene O_3 UV (354 nm)	CCNc	6-12×10^3 cm^{-3}	Unknown	D_{pp} 18-27 nm D_m 60, 90 and 150 nm
(Lambe et al. 2015)	Flow reactor	Premixed flat burner flame of ethylene	H_2SO_4 α-pinene m-xylene O_3 OH UV (254 nm)	CCNc	Unknown	Unknown	D_m 200 and 222 nm
(Grimonprez. 2016)	Simulation chamber (50 L)	Diffusion flame of kerosene	O_3	CCNc	9-13×10^4 cm^{-3}	D_m increase ratio 1.3	$D_f = 1.7$ D_m 150 and 300 nm

*VSCNC: Variable supersaturation condensation nucleus counter

**FCOM: Flow-cell optical microscopy

***H-TDMA: Hygroscopic Tandem Differential Mobility Analyzer

The main experimental difficulty of this work is related to the control of the particle number concentration in the reactors. In order to limit the effect of the coagulation on the activation process and focus on the potential change of morphology due to the aging, the number concentration of soot particles has to be maintained below a critical threshold. At the same time, care has to be taken to ensure that the number concentration of particles after the aging process is larger than the detection limit of the CCNc. The experimental configuration described in chapter 2 has been chosen to study hygroscopic properties of soot particles: the configuration with DMA selection aims to study "monodisperse" soot, while the configuration without DMA selection aims to study polydisperse soot. To do so, two conditions have been realized during experiments:

- The initial concentration of soot particles in the chamber is lower than 5×10^4 cm^{-3} in order to limit the coagulation.
- The (mobility) size distribution and the morphology of soot particles are recorded before and after the aging process respectively.

By using the high dilution sampling system described in chapter 2, the kerosene diffusion flame in the laboratory is able to provide size distributions of soot with mode in the range between 50 and 160 nm and with σ_{geo}~1.5. The initial concentration of soot particles is easily controlled by tuning the injection time. Size selection by the DMA combined with the CCNc has been chosen for studying the hygroscopic properties of “monodisperse” soot with mobility diameter of 150 nm in the LASC (124 L) and in the CESAM (3.4 m^3).

3. “Monodisperse” soot particles exposed to O_3 in the LASC

3.1. Protocol of the aging process of “monodisperse” soot in the LASC

Because of the efficiency of the DMA neutralizer and therefore of the charging process during size selection, only around 20% of the particles in the inlet flow are selected for the given size of 150 nm (chapter 2). In fact, with the DMA installed before the CCNc and the flow ratio set to 10 (flow ratio is the ratio between sheath flow and sample flow), the selection ratio (selected particle concentration over the total concentration) has been estimated experimentally as 3.8±0.5%. The selection ratio is much lower than the expected 20% because σ_{geo} of soot in the simulation chamber and sampled from flames is around 1.6 rather than 1. Technically, there are two opposite constraints on the upper and on the lower limit of the number concentration of “monodisperse” particles in the reaction chamber. First, the initial number concentration in the LASC should be lower than 5×10^4 cm^{-3} in order to limit the coagulation and preserve a constant mobility diameter of the investigated particles during the aging experiment. Second, the final number concentration after aging has to be larger than 50 cm^{-3} that is the detection limit of the CCNc. In practice, if the initial number concentration of “monodisperse” soot injected into the CCNc is lower than 2000 cm^{-3} (5×10^4 cm^{-3} times 4%, see the previous paragraph), after the aging with 1.1 $Lmin^{-1}$ nitrogen compensation, not enough particles remain in the LASC to provide a detectable signal at the end of the experiment. In order to avoid this limitation, σ_{geo} of soot size distribution has been reduced to 1.1, thus increasing the selection ratio.

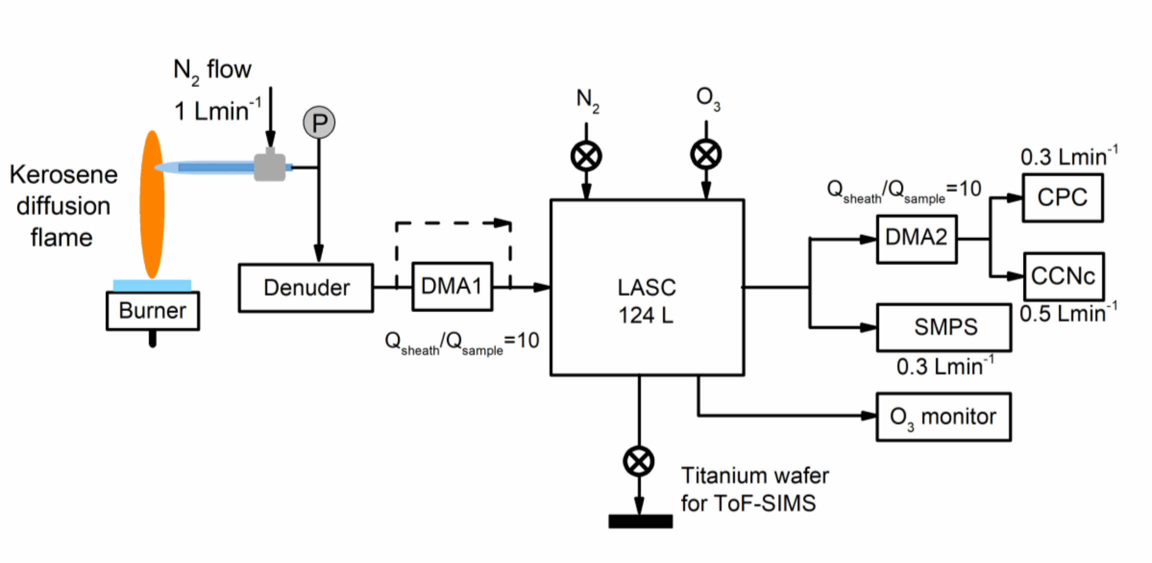

Figure IV-3-1 Experiment setup for studying the hygroscopic properties of "monodisperse" soot exposed to O_3 in the LASC.

Figure IV-3-1 shows the experimental setup to study the hygroscopic properties of size selected soot in the LASC. Kerosene diffusion flame provided soot particles. The quartz probe samples soot particles at 70, 100, 130 and 140 mm HAB, which are studied in this work. The diffusion denuder after the sampling system aims to remove most of the gases in order to let only the particle pass in the LASC. The DMA1 is installed before the LASC (flow ratio equal to 10) to provide a lower soot concentration with $\sigma_{geo}{\sim}1.1$, which ensure enough "monodisperse" soot particles in the CCNc (initial number concentration larger than 2000 cm^{-3}). The dash line represents the investigation of the previous work (S. Grimonprez 2016). In the LASC, the temperature is controlled to be 22°C constantly. The relative humidity during the experiment is lower than 0.2%. Ozone is generated by the photolysis of oxygen (chapter 2). The initial ozone concentration is controlled to be around 1.2 ppm for all experiments in the LASC. On-line measurements are performed using the ozone analyzer, the size mobility particle sizer (SMPS) and the configuration of the DMA, CPC and CCNc to record the ozone concentration, soot size distribution and the activated fraction (F_a) of the "monodiperse" soot particles with a mobility size of 150 nm. At the end of each experiment, soot particles are collected in order to obtain information on their chemical composition by using the technique secondary ions mass spectrometry (SIMS) which is presented in chapter 5.

Table IV-3-1 Comparison of the size distribution (middle column) and total concentration (right column) of soot particles in the LASC before and after aging, and with and without size selection (obtained with DMA1). [Total] is the total concentration of soot particles, [CCNc] is the concentration of “monodisperse” soot into the CCNc. In the protocol including DMA1, black and blue data series represent the size distribution at t = 0 and t = 400 minutes aging. Black solid dots and black hollow dots represent the total concentration as function of time. In the protocol without DMA1, red and green data series represent the size distribution at t = 0 and t = 400 minutes of polydisperse soot in the LASC. Black solid dots and black hollow dots represent the total concentration as function of time. In the bottom row, the comparison of the two modes agains time is shown. Black down triangles and red up triangles are the size distribution mode as function of time for soot in the LASC provided by the two protocols.

<table>
<tr><th>Protocol</th><th>Size distribution</th><th>Total concentration</th></tr>
<tr><td>With DMA1</td><td>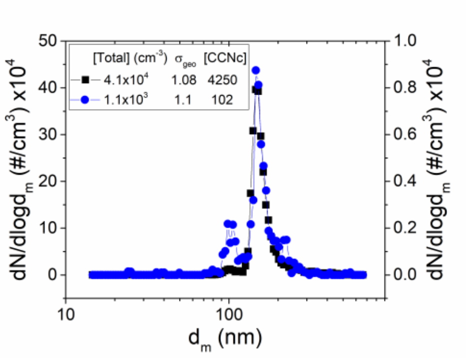
</td><td>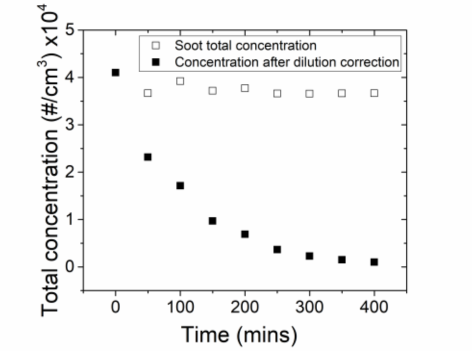
</td></tr>
<tr><td>Without DMA1</td><td>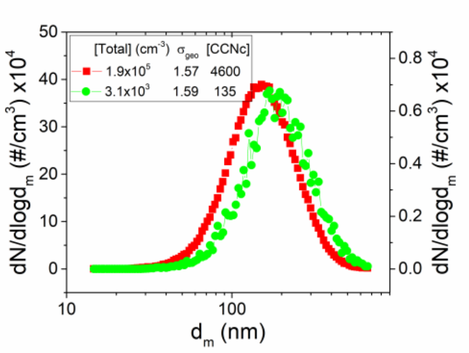
</td><td>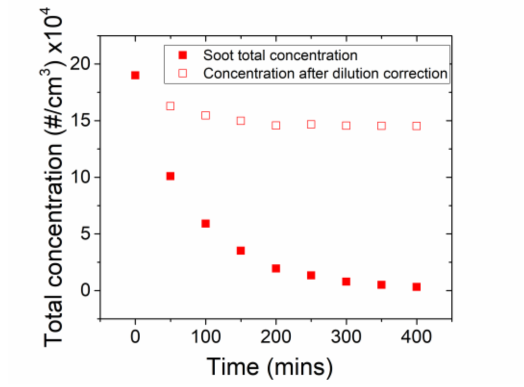
</td></tr>
<tr><td>Comparison of the distribution modes</td><td>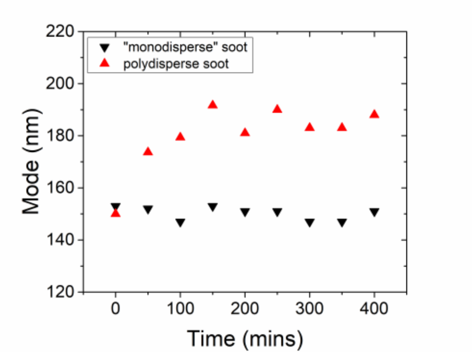
</td><td></td></tr>
</table>

As shown in Table IV-3-1, the evolution of the size distribution of soot particles in the LASC with and without DMA1 has been compared at the beginning of the experiment. Soot particles are sampled at 70 mm HAB. With DMA1 installed before the LASC, σ_{geo} of soot is 1.09±0.01. During the 400 min long aging experiment, the total concentration decreases from 4.1×10^4 cm^{-3} down to 1.1×10^3 cm^{-3} due to the dilution of 1.1 Lmin^{-1} produced by the inlet flow of nitrogen required to compensate the sample flow of the instruments connected to the LASC chamber (0.3 Lmin^{-1} for the CPC, 0.3 Lmin^{-1} for the SMPS and 0.5 Lmin^{-1} for the CCNc). The concentration corrected by the dilution is stable around $3.9\pm0.2\times10^4$ cm^{-3}. The mode of the distribution is constant as 150±2.5 nm. The concentration of “monodisperse” soot into the CCNc in this case varies from 4250 cm^{-3} down to 102 cm^{-3}, which is still in the working range of the CCNc. The average selection ratio in this case is 9.8±0.5%. Without using DMA1, the initial concentration of soot particles is 1.9×10^5 cm^{-3} in order to obtain the same concentration of “monodisperse” soot concentration into the CCNc (4600 cm^{-3}) compared to the previous protocol. During the dilution of 1.1 Lmin^{-3} for 400 min, the total concentration decreased down to 3.1×10^4 cm^{-3}. The selection ratio in this case is 3.4±0.9%. The concentration corrected by the dilution decreased from 1.9×10^5 cm^{-3} to 1.4×10^5 cm^{-3} with a decreasing ratio of 26%. The mode of the size distribution increased from 150 nm to 183 nm. To compare these two protocols, both of them provide the “monodisperse” soot concentration into the CCNc. However, from the evolution of the corrected concentration and the mode of the size distribution, soot particles provided without using DMA1 has a non-negligible effect on the coagulation. As concluded in the previous comparison, the protocol with using DMA1 before the chamber has been chosen to apply the experiments of “monodisperse” soot study in the LASC (this section) and in the CESAM (section IV-3.2).

With the setup presented in Figure IV-3-1, twelve tests have been performed in the LASC. Experimental conditions for soot aging processes are shown in Table IV-3-2. Three soot samples at 70, 100, 130 and 140 mm HAB in the kerosene diffusion flame have been studied in the LASC in controlled condition of temperature (23°C), relative humidity (<0.2%) and pressure (1000 mbar). For each test, ozone is generated directly into the LASC up to 1.3 ppm in the first time. Then, soot particles are injected into the LASC. The injection time is controlled to ensure a total concentration lower than 5×10^4 cm^{-3} in order to limit the coagulation effect. Soot particles are exposed to O_3 with the dilution flow of 1.8 Lmin^{-1} (0.8 for the CCNc and CPC, 1 for O_3 monitor). After the given aging time, the activation of “monodisperse” soot selected by the DMA is measured. In addition, the size distribution of soot particles is measured immediately after the soot injection and before the measurement of the activation of soot particles. Finally, after the aging process, samples are collected for SIMS analyses.

Table IV-3-2 Experimental conditions of aging process with O_3 in the LASC for studying the hygroscopic property of "monodisperse" soot particles.

Test name	Date yy.mm.dd	HAB (mm)	Residence time (min)	RH (%)	[O_3] initial (ppm)
LASC1	17.09.25	70	23	<0.2	0
LASC2	17.09.25	70	60	<0.2	1.35
LASC3	17.09.26	70	148	<0.2	1.30
LASC4	17.10.10	100	11	<0.2	0
LASC5	17.10.10	100	62	<0.2	1.25
LASC6	17.10.11	100	149	<0.2	1.20
LASC7	17.10.11	130	10	<0.2	0
LASC8	17.10.12	130	66	<0.2	1.30
LASC9	17.10.12	130	141	<0.2	1.35
LASC10	17.09.26	140	17	<0.2	0
LASC11	17.09.27	140	64	<0.2	1.30
LASC12	17.09.27	140	148	<0.2	1.35

3.2. Evolution of the size distribution of soot particles exposed to O_3 in the LASC

The evolution of the size distributions of soot during aging processes is studied in this section in order to understand the role of O_3 on the change of the morphology. To achieve this goal, soot particles sampled from four HABs (70, 100, 130 and 140 mm) in the kerosene diffusion flame have been exposed to N_2 in the LASC during three hours. The mobility size distribution has been recorded as function of time. Table IV-3-3 shows the comparison of the evolution of soot particles exposed to N_2 and exposed to N_2/O_3 in the LASC, where the initial O_3 concentration is around 1.27 ppm. In all cases, the initial concentration of soot is in the range 2.1×10^4 cm^{-3} to 4.5×10^4 cm^{-3}. As a reference, blank experiments have been performed in the same conditions as the aging but without O_3. In this case, the increase ratio of the mode is less than 1.05. By comparing the size distribution at t = 3 minutes and t = 3 hours, two shoulders (at 100±5 nm and 230±10 nm) are observed on the left and the right of the main mode of the size distribution after the exposure for all soot samples. These shoulders are more evident for soot sampled from 130 and 140 mm HAB than soot sampled from 70 and 100 mm HAB. For the blanks and soot exposed O_3, the increase ratio of the mode is less than 1.05, which is very close to the value measured in the blank. The effect of the coagulation is therefore considered as negligible. Two shoulders with same modes (102±6 nm and 231±9 nm) have been observed as well.

Table IV-3-3 Evolution of size distribution of size selected soot exposed to N_2 and N_2/O_3. Soot samples are extracted from 70, 100, 130 and 140 mm HAB respectively. Multi-charge corrections were applied for all the size distributions. Black square dots line represents the size distribution at t = 3 minutes, blue round dots line represents the size distribution at t = 3 hours.

HAB (mm)	Soot exposed to N_2	Soot exposed to N_2 with O_3 (1.27±0.7 ppm)
70	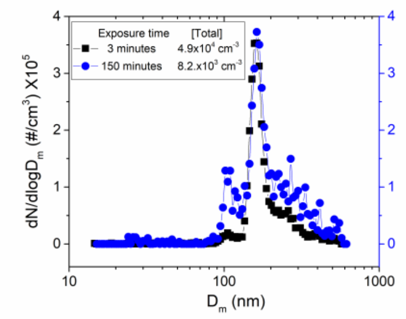	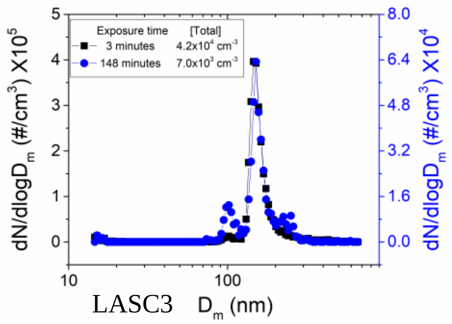
100	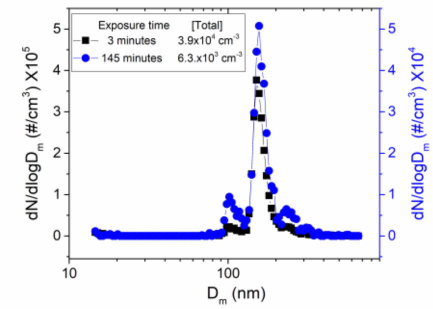	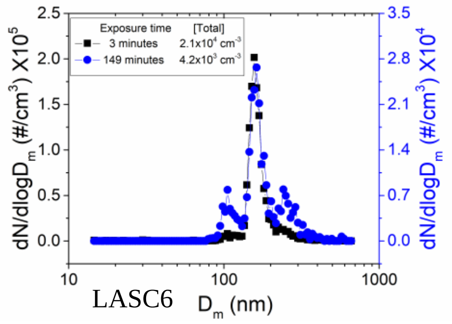
130	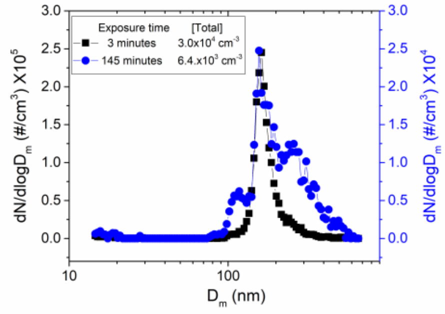	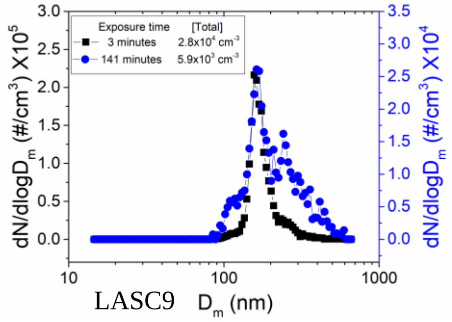

140

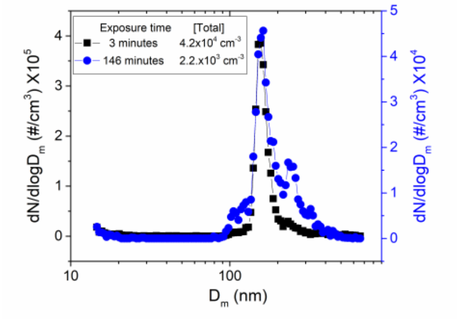

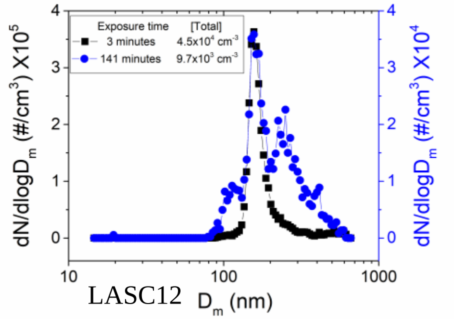

LASC12

By comparing the evolution of the size distribution of soot in two conditions: blank and exposed to O_3, the presence of O_3 change neither the mode of the size distribution, nor the shoulders. Compared to the size distribution generated without the DMA (Table IV-3-1), the shoulders exist for the investigation with the DMA which selects a given size before soot particles enter the LASC. There might be a charge effect behand this shoulders due to the working principle of the DMA. Though we could not give a definitive explanation for the presence of these tow shoulders, O_3 basically has no influence on the size distribution of soot particles, and the coagulation effect is negligible for the study of “monodisperse” soot particles in the LASC.

3.3. Link between aging with O_3 and activation of soot particles

$F_a - SS$ curves of the “monodisperse” soot particles with mobility diameter of 150 nm are presented in Figure IV-3-2. In each panel, $F_a - SS$ obtained with fresh soot (black dots), soot after 60 minutes exposition (red dots) and soot after 150 minutes exposition (blue dots) are shown. Lines represent the fittings using the modified κ-Köhler model and setting σ_{geo} and κ as free parameter (Chapter 3), while the black line represents the Kelvin limit (κ = 0). According to the experimental data, the activation of fresh soot is always zero at supersaturation as high as 1.8%, which well agrees to the conclusions of several works in the literature (Petzold et al. 2005; Zhang et al. 2008; Khalizov et al. 2009; Tritscher et al. 2011; Wittbom et al. 2014; Lambe et al. 2015). The activation becomes significant for exposure time larger than 10^{17} cm^{-3} s (100 ppb ozone for 18.8 hours). Soot at HAB = 70 mm is the most active ($\kappa = 1.9\times10^{-3}$), whereas soot at HAB = 130 mm is least active ($\kappa = 2.5 \times 10^{-4}$). This behavior is mentioned as well by Grimonprez (Symphorien Grimonprez et al. 2018). σ_{geo} estimated from the soot activation curves are in the range of 1.07 and 1.16 which have a good agreement with the experimental σ_{geo} of 1.1 presented in section IV-3.2.

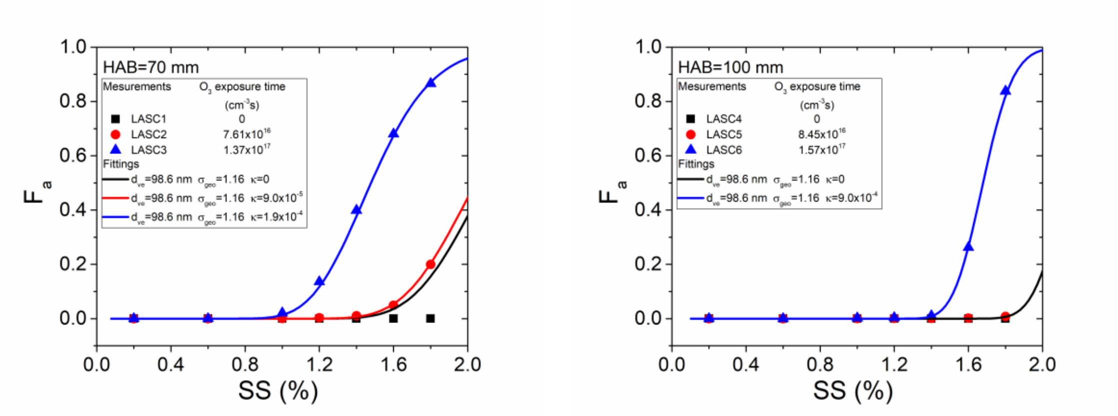

HAB=70 mm

HAB=100 mm

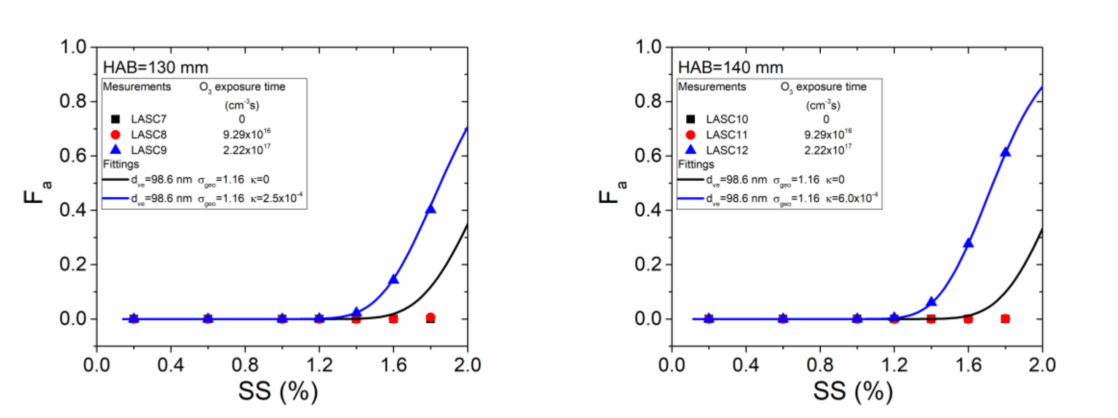

HAB=130 mm

HAB=140 mm

Figure IV-3-2 Activation curves of size selected soot exposed to O_3 in the LASC chamber.

In the literature, O_3 is considered as an important oxidizer in the reaction of polycyclic aromatic hydrocarbons (PAHs) in the atmosphere (Perraudin et al. 2007). In our case, the reaction of the PAHs adsorbed on the surface of soot and O_3 potentially results in the formation of polar compounds that modify the hygroscopic properties of the otherwise hydrophobic fresh soot particles. In order to understand the different hygroscopic behavior of the aged soot from different HABs, the time dependent O_3 concentration is assumed to follow the first order kinetics:

$$[O_3]_t = [O_3]_0 \exp\left[-(k_{wall} + k_{soot})t\right] \qquad \text{Equation IV-3-1}$$

where $[O_3]_0$ is the initial O_3 concentration and $[O_3]_t$ is the O_3 concentration at time t, k_{wall} is the ozone loss rate by the inner wall of LASC, k_{soot} is the ozone loss rate by soot particles. The black, red, blue, purple and green data points represent the O_3 concentration of LASC 3, 6, 9, 12 and the background check without soot, respectively. The high correlation coefficient strengthens the hypothesis of a first order kinetics.

The ozone loss rate and a short description of the samples (the same already detailed in Table IV-2-3) are given in Table IV-3-4. The ozone loss rate is calculated from the slope of the linear fits from Figure IV-3-3. Clearly, the ozone loss rates of the background test and LASC9 are very close. The ozone loss rate of LASC6 and LASC12 is larger than the previous two tests. The ozone loss rate of LASC3 is the largest. We suppose that k_{wall} is identical for all experiments performed in LASC, and therefore k_{soot} can be calculated by difference as shown in the last line of Table IV-3-4. From the background measurement, the loss rate due to the reactor walls can be easily estimates as $k_{wall} = (1.49 \pm 0.03) \times 10^{-5}$ s^{-1}. k_{soot} of ozone in LASC3 is 40 times higher than that in LASC9. By comparing κ and k_{soot}, the soot particles exposed to O_3 in LASC9 are the least active, which corresponds to the lowest k_{soot}. Potentially, the ozone loss rate explains that soot from HAB=130 mm adsorb or absorb less ozone during the aging process. More information on the particles chemical composition is given in chapter 5.

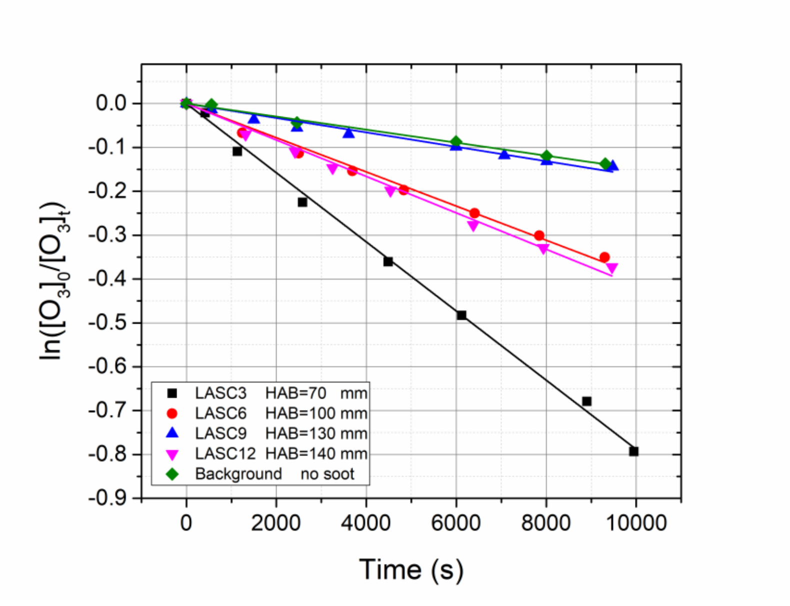

Figure IV-3-3 Plot of $ln([O_3]_0/[O_3]_t)$ vs. time in LASC 3, 6, 9 and 12 after the dilution correction. O_3 concentration data were corrected by dilution loss.

Table IV-3-4 Ozone loss rate in LASC 3, 6, 9 and 12.

Test name	Background	LASC3	LASC6	LASC9	LASC12
Soot source	No soot	HAB=70 mm	HAB=100 mm	HAB=130 mm	HAB=140 mm
$k_{wall} + k_{soot}$ (10^{-5})	1.49±0.03	7.9±0.1	3.89±0.08	1.64±0.06	4.15±0.08
k_{soot} (10^{-5})	0	6.4±0.1	2.40±0.09	0.15±0.07	2.66±0.09
κ (10^{-4})	None	19.0	9.0	2.5	6.0

4. "Monodisperse" soot particles exposed to O_3 and SO_2 in the CESAM chamber

4.1. Protocol of the aging process of "monodisperse" soot in the CESAM

The experimental setup shown in Figure IV-4-1, similar to that in Figure IV-3-1, has been designed to generate the monodisperse soot aging experiments in the CESAM which provided a controlled atmospheric condition of temperature ($T = 20$°C), pressure ($p = 1013$ mbar), relative humidity ($RH = $0-20%) and simulated solar radiation. The soot injection system, hygroscopic properties measurement system, N_2/O_3 injection, SMPS, ozone analyzer and sample collection for ToF-SIMS analysis are common parts between the experiments in the CESAM and in the LASC. DMA1 is installed before the CESAM in order to reduce σ_{geo} of the size distribution in the CESAM. DMA2 with a flow ratio of 10 is used to provide "monodisperse" soot particles into the CCNc. σ_{geo} of "monodisperse" soot particles is estimated experimentally as 1.1. The injection of SO_2/H_2O, UV radiation system, nano-SMPS and other gas analyzers (FTIR, SO_2 and NO_x) are specific for soot aging experiments in the CESAM.

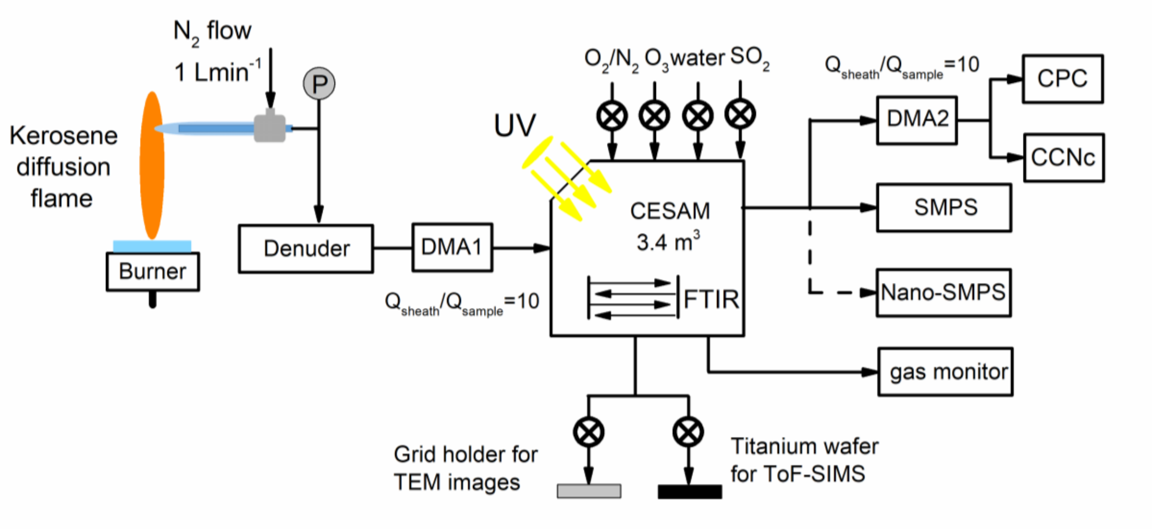

Figure IV-4-1 Configuration of the setup for soot aging experiments performed in the CESAM.

In this work, the online determination of the size distribution by SMPS, the measurements of the concentration of $O_3/SO_2/NO_x/CO_2$ and the measurement of the hygroscopic properties are performed in parallel. Ex-situ morphology of soot by TEM analysis and chemical composition by SIMS techniques are combined. Soot particles sampled from the kerosene diffusion flame at 130 mm HAB have been studied due to their low activity as CCNs after aging with O_3 (section IV-3.3). To study the effect of the environmental conditions on the activation of soot particles, O_3 (0.5-1 ppm), *RH* (0-20%), SO_2 (100 ppb) and irradiation with UV have been performed in different order to study the role of each reactant on the activity of "monodisperse" soot as CCNs.

Table IV-4-1 shows experimental conditions of soot aging process in the CESAM. Test CESAM0 without soot particles has been done as the background check in order to know the interactions between reactants (O_3, H_2O, SO_2 and UV radiation), and to be compared with other tests as the reference. Then CESAM4 and CESAM6 provided the aging process of soot exposed to O_3/H_2O and of soot exposed to OH radicals respectively. CESAM4 aimed to make the comparison with soot aging process in the LASC (section IV-3). CESAM6 aimed to make a comparison with the activity of soot as function of OH^- exposure time obtained in the campaign CESAM2015 already presented in the Ph.D of Grimonprez. In CESAM7, a long time aging process of 400 min has been performed to verify the role of SO_2 on the change of the activity of soot particles after exposing to OH radicals in the CESAM. A significant influence is observed, which demonstrated that SO_2 play potentially an important role on the hygroscopic properties of soot particles. To verify this hypothesis, three tests (CESAM1, 2 and 3) have been performed in order to study the role of the injection order of O_3, SO_2 and H_2O on the activation of soot particles. The background check with soot particles exposed to N_2/O_2 has been done in CESAM5. TEM samples are collected at the end of the aging process in CESAM2, 5 and 7 in order to know the morphology of soot particles (section IV-4.4) exposed to O_3/SO_2, N_2/O_2 and all reactants (O_3, H_2O, SO_3 and irradiation of UV). SIMS samples are collected at the end of the aging process in CESAM1, 2, 3, 4 and 5 in order to give information on the chemical composition of the aging soot particles, and to correlate it to the changing of hygroscopic properties (chapter 5).

Table IV-4-1 Experimental conditions of soot aging process in the CESAM to study the role of SO_2 on the hygroscopic properties of "monodisperse" soot particles sampled at 130 mm HAB of the kerosene diffusion flame. [O_3], [SO_2] and [OH^-] are the concentration of ozone, sulfur dioxide and OH^-, respectively.

Test name	Date yy.mm.dd	HAB (mm)	Residence time (min)	RH (%)	[O_3] initial (ppm)	[SO_2] initial (ppb)	UV radiation	[OH^-] (ppt)
CESAM0	18.02.13	No	40	20	1.2	100	Yes	0.19
CESAM1	18.02.23	130	90	<0.2	0.50	100	No	0
CESAM2	18.02.21	130	156	<0.2	1.10	110	No	0
CESAM3	18.02.20	130	204	20	1.10	109	No	0
CESAM4	18.02.15	130	107	20	0.53	0	No	0
CESAM5	18.02.22	130	14	<0.2	0	0	No	0
CESAM6	18.02.15	130	140	20	1.2	0	Yes	0.17
CESAM7	18.02.16	130	400	20	1.2	100	Yes	0.18

4.2. Hygroscopic properties of particles formed in homogeneous nucleation regime

In the CESAM campaign, the impact of O_3, SO_2, H_2O and UV radiation have been on the hygroscopic properties of soot particles. However, these reactants can also initiate the homogeneous nucleation via the formation of H_2SO_4 (Metzger et al. 2010) following the chain of reactions:

$$O_3 + h\nu(\lambda < 310\ nm) \rightarrow O + O_2$$

$$O + H_2O \rightarrow 2OH$$

$$2OH + SO_2 \rightarrow H_2SO_4$$

As shown in the time scale on the top of Figure IV-4-2, water, O_3 and SO_2 are injected in the CESAM one by one. The homogeneous nucleation of particles is observed immediately after UV irradiation. This finding is remarkably similar to that reported by (K. Li et al. 2017). The time evolution of the particle mobility distribution is also shown in Figure IV-4-2. The nano-particles with $D_m = 2.5$ nm are measured using a nano-SMPS TSI model 3085 specifically installed for this experiment. The mobility size of the nucleated particles increased from 2.5 nm to 40 nm in 60 min, following the well-known “banana plot” trend (K. Li et al. 2017).

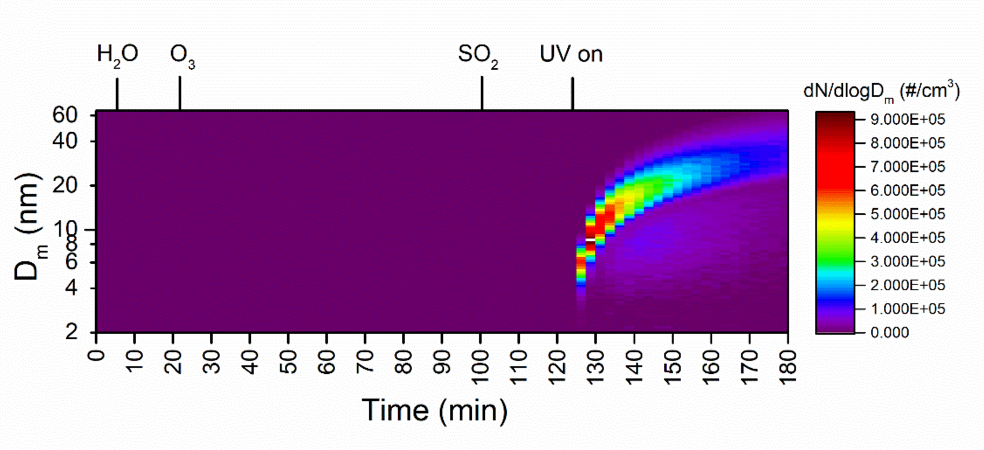

Figure IV-4-2 Evolution of the size distribution of the homogeneously nucleated particles in condition of $H_2O/O_3/SO_2$ exposure and UV irradiation in CESAM.

Two cycles of measurements by CCNc are performed for size selected particles at 40 and 60 nm. The activation data are presented in Figure IV-4-3. Black square dots and red round dots represent the activation of nanoparticles having $D_m = 40$ nm and $D_m = 60$ nm, respectively. The black and red lines represent the fits by the modified κ-Köhler model. Remarkably, the two different sizes result in the same value of $\kappa = 0.55$. In similar experimental conditions (mixture of H_2O, O_3 and SO_2 exposed to UV radiation), the homogeneous nucleation of H_2SO_4 droplets has been observed already (K. Li et al. 2017). However, the result of $\kappa = 0.55$ in this work is quite different from $\kappa = 0.9$ of pure H_2SO_4 droplets reported by (M. D. Petters and Kreidenweis 2007). This difference suggests that the nano-particles from the homogeneous nucleation have different chemical composition than pure H_2SO_4, and might for instance be a mixture of water and H_2SO_4.

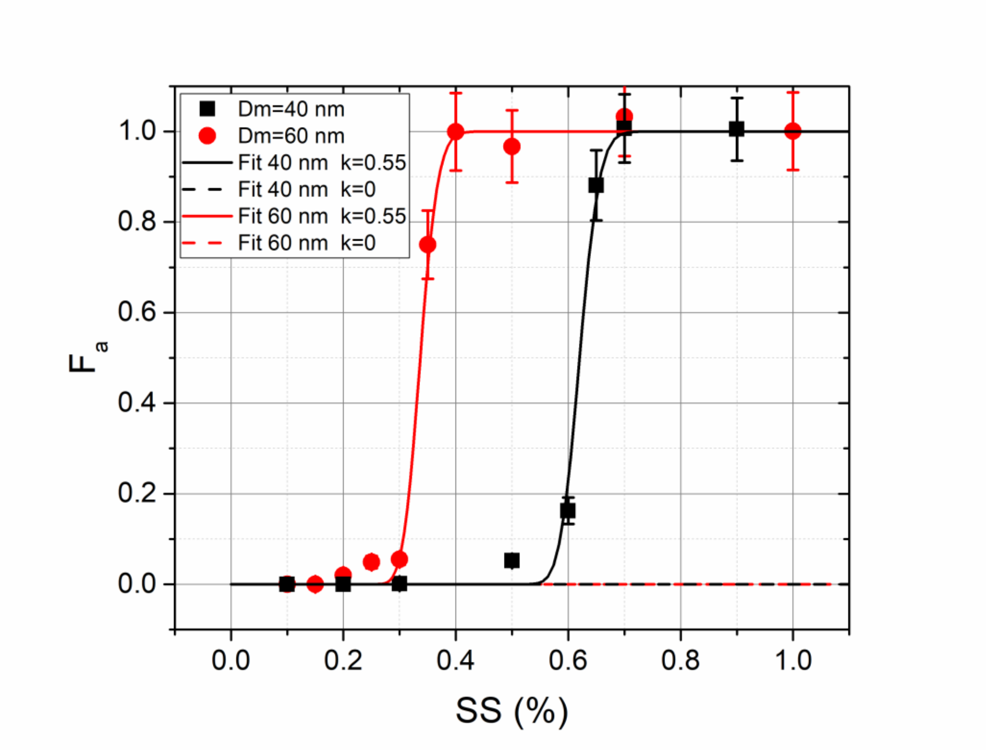

Figure IV-4-3 Activation curves of size selected nano-particles (40 and 60 nm) in regime of homogeneous nucleation from a gas mixture containing H_2O, O_3 and SO_2 and exposed to UV radiation.

4.3. Evolution of the size distribution of soot particles in the CESAM

In all tests involving soot particles, the initial concentration of soot has been maintained below 5×10^4 cm^{-3} by controlling the injection time in order to respect the condition discussed in section IV-3.1 for limiting the coagulation effect. Size distributions of soot particles in the CESAM have been recorded on line by the SMPS. A representative case (CESAM7) is shown in this section (Figure IV-4-4): soot particles exposed to O_3, H_2O, SO_2 and UV radiation in a long time aging process of 400 minutes. Soot aerosols are sampled from the kerosene diffusion flame at 130 mm HAB, and then injected into the CESAM during 75 min. After waiting for the observation of the activation of soot particles in the CCNc, O_3 is generated into the CESAM up to of 1.2 ppm. Water vapor is then generated using a high pressure cooker with several injections until the relative humidity arrives to 20%. UV irradiation is initiated 20 min after the injection of water vapor to provide OH radicals due to the photolysis process presented in chapter 2. Two measurements of the activated fraction (F_a) as function of supersaturation (SS) have been done for "monodisperse" soot particles. In order to test the role of SO_2 on the activation, UV irradiation is turned off and SO_2 is injected until its concentration arriving 100 ppb. One measurement of F_a-SS has been done after the injection of SO_2. Another measurement of $F_a - SS$ has been done for soot particles exposed to SO_2 and OH^-.

Figure IV-4-4 shows the evolution of the size distribution of soot particles in the CESAM. DMA1 is set to select soot particles with a mobility diameter of 150 nm. In the CESAM, the main mode (dark red points in the figure) has mobility diameter of 157±2 nm at the beginning of soot injections. 20 min later, a second mode is observed with mobility diameter of 230±9 nm which corresponds to the observation of a right shoulder in the size distribution in the LASC (section 3.2). During the aging process of soot exposed to O_3, H_2O, SO_2 and UV radiation in 400 min, the main mode increased from 157±2 nm to 170±4 nm corresponding to a mode increase ratio of 1.08. In conclusion, the mode of the size distribution of soot particles in the CESAM is stable around 164±9 nm. We assume that the coagulation of soot particles in this case is negligible. These negligible coagulations in the CESAM have been observed in CESAM1-6 as well.

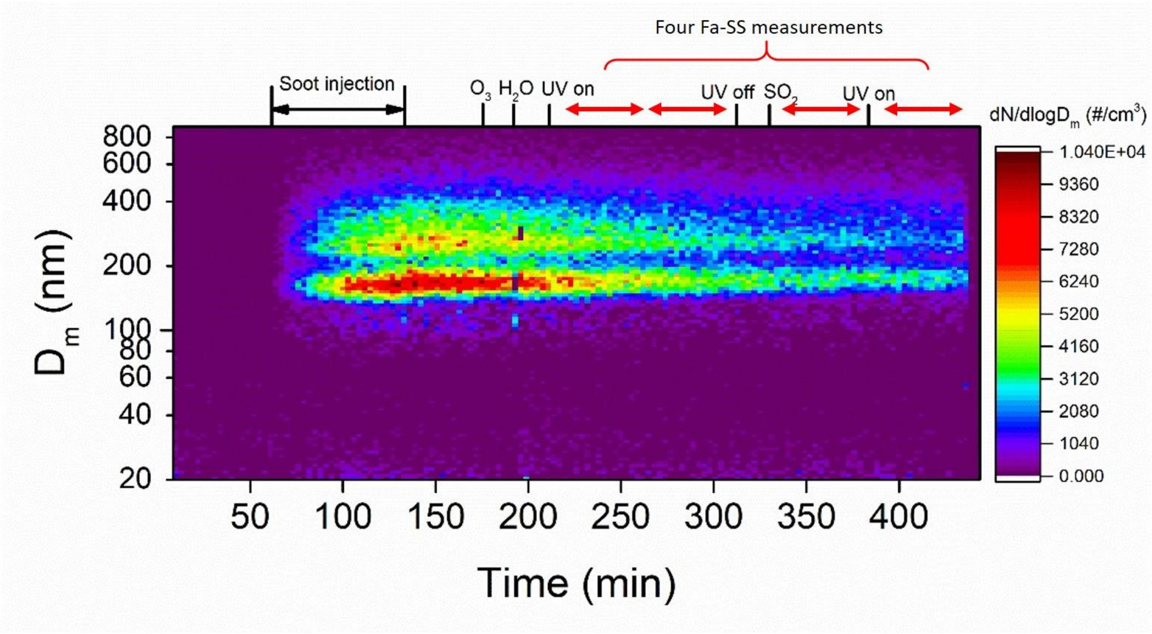

Figure IV-4-4 Evolution of the size distribution of soot exposed to $H_2O/O_3/SO_2$/UV in CESAM.

4.4. Evolution of the morphology of soot in the CESAM

TEM samples are collected for CESAM 2, 5 and 7, where soot particles are exposed to O_3/H_2O, N_2/O_2 and $O_3/SO_2/H_2O$/UV respectively. Table IV-4-2 shows the results of the TEM analysis which provides the primary particle diameter (d_{pp}) and the fractal dimension (D_f) of soot samples.

Table IV-4-2 Determination of the morphological parameters of soot particles in CESAM chamber. Red bars represent the counts on function of the primary particle diameter d_{pp}. The blue line represents the lognormal fit of the distribution of d_{pp}. The black dots represent the relation between $ln\ N_p$ and $ln\ (L_{2D}/d_{pp})$ of soot projection from which the fractal dimension is obtained. The red line represents the linear fit. k_g and D_f are the fractal prefactor (intercept) and fractal dimension (slope).

Test name	Primary particle diameter d_{pp}	2D projection of soot particles $N_p = k_g(L_{2D}/d_{pp})^{D_f}$
CESAM2 Soot exposed to O_3 and H_2O, 156 min exposure.	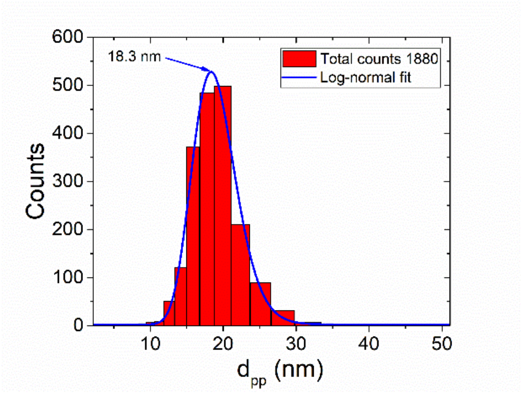 Mode=18.3±0.2 nm σ_{geo}=1.17±0.01	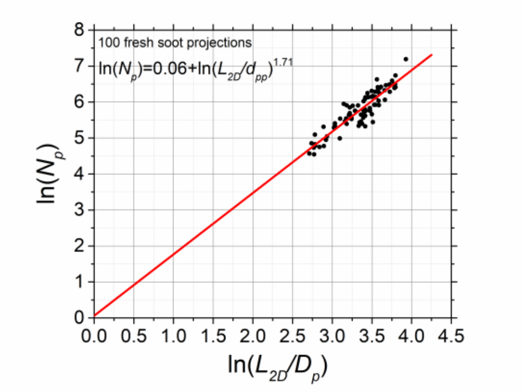 D_f=1.71 k_g=1.06
CESAM5 Soot exposed to N_2 and O_2, 14 min exposure.	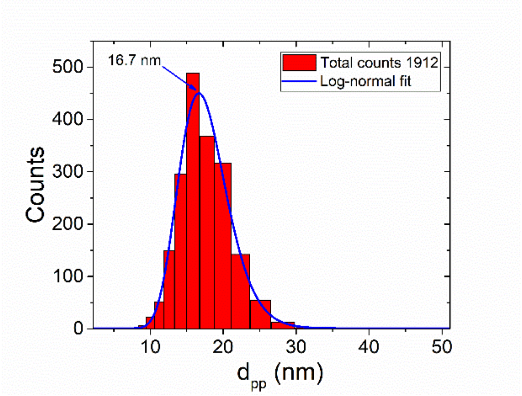 Mode=16.7±0.2 nm σ_{geo}=1.21±0.01	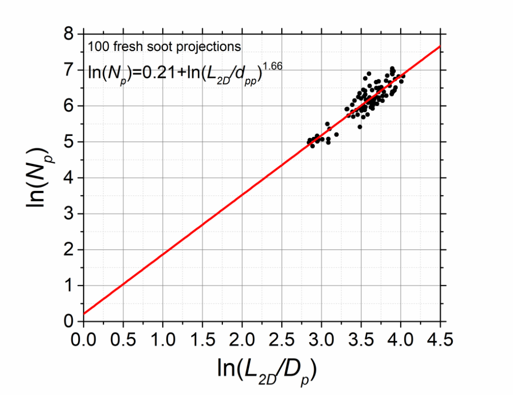 D_f=1.66 k_g=1.23

CESAM7 Soot exposed to O_3, SO_2, H_2O and UV radiation, 400 min exposure.	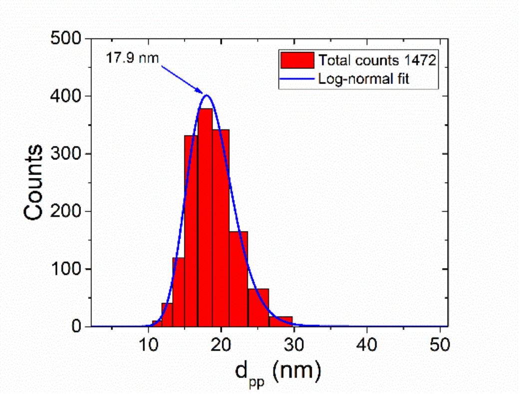	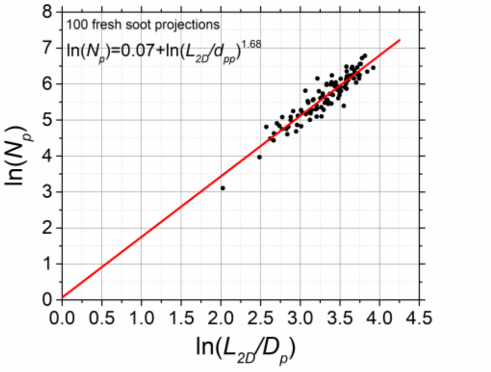
	Mode=17.9±0.2 nm σ_{geo}=1.18±0.01	D_f=1.68 k_g=1.07

The principle of the TEM analysis is presented in chapter 3. d_{pp} of fresh soot is estimated as a lognormal distribution with mode 16.7 nm and σ_{ve} 1.17 (experiment CESAM5). According to the value obtained in CESAM2 and CESAM7, the aging process with O_3, SO_2, H_2O and UV radiation increased the average of d_{pp} by 1.4±0.3 nm. The fractal dimension (D_f) of soot particles in all cases varies from 1.66 to 1.71 which is well consistent with typical values found in the literature (Köylü et al. 1995; Caiet al. 1995; Samson et al. 1987; Tian et al. 2006). In conclusion, the aging process of soot particles with O_3, SO_2, H_2O and UV radiation in the CESAM slightly increased d_{pp} (around 8% increase) and D_f (around 2% increase). Therefore, we concluded that the exposing to O_3, SO_2, H_2O and UV radiation did not significantly modify the morphology of soot particles in the CESAM campaign.

4.5. Role of SO_2 on the activation of “monodisperse” soot as CCNs

4.5.1. Evolution of the activation of soot in the aging process with O_3, SO_2, H_2O and UV radiation

As mentioned in section IV-4.1, the soot aging process with O_3, SO_2, H_2O and UV radiation in CESAM7 has been performed to study the role of SO_2 on the aged soot particles as CCN. Figure IV-4-5 recalls the protocol of CESAM7 which is already presented in section IV-4.3.

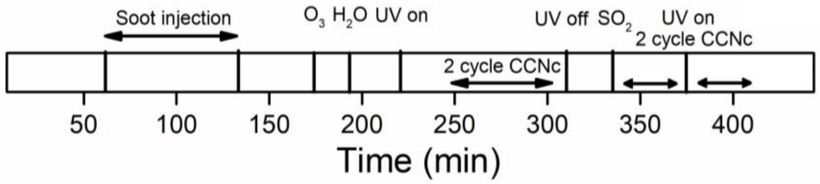

Figure IV-4-5 Protocol of CESAM7: "monodisperse" soot from HAB=130 mm exposed to OH radicals.

In the following experiments, it is important to notice that the presence of homogenous nucleation of droplets as discussed in section IV-4.2 cannot be ruled out. However, the mobility of the droplets formed by homogeneous nucleation is estimated to cap at 60 nm, and therefore the presence of a DMA filter upstream the CCNc effectively removes them from the sample flow and prevents any interference with the measurement of the activation curves.

Four F_a-SS curves have been obtained in CESAM7 and are presented in the left panel of Figure IV-4-6. Two of them (red up triangle dots and green down triangle dots) represent "monodisperse" soot particles exposed to OH radicals, and the other two (blue diamond dots and cyan left triangle dots) represent "monodisperse" soot particles exposed to OH radicals and SO_2. The black dot represents the single F_a of fresh soot at $SS = 1.6\%$. The lines in the figure represent the fittings of activation curves applied by the modified κ-Köhler model proposed in chapter 3. The volume equivalent diameter (d_{ve}) is estimated based on the morphology parameters: $d_{pp} = 16.7$ nm and $D_f = 1.68$ presented in section IV-4.4. σ_{geo} is estimated to be 1.17 for all activation curves. During the aging process in CESAM7, κ increased from 0 to 0.18.

The critical supersaturation (SS_c) of these four activation curves as function of OH radicals are presented in the right panel of Figure IV-4-6 using the same symbol as in the left panel. SS_c is defined as the supersaturation when F_a is equal to 0.5. These four critical supersaturations are compared with the results of the previous work in Grimonprez's Ph.D. which are represented as magenta square dots. The SSc of soot exposed only to OH radicals follows well the decreasing tendency. After introducing SO_2 in CESAM, the SS_c (~1.0) of soot particles quickly decreases down to a much lower value (~0.3) than that (~0.8) expected from (S. Grimonprez 2016). This sudden decrease of the SS_c after the injection of SO_2 shows that SO_2 plays a role on hygroscopic properties of "monodisperse" soot particles.

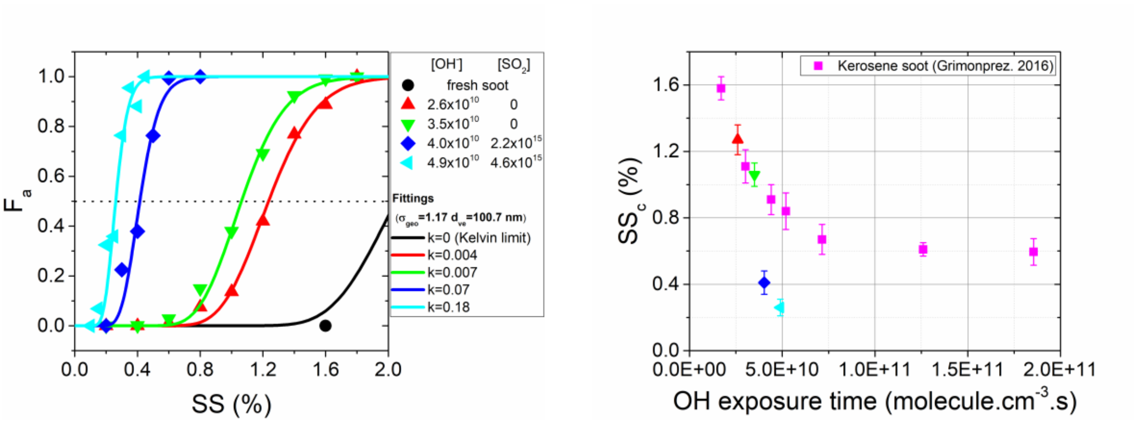

Figure IV-4-6 Left panel: $F_a - SS$ of soot particles exposed to O_3, SO_2, H_2O and UV radiation in CESAM7. Right panel: critical supersaturation (SS_c) of the activation curve of soot exposed to OH^- in CESAM7 and comparison with the results of (Grimonprez 2016). SS_c is defined as SS where F_a=0.5.

4.5.2. Necessity of O_3 and SO_2 to activate soot particles

CESAM7 demonstrates that the presence of SO_2 accelerates the activation of soot exposed to OH radicals. Additionally, two more tests (CESAM1 and 2) have been performed reducing the number of reactants in order to find the key reactant(s) on the activation of soot particles. Figure IV-4-7 shows the evolution of the concentration of O_3 and SO_2 and the F_a at SS =1.6%. In CESAM1, O_3 is injected first until the concentration arrives to 500 ppb. In such conditions, no activation is observed in 30 min after the injection of O_3, which is in good agreement with the observation in the LASC (section IV-3.3). SO_2 injection begins at 11:50, after that the F_a ("monodisperse" soot particles with 164 nm mobility diameter) increases very quickly and arrives to 1 in around 3 minutes. In CESAM2, the order of the injection between O_3 and SO_2 has been switched. The concentration of SO_2 is increased up to 100 ppb first. No activation at SS =1.6% is observed in 30 minutes after the injection of SO_2, which demonstrates that SO_2 alone cannot activate soot particles to form water droplets. O_3 is injected second, after that the activation (again "monodisperse" soot particles with 164 nm mobility diameter) increases and arrives to 1 in around 3 min after the injection of O_3. The activation of soot particles in CESAM1 and 2 is observed without the participation of water vapor, specifically the relative humidity is lower than 0.2% during the all experiments. It is also noteworthy that, from the SIMS surface analyses detailed in Chapter 5, further evidence could be obtained that the activation reaction involves the particles rather than the gas phase.

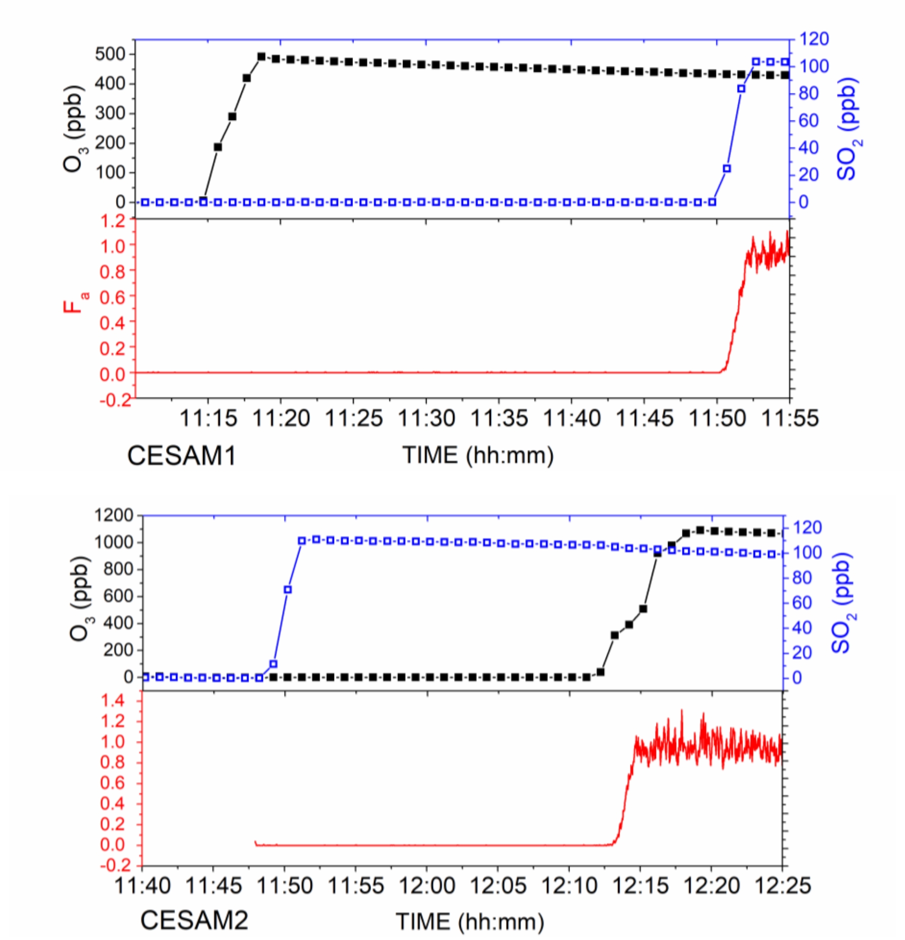

Figure IV-4-7 The evolution of O_3, SO_2 concentration and F_a in CESAM1 and CESAM2. Black and blue dotted lines represent respectively the concentration of O_3 and SO_2. Red lines represent the activation at $SS = 1.6\%$.

4.5.3. The role of water vapor on the hygroscopic properties of soot particles

A new experiment (CESAM3) with $RH = 20\%$ was performed in order to study the role of water vapor on the activation of soot exposed to O_3 and SO_2. The injection order is presented in Figure IV-4-8. Soot particles are injected first. 30 min after the injection of soot, SO_2 is injected. There is no activation at $SS = 1.6\%$ for 20 minutes. Then, the relative humidity is increased up to 20%. After the injection of water vapor, there is no activation at $SS = 1.6\%$. In the end, O_3 is injected up to 1.2 ppm. At this point, the activation occurs quickly. Four cycles of $SS = 1.6\%$ for "monodisperse" soot particles with size of 164 nm have been measured by the CCNc in the next 2 hours.

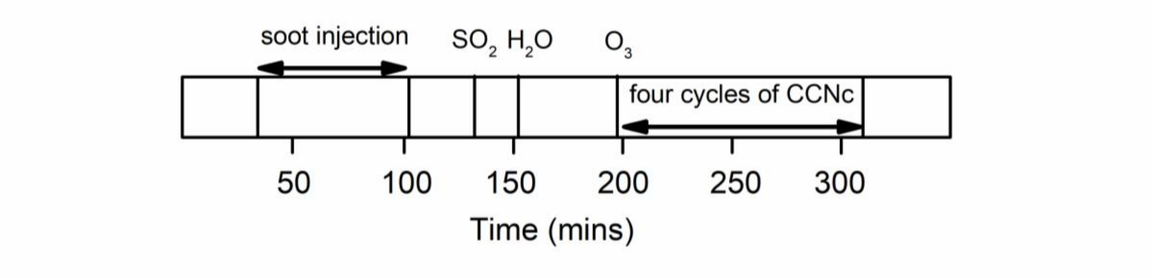

Figure IV-4-8 Protocol of CESAM3: "monodisperse" soot from HAB = 130 mm exposed to SO_2, H_2O and O_3.

The SS_c of soot activation curves in CESAM3 is presented in Figure IV-4-9 against SO_2 exposure. Globally, SS_c of soot follow a net decreasing tendency. With increasing the SO_2 exposure time, SS_c reaches a plateau around 0.15%. The SSc of soot particles exposed to H_2O have lower value compared to that for soot exposed only to O_3 and SO_2. By comparing the SS_c between CESAM1, 2 and 3, water vapor might play a role to decrease the SS_c of soot particles. The decrease of SS_c at high RH i.e. the presence of water vapor makes soot more hydrophilic is consistent with the findings reported by He et al. (He et al. 2017). However, one RH is not enough to draw definitive conclusions, and more data are required to confirm the observed behavior of relative humidity on soot activation.

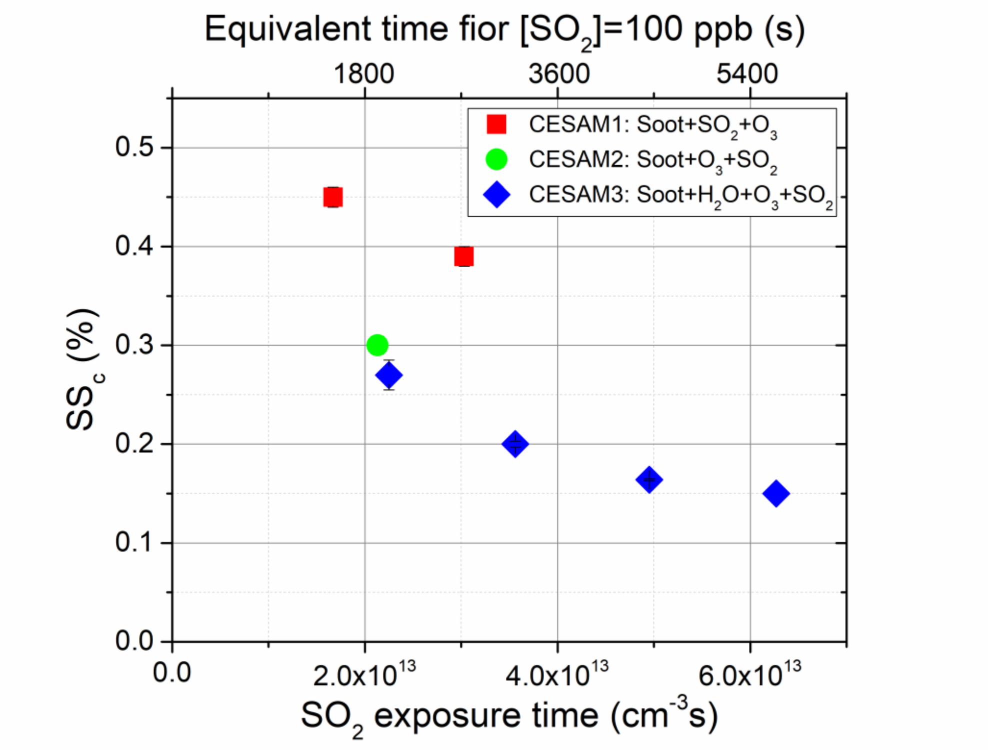

Figure IV-4-9 SS_c of soot activation on function of SO_2 exposure time in CESAM1, 2 and 3. SO_2 exposure time is counted from the time O_3 and SO_2 are present at the same time.

5. Polydisperse soot particles exposed to O_3 in the LASC

5.1. Protocol of the aging process of polydisperse soot in the LASC

"Monodisperse" soot particles are studied in the previous sections to show the role of O_3 and SO_2 on the hygroscopic properties of soot particles by measuring F_a during the aging processes. However, one of the possible applications of the modified κ-Köhler model proposed in chapter 3 is to provide a method to study directly polydisperse soot particles without DMA selections, as for lognormal size distributions σ_{geo} is included and accounted for in the model. In this section, a simpler experimental setup without DMA selection has been used in the LASC to study the activation of soot particles exposed to O_3 in order to (1) verify the validation of the modified κ-Köhler model on polydisperse soot particles, (2) compare the estimated κ of "monodisperse" and polydisperse soot particles from the same flame.

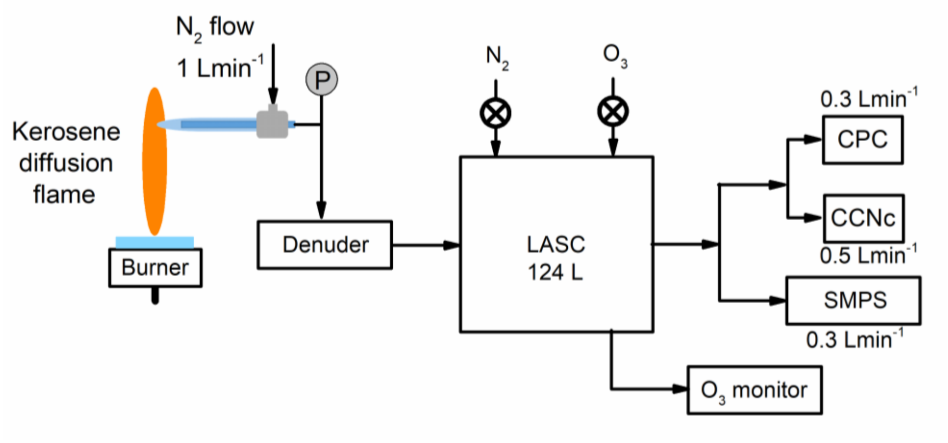

Figure IV-5-1 Setup for studying the hygroscopic properties of polydisperse soot in the LASC.

Figure IV-5-1 shows the experimental setup to study polydisperse soot particles in the LASC. In all experiments the following parameters are used: temperature of 23°C, pressure of 1000 mbar and relative humidity lower than 0.2%. In the experiments, ozone is injected first into the LASC at concentration of 1.2 ppm. Then, soot particles are sampled at 70 mm HAB in the kerosene diffusion flame, passed in the diffusion denuder to remove most volatile species, and finally injected into the LASC with a total concentration lower than 5×10^4 cm^{-3} once again to limit coagulation phenomena. The size distribution, total concentration of polydisperse soot particles and the concentration of O_3 are monitored on line using the SMPS, CPC and O_3 analyzer, respectively. During the aging process in the LASC, two cycles of $F_a - SS$ have been measured by the CCNc at residence time of 98 minutes and 130 minutes.

5.2. The evolution of size distribution of soot exposed to O_3 in the LASC

The size distribution of soot particles in the LASC at $t = 3$ minutes and $t = 130$ minutes are presented and compared in Figure IV-5-2 in order to study the influence of O_3 on the evolution of the mobility diameter. At $t = 3$ minutes, the soot particles are freshly emitted, the total concentration is 5.8×10^3 cm^{-3} with σ_{geo} of 1.44 and mode of 138 ± 3 nm. After 130 min aging with O_3, the total concentration of soot particles in the LASC decreased to 9.0×10^3 cm^{-3} due to the dilution and nitrogen compensation. σ_{geo} and mode of the size distribution after aging is 1.46 and 139 ± 4 nm. In conclusion, the mode and σ_{geo} of the size distribution of soot particles remained constant and within the estimated incertitude during the aging with O_3.

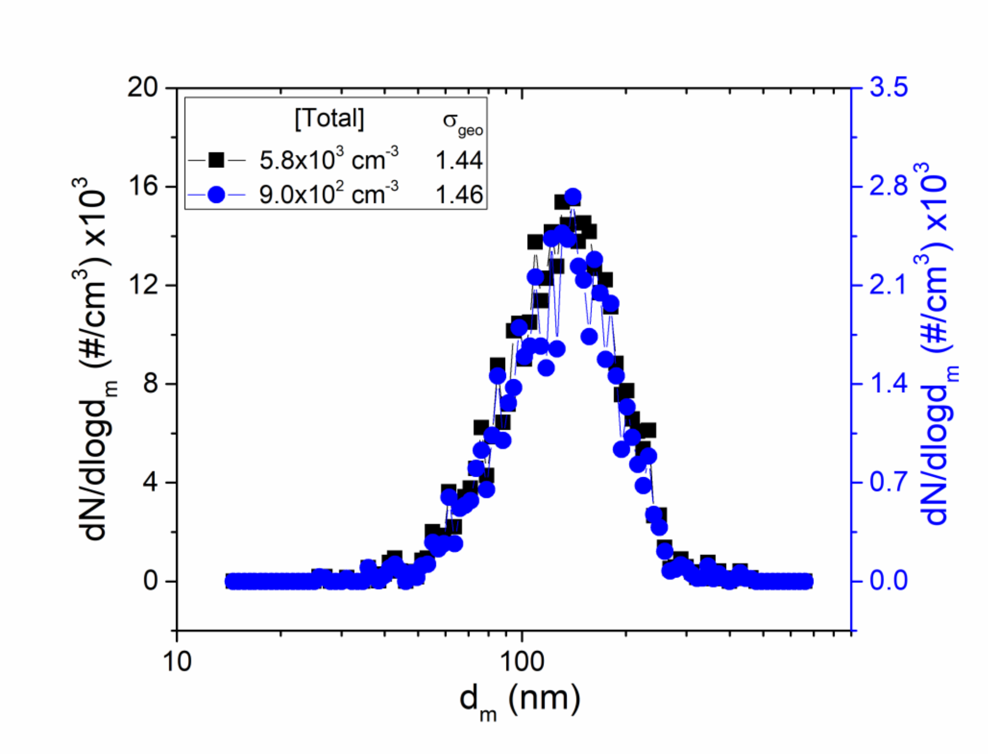

Figure IV-5-2 Evolution of size distribution of polydisperse soot exposed to O_3. Soot is sampled at 70 mm HAB. Black square dots and blue round dots represent the size distribution at t = 3 minutes and t =130 minutes, respectively.

5.3. The activation of polydisperse soot exposed to O_3 in the LASC

The activation curves of the polydisperse soot during the aging process with O_3 are presented in Figure IV-5-3. Red square dots and green round dots represent respectively $F_a - SS$ of polydisperse soot particles at t = 98 minutes and t = 130 minutes, respectively. The lines represent the fitting curves calculated using the modified κ-Köhler model presented in Chapter 3. In the CESAM chamber, the morphology of soot particles aged in conditions very similar to this experiment (soot sampled at the same HAB and using the same sampling conditions, same aging process) did not change significantly during the aging process. Based on this observation, although detailed measurements on the morphology of the particles were not performed during this experiment, we assume that the morphology of soot in this experiment did not change either and is similar as the morphology in the CESAM presented in section IV-4. Then, the volume equivalent diameter (d_{ve}) calculated as 89.3 nm based on the mobility diameter of 138 nm, d_{pp}

of 16.7 nm and D_f of 1.67 are used in the calculation of the activation curves, with all these parameters estimated as explained in section IV-4.4. The free parameter σ_{geo} is calculated as 1.47 from the fit of these two activation curves. In Figure IV-5-3, the red and green lines represent the activation curve of polydisperse soot particles with ozone exposure time of 9.78×10^{16} $cm^{-3}s$ and 1.13×10^{17} $cm^{-3}s$. The black line represents the theoretical Kelvin limit of the polydisperse soot particles in this experiment, i.e. polydisperse soot with mode of 138 nm and σ_{geo} of 1.47 which returns a nearly perfect agreement with the experimental σ_{geo} of 1.45 ± 0.1 presented in section IV-5.2. In this case, the hygroscopicity κ of polydisperse soot sampled from 70 mm HAB arrives as high as 1×10^{-3} which is in the same range of κ (1.9×10^{-3}) of “monodisperse” soot sampled from the same height presented in section IV-3.3.

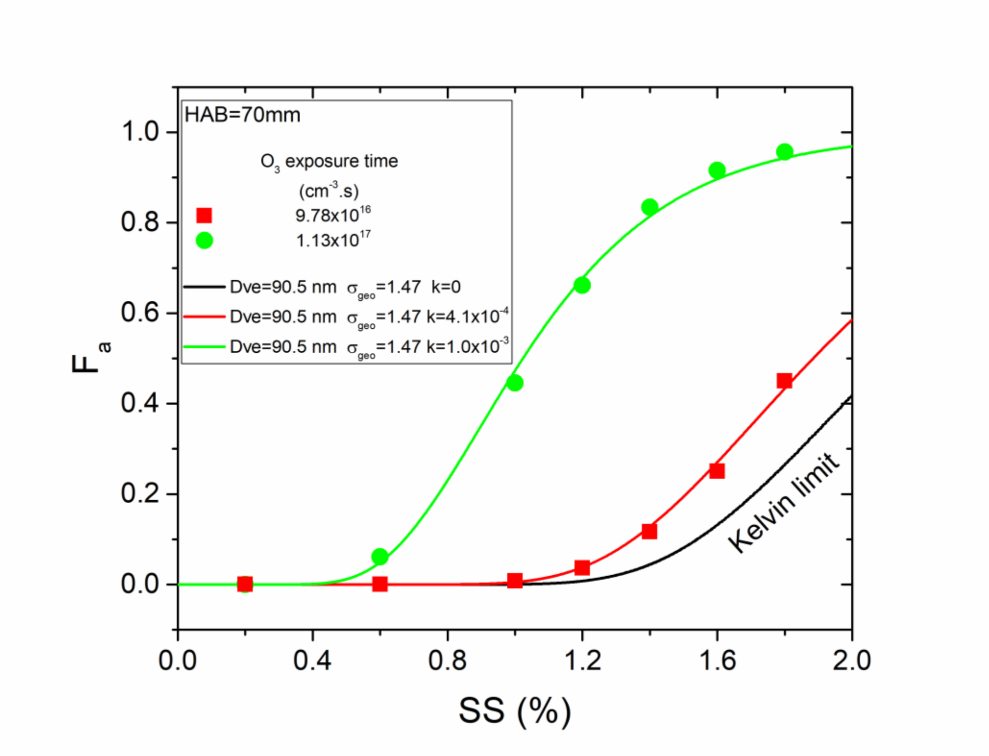

Figure IV-5-3 Activation curves of the polydisperse soot exposed to O_3 in LASC

6. Conclusions

This chapter focuses on the role of O_3 and SO_2 on the activation of soot particles as CCNs. The (mobility) size distribution, the morphology and the hygroscopicity κ are all important indicators to understand the hygroscopic properties of soot particles. In all aging experiments performed in the LASC and in the CESAM, the mode increase ratio of the size distribution is under 1.08 which demonstrates the small influence of O_3 and SO_2 on the size distribution of soot particles. According to the study of the morphology of soot particles, d_{pp} and D_f are stable within 17.4±0.7 nm and 1.68±0.03. We found that the aging process with O_3, H_2O, SO_2 and UV radiation does not significantly change the morphology of soot particles.

Soot sampled at HAB of 70, 100, 130 and 140 mm are studied. A long exposure time (100 ppb for 18.8 hours) is required for O_3 to activate soot particles with SS as high as 1.6%. However, the participation of SO_2 immediately activates soot in the same condition of pressure, temperature and relative humidity. Both O_3 and SO_2 are required to achieve this activation no matter which one is present first. With the SO_2 exposure time of 5×10^{15} cm^{-3} s (100 ppb for 1.25 hour), the supersaturation required to activate soot particles decreases to values as low as 0.15%. In this chapter, the modified κ-Köhler model is applied for determining κ of "monodisperse" and polydisperse soot. The model works well on the fitting of the activation curves of soot, especially the good agreement of σ_{geo} form the fitting estimation and the experimental measurements.

Table IV-6-1 Comparison of σ_{geo} from experimental size distribution in the LASC and CESAM and from the fitting of activation curves.

Test name	LASC 2-3	LASC 5-6	LASC 8-9	LASC 11-12	LASC 13	CESAM 0	CESAM 1-2
Experimental σ_{geo}	1.1±0.1	1.1±0.1	1.1±0.1	1.1±0.1	1.44±0.08	1.1±0.1	1.1±0.1
Fitted σ_{geo}	1.16	1.07	1.14	1.13	1.47	1.06	1.17

To better understand the level of the hygroscopic properties of soot in these two campaigns, the $SS_c - d_p$ data are presented in Figure IV-6-1. The black lines are calculated by Köhler theory for dry spherical particles. Red line corresponds to the hygroscopic properties of

$(NH_4)_2SO_4$. By considering the morphology of soot particles, $D_f = 1.68$ is used for obtaining the equivalent diameter d_{ve}. Green square dots represent soot exposed to O_3 in LASC. Blue round dots represent soot exposed to OH^- and cyan triangles represent soot exposed to both O_3 and SO_2. Magenta triangles the results of nano-particles formed in homogeneous nucleation, and are used as a blank. These results show that soot exposed to O_3 and SO_2 can be activated such that it plays the same role as ammonium sulfate aerosol, which is known to be one of the most hygroscopic particles, acting as CCN, in the troposphere.

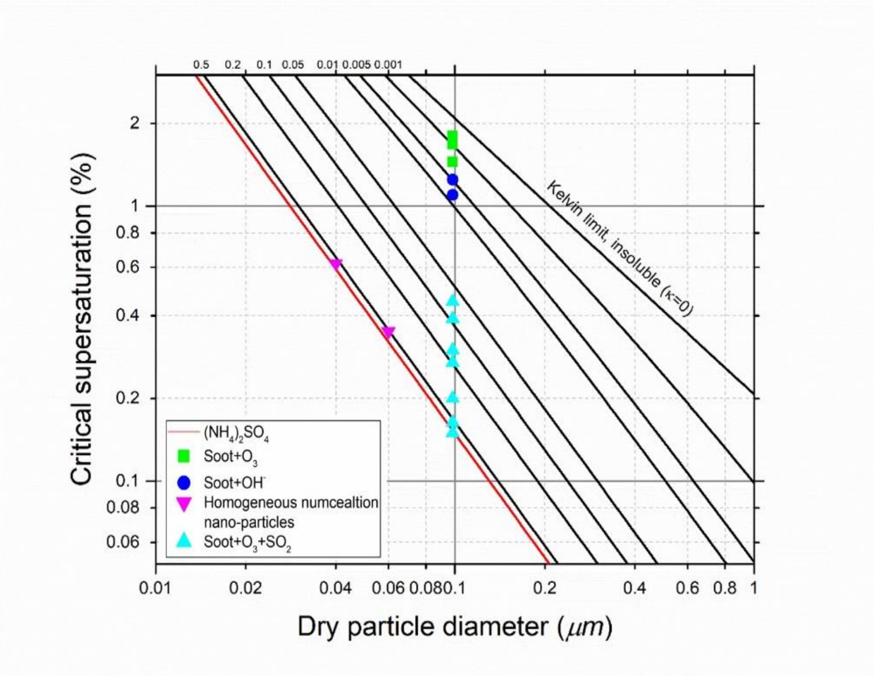

Figure IV-6-1 SS_c vs. dry particle diameter plot of aged soot in LASC and CESAM. d_{ve} = 98.3 nm is calculated according to the model developed in Chapter 3.

Chapter V Analysis of the chemical composition of soot particles exposed to O_3 and SO_2

1. Introduction

The aim of this chapter is to get information on the chemical composition of the particles that act as CCNs, and particularly on the changes induced by the aging process that turns fresh inactive soot into active aged particles. To this purpose, we used Secondary Ion Mass Spectroscopy (SIMS) that is a surface analysis technique specifically developed to get information on the first monolayers. We developed a sampling technique that allows the separation of the contributions of the condensable gas and of the solid particles. Then, we compared samples before and after aging with different oxidizers of atmospheric interest. The investigated oxidizers include ozone and a mixture of ozone and sulfur dioxide, and to track the reaction of oxygen containing hydrocarbons (OCH) and sulfur containing compounds (SCC) are followed in the mass spectra. Finally, we reduced the data using multivariate analysis methods that enhance/highlight the differences between groups of samples, allow them to be classified and find the most representative mass of each class of samples. In this chapter, the principle of SIMS is first introduced in section V-1. Then, the protocol to reduce the mass spectra into chemical information (data reduction) is shown in section V-2. In section V-3, two statistical procedures are used for the data mining and interpretation: Principle Component Analysis (PCA) and Hierarchical Cluster Analysis (HCA). For better understanding the working principles of PCA and HCA in practice, an interesting database on forest fires is analyzed and is shown in section V-3.3. Finally, the analysis results of soot mass spectra from the experiments corresponding to chapter 4 are presented in section V-4, and discussed in section V-5.

1.1. Principles of Time of Flight-Secondary Ions Mass Spectrometry (ToF-SIMS)

For studying the chemical composition of soot during the aging process, the ToF-SIMS[5] instrument from ION-TOF GmbH available at the Regional Platform of Surface Analysis (Unité de Catalyse et Chimie du Solide, UCCS, Université de Lille) was used. A global overview of the ToF-SIMS 5 instrument is shown in Figure V-1-1 (a). It consists of an analysis chamber on the bottom, a Time of Flight (ToF) analyzer on the top and two ion guns providing Bi_3^+, Cs^+ or O_2^+ beside the spectrometer. During the analysis, the sample is transported in the analysis chamber.

The maximum surface which can be analyzed with this instrument (in this configuration) is 500 µm × 500 µm. Figure V-1-1 (c) gives a scheme of the ion impaction on the surface of the sample. High energy Bi_3^+ clusters hit the sample surface: the emission of atoms and molecules follows the collision. The particle energy is transferred to the atoms of the solid sample which then carry out a small percentage of atoms and molecules in ionized state (between 1% to 5 % from the ejected matter). The formed secondary ions are then accelerated in the extraction field. After that, ions enter in the time-of-flight (ToF) analyzer equipped with an electrostatic mirror as shown in Figure V-1-1 (b).

The vacuum level with a pressure of 10^{-7} mbar is required to increase the mean free path of the accelerated ions above the length of the instrument, i.e. to allow them to travel freely to the detector and to avoid the interaction between primary and secondary ions with gas molecules in the analysis chamber. SIMS can be operated in two working modes. The static mode for the surface analyses can probe the first monolayer down to 0.8 nm depth. While the dynamic mode for the in-depth distribution analysis of trace elements can probe from few nm to few µm depths. In the former, primary ions (Bi_3^+) of 25 keV with a current of 0.3 pA are generated for the first monolayer analysis, while in the latter primary ions (Cs^+ or O_2^+) are generated for the in-depth distribution analysis. In our case, the first mode was used in order to get an overview of all species in one sample. By changing the polarity of the acceleration plates and of the reflection, positive or negative ions can be independently selected during the ion extraction phase.

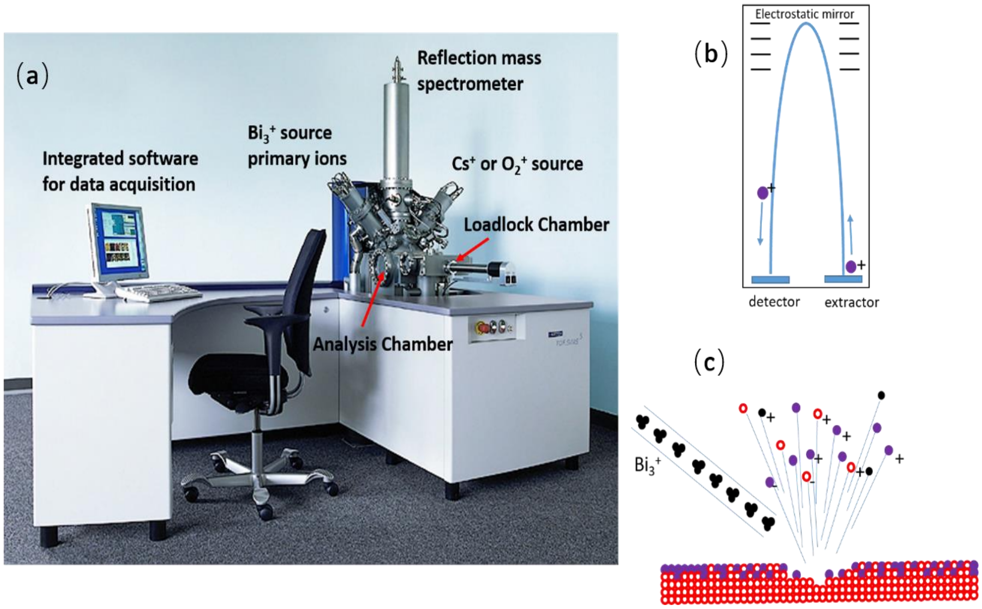

Figure V-1-1 (a) ToF-SIMS[5] setup image provided by ION-TOF GmbH. It contains load-lock chamber, analysis chamber, ions sources, ToF-SIMS tube and data acquisition integrated software. (b) Ion path in the ToF. (c) Sample ionization on sample surface.

The conversion from t_{ToF} to *m/z* is called mass calibration. Due to the initial energy distribution of the generated ions, t_{ToF} of the atoms having the same *m/z* are detected as a Gaussian distribution ("peak"). A critically important parameter during the mass analysis is the so-called mass resolution, which is described as: *m/Δm*, where *Δm* is the peak width (usually the full width at half maximum) of a given peak of accurate mass *m*.The mass resolution obtained in practice depends on the maximum resolving power of the instrument. In our case, the resolving power is around 10000, but the mass resolution in practice is in the range of 6000 to 7000. A high mass resolution leads to narrow peaks and a more accurate matching of *m/z* determined experimentally to only one of the possible exact masses (M_r). Therefore, the peak identification has a higher confidence level that is usually measured as the difference between the measured *m/z* and the proposed M_r.

1.2. Soot sample collection

An impactor system was developed to sample soot particles on titanium (Ti) wafers downstream the reactor chambers. Titanium wafers were purchased from PI KEM Ltd. They were polished on one side with $10\ \mathrm{mm} \times 10\ \mathrm{mm}$ surface area and 0.5 mm thickness. In Figure V-1-2 (a), the configuration consists of a valve for isolating the chambers (Chapter 2), a sample impactor and a tube for compensating the pressure with clean air after the sample collection. In the sample impactor, a metallic tube placed on the top of the Ti wafer at a distance of 1mm from the surface. The wafer was placed over a metallic mesh keeping some space between its edges and the border of the sample holder. All the flow is introduced to impact on the center of the wafer and is redirected to the exhausts by passing through the remaining space. In order to collect enough material on the wafer, the collection was performed during 20 minutes in which the pressure inside the reactor varied from the initial 1000 mbar down to 200 mbar. Some examples of collected samples are shown at the bottom of Figure V-1-2 (c). The black spot contains the soot particles (possibly mixed with adsorbed/deposited gas phase) and the yellowish circle around the black spot contains the condensable gas only. This separation of the black spot and yellowish circle is due to the different mass impacted on the wafer. The high mass soot particles are collected on the center as the spot, and the low mass molecule diffuse all over the wafer surface.

Before and after performing the sampling, the wafers were stored in glass boxes sealed with Teflon film. In almost all cases the samples were prepared one day before performing the surface analyses.

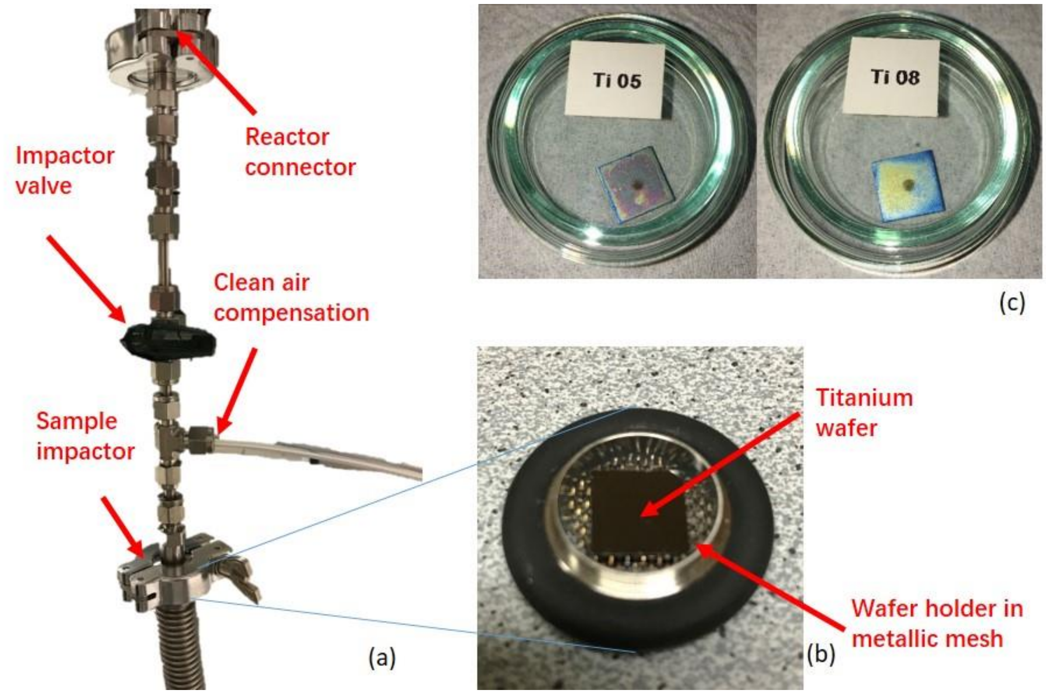

Figure V-1-2 Sample impactor configuration and the example of soot sample on Titanium wafer.

2. Data acquisition for mass spectra

In order to increase the reliability of the mass spectra to represent the sample, several positions were selected to be analyzed. In Figure V-2-1, three random position (white squares) in the central spot were selected to represent soot, and three additional random positions (red squares) in the outside the soot spot were selected to represent the condensed gases. Consequently, each sample is represented by 6 mass spectra. By consulting a protocol already published (Irimiea et al. 2018), a series of operations were performed during the data acquisition.

Figure V-2-1 Soot spot collected on the wafer.

2.1. Mass calibration

A common issue in high resolution mass spectrometry is the systematic shift between the t_{ToF} and the observed *m/z* that is often due to poor calibration or slight changes in the analytical parameters over different acquisitions. Therefore, systematic shifts sometimes appear in repeated acquisitions that might result in the same compound to be attributed different accurate mass. To minimize this uncertainty, the *m/z* axis are re-scaled and shifted in order to maximize the correlation between different samples and the calculated *m/z* of a group of reference peaks. The pattern of carbon fragment ions at low *m/z* and PAHs is assessed from the analysis of PAH standards and can be used as a reference to align the peak sequence. A fast mass calibration was initially performed by SurfaceLab software. This process was easily done using C^+, CH^+ and CH_2^+ because of their symmetrical shape. Then mass spectra were checked again with using some polyaromatic hydrocarbon molecular ions well-known to form in the flame such as $C_{10}H_8^+$, $C_{16}H_{10}^+$ and $C_{24}H_{12}^+$ (D'anna, et al. 2004; Wang 2011).

2.2. Smoothing

Being the primary purpose of the data reduction the measurement of both the accurate mass (*m/z* value of the center of the peaks) and the peak integrated area, a low smooth ratio algorithm was preferred to avoid excessive peak height reduction. A satisfying compromise between noise reduction and peak height reduction is found with a fast Fourier transform algorithm (FFT), three points sampling (corresponding to 105 Hz cutoff frequency) that efficiently removes the high frequency noise in exchange of approximately 5-10% reduction of the peak intensity. An example of the comparison is shown in Figure V-2-2, the smoothing procedure keeps the peak information.

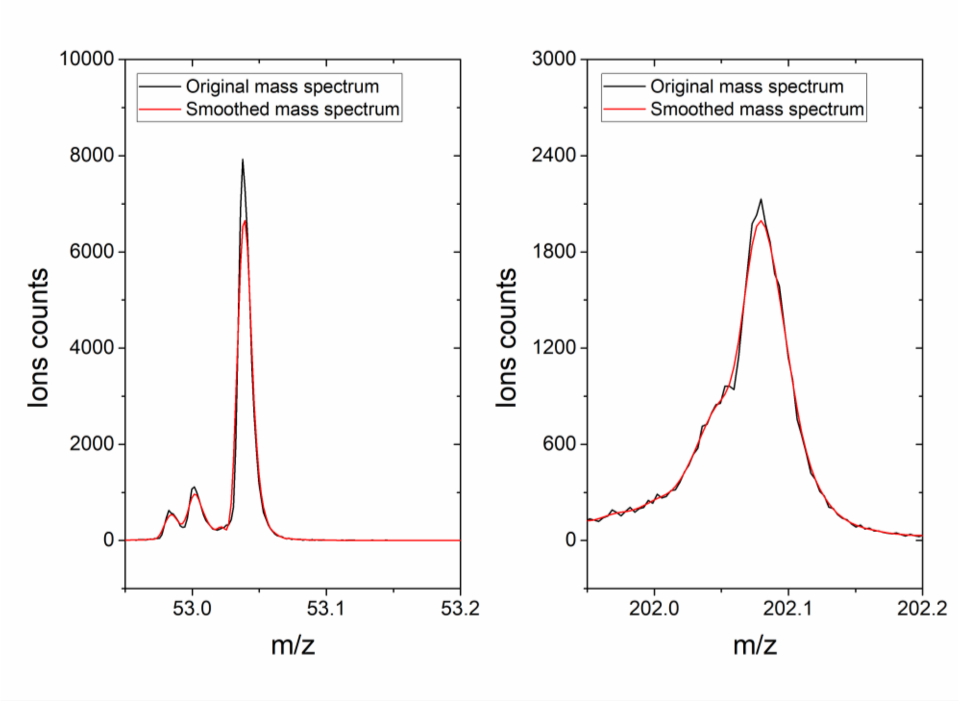

Figure V-2-2 Comparison of the peaks before and after the smoothing procedure at high m/z and low m/z.

2.3. Peak finding and integration

After the smoothing, the integration was performed to reduce the mass spectrum and make it represented only by accurate mass (*m*/*z*) and the intensity (the area integration of the peak). A peak finding algorithm based on second derivative filtering was used to automate the peak finding. Only the peaks above three times the standard deviation of the noise were treated as signals and thus integrated. Figure V-2-3 shows the coherence between the ion counts and the integration of peaks both in low and high *m*/*z* range. The integrated intensities are correlated to the ion counts of the peaks which allow the integrated intensity values and the center values of the peaks to represent the whole mass spectrum.

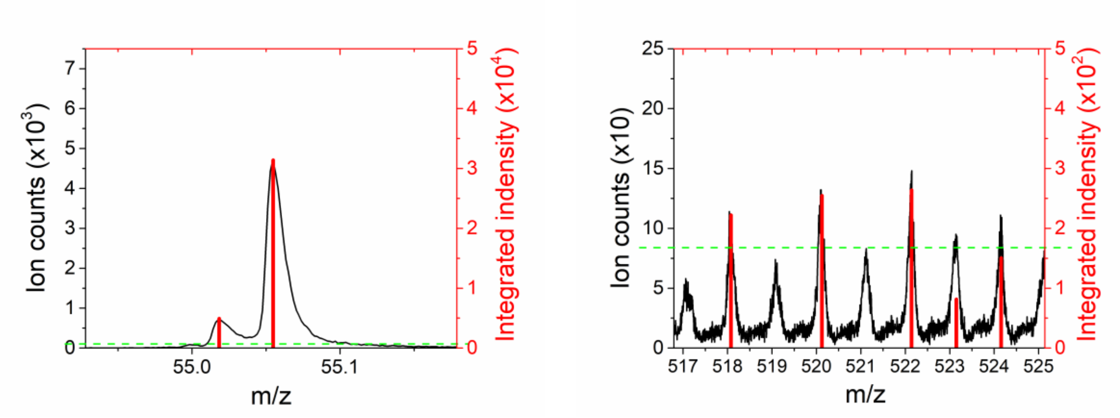

Figure V-2-3 Peak finding and integration. Black lines represent the mass spectrum; red bars represent the integrated value of the corresponding peak and green dashed line represents the filter level.

2.4. Mass defect analysis

Even though the peak finding procedure has been done automatically, the identification of the accurate mass was still difficult due to the large number of combinations of different elements that can result in a very similar accurate mass. Fortunately, mass defect analysis greatly helped in the assignment of a molecular formula to the selected accurate mass and therefore to the definition of a working peak list. In order to accurately describe the procedure, several important definitions on mass spectrometry are recalled according to the 2013 IUPAC (International Union of Pure and Applied Chemistry) recommendations (Murray et al. 2013):

- ***Accurate mass.*** Experimentally determined mass of an ion of known charge.
- ***Exact mass.*** Calculated mass of an ion or molecule with specified isotopic composition.
- ***Nominal mass*.** Mass of a molecular ion or molecule calculated using the isotope mass of the most abundant constituent element isotope of each element rounded to the nearest integer value and multiplied by the number of atoms of each element.
- ***m/z.*** Abbreviation representing the dimensionless quantity formed by dividing the ratio of the mass of an ion to the unified atomic mass unit, by its charge number (regardless of sign). The abbreviation is written in italicized lowercase letters with no spaces. *m*/*z* is recommended as an abbreviation to represent the dimensionless quantity that is used almost universally as the independent variable in a mass spectrum. The abbreviation m/z should not be used as a variable in a mathematical equation. Instead, the variables m (in kg) and q (in C) should be used to denote mass and charge

The nuclear binding energy is slightly different for every nuclide. Therefore, different atoms, molecules or ions have slightly different unique mass even if they have the same nominal mass. The mass defect Δ is defined as the difference between the exact mass of an atom, molecule or ion and the nominal mass. As we know, ^{12}C has a mass defect of zero by definition, and all other elements have a positive or negative mass defect. For example, ^{1}H has a large positive mass defect (+0.007825), ^{16}O has a small negative mass defect (-0.005085), etc. The plot of the mass defect Δ against the atomic mass (mass defect plot) is thus a powerful tool to identify unknown species (Hughey et al, 2001; Sleno 2012). In principle, this procedure can be applied to any atom, molecule, ion or even cluster once its mass defect is known.

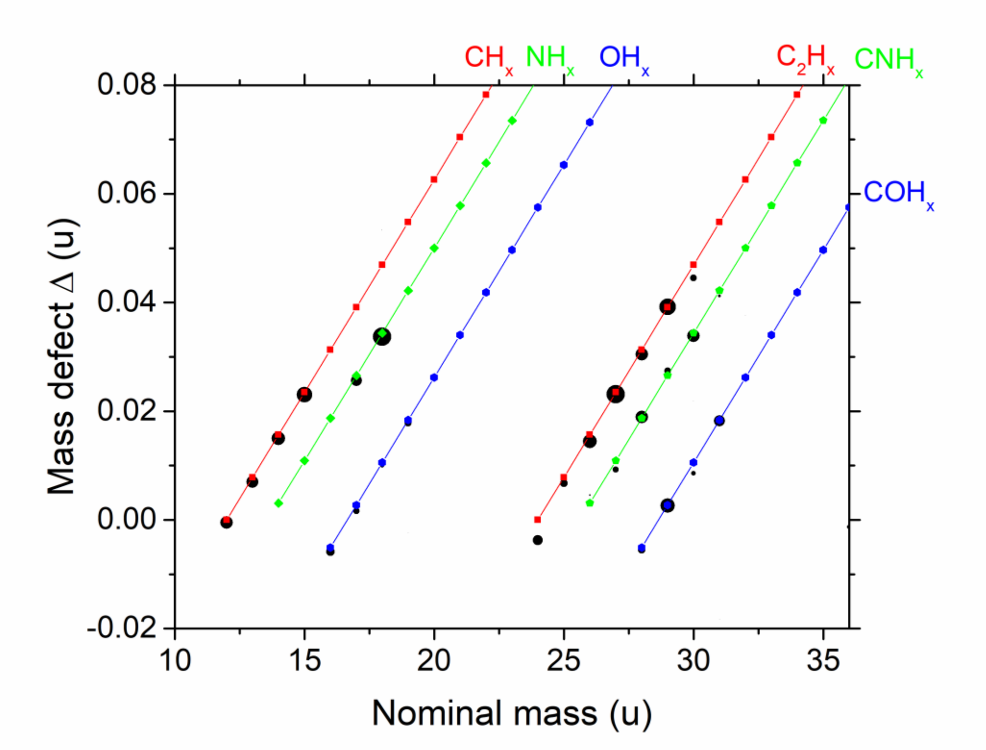

Figure V-2-4 Example of mass defect plot obtained from the reduction of a mass spectrum of fresh soot of a kerosene diffusion flame. Solid black rounds represent the mass defect and the normalized integration of the peaks, dots in red, green and blue represent the possible combinations of C/H, C/N/H and C/O/H respectively.

Mass defect plots are powerful tools since series of homologous ions (for instance, C^+, CH^+, CH_2^+, CH_3^+) line up and become easy to recognize. Furthermore, since every data point (black round in the figure) corresponds to a different peak in the mass spectrum, even very complex mass spectra can be represented in a relatively simple plot. In Figure V-2-4, the red line in the left represents the possible combination of H and one C. Clearly, four solid rounds correspond well to the hollow red dots. They are C^+, CH^+, CH_2^+, CH_3^+ and CH_4^+ respectively. In general, there are always several possibilities of the element combination on one data point.

By following the mass defect analysis, most of the peaks can be identified with reasonable confidence (maximum distance of the accurate and exact mass below 5 ppm) and thus be given a the corresponding molecule formula. Figure V-2-5 shows a mass defect plot with identifications. The green solid stars represent the background species containing Ti from the wafer and Na, K, Al, from the room dust. The black solid stars represent the hydrocarbon species which come from the soot. The red solid stars represent the oxygen containing species. There are few peaks that cannot be identified by this procedure.

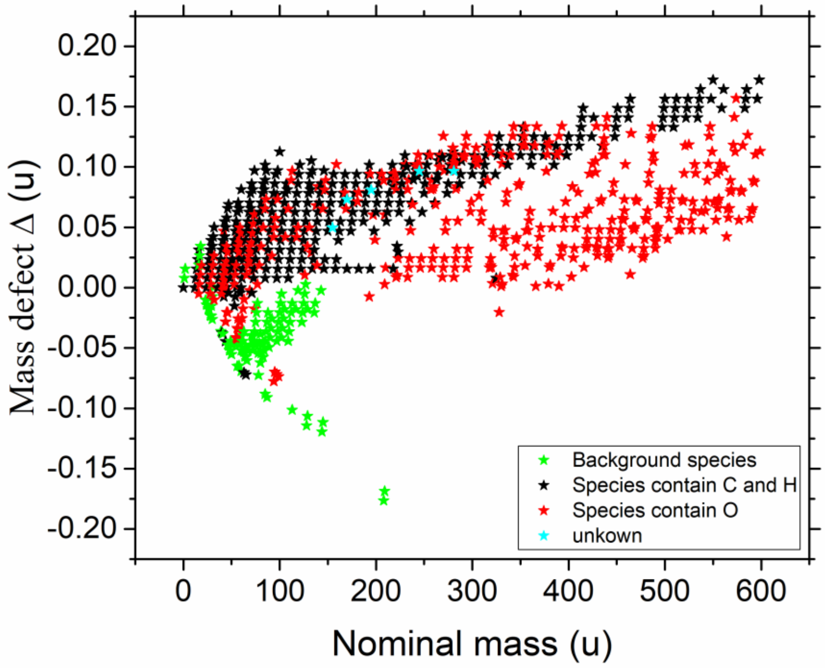

Figure V-2-5 Example of the mass defect plot of a mass spectrum of soot particles. Stars in green, black, red and cyan represent the background species, C_xH_y species, oxygen species and unidentified species, respectively.

2.5. Normalization

ToF-SIMS is a powerful tool to identify the chemical composition qualitatively, but not quantitatively due to the difficulty of controlling the ionization process. In general, the ion counts are different among the samples. To compensate at least partially for these differences, the mass spectra were normalized by the total ion count after background removal. Many peaks containing background signals (Ti from the deposition wafers for instance) are identified by mass defect as explained in section V-2.4, or by comparison with the blank samples. So, before doing the normalization of the mass spectra, all peaks which contain identified background signals were removed and the total ion count calculated on the peaks from soot only.

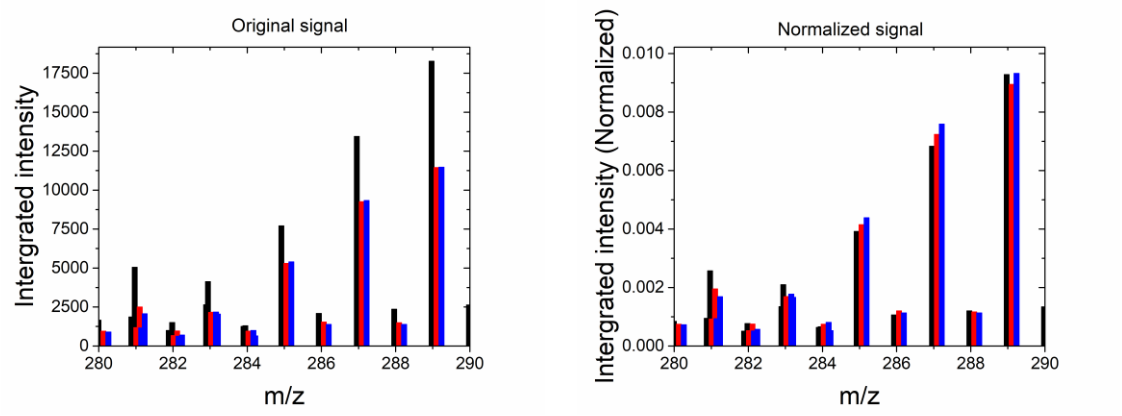

Figure V-2-6 The non-normalized (left) and normalized (right) peak integrated intensity of a real example: fresh soot at 70 mm HAB. Three samples are represented by color in black, red and blue.

Figure V-2-6 shows the difference of the integrated intensity of peaks of three mass spectra before and after the normalization procedure. These three mass spectra were obtained from the analysis of random position on the soot central spot of the wafer where the soot particles in the same experiment are impacted on (section V-1.2). The original intensity of these three mass spectra for the same peak are significantly different. However, the normalization procedure reduces the discrepancies of these three mass spectra and provides a better repeatability of the sampling.

3. Multivariate analysis applied to mass spectrometry

In practice, a typical SIMS mass spectrum of soot contains over one thousand peaks. In order to analyze effectively this huge amount of data, and thus to identify the main contributions to the total variances of the database of samples, two statistical procedures were applied: Principle Component Analysis (PCA) and Hierarchical Cluster Analysis (HCA). From a theoretical point of view, PCA is an orthogonal transformation that projects a set of observations onto linearly uncorrelated variables denoted as principal components, allowing one to highlight similarities and differences within the dataset (Abdi and Williams 2010; Bro and Smilde 2014). In a more colloquial way, PCA is a statistical method which identifies patterns in large datasets (Tanaka 1988) and provides a base to classify the samples. This statistical approach has enormous applications, especially whenever large databases are to be reduced. Additionally, HCA attempts to group a set of objects in such a way that objects in the same group (*cluster*) are closer to each other than to those in other groups. In this section, both PCA and HCA are introduced from the theory to the practice to understand the working principles.

3.1. Principle Component Analysis (PCA)

PCA was first proposed in statistics by Karl Pearson, who formulated the analysis as finding "lines and planes of closest fit to systems of points in space" (Pearson 1901). PCA was briefly mentioned by Fisher and Mackenzie as more suitable than analysis of variance for the modelling of response data (Fisher and Mackenzie 1923). Then, PCA was extensively used in electrical engineering and images analysis. PCA was firstly applied in chemistry by Malinowski around 1960, then a large number of chemical applications have been published after 1970 (Malinowski 2002). Recently, using PCA to analyze the mass spectra information from SIMS is a more and more effective method to approach the data reduction and identify the chemical information (Wagner et al. 2004; H. Wang et al. 2004; Pei et al. 2008).

Multivariate databases are difficult to understand. For instance, there might be hidden correlations between many variables. If each variable was analyzed separately, the analysis would often appear independent rather than correlated, and potentially miss important information or lead to the wrong conclusions. Therefore, it is necessary to find a method to reduce the complexity of the data without loss of information contained in the original variables, thereby achieving a comprehensive analysis of the collected data. Since there is a potential correlation between variables, PCA provides a method that keeps the representativeness of the data and reduces the number of the variables. Intuitively, PCA aims to reduce the number of dimensions of the observation thus simplify the analysis.

A simple example is presented in Figure V-3-1. Suppose that each observation is represented by the 2 variables X and Y. All the observations can then be plotted in a two-dimension coordinate system. These observations could be represented also with two orthogonal vectors $\overrightarrow{u_1}$ and $\overrightarrow{u_2}$ where the variance of the projections of observations on $\overrightarrow{u_1}$ is maximized. To reduce the dimensionality of the observations while keeping the representativeness of the data at the same time, the projection on $\overrightarrow{u_1}$ is the best choice because it accounts for most of the variance of the observations. In an extreme case, if the norm of $\overrightarrow{u_2}$ was zero, then the projection on $\overrightarrow{u_1}$ would represent the total variances of the observations. A new coordinate system based on $\frac{\overrightarrow{u_1}}{|\overrightarrow{u_1}|}$ and $\frac{\overrightarrow{u_2}}{|\overrightarrow{u_2}|}$ then represents the observations. Mathematically, vectors $\overrightarrow{u_1}$ and $\overrightarrow{u_2}$ are the eigenvectors of the correlation (or covariance) matrix scaled by the square root of the corresponding eigenvalue. The higher the eigenvalue, the more information the projections contain.

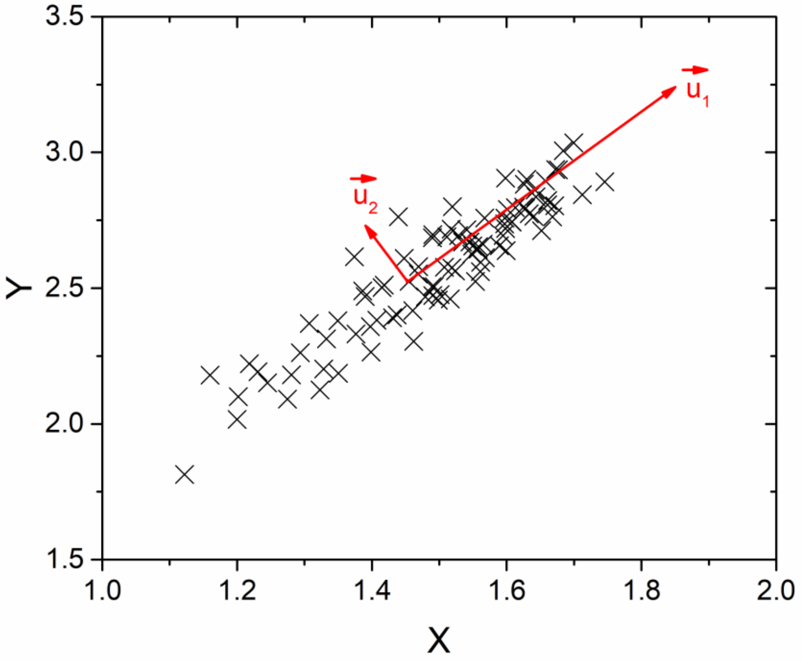

Figure V-3-1 An example to show how PCA works for a two-dimension database.

Generally, for a database which contains n observations and m variables, a series of orthogonal vectors $\vec{u}_i$ need to be created where *i* is the integer between 0 and m. The database can be transformed to a coordinate system defined by the vectors $\vec{u}_i$ representing most of the data. These vectors are the directions of the so-called principal components (PCs) that are usually classified in PC1, PC2 etc. following the decreasing numerical value of their eigenvalues.

Mathematically, to find out the PCs, the eigenvectors and eigenvalues of the database are required to be estimated. Suppose that we have a database which contains n observations and m variables. The database can be described as a matrix **Z**:$\{\vec{Z}_1, \vec{Z}_2, \dots, \vec{Z}_m\}$ where $\vec{Z}_i (0 \leq i \leq m)$ are column vectors. At first, the normalization to zero mean of matrix **Z** is a general procedure, i.e. the sample mean of each column needs to be shifted to zero. The mean vector is:

$$\vec{\mu} = \frac{1}{n}\sum_{i=1}^{n} \vec{Z}_i \qquad \text{Equation V-3-1}$$

Then the new matrix **X** can be evaluated as: $\mathbf{X} = \{\vec{x}_1, \vec{x}_2, \dots, \vec{x}_n\} = \{\vec{Z}_1 - \vec{\mu}, \vec{Z}_2 - \vec{\mu}, \dots, \vec{Z}_n - \vec{\mu}\}$.

All the observations are projected on the vector $\vec{u}_1$ which defines the direction of PC1. The total variance of the projections of matrix **Z** on $\vec{u}_1$ is:

$$Var(\mathbf{Z} \cdot \vec{u}_1) = \frac{1}{n}\sum_{i=1}^{n} |\vec{x}_i \cdot \vec{u}_1|^2 = \frac{1}{n}\sum_{i=1}^{n} (\vec{x}_i \cdot \vec{u}_1)^2 \qquad \text{Equation V-3-2}$$

Where $\vec{x}_i \cdot \vec{u}_1$ could be replaced by matrix manipulation: $\vec{x}_i \cdot \vec{u}_1 = \boldsymbol{x}_i^T \boldsymbol{u}_1$. Then we get $(\boldsymbol{x}_i^T \boldsymbol{u}_1)^2 = (\boldsymbol{x}_i^T \boldsymbol{u}_1)^T (\boldsymbol{x}_i^T \boldsymbol{u}_1) = \boldsymbol{u}_1^T \boldsymbol{x}_i \boldsymbol{x}_i^T \boldsymbol{u}_1$. The total variance can be described as:

$$Var(\mathbf{Z} \cdot \vec{u}_1) = \frac{1}{n}\sum_{i=1}^{n} \boldsymbol{u}_1^T \boldsymbol{x}_i \boldsymbol{x}_i^T \boldsymbol{u}_1 \qquad \text{Equation V-3-3}$$

$\boldsymbol{u}_1$ is independent from $\boldsymbol{i}$, so $\boldsymbol{u}_1$ can be taken out of the summation. Thus, Equation V-3-3 finally is evaluated to:

$$Var(\mathbf{Z} \cdot \vec{u}_1) = \frac{1}{n} \boldsymbol{u}_1^T \left(\sum_{i=1}^{n} \boldsymbol{x}_i \boldsymbol{x}_i^T\right) \boldsymbol{u}_1 = \frac{1}{n} \boldsymbol{u}_1^T \boldsymbol{X} \boldsymbol{X}^T \boldsymbol{u}_1 \qquad \text{Equation V-3-4}$$

As we know, $\boldsymbol{u}_1$ is the direction of PC1. So, the total variance $Var(\mathbf{Z} \cdot \vec{u}_1)$ arrives the maximum. $\boldsymbol{u}_1$ can be estimated with:

$$\boldsymbol{u}_1 = \arg max \left(\frac{\boldsymbol{u}_1^T \boldsymbol{X} \boldsymbol{X}^T \boldsymbol{u}_1}{\boldsymbol{u}_1^T \boldsymbol{u}_1} \right) \qquad \text{Equation V-3-5}$$

The k^{th} principal component can be found by subtracting the first $k - 1$ principal components from matrix **X**:

$$\boldsymbol{X}_k = \boldsymbol{X} - \sum_{s=1}^{k-1} \boldsymbol{X} \boldsymbol{u}_s \boldsymbol{u}_s^T \qquad \text{Equation V-3-6}$$

And the vector $\boldsymbol{u}_k$ is estimated from the maximum variance from this new data matrix:

$$\boldsymbol{u}_k = \arg max \left(\frac{\boldsymbol{u}_k^T \boldsymbol{X} \boldsymbol{X}^T \boldsymbol{u}_k}{\boldsymbol{u}_k^T \boldsymbol{u}_k} \right) \qquad \text{Equation V-3-7}$$

The number of variables and principle component is the same.

3.2. Hierarchical Cluster Analysis (HCA)

HCA is a method of cluster analysis which seeks to build a hierarchy of clusters by calculating the distance between couples of observations. For analyzing the same database **Z** mentioned above in section V-3.1, a commonly used measure of the distance is the Euclidean distance between any two observations *i* and *j* described as:

$$|\vec{Z}_i - \vec{Z}_j| = \sqrt{\sum_k (z_{i,k} - z_{j,k})^2} \qquad \text{Equation V-3-8}$$

Where $\vec{Z}_i$ and $\vec{Z}_j$ are the vectors of the observation *i* and *j*, *k* is the number of the variable, $z_{i,k}$ is the *k*th variable of observation *i* and $z_{j,k}$ is the kth variable of observation *j*. By considering the Euclidean distance value calculated by Equation V-3-8, the observations can be clustered and represented in a diagram called dendrogram. Cutting the dendrogram at different heights yields different clustering, therefore a selection criterion is required. Often, a limit to the number of clusters (number criterion) or the maximum distance between clusters than the previous aggregation (distance criterion) is used as criteria to decide the exact cutting position.

3.3. PCA and HCA: a practical example

For better understanding how PCA and HCA work, a database about forest fire from UCI Machine Learning Repository was chosen to be treated by software Origin for showing some practical details. We selected this database because it was never been treated by PCA and HCA. The database of forest fires in northeast of Portugal was collected to classify the forest fire and to predict the burning area (Cortez and Morais 2007).

In Table V-3-1, the database is described with the Canadian Forest Fire Weather Index system (FWI) to account for the effects of fuel moisture and wind on fire behavior. The parameters considered in the database are the Fine Fuel Moisture Code (FFMC, is an indicator of the relative ease of ignition and the flammability of fine fuel), the Duff Moisture Code (DMC, an indication of the average moisture content of loosely compacted organic layers), the Drought Code (DC, is an indicator of seasonal drought effects on forest fuels), and the Initial Spread Index (ISI is a numeric rating of the expected rate of fire spread), the temperature and relative humidity of the air and the wind velocity.

Table V-3-1 The database of forest fires in northeast of Portugal. *(Cortez and Morais 2007)*

		Variances (m=13)												
	Sample name	X (0-9)	Y (0-9)	Month (1-12)	Day (1-7)	FFMC	DMC	DC	ISI	Temp (℃)	RH (%)	Wind (km.h^{-1})	Rain (mm. m^{-2})	Area (ha)
Observations (n=517)	1	7	5	3	5	86.2	26.2	94.3	5.1	8.2	51	6.7	0	0
	2	7	4	10	2	90.6	35.4	669.1	6.7	18	33	0.9	0	0
	3	7	4	10	6	90.6	43.7	686.9	6.7	14.6	33	1.3	0	0
	4	8	6	3	5	91.7	33.3	77.5	9	8.3	97	4	0.2	0
	5	8	6	3	7	89.3	51.3	102.2	9.6	11.4	99	1.8	0	0
	……	……	……	……	……	……	……	……	……	……	……	……	……	……
	517	6	3	11	2	79.5	3	106.7	1.1	11.8	31	4.5	0	0

The Euclidian distance between any two observations were calculated according to Equation V-3-8. The smaller the distance, the closer the observations. The observations are presented in Figure V-3-2 as function of distance. By adding a distance filter, the observations with a lower distance than the filter could be grouped in one cluster. With increasing the distance of the filter, the number of the clusters decreases until all observations are considered as one cluster. In HCA of forest fire data, observations are significantly separated into two clusters highlighted in green and red in the figure.

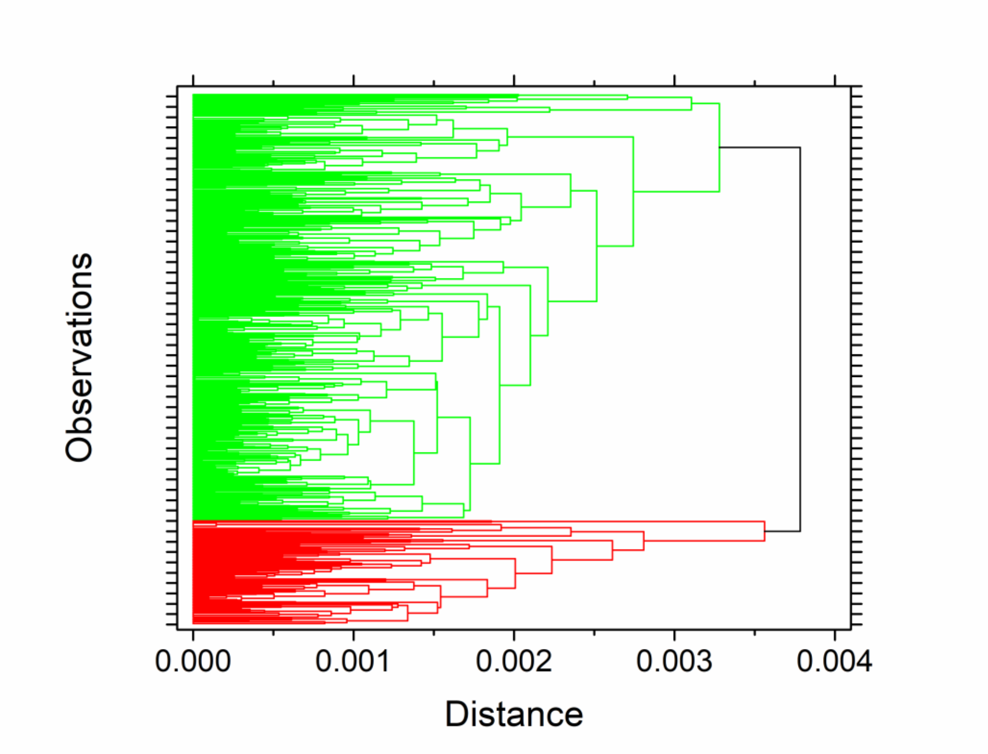

Figure V-3-2 HCA results of the forest fire database.

The forest fire data were then analyzed by PCA so that the database could be presented by as few PCs as possible (section 3.1). Figure V-3-3 (a) represents the percentage of the variance explained by each PC (see plot). The first three PCs explain 44.3%, 20.2% and 16.3% of the total variance, respectively. As an example, the scores of 517 observations on PC1 and PC2 are presented in Figure V-3-3 (b). Dots in green and red correspond to the observations separated into two clusters from HCA results. The two clusters are separated by PC1 as well. The loadings of the PC1 and PC2 are presented in Figure V-3-3 (c) and (d) respectively. PC1 is dominated by the variables DMC, DC, ISI and the temperature. PC2 is dominated by the variables ISI and the wind speed.

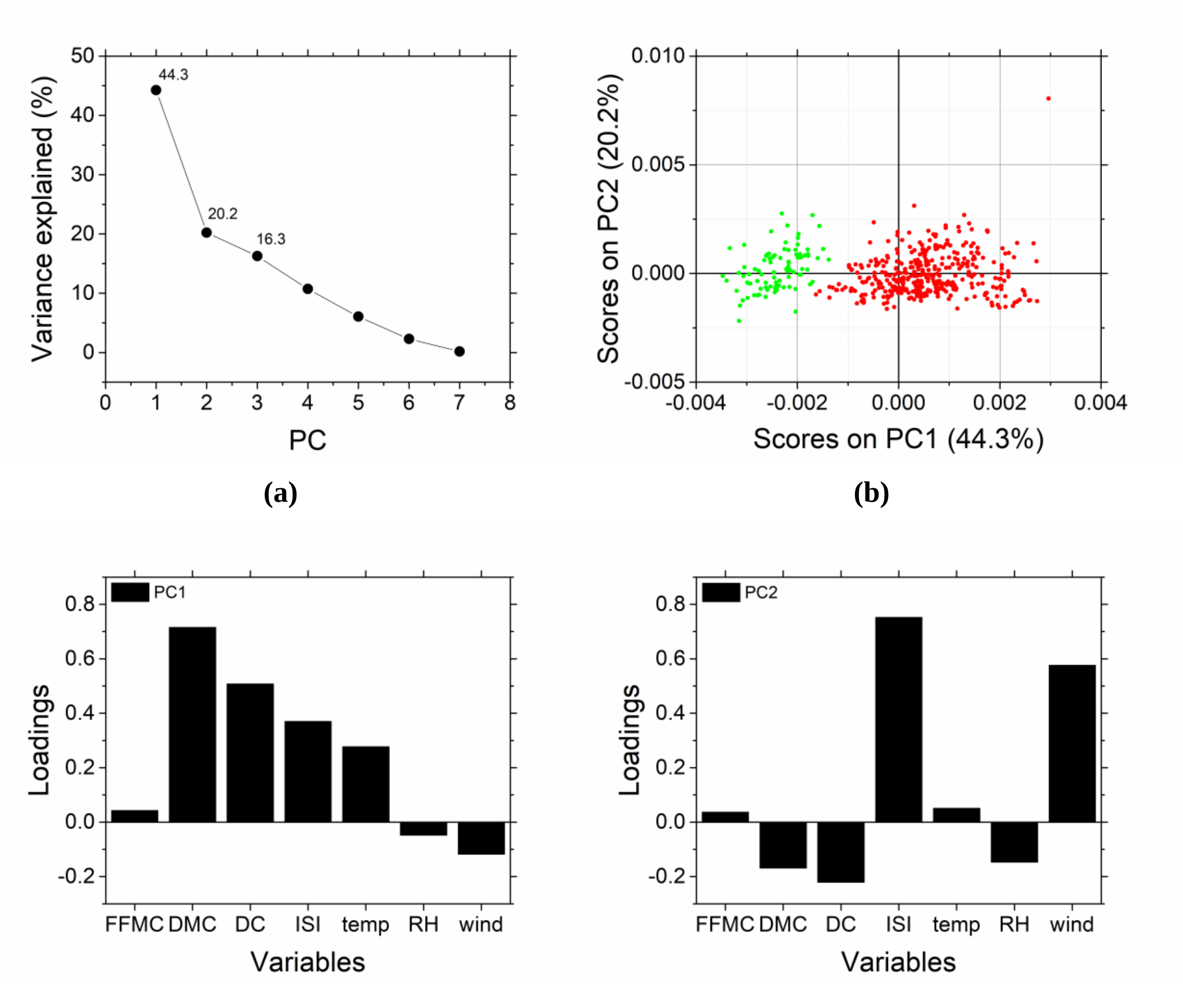

(a) (b)

(c) (d)

Figure V-3-3 PCA on the forest fire data. (a): scree plot of PCA. (b): PC2 vs. PC1 scores plot, where dots in red and green represent the data clusters of 1and 2 obtained by HCA, respectively. (c): loadings of PC1. (d): loadings of PC2.

The comparison of HCA (Figure V-3-2) and PCA (Figure V-3-3) only shows that at least two different behaviors occur. Finding the correspondence of these behaviors with specific variables can be challenging: to reach a deeper understanding of the database and to find hidden correlations between observations and variables, it is usually helpful to add as much information as possible to the score plots. For instance, in Figure V-3-4, the data points are color coded on the day of the week (left panel) and on the month (right panel) the fire broke out. No clear dependence on the day of the week can be observed on the left panel (the days are roughly homogeneously scattered in the plot), meaning that a fire is equally likely to break out in any day of the week. On the other hand, a separation of the fires occurring in winter and summer months is evident on the right panel (fires in winter months are clustered on the left and fires in summer months are clustered on the center-right of the score plot). This strongly suggests a seasonal dependence of the fire behavior that is carried in PC1. Further information can be extracted from the loading plots. Summer fires have mostly positive scores on PC1 that is controlled by DMC, DC, ISI and air temperature. DMC, DC and air temperature are related directly or indirectly to the moisture content of the fuel, while ISI to the rate of fire spread. In other words, during summer the drier the organic layer the more likely a large fire breaks out and quickly spread. However, the situation in winter is very different as none of the variables have large scores in PC1<0, and the most important variable are the wind speed instead. As an additional example of information that PCA can provide, DMC and DC behave very similarly (their loadings have the same sign and similar numerical values), so in this first approximation it is reasonable to expect that they do not carry independent information, and probably only one of them would be sufficient to describe the fire behavior. Of course, in all the discussion, the percentage of the explained variance given by scree plot remains fundamental: PC1 and PC2 together explain the 64.5% of the total variance, so before giving definitive conclusion the analysis of the minor components like PC3, PC4 and even PC5 should be provided as well.

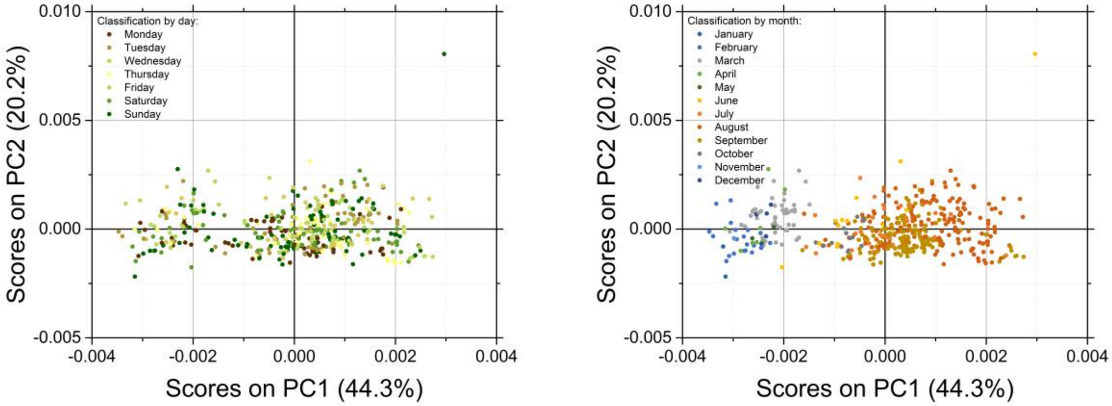

Figure V-3-4 Score plots on PC1 and PC2 of forest fire data classified by day (left) and by month (right).

4. ToF-SIMS results of soot particles exposed to O_3 and or SO_2

Two series of soot aging experiments that aim to study the influence of O_3 and SO_2 on the hygroscopic properties of soot were performed in the LASC chamber situated in laboratory PC2A, Lille and in the CESAM chamber situated in laboratory LISA, Créteil. The role of O_3 on the hygroscopic properties change of soot particles was studied first in Lille with the soot particles extracted from four different heights above the burner (HABs) in the flame, which provided the different maturity of soot particles (Dobbins et al. 2006). Then, the role of O_3 and SO_2 on the hygroscopic properties of soot particles was studied in the CESAM chamber. The results of the hygroscopic properties of soot and aged soot are shown in chapter 4. The sample parameters are recalled in Table V-4-1 to have a global view of the data collected and discussed in this section.

Table V-4-1 ToF-SIMS samples of soot particles from aging experiments exposed to O_3/SO_2. X means no data available due to the out range of the supersaturation of the CCNc (0.1-2.0%).

ToF-SIMS Sample	HAB (mm)	Residence time (min)	$[O_3]$ initial (ppm)	$[SO_2]$ initial (ppb)	$[O_3]$ exposure time ($cm^{-3}s$)	$[SO_2]$ exposure time ($cm^{-3}.s$)	SS_c (%)
LASC1	70	23	0	0	0	0	X
LASC2	70	60	1.35	0	7.61×10^{16}	0	2.21
LASC3	70	148	1.30	0	1.36×10^{17}	0	1.50
LASC4	100	11	0	0	0	0	X
LASC5	100	62	1.25	0	8.45×10^{16}	0	X
LASC6	100	149	1.20	0	1.57×10^{17}	0	1.69
LASC7	130	10	0	0	0	0	X
LASC8	130	66	1.30	0	9.29×10^{16}	0	X
LASC9	130	141	1.35	0	2.22×10^{17}	0	1.85
LASC10	140	17	0	0	0	0	X
LASC11	140	64	1.30	0	9.46×10^{16}	0	X
LASC12	140	148	1.35	0	1.45×10^{17}	0	1.75
CESAM1	130	90	0.50	100	2.74×10^{16}	2.45×10^{15}	0.30
CESAM2	130	156	1.10	110	5.54×10^{16}	5.65×10^{15}	0.45
CESAM3	130	204	1.10	109	1.09×10^{17}	1.08×10^{16}	0.17
CESAM4	130	107	0.53	0	1.45×10^{16}	0	0.50
CESAM5	130	14	0	0	0	0	X

For the surface analysis, soot sample were collected after the aging process in the simulation chambers. ToF-SIMS analyses were performed to relate the surface chemical composition to the change of the hygroscopic properties of soot particles. In total, 12 experiments were done for the aging process in the LASC that resulted in 36 positive polarity mass spectra, while, 5 experiments were done for the aging process in the CESAM that resulted in 30 positive polarity mass spectra and 30 negative polarity mass spectra.

4.1. Soot exposed to O_3 in the LASC

By following the data acquisition procedure presented in section V-2, the peaks and their normalized integrated area are extracted from all 36 mass spectra in positive polarity. 727 peaks are considered for the mass defect analysis mentioned in section V-2.4. The mass defect plot containing the accurate mass is shown in the left panel of Figure V-4-1. 585 peaks are attributed to species that contain C, H, O and N from soot (points in black, red and blue in the right panel), while 142 peaks come from the background (points in green in the eight panel) which contains Ti from the wafer surface and inorganic species such as Na, K, Al attributed to environmental contaminants. The high mass hydrocarbon (m/z >180) species are represented by PAHs (Faccinetto et al. 2011). The subset of 585 organic peaks (variables) from the 36 mass spectra (observations) is analyzed both in PCA and HCA.

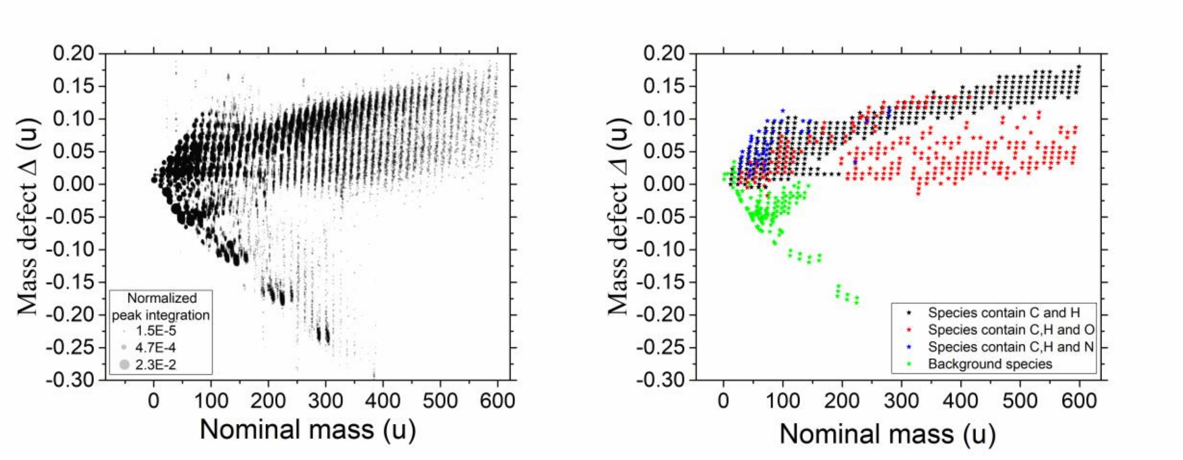

Figure V-4-1 Mass defect plot containing all peaks extracted from mass spectra of soot exposed to O_3 (left) and attributions (right).

The result of HCA on these 36 positive mass spectra is shown in Figure V-4-2. Three clusters are separated significantly. Fresh soot samples obtained at 70 mm and 100 mm HAB are in the data cluster 1 (red lines), soot samples obtained at 70 mm and 100 mm HAB and aged with O_3 (1h30 and 3h00 exposure time) are in the data cluster 2 (green lines), and finally soot samples obtained at 130 mm and 140 mm HAB both fresh and aged with O_3 are in the data cluster 3 (blue lines). Two mass spectra of sample 140 mm HAB of soot exposed to O_3 (1h43 and 3h06 exposure time) are also in data cluster 2.

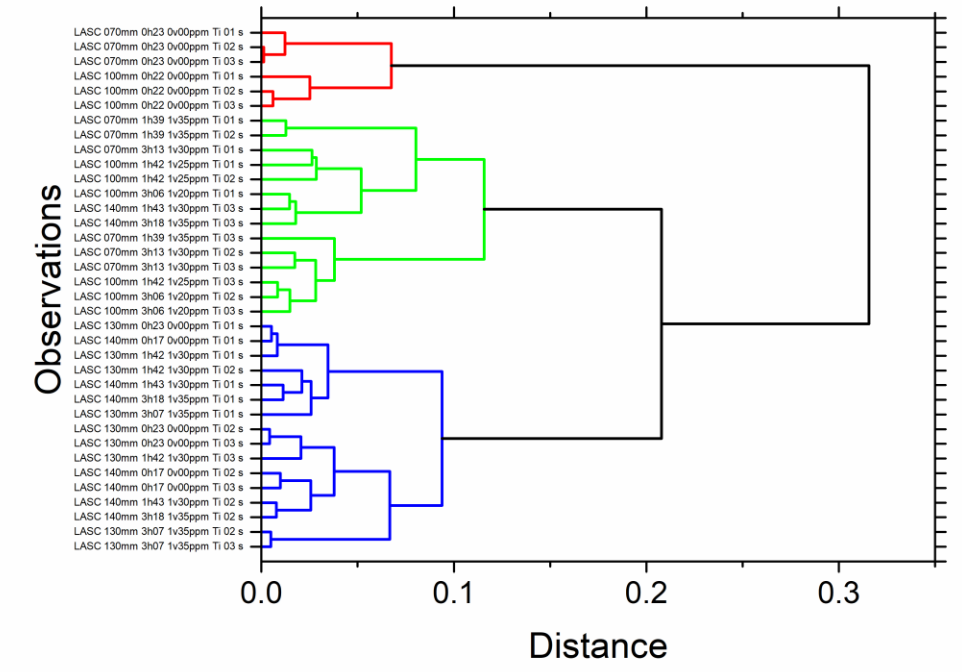

Figure V-4-2 Dendrogram obtained from the 36 mass spectra of soot samples, including fresh soot particles and aged soot particles exposed to O_3.

Figure V-4-3 shows PCA results of 36 mass spectra of soot particles exposed to O_3. The percentage of the total variance explained by the first twenty PCs are presented in the scree plot of figure (a), where PC1 (71.4%) and PC2 (16.3%) explain around 87.7% of the total variance.

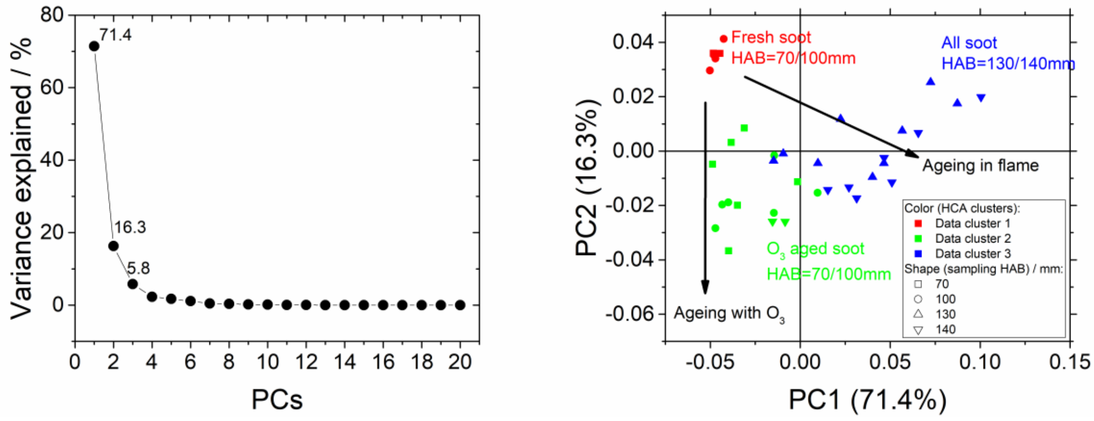

(a) **(b)**

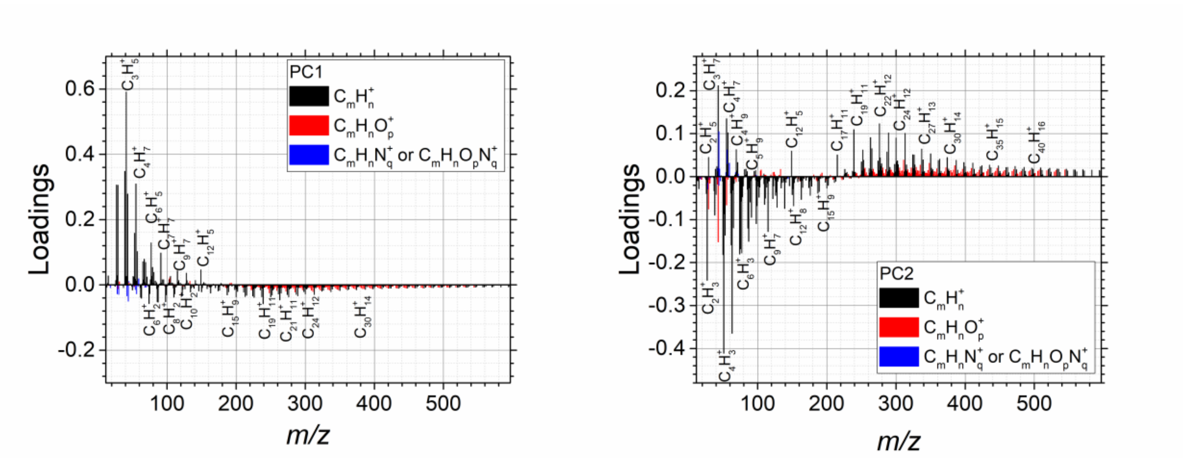

(c) **(d)**

Figure V-4-3 PCA results of 36 mass spectra of soot particles exposed to O_3. (a): scree plot of PCA. (b): PC2 vs. PC1 scores plot, where dots in red, green and blue represent the data clusters of 1, 2 and 3 obtained by HCA, respectively. Shapes in square, circle, up triangle and down triangle represent the HAB of 70mm, 100mm, 130mm and 150mm, respectively. (c): loadings of PC1. (d): loadings of PC2.

The scores on PC1 and PC2 of the 36 observations are presented in the scores plot in Figure V-4-3 (b) that highlights the different HABs in different data point shapes (square: 70 mm, circle: 100 mm, up triangle: 130 mm and down triangle: 140 mm HAB) and HCA observations in different colors (red: data cluster 1, green: data cluster 2 and blue: data cluster 3). The loadings of PC1 and PC2 are presented Figure V-4-3 (c) and (d), where the black bars represent the hydrocarbons, and the red and blue bars represent oxygen (mostly oxygen containing CH) and nitrogen containing compounds (NCC), respectively. On the one hand, in PC1 (71.4% of explained variance), the loadings of ions having high H/C ratio in the low mass range are significantly positive, such as $C_3H_5^+$, $C_4H_7^+$, $C_6H_5^+$, $C_7H_7^+$, $C_9H_7^+$ etc. However, ions having low H/C ratio have negative loadings, such as $C_6H_2^+$, $C_8H_2^+$, $C_{10}H_2^+$ etc. In the region of m/z >180, all species have negative loadings and mostly consist of polycyclic aromatic hydrocarbon (PAHs) and OCH. In PC2 (16.3% of explained variance), the low H/C ratio ions are negative. However, PAHs and OCH are positive.

Globally, in the scores plot, the samples of soot at 70 and 100 mm HAB are well separated and far from the samples at 130 and 140 mm HAB. At 70 and 100 mm HAB, the fresh soot samples are well separated from the aged soot samples by PC2. However, At 130 and 140 mm HAB fresh and aged soot samples cannot be separated. Two important conclusions can be drawn from the score plot of Figure V-4-3 (b). First, the process of soot aging *in the flame* can mostly be associated to the change of sign of PC1. Second, the process of soot aging *with* O_3 can be quite clearly associated to PC2, i.e. the observations located in PC2<0 correspond to the lower SS_c. It is interesting to notice that the disappearance of PAHs and the aging of soot with O3 are correlated. Samples aged with O3 all have large negative scores in PC2 in Figure V-4-3 (b). However, in the loadings plot of PC2 in Figure V-4-3 (b), high mass PAHs and oxygen containing hydrocarbons are virtually absent, while they are prominent in PC2>0 that is instead found associated to fresh soot.

4.2. Soot exposed to O_3/SO_2 in the CESAM

Both positive and negative polarity mass spectra were recorded to study the potential inorganic species which contain sulfur. The results of PCA and HCA results of negative polarity mass spectra are presented in section 4.2.1 to understand the role of S on the change of activation of soot. The PCA and HCA results of positive polarity mass spectra are then presented in section V-4.2.2.

4.2.1. Negative polarity SIMS

At first, the mass defects of the peaks from all negative polarity mass spectra is shown in the left panel of Figure V-4-4. The data point size is proportional to the peak normalized area. The data points with positives mass defects are mostly hydrocarbon and OCH. The data points with negative mass defects and high nominal mass mostly correspond to Ti containing species. This time, 546 peaks were identified and presented in the right panel of Figure V-4-4. 135 are attributed to hydrocarbons, OCH and NCC, 37 to sulfur containing compounds (SCC), and 374 of all to the background species which mainly contains Ti from the wafer surface and inorganic species such as P^-, Cl^- and V^-. The 546 peaks (variables) from 30 mass spectra (observations) are analyzed both in PCA and HCA.

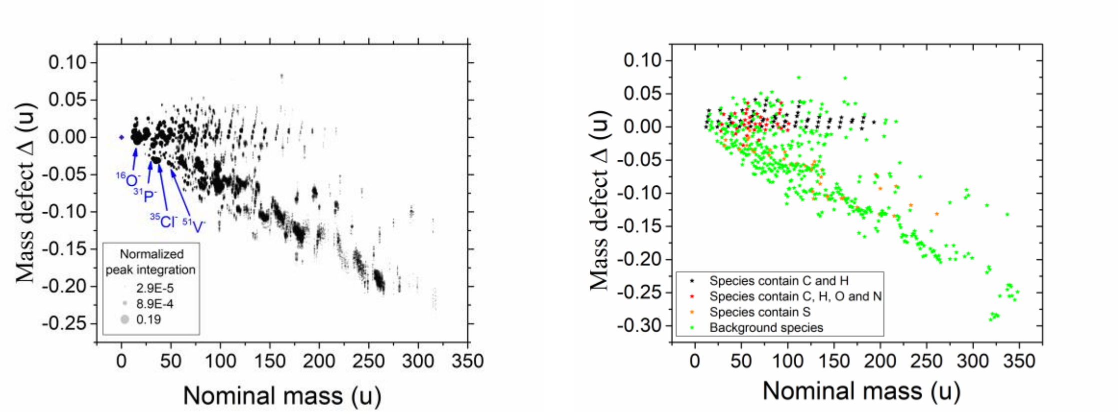

Figure V-4-4 Mass defect plot containing all peaks extracted from negative polarity mass spectra of soot exposed to SO_2/O_3 (left) and attributions (right).

The result of the HCA of these 30 negative polarity mass spectra is shown in Figure V-4-5. Four clusters are significantly separated. Data cluster 1 (red lines) contains the condensable gas of all samples except CESAM4, and furthermore it contains soot of sample CESAM5. Data cluster 2 (green lines) contains sample CESAM4 (both solid phase and condensable gas). Data clusters 3 (blue lines) and 4 (cyan lines) contain only soot of sample CESAM1, 2 and 3. By comparing the HCA results and experimental results presented in Table V-4-1, all condensable gas samples and solid phase samples without exposed to SO_2 are in cluster 1 and 2, which potentially shows the similar chemical compositions. Solid samples exposed to SO_2 in cluster 3 and 4 have similar chemical compositions. In order to know the principal components which represent more the samples, PCA analysis results are shown below.

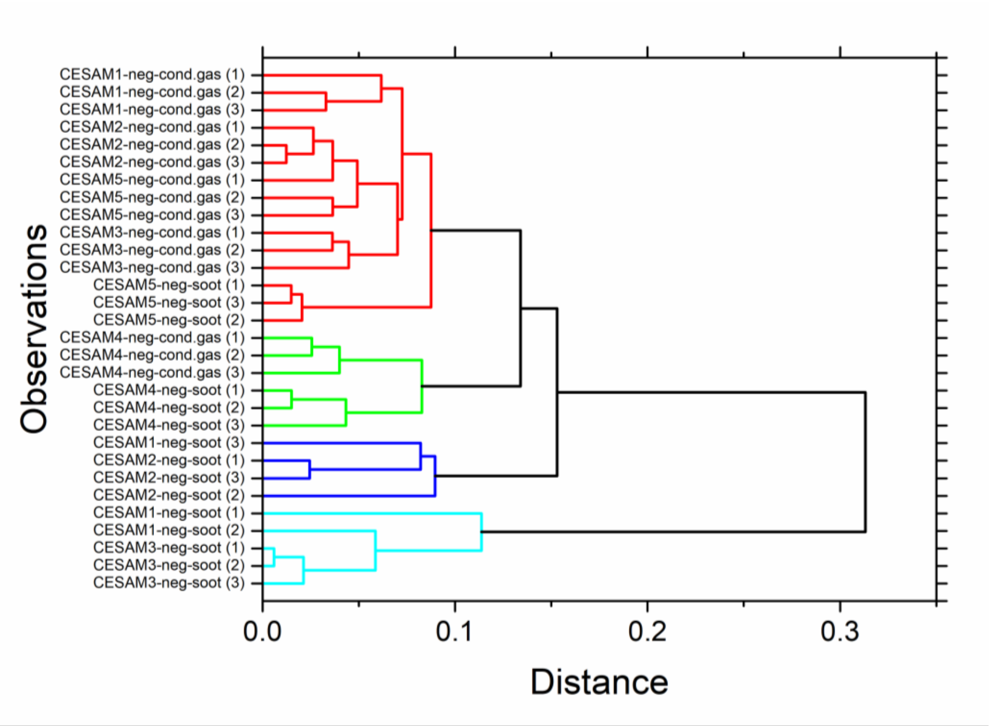

Figure V-4-5 Dendrogram obtained from the 30 negative polarity mass spectra of soot samples, including fresh soot particles and aged soot particles exposed to SO_2/O_3.

Figure V-4-6 shows PCA results of 30 mass spectra of soot particles exposed to SO_2 and O_3. The percentage of the variance explained by the first twenty PCs are presented in the scree plot in Figure V-4-6 (a), where PC1 (79.0%) and PC2 (12.1%) explain the 91.1% of the total variance. The PC1 vs. PC2 scores plot is shown in Figure V-4-6 (b). Hollow points represent the condensable gas, while solid points represent soot. The data points are coded in colors which correspond to the HCA clusters. The loadings of PC1 and PC2 are presented in Figure V-4-6 (c) and (d), where the black bars represent the hydrocarbons, the red bars represent the OCH, the blue bars represent NCC and the yellow bars represent SCC. In PC1 (79.0% of explained variance), the loadings of SCC are positive, such as SO_3^-, SO_4^-, SO_4H^-, $H_3S_2O_8^-$ etc. It is interesting to notice how in negative polarity the cast majority of detected SSC are attributed to inorganic sulfur like the above mentioned compounds, and only a comparatively small number of compounds are attributed to organic sulfur (for instance, CH_3S^-). Hydrocarbons are positive but small loadings. However, all the other elements that could be associated to the blank have negative loadings, such as O^-, OH^-, Cl^-, TiO_3H^- etc. In PC2 (12.1% of explained variance), the loadings of the hydrocarbons are mostly positive, most of the loadings of SCC are negative, while the loadings of other elements are negative except F^-.

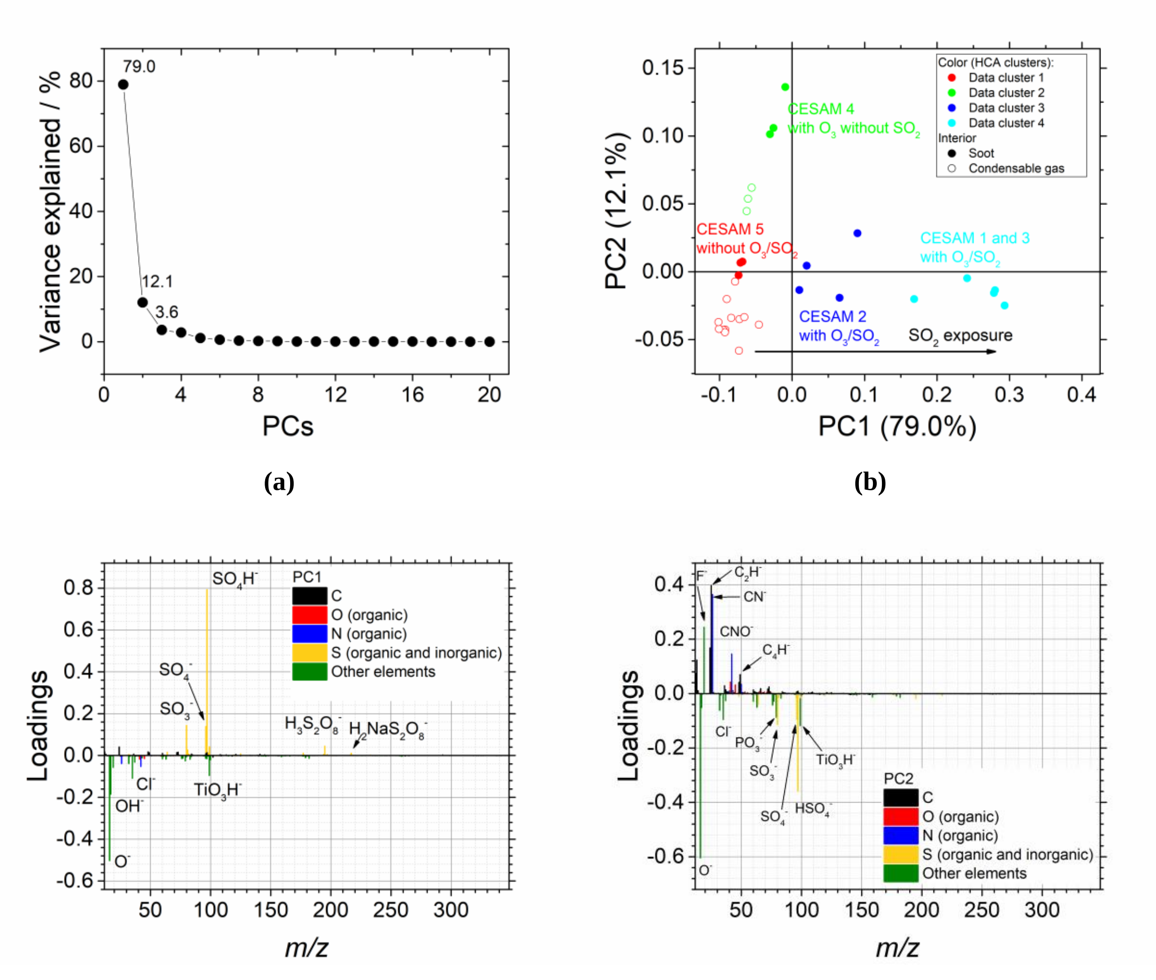

Figure V-4-6 PCA results of 30 negative polarity mass spectra of soot particles exposed to SO_2/O_3. (a): scree plot of PCA. (b): scores plot of PC1 and PC2 by presenting the data clusters from HCA, where dots in red, green, blue and cyan represent the data clusters of 1, 2, 3 and 4 respectively. Hollow and solid dots represent condensed gas and soot, respectively. (c): loadings of PC1. (d):

loadings of PC2.

Soot of samples CESAM1, 2 and 3 exposed to SO_2 and O_3 have high scores in PC1>0. All condensable gas have the scores in PC1<0, same as the soot from CESAM4 and CESAM5. According to the experiment conditions (Table V-4-1), four clusters are classified and associated to the SO_2 exposure. In the PC1 loadings plot of Figure V-4-6 (c), SCC are associated with PC1 as well, and gives a good base to classify the observations. However, the role of PC2 is not yet clear due to the mixture of the observations on the scale of PC2 scores.

In order to limit the influence of background species on the PCA/HCA analysis, the 374 peaks identified and attributed to the background are removed and PCA and HCA is performed a second time on the reduced dataset of 172 peaks.

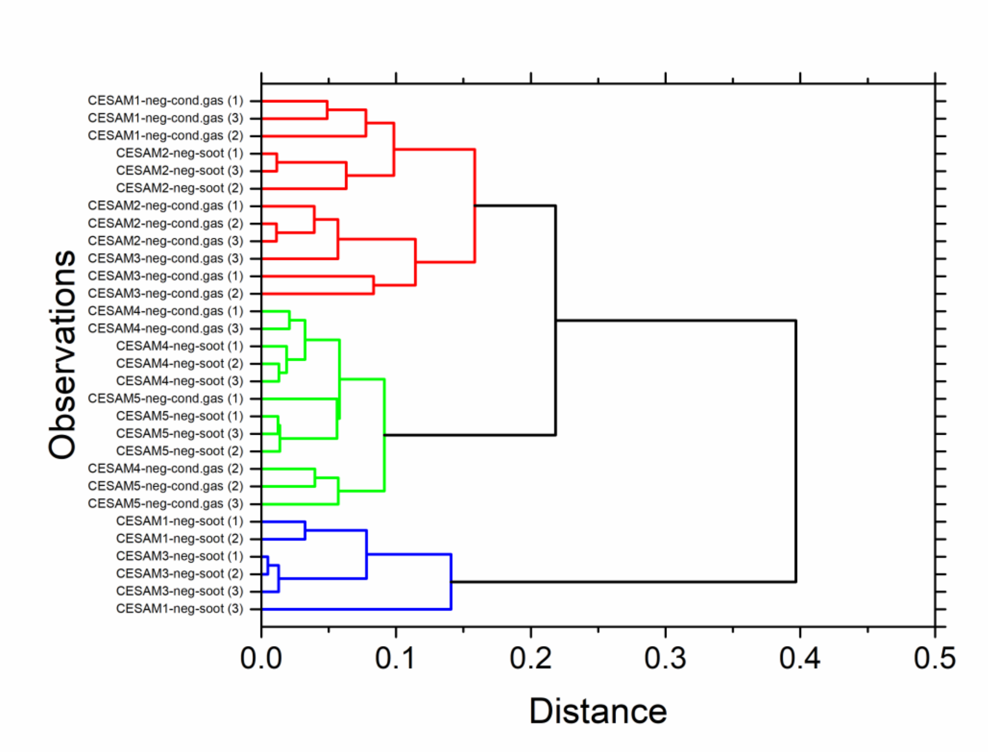

Figure V-4-7 Dendrogram after background removal obtained from the 30 negative polarity mass spectra of soot samples, including fresh soot particles and aged soot particles exposed to SO_2/O_3.

Figure V-4-7 shows the result of the HCA of these 30 background removing mass spectra in negative polarity. Three clusters are separated. The condensable gas of sample CESAM1, 2 and 3, are classified in data cluster 1 (red). The soot and condensable gas from sample CESAM4 and 5 are classified in data cluster 2 (green lines). Finally, soot from sample CESAM1 and 3 are classified in data cluster 3 (blue lines).

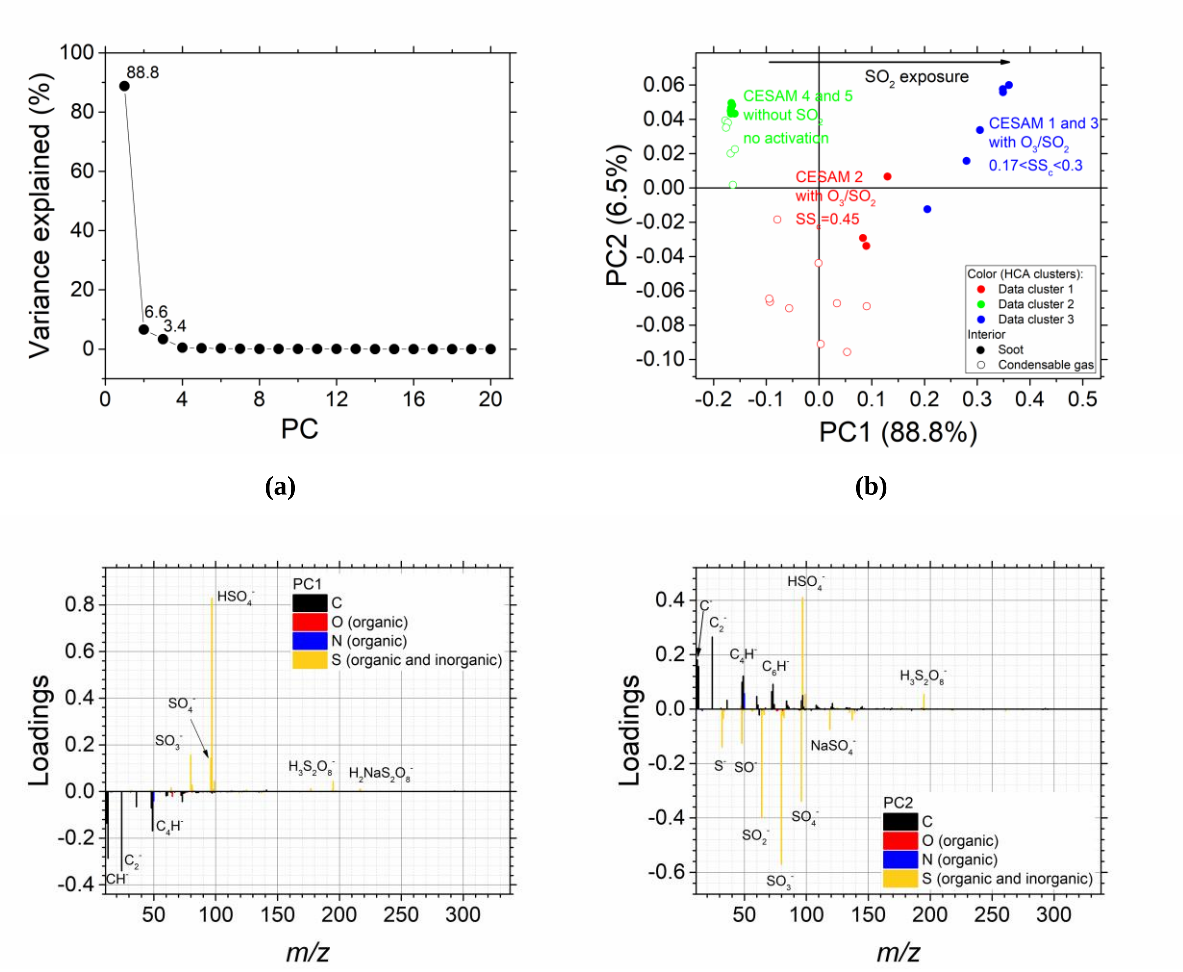

(a)

(b)

(c)

(d)

Figure V-4-8 PCA results after background removal of soot particles exposed to SO_2/O_3. (a): scree plot of PCA. (b): scores plot of PC1 and PC2 by presenting the data clusters from HCA, where dots in red, green and blue represent the data clusters of 1, 2 and 3 respectively. Dots in hollow and solid represent the condensable gas phase and solid phase of the sample respectively. (c): loadings of PC1. (d): loadings of PC2.

Figure V-4-8 shows the PCA results of 30 background removing mass spectra of soot particles exposed to SO_2 and O_3. In the scree plot of Figure V-4-8 (a), PC1 (88.8%) and PC2 (6.6%) explain the 95.4% of the total variance.

Soot of sample CESAM 1 and 3 exposed to SO_2 and O_3 has high positive scores in PC1. It is important to notice that these samples are activated at low SS_c. Consistently, soot of sample CESAM2 exposed to SO_2 and O_3 has lower but still positive scores in PC1 and is activated at higher SS_c. On the other hand, fresh soot of sample CESAM4 and 5 has negative scores in PC1.

The mass spectra of the condensable gas of all samples tend to show similar behavior (CESAM1, 2, 3 can be found mixed up in cluster 1, while CESAM4 and 5 in cluster 2) and to have negative scores on PC1, although a few samples extend to PC1>0. This clear difference in the behavior of the soot particles and of the condensable gas, once compared with the results of the activation experiments (chapter 4) allows attributing the activation to the soot particles rather than the condensable gas. Furthermore, in the PC1 loadings plot, PC1>0 is clearly dominated by SCC. Therefore, the reactivity of soot with SO_2 is conclusively associated to PC1 and to the activation of the soot particles.

PC2 only explains the 6.6% of the total variance and is therefore much less critical than PC1. Condensable gas of CESAM 1, 2 and 3 have negative scores in PC2, while all other samples are not clearly separated by this component. However, for the same sample, the PC2 score of condensable gas is always lower than that of soot. In conclusion, the role of PC2 on the observations of negative mass spectra is not so clear compared to the role or PC1.

4.2.2. Positive polarity SIMS

The left panel of Figure V-4-9 shows the mass defect of the peaks extracted from all 30 mass spectra in positive polarity. The dot size is proportional to the peak integrated area. The right panel shows the mass defect of 861 identified peaks, where 371 of them are attributed to ions containing C, H, O and N, 20 of them to SCC, and 470 of them to the blank (Na^+, Mg^+, K^+, Ti^+ and V^+). The full database of 861 peaks in 30 positive polarity mass spectra is studied both in PCA and HCA.

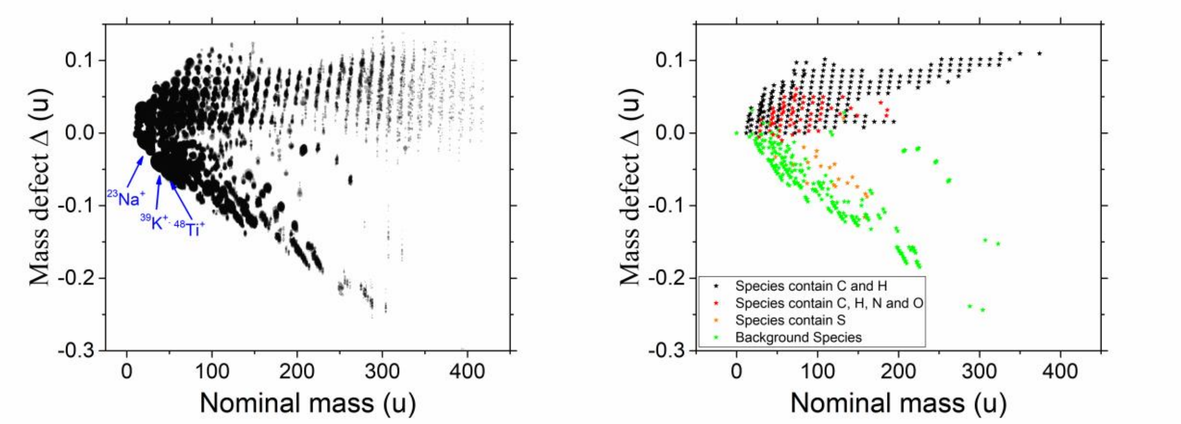

Figure V-4-9 The mass defect plot of peaks extracted from positive polarity mass spectra of soot exposed to SO_2/O_3 (left) and the mass defect plot of the identified peaks of that (right).

Figure V-4-10 shows the result of the HCA on the full database. Only two clusters are separated, and so far, the clustering is less than ideal. Soot of sample CESAM1 and 3, one soot sample of CESAM2, one soot sample of CESAM4 and one condensable gas sample of CESAM3 are in data cluster 2 (green lines). All other samples are clustered in data cluster 1 (red lines).

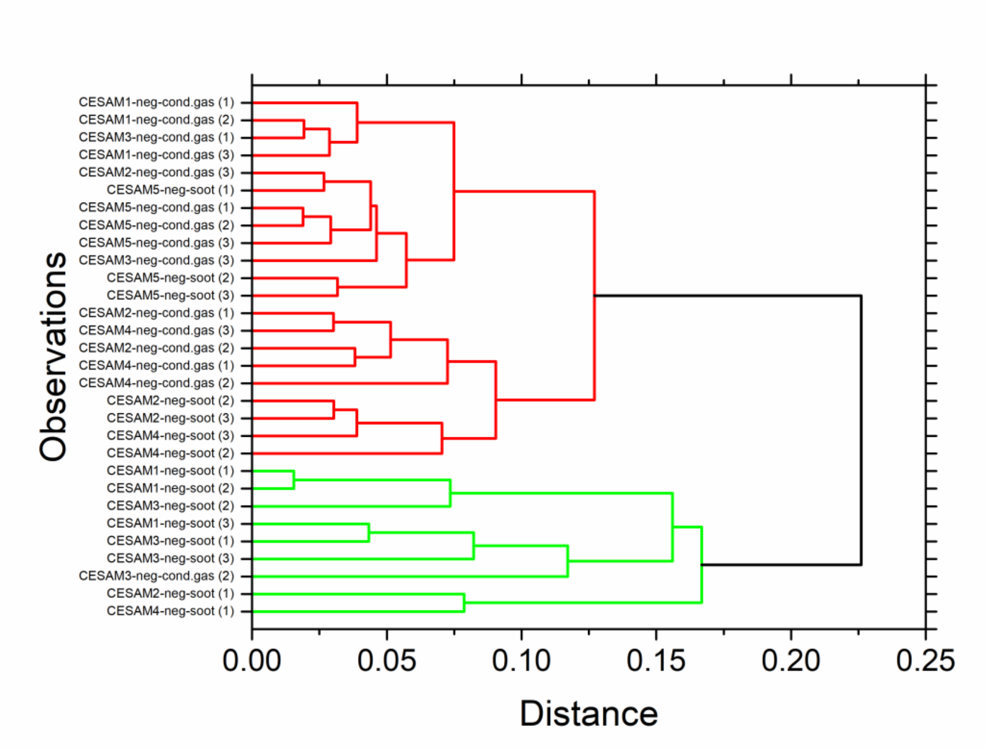

Figure V-4-10 Dendrogram of HCA obtained from the 30 positive polarity mass spectra of soot samples, including fresh soot particles and aged soot particles exposed to SO_2/O_3.

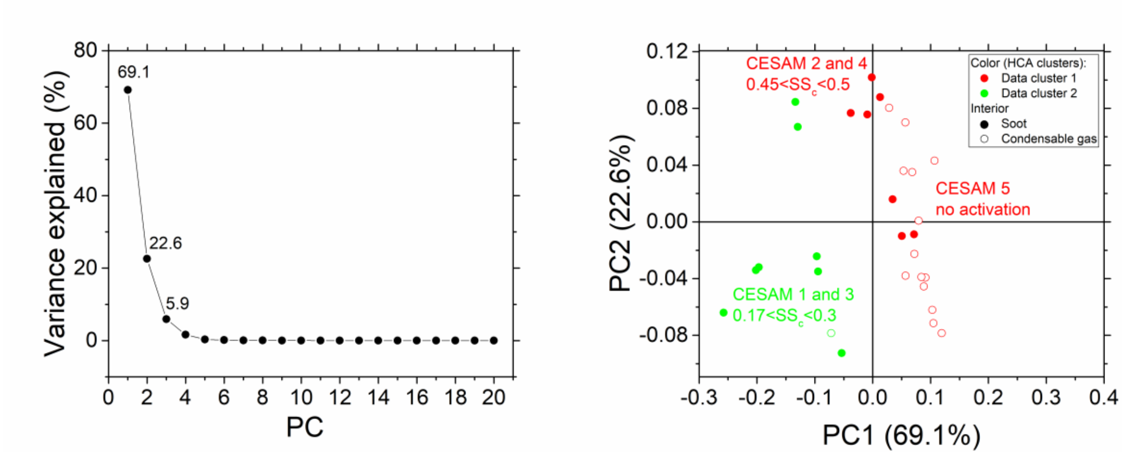

(a) (b)

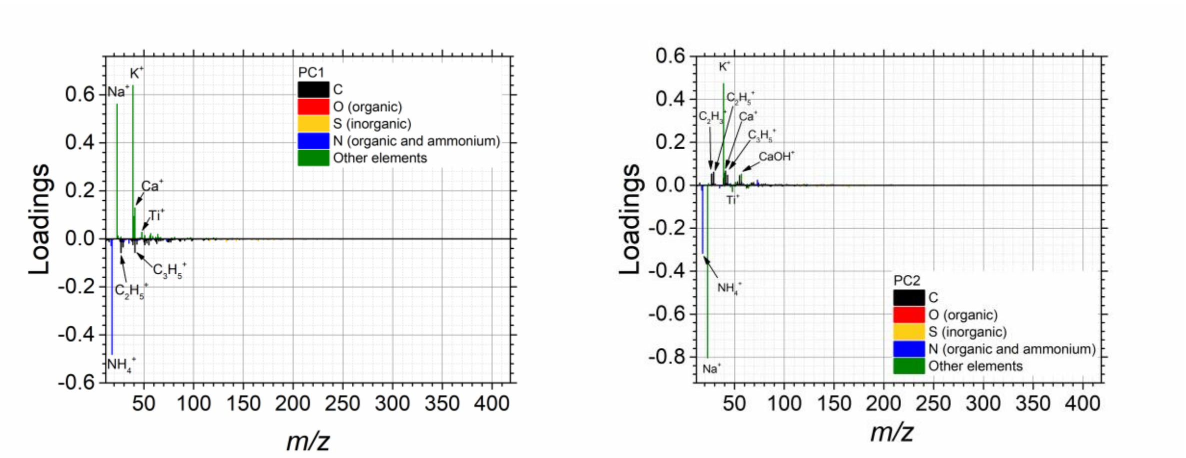

(c) (d)

Figure V-4-11 PCA results of 30 positive polarity mass spectra of soot particles exposed to SO_2/O_3. (a): scree plot of PCA. (b): scores plot of PC1 and PC2 by presenting the data clusters from HCA, where red and green dots represent the HCA data clusters of 1 and 2 respectively. Hollow and solid dots represent the condensable gas and the solid phase of the sample respectively. (c): loadings of PC1. (d): loadings of PC2.

Figure V-4-11 shows PCA results of 30 positives mass spectra of soot particles exposed to SO_2 and O_3. PC1 (69.1%) and PC2 (22.6%) explain 91.7% of the total variance. The PC1 vs. PC2 scores plot is shown in Figure V-4-11 (b). Hollow and filled data points represent condensable gas and soot, respectively. The data points are coded by colors corresponding to clusters in HCA. The loadings of PC1 and PC2 are shown in Figure V-4-11 (c) and (d), respectively. In PC1 (69.1% of explained variance), all the background species have positives loadings, while OCH and SSC have negatives loadings. Unlikely, the negative polarity mass spectra, in positive polarity all the detected SSC are attributed to inorganic sulfur. The loadings of Na^+, K^+ and NH_4^+ are significantly larger than the others. For instance, the observations are separated in PC1 according to the SS_c of soot, i.e. the soot of sample CESAM 1, 2, 3 and 4 locate in PC1<0 and the soot of sample CESAM5 are located in PC1>0. However, in PC2, the observations are mixed.

In PC1, the loadings of the identified background species have opposite sign than the loadings of OCH and SSC, which is a situation similar to the PCA of negative polarity mass spectra (section V-4.2.1). Once again, it is reasonable to remove the background species identified by PCA, and to analyze the reduced database of 30 positive polarity mass spectra (observations) with 391 organic species (variances) were analyzed again by PCA and HCA.

Figure V-4-12 shows the result of the HCA on the reduced database. Three clusters are separated. Soot of sample CESAM2, 4 and 5 and condensable gas of sample CESAM2 and 3 are classified in data cluster 1 (red lines). The condensable gas of sample CESAM1, 4 and 5 are classified in the data cluster 2 (green lines). Soot of sample CESAM1 and 3 are classified in data cluster 3 (blue lines).

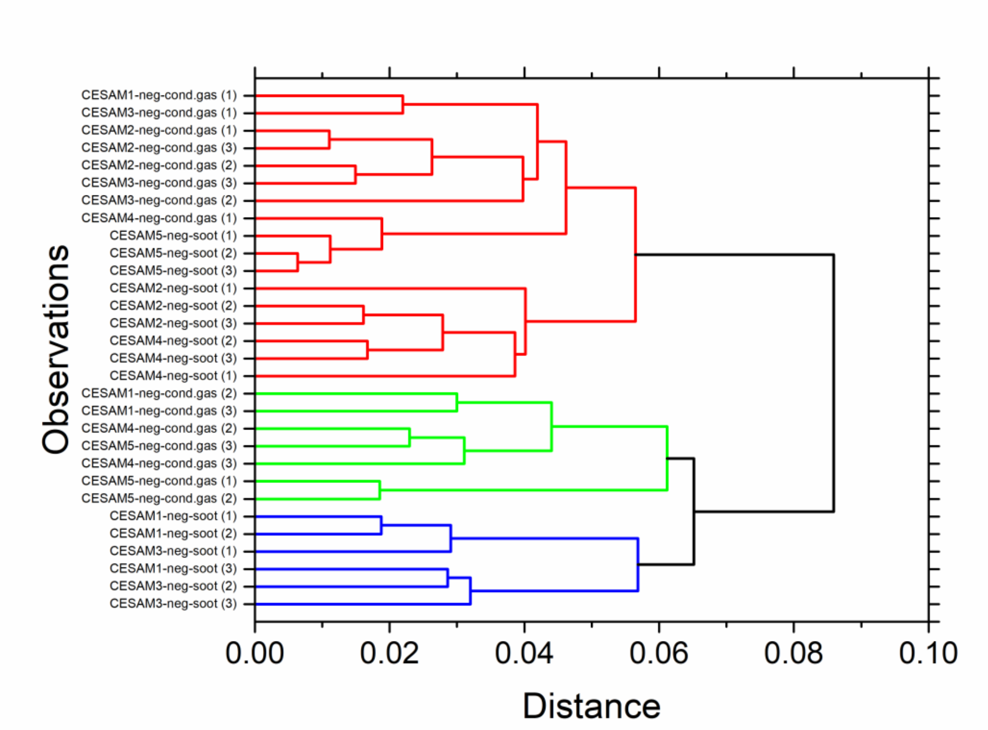

Figure V-4-12 Dendrogram after background removal obtained from the 30 positive polarity mass spectra of soot samples, including fresh soot particles and aged soot particles exposed to SO_2/O_3.

Similarly, Figure V-4-13 shows the PCA results on the reduced database. PC1 (60.7%) and PC2 (16.0%) explain the 76.7% of the total variance. The PC1 vs. PC2 score plot is shown in Figure V-4-13 (b), where hollow and solid data points represent the condensable gas and soot respectively. The different colors are consistent with the HCA clusters. The loadings of PC1 and PC2 are presented in Figure V-4-13 (c) and (d), where the black bars represent hydrocarbons, the red bars represent the OCH and the blue bars represent the NCC. In PC1 (60.7% of explained variance), most the OCH, hydrocarbons with low H/C ratio and SCC have negative loadings. However, hydrocarbons with high H/C ratio and NCC have positive loadings. In PC2 (16.0% of explained variances), the loadings of hydrocarbon with high H/C ratio, NCC and SCC are positives. However, the loadings of OCH and hydrocarbons with low H/C ratio are negative.

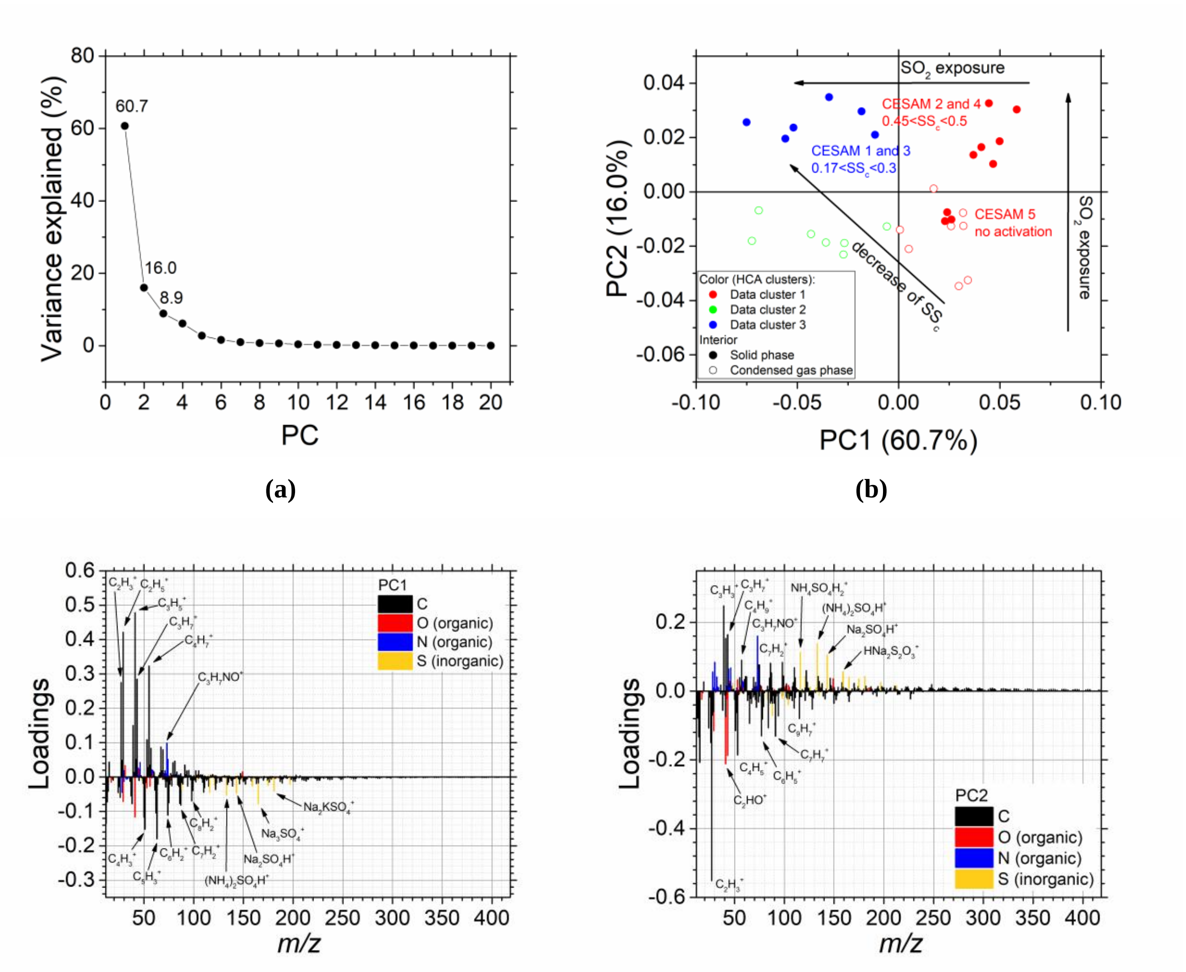

(a)

(b)

(c)

(d)

Figure V-4-13 PCA results of 30 positive polarity mass spectra of soot particles exposed to SO_2/O_3 after background removal. (a): scree plot of PCA. (b): scores plot of PC1 and PC2 where red, green and blue dots represent the HCA data clusters of 1, 2 and 3 respectively. Hollow and solid dots represent the condensable gas and the solid phase, respectively. (c): loadings of PC1. (d): loadings of PC2.

Although less resounding than in the PCA of negative polarity mass spectra, high loadings in PC1<0 and PC2>0 are still found associated to the presence of SSC, and the corresponding samples show the lowest SS_c (chapter 4). From Figure V-4-13, PC2>0 is associated to activated soot particles, as CESAM5 is the only sample that is not exposed to O_3 or SO_2 and appears in PC2<0. Therefore, consistently with the PCA of the negative polarity mass spectra, the activation is attributed to soot particles and not to the condensable gas.

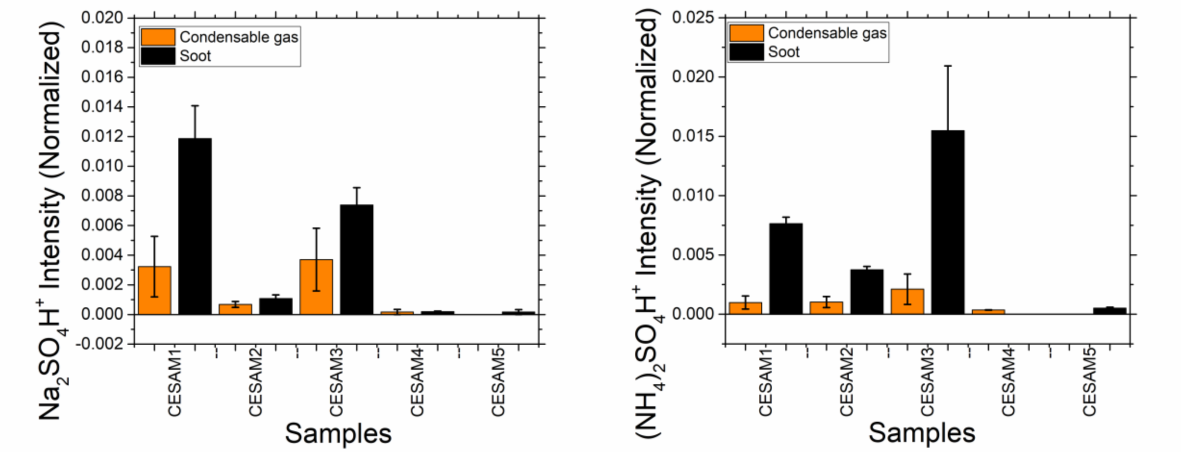

Figure V-4-14 Peak intensity of $Na_2SO_4H^+$ (left) and $(NH_4)_2SO_4H^+$ (right) in the samples exposed to SO_2 and O_3.

Figure V-4-14 compares the normalized intensity of two selected SCC in soot and in condensable gases. The peak intensity of $Na_2SO_4H^+$ and $(NH_4)_2SO_4H^+$ is shown in the left and right panel respectively. Samples CESAM 4 is only exposed to O_3, while sample CESAM5 is the blank of this experiment. The relative intensity of $Na_2SO_4H^+$ and $(NH_4)_2SO_4H^+$ are significantly large in soot than in condensable gas, i.e. their formation process at some point is strongly suspected to have involved the soot particle surface.

5. Conclusions

In this chapter, the working principle of ToF-SIMS is explained in section V-1. Section V-2 introduces the protocol adopted to treat the data and prepare them for the multivariate analysis. Briefly, it consists in transferring the integrated area of each peak into a matrix of m observations (the mass spectra) and n variables (the accurate mass). Two multivariate analysis methods (PCA and HCA) are introduced and used in section V-3. The association between HCA and PCA is practically explained by a database on forest fire database. The SIMS analyses of samples containing both soot and condensable gas from two measurement campaigns are presented in section V-4 and analyzed using PCA and HCA. The reaction was followed in the mass spectra by searching specific products like oxygen containing hydrocarbons (OCH) and sulfur containing compounds (SCC). The soot samples exposed to O_3 are analyzed in positive polarity mode only where the vast majority of OCH are found, while the soot samples exposed to O_3 and SO_2 were analyzed in both positive and negative polarity modes since SCC are preferentially found in the latter.

Finally, relations between several important variables and experimental conditions are shown in the Table V-5-1.

Table V-5-1 Logical table of PCA results of the kerosene soot exposed to O_3 and SO_2. HAB is height above the burner, $[O_3]_t$ is ozone exposure time, $[SO_2]_t$ is sulfur dioxide exposure time, SS_c is the critical supersaturation, PAHs are Polycyclic Aromatic Hydrocarbons, SCC is the sulfuric containing compounds, H/C>1 represents the high H/C ratio hydrocarbon, H/C<1 represents the low H/C ratio hydrocarbon. Cell in red represent the positive relation and cell in green represent the negative relation.

	HAB	$[O_3]_t$	$[SO_2]_t$	SS_c	PAHs	SCC
HAB				🟥	🟩	
$[O_3]_t$				🟩	🟩	
$[SO_2]_t$				🟩	🟩	🟥
SS_c	🟥	🟩	🟩		🟥	🟩
PAHs	🟩	🟩	🟩	🟥		
SCC			🟥	🟩		

HAB, O_3 exposure and SO_2 exposure are independent variables of the experiment. HAB and SS_c are positively correlated, i.e. soot from the higher HAB is less efficient as CCN as already shown in (Symphorien Grimonprez et al. 2018). A proposed link between the HAB and SS_c involves large aromatic hydrocarbons like PAHs. Pare negatively correlated to HAB, i.e. they disappear with increasing the HAB due to the soot oxidation in the flame, becoming prominent, which is in good agreement with (Lemaire, Faccinetto, et al. 2009). Besides, PAHs normalized intensities are negatively correlated to O_3 and SO_2 exposure as well, which is evidence they take part to the overall reaction of soot with O_3 and SO_2. The normalized intensities of SCC are (obviously) positively correlated to SO2 exposure and negatively associated to SSc (see chapter 4), i.e. the reaction of soot with O_3 and SO_2 is the key factor that increases the efficiency of soot as CCNs. Most of the hydrocarbons are likely fragment ions of larger molecular ions, however the mass spectra proved to be too complex to identify individual fragmentation patterns. For the same reason, the products of the oxidation of PAHs and of their reaction with SO_2 could not be unambiguously identified. From the point of view of the chemical composition, in conclusion, both O_3 and SO_2 give fundamental contributions to the increase of soot efficiency as CCNs, while being associated to the decrease of the concentration of large organic molecules like PAHs.

Chapter VI Lille Ice Nucleation Chamber (LINC) development

1. Introduction

Aircraft engines emit a large range of gaseous and aerosol pollutants in the higher troposphere, where soot aerosols and especially the aged soot aerosols might act as nuclei to form water droplets (CCN) or ice crystals (IN). The heterogeneous nucleation of ice crystal plays an important role in high troposphere on the formation of clouds, such as cirrus clouds and the artificial cirrus-like clouds. In order to study the heterogeneous nucleation process of ice in the laboratory, the continuous flow diffusion chamber *Lille ice nucleation chamber* (LINC) is being developed. In section VI-2, the homogeneous and heterogeneous nucleation processes at low temperature are briefly presented, while Section VI-3 shows the configuration of the LINC. A series of early tests with ammonium sulfate aerosols in the LINC are presented in section 4.

2. Nucleation process in high troposphere

The two main processes leading to the formation of ice in clouds are the homogeneous nucleation of super-cooled water ($T <$ -36°C) and the heterogeneous nucleation induced by aerosol particles. The rate of the ice formation from homogeneous nucleation is predicted by the so-called classical nucleation theory (Pruppacher and Klett 1978; Jeffery and Austin 1997). Alternative approaches that relate the homogeneous nucleation rate of solutions to that of pure water have also been developed (Sassen and Dodd 1988; Koop et al. 2000). Heterogeneous ice nucleation is ultimately initiated by IN, a subset of water-insoluble aerosol particles which nucleate ice under certain conditions of supercooling between 0 and -36°C or ice supersaturation at temperature below 0°C. Several heterogeneous ice nucleation modes have been classified by G. Vali in 1985, and his proposition has been since largely adopted by the scientific community (Vali 1985). The fundamental distinction lies in whether ice forms directly from the vapor phase or rather from the supercooled water:

- Deposition nucleation: ice is formed directly from an environment supersaturated with respect to ice but not supercooled water.
- Freezing nucleation: ice is formed from an environment supersaturated with respect to both ice and supercooled water. Since supersaturation with respect to water is always larger than

respect to ice, freezing nucleation necessarily involves the formation of liquid supercooled water. Three additional cases are usually identified:

− Immersion freezing: induced by a particle immersed in the body of supercooled water.

− Condensation freezing: similar to immersion freezing, but occurs when a particle acts as CCN then immediately induces freezing of the condensed water.

− Contact freezing: induced by a particle upon contact with the supercooled liquid water.

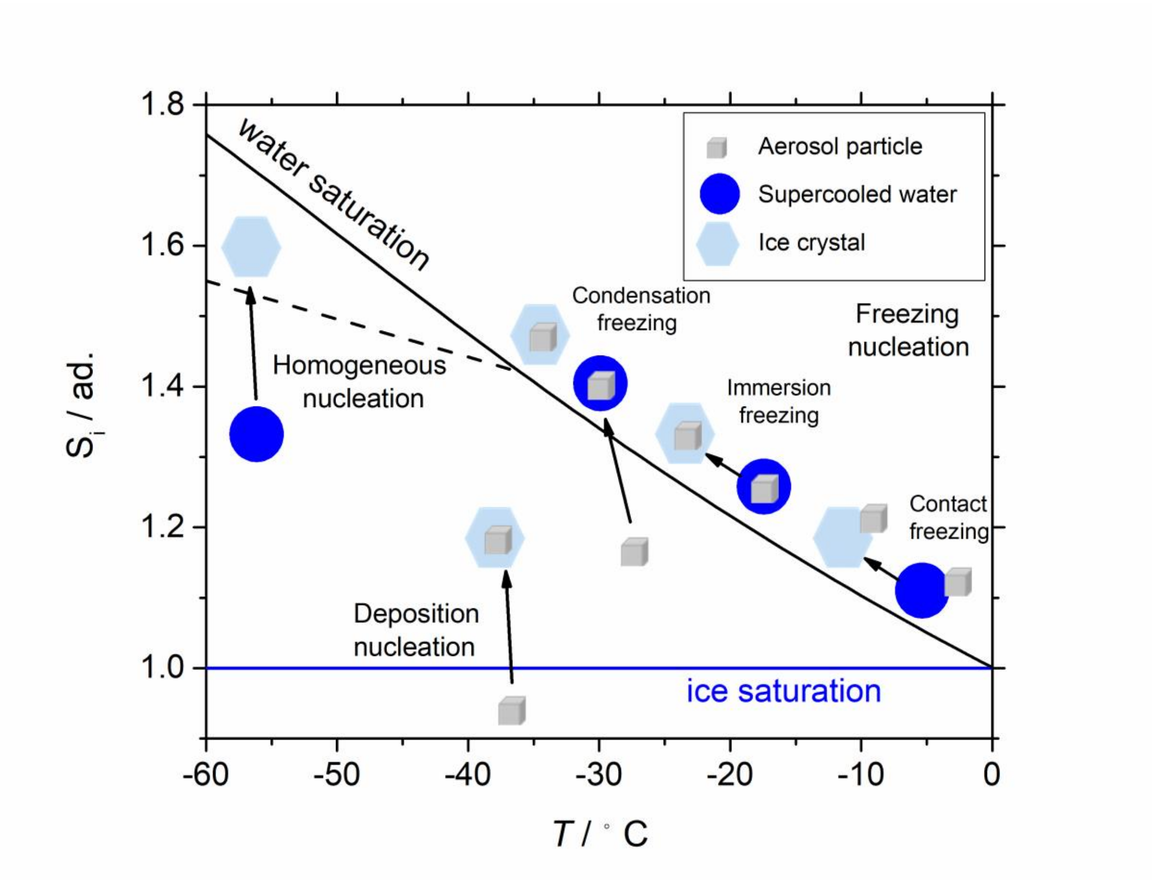

Figure VI-2-1 Representation of the different ice nucleation modes in the ice saturation (S_i) vs. temperature (T) space (Hoose and Mohler 2012)**.**

A schematic representation of the nucleation of water and ice in the ice saturation (S_i) vs. temperature (T) space is reported in Figure VI-2-1. The black and the blue solid lines represent the saturation condition with respect to supercooled water and ice, respectively, where the water saturation (S_w) is defined as the ratio of the water vapor pressure (p_v) and the saturated water vapor pressure over flat water (p_w^s); the ice saturation (S_i) is defined as the ratio of p_v and the saturated water vapor pressure over flat ice (p_i^s). Data on the saturation vapor pressure of water and ice are readily available in the literature, or can be calculated with high accuracy using numeric approximation like the improved Magnus form (Alduchov and Eskridge 1996). Above $S_i = 1$ (solid blue line), ice is the thermodynamically stable phase. Supercooled liquid water and the gas phase are in equilibrium along S_w (solid black diagonal line). At temperature below -36°C, water and water solutions undergo homogeneous freezing. The dashed line is a reference isoline for the homogeneous nucleation (Koop et al. 2000).

Typical atmospheric concentrations of IN are ~1 L^{-1} at -20°C and ~10 L^{-1} at -30°C (DeMott et al. 2010), i.e. around six orders of magnitude less than typical urban total atmospheric aerosol. Such a low concentration and the fact that IN may act in supercooled water, supersaturated vapor, or at the interface between the two phases, make any measurements related to the identification and characterisation of IN difficult.

3. The design of LINC

Four main types of experimental facilities were developed to study of heterogeneous ice nucleation in laboratories: continuous flow diffusion chambers (CFDCs), continuous flow mixing chambers (CFMCs), static diffusion chambers (SDCs) and aerosol interactions and dynamics of the atmosphere (AIDA). AIDA is the only facility which consists of a very large cloud generator chamber (84 m^3) assembled at the Karlsruhe Institute of Technology in Karlsruhe (Möhler et al. 2006). Typical experiments at AIDA involve the study of ice nucleation on particularly relevant natural ice nucleating aerosols, including desert dust and soot particles. SDCs are more efficient to study the contact freezing of aerosol particles (Kulkarni et al. 2009; Dymarska et al. 2006). In a static diffusion chamber the aerosol particles are deposited on a substrate or suspended and exposed to ice supersaturations for long enough to observe ice nucleation induced by the particles. CFDC and CFMCs are two kinds of continuous flow chamber. CFMC is a device of relatively recent design that creates supersaturation by the mixing of particle-free warm, humidified air and cold dry air (Bundke et al. 2010). CFDCs were initially devised to investigate the behavior of aerosol particles for aeronautic applications under steady conditions of relative humidity and temperature up to 10 s of exposure time. The very first instruments developed for investigating aerosol-induced ice nucleation was in fact a CFDC, and despite the little number of operational devices, in the 25 years since the work originally published by Rogers in 1988 (Rogers 1988), a series of important development process has been accomplished. CFDCs allow continuous measurements in a supersaturated environment, and can be adapted to portable instrument for field measurements or aircraft applications (Rogers et al. 2001).

In the literature, a lot of research on soot aerosols in ice nucleation chambers that lead to very few results (Hoose and Mohler 2012). In order to better understand the hygroscopic properties of soot as IN, an ice nucleation chamber is required to study the heterogeneous ice nucleation of soot particles from the laboratory flames. According to the stability and the reproducing conditions reported in the literature, CFDC is considered to be the best choice for studying and simulating the ice nucleation process in the exhausts of jet aircraft engines (Kanji and Abbatt 2009; DeMott et al. 2010; Nicolet et al. 2010; Jones et al. 2011). So far, the accurate control over temperature and relative humidity are only dependent on the wall temperature. A new instrument to investigate heterogeneous ice nucleation, the Lille ice nucleation chamber (LINC), is being developed in the laboratory PC2A in Lille.

3.1. LINC working principle

In the nucleation chamber of the LINC, a seeding aerosol stream passes through two ice-coated walls cooled down to slightly different temperature usually referred to as cold wall (T_c) and warm wall (T_w), highlighted in cyan in Figure VI-3-1. The diffusion of water vapor between the ice-coated walls forces a steady state water vapor pressure field (orange solid line) which is linear with respect to the transverse axis x of the chamber. Since the dependence of the saturation vapor pressure of water/ice on temperature is exponential (black and blue solid lines), a convenient choice of the wall temperature allows the creation of a supersaturated region with respect to ice (SS_i) and, if desired, water (SS_w), at the position of the aerosol stream (stripe pattern fill). The aerosol stream is usually shielded within dry airflows to prevent unwanted particle deposition on the reactor walls due to thermophoresis. In order to study the ice nucleation of the aerosols, the temperature of two walls need to be controlled to ensure $SS_w < 1$.

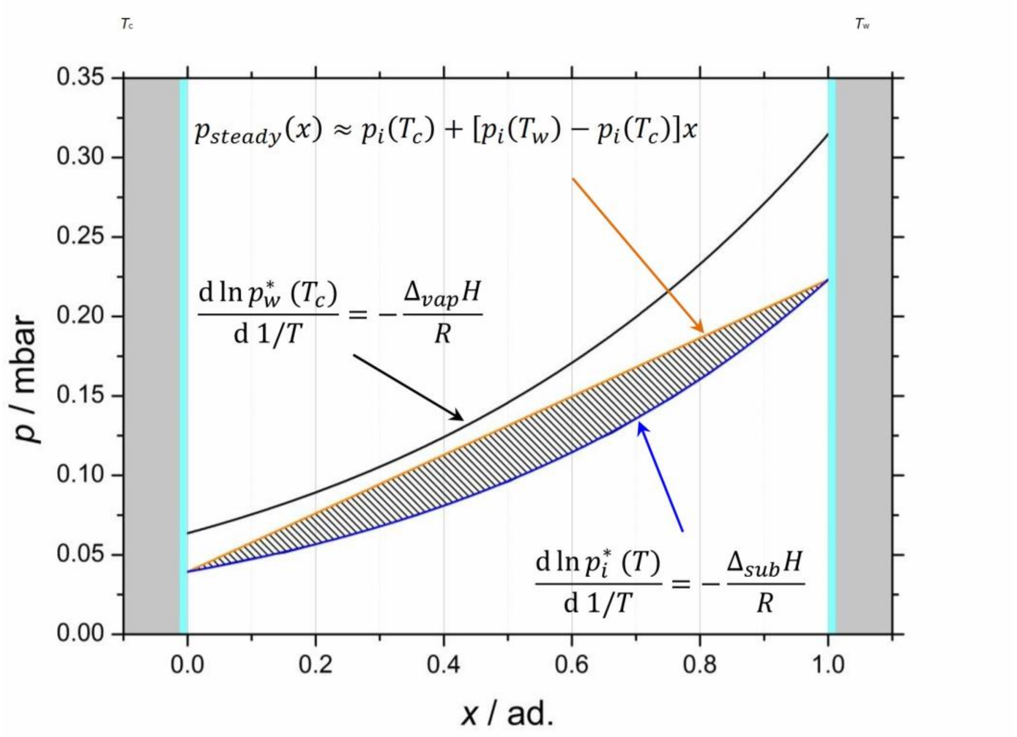

Figure VI-3-1 Working principle of the LINC in the nucleation chamber. Two opposing walls are cooled down below the melting point of bulk water and covered with a thin layer of ice. During the phase transition, the water vapor partial pressure is only function of the temperature and on the droplet/particle size (generalized Clausius-Clapeyron relation). In steady state, heat and diffusion of water vapor lead to a linear gradient which forces a supersaturation with respect to ice (and potentially water) between the walls. In the figure, the pattern fill indicates the region supersaturated with respect to ice. Notice that in this specific case the flow is not supersaturated with respect to supercooled water (is located below the black solid line indicating coexistence of gas and liquid supercooled water).

According to simulations and data available in the literature (Rogers 1988; Kanji and Abbatt 2009; Baschek et al. 2008), both the sheath flow channels and the aerosol injection nozzle are required to provide sufficient injection velocity in the nucleation chamber. A total flow of 10 Lmin^{-1} was selected to ensure a laminar flow inside the nucleation chamber where the Reynolds number is around 100. Detailed calculations run on the basis of the theory developed by Sinerwalla and Tomlinson (Tomlinson and Fukuta 1985) show the competition of two different effects to determine the overall flow velocity along the nucleation chamber. A parabolic contribution comes from the friction on the walls, and a cubic contribution comes from the buoyant convective circulation induced by the temperature difference between the walls. This results in a skewed velocity profile where the maximum flow velocity is closer to the cold wall as clearly shown in Figure VI-3-2. The total velocity and the two effects on the velocity are described by the Equation VI-3-1, Equation VI-3-2 and Equation VI-3-3.

$$v_{tot} = v_{fr} + v_{bu} \qquad \text{Equation VI-3-1}$$

$$v_{fr}(x) = \frac{3}{2} v_{av} \left(1 - \frac{(x - l_{eff})^2}{l_{eff}^2} \right) \qquad \text{Equation VI-3-2}$$

$$v_{bu}(x) = \frac{\rho_a g l_{eff}^2}{6\eta_a} \left(\frac{T_w - T_c}{T_w + T_c} \right) \left(\frac{(x - l_{eff})^3}{l_{eff}^3} - \frac{(x - l_{eff})}{l_{eff}} \right) \qquad \text{Equation VI-3-3}$$

where x is the distance from the cold wall, v_{av} is the average velocity calculated as the ratio between total flow and chamber section, l_{eff} is the half-distance between the walls, ρ_a and η_a are the average density and dynamic viscosity of air respectively, g is the acceleration due to gravity, and finally T_w and T_c are the temperature of the warm and cold wall respectively.

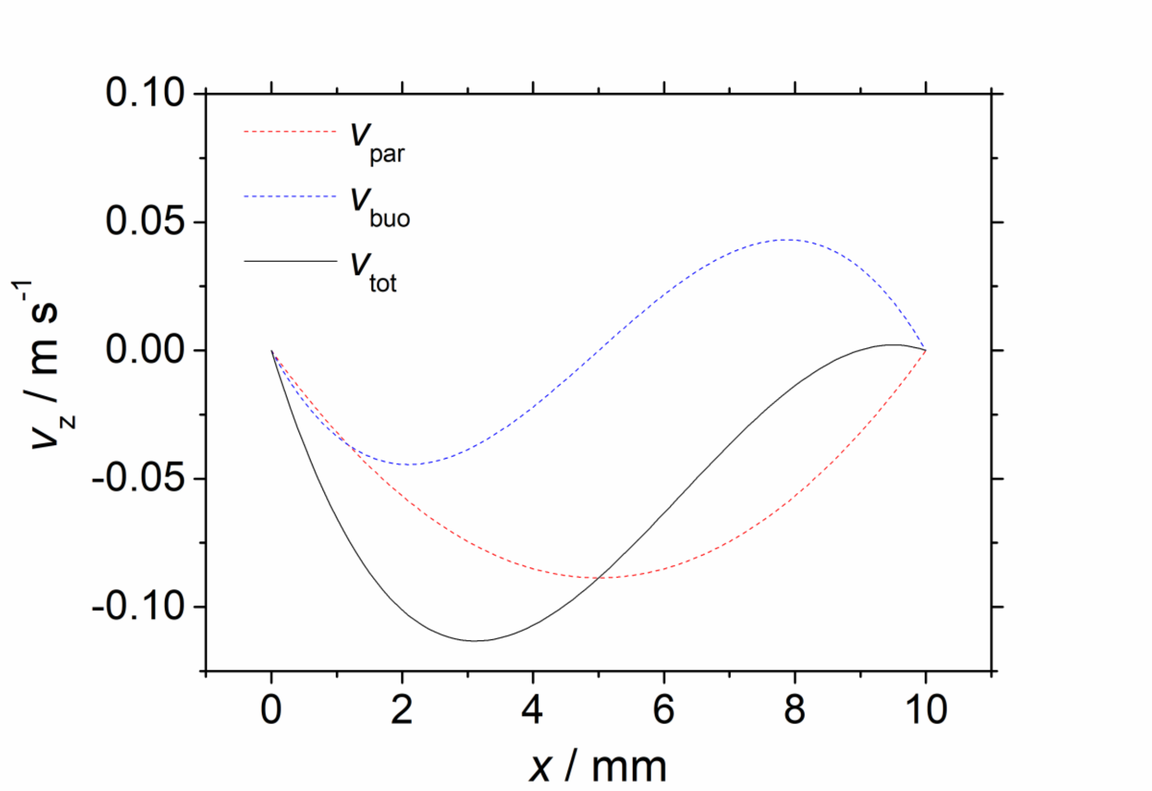

Figure VI-3-2 Contributions to the vertical component of the velocity (black solid line): parabolic contribution due to wall friction (red dashed line) and cubic contribution due to buoyancy (blue dashed line).

In order to study the ice nucleation of aerosol in the nucleation chamber, S_w should be lower than 1 to avoid water condensation nucleation (Figure VI-3-1). Beside, v_{bu} has to be limited to avoid vortex mixing (Figure VI-3-2). By considering these two limits, the temperature of the cold and warm wall needs to be accurately controlled. At 10 Lmin^{-1} total flow rate and 850 mbar pressure, the working range (red scatter line) of S_i in the LINC is presented in Figure VI-3-3. The LINC provides S_i as high as 1.4 with a temperature down to -60°C. Theoretically, the deposition nucleation and freezing nucleation can be performed in the LINC.

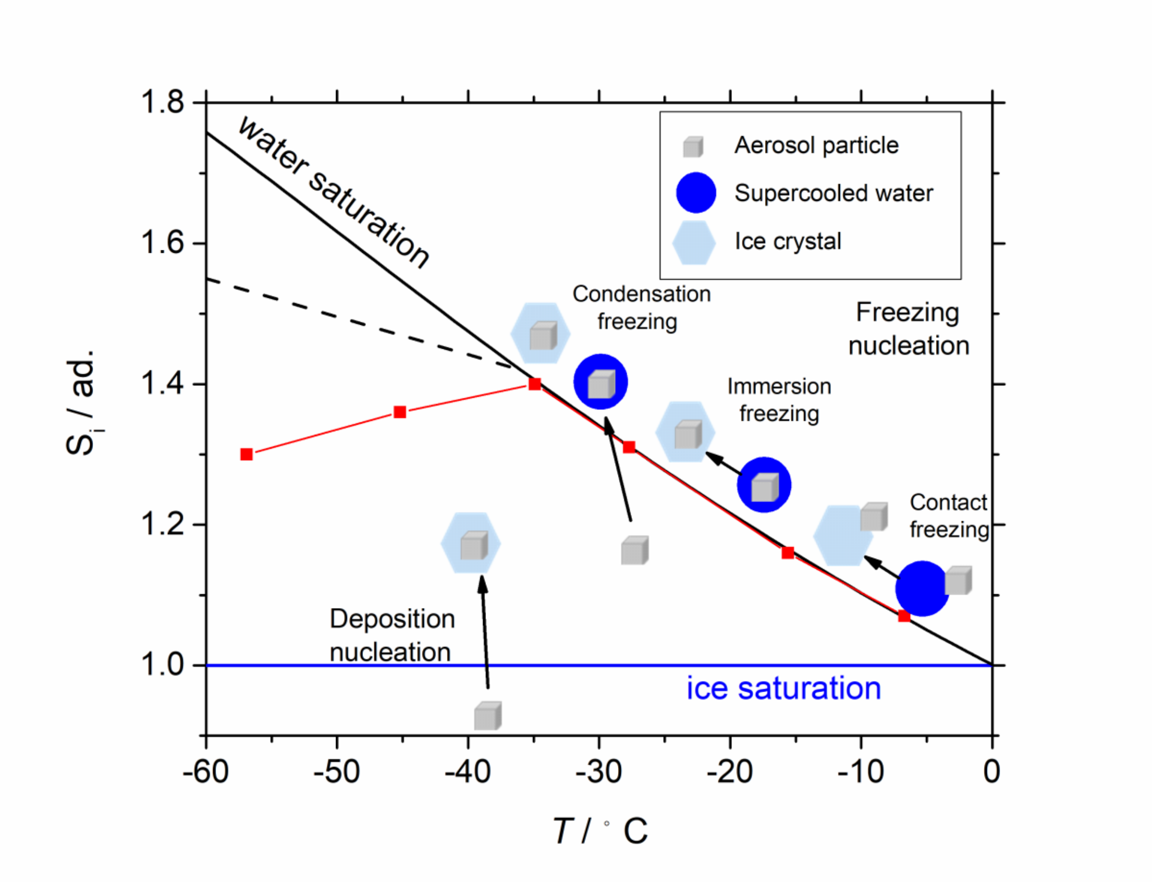

Figure VI-3-3 Working range of the LINC with respect to ice saturation (S_i). Red scatter line represents the theoretical working range for studying the ice nucleation of aerosols.

3.2. LINC development and implementation

An overview of the LINC facility is shown in Figure VI-3-4. The system features three main components. The injector, on the top, accelerates the sample flow inside the following nucleation chamber. The nucleation chamber, located in the middle, is the very core of the apparatus where the seeding aerosols particles are exposed to water/ice supersaturation and water droplets/ice particles nucleate and grow up to a detectable size. In the evaporation chamber, on the bottom, the operating conditions can be modified independently of the nucleation chamber thus permitting to remove unwanted water droplets and leaving the ice particles only. Ice particles can then be counted at the instrument exit by scattering- or extinction-based optical techniques for instance.

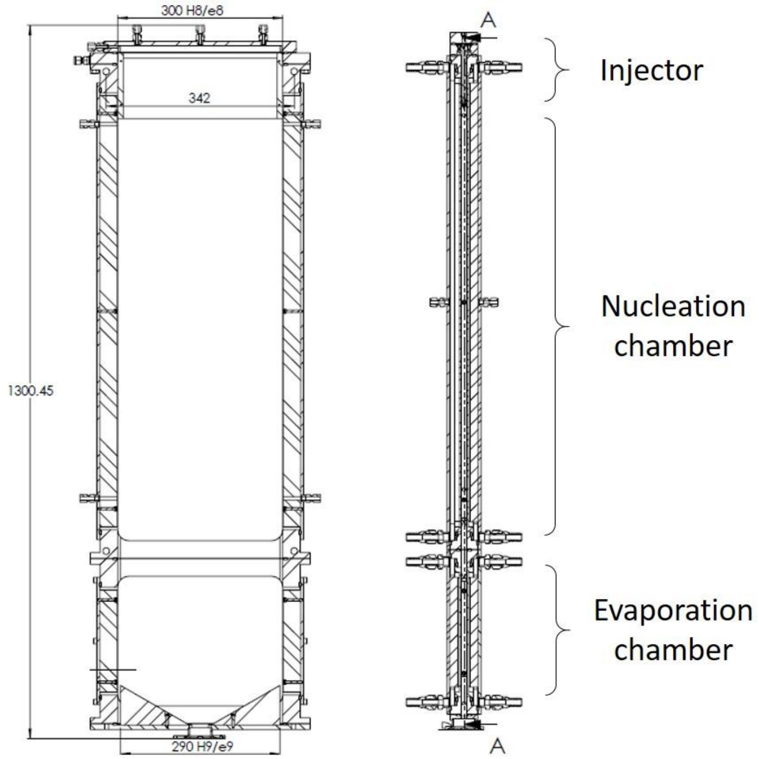

Figure VI-3-4 LINC overview. Three main parts can be identified: the injection system (on the top), the nucleation chamber (in the middle) and the evaporation chamber (on the bottom). The apparatus is vertically mounted.

The detailed scheme of the LINC inlet section is shown in Figure VI-3-5, and it consists of two shaped stainless steel flanges mounted on the top of the nucleation chamber frame that together form the channel for the sample and the two sheath flows and keep the injector in the correct operating position. The upper flange seals the nucleation chamber and contains a channel that distributes the aerosol sample flow over the whole width of the device. The lower flange is directly fixed on the nucleation chamber frame and contains the injector socket. The injector itself is formed by two long, thin, symmetric blades bolted to the middle flange and extending 12 cm inside the nucleation chamber. The large inlet cross section allows the sample flow to distribute homogeneously almost over the whole width of the chamber, while the thin outlet created by the injector blades (400 µm) directs the flow downwards and creates the pressure drop required to inject the sample flow into the center of the nucleation chamber. According to ZINC design (Baschek et al., 2008), the sample flow is injected in the central part of the nucleation chamber only. This avoids the aerosol particles to be exposed to regions where flow and humidity conditions are perturbed by the influence of the side walls.

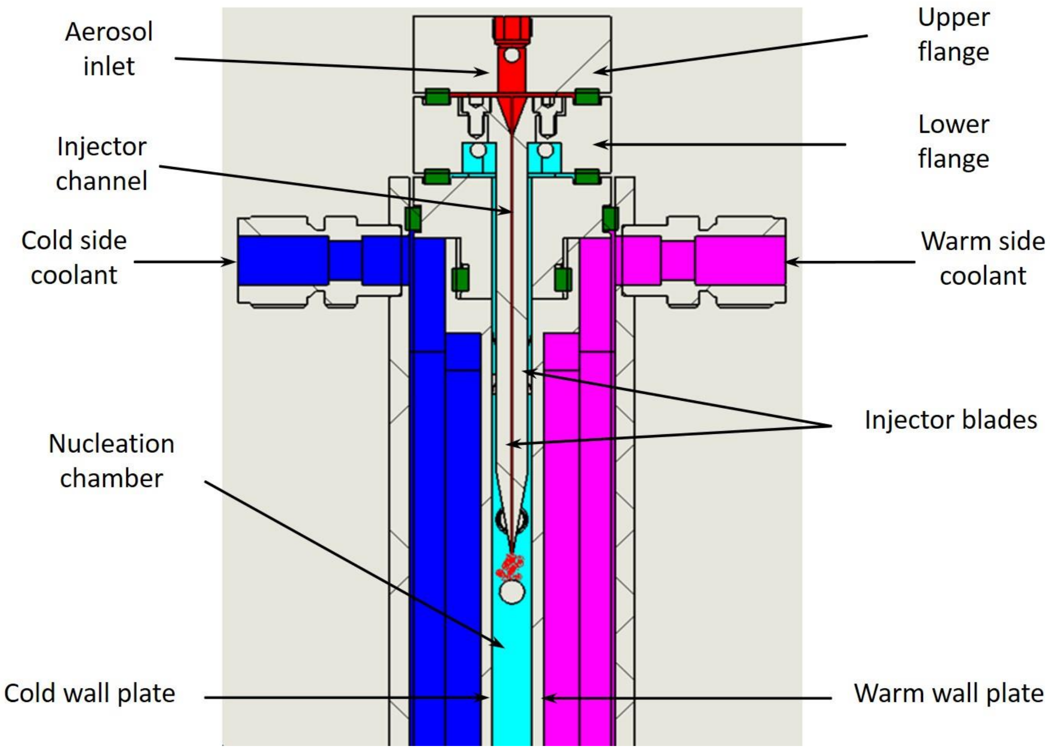

Figure VI-3-5 Detailed scheme of the uppermost part of the nucleation chamber including the aerosol injection system. The channel created by the injector blades and the inlet channels of the sheath flows are 0.4 mm and 1.0 mm wide respectively. The nucleation chamber is 10 mm wide.

Both the nucleation and the evaporation chambers feature an independently mounted stainless steel frame on which two aluminum plates are mounted parallel face-to-face that are the cold and warm wall described in the introduction. When the system is operational, the aluminum plates are to be covered with a thin layer of ice and cooled down to generate the supersaturated region. Therefore, to improve the adherence of ice, the plate surface has been first milled to create a regular, rough pattern and then anodized to increase the resistance to corrosion. Shaped stainless steel lids enclose the aluminum plates on the frame’s outer side to create the path for the coolant. A series of temperature sensors are installed at the inlet and outlet ports of the cooling system, and on dedicated ports in the center of the lids.

4. Ice nucleation test with ammonium sulfate aerosols in the LINC

Since the LINC is being developed, several calibration tests have been performed with ammonium sulfate aerosols. The currently active configuration of the LINC is shown in Figure VI-4-1 below, and combines the nucleation chamber to the seeding aerosol generation by atomization (see Chapter 2) and the ice particle optical detector. In order to run an ice nucleation experiment, the aerosol generation system (top right in Figure VI-4-1) provides the seeding aerosol that is injected into the nucleation chamber where it triggers the heterogeneous nucleation of supercooled water droplets and/or ice particles (vertical left side in Figure VI-4-1). At the nucleation chamber outlet, an aerodynamic particle sizer (APS) counts the ice particles and supercooled water droplets (bottom part of Figure VI-4-1).

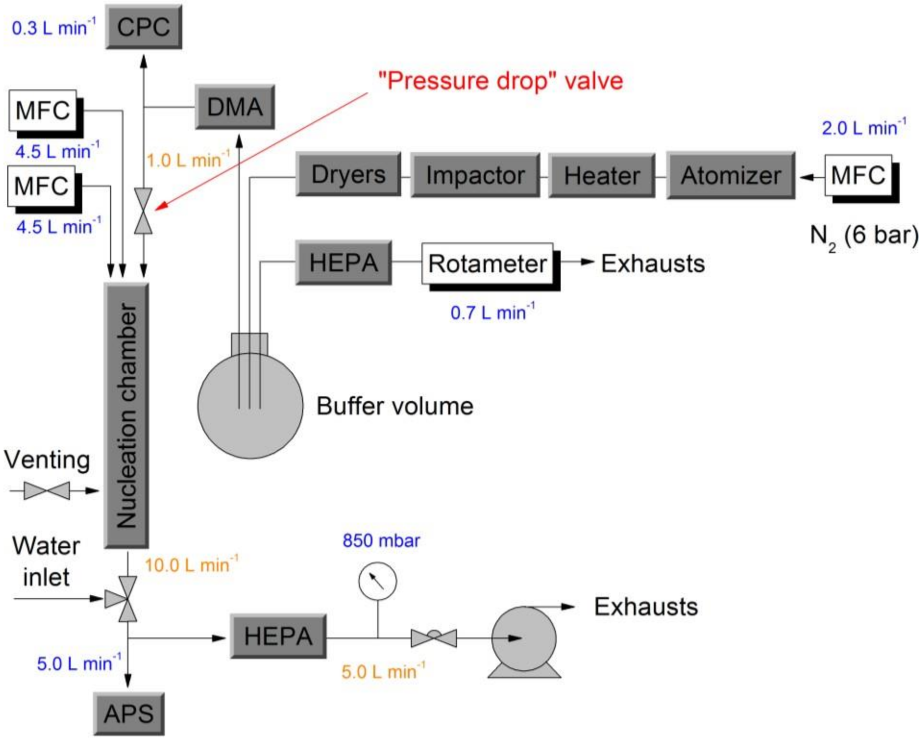

Figure VI-4-1 Overview of the current LINC setup: injection system (top-right), nucleation chamber (middle left), particle counting system and flow regulation (bottom). Acronyms used are: MFC (mass flow controller), HEPA filters (high-efficiency particulate arrestance), APS (aerodynamic particle sizer). Blue values are measured, orange values are calculated.

In a typical activation experiment, the output flow of the atomizer is first dried by heating up to 120°C, then by removing the remaining droplets by impaction, and finally by removing the residual water by diffusion (diffusion driers loaded with silica gel, orange). Finally the dry ammonium sulfate aerosols ($RH < 0.2\%$) arrive to a buffer volume which stabilizes the flow before entering the DMA. From the exit of the DMA, aerosols are injected into the LINC from the top injector, a CPC monitors the concentration of aerosol in parallel. The concentration of aerosol injected into the LINC is stable around 4×10^5 cm^{-3}. The pressure drop regulates the flowrate of the aerosol flow to 1 Lmin^{-1} which corresponds to 0.7 Lmin^{-1} in the rotameter connected to the exhaust. Two MFCs provide the sheath flow with a total flowrate of 9 Lmin^{-1} to protect the aerosols and limit the diffusion losses in the chamber. The APS measures the size of the nucleated ice particles with aerodynamic diameter between 0.5 to 20 μm. An additional advantage of this configuration is that the separation of the seeding aerosol particles (d_p ~100 nm) and nucleated ice particles ($d >$ 500 nm) is easily obtained based on their size. In order to ensure the working flowrate of the APS and the working pressure in the LINC, a pump after the outlet of the LINC is used to maintain the flow.

A series of ice nucleation experiments with selected ammonium sulfate aerosols (100 nm) were performed. Two examples of the size distribution of ice particles determined by APS are shown in Figure VI-4-2. In these two cases, the ice saturation is 1.09 and 1.14, respectively. The aerodynamic diameter of the nucleated ice particles is between 1 and 10 μm. By comparing the concentration of ammonium sulfate aerosol injected into the LINC, the activated fraction ($F_{a,ice}$) is estimated to be around 2%. However, it is important to notice that this estimation is subject of large incertitude, as within the established experimental protocol detailed knowledge on the overall particle loss inside the nucleation chamber is still missing.

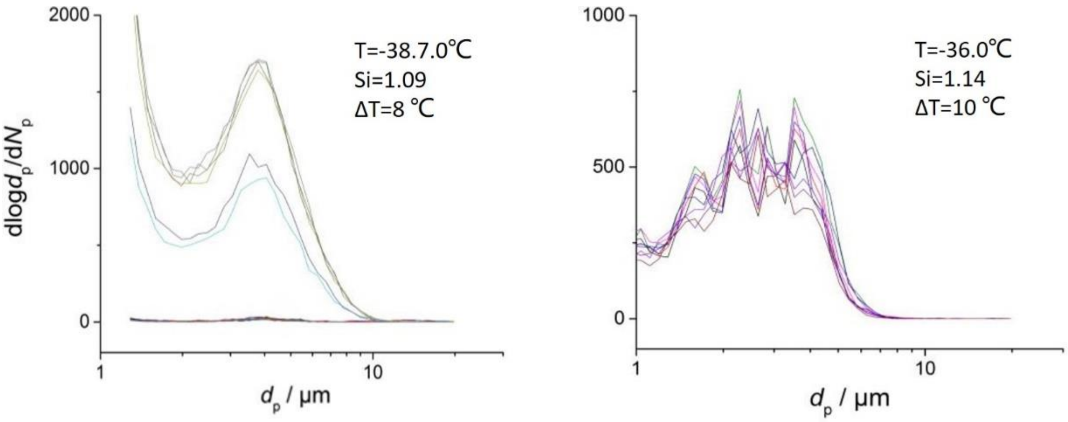

Figure VI-4-2 Examples of large particle distributions obtained using the APS at the LINC outlet in stable flow and IN concentration conditions. Each curve represents a different scan in the same experimental conditions. Sometimes, data are not reproducible to be further treated.

The ice nucleation conditions for ammonium sulfate aerosol in our work are compared with the literature in Figure VI-4-3. Ice particles formation is observed in deposition nucleation mode (i.e. below the water saturation curve) only when $T <$ -33°C. These early results are rather promising, but the protocol still needs to be improved as briefly discussed below.

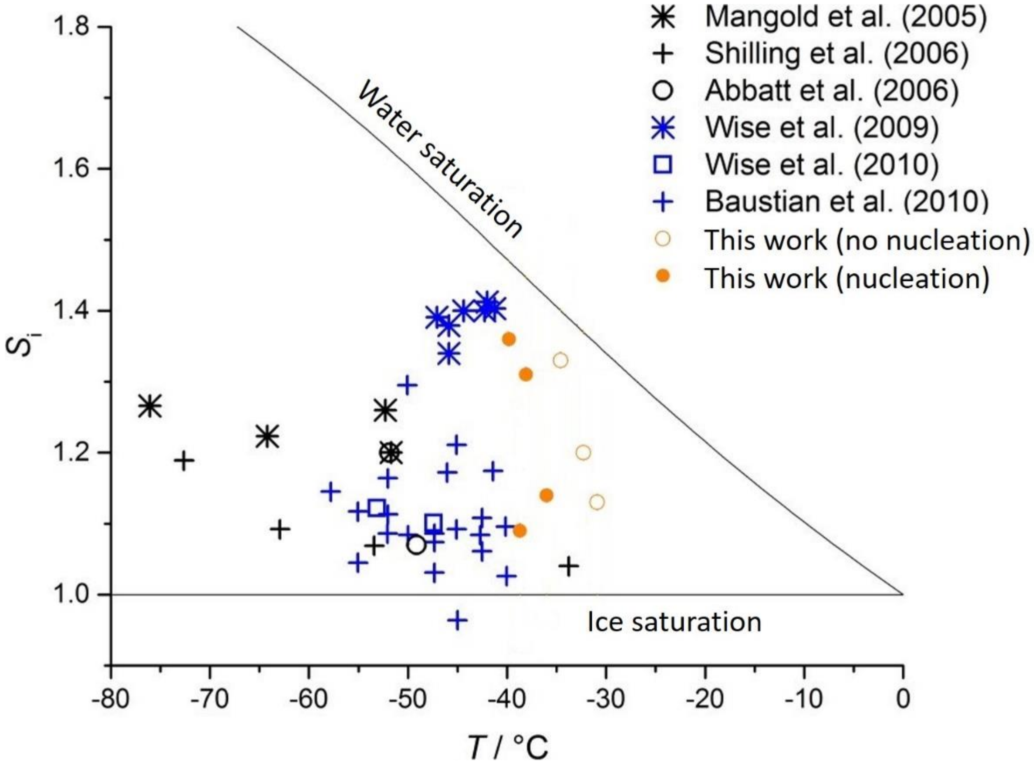

Figure VI-4-3 Comparison of the ice nucleation onset temperatures and saturation ratios for ammonium sulfate in this work and the results reported by (Hoose and Mohler 2012)**.**

5. Conclusions and prospective

The LINC is CFDC type chamber for studying the ice nucleation at low temperature which aims to simulate the environmental condition of the high troposphere. According to the theoretical calculation, the LINC provides the ice saturation S_i as high as 1.4 with temperature as low as -60°C. With these parameters, the LINC aims to study the nucleation of soot aerosols in the process of deposition and freezing. Early tests with size selected ammonium sulfate aerosols generated by atomization were performed to verify the experimental protocol. Our first measurement of deposition nucleation indicated that IN are well produced into the LINC within a temperature range in good agreement with the results of the literature. Unlike the case $T >$ 0°C, the activated fraction of the aerosols at $T > 0$°C are very low and were never found to exceed 2%.

More experiments are required to improve the protocol and introduce a quantitative approach, especially for a more accurate determination of the activated fraction. According to the nucleation results in this work, the temperature of -33℃ seems like a critical parameter for initiating the deposition nucleation of size selected ammonium sulfate aerosols with $d_m = 100$ nm.

Some improvements are prospected to realize for improving the protocol of the calibration of the LINC before seeding soot aerosols.

- The optical counter

  As remind in the configuration of the LINC (Figure VI-4-1), an APS was used for measuring the size distribution of the ice particles. Though the APS succeeded estimating the particles size within a range of 0.5 to 20 μm, the working temperature of the APS is the room temperature (20℃). This gradient of the temperature between the LINC and the APS could change the size after the formation of the ice particles. In order to have an accurate information of the ice particles formed in the LINC, an optical particle counter is prospected to count the number of the ice particles in isolated conditions which corresponds to the low temperature in the LINC.
- Production of the ice layer

  As mentioned in section VI-3.1, the production of the ice layers in the nucleation chamber is difficult to be reproduced. In the current configuration, both two walls are set at -20°C and liquid water is filled from the bottom. The overall process requires about during 2 minutes. However, due to the different freezing time in vertical of the chamber, the thickness of the ice layer is not homogeneous, i.e. the ice layer is thicker at the bottom than that on the top. This proved to be a major, unforeseen problem as the changing inner section of the chamber affects all theoretical calculations on flows and therefore on the supersaturation, and will most likely require some important modifications like setting the chamber horizontal in order to be solved.
- Temperature profile inside the nucleation chamber

  A series of temperature sensors are installed on the outside of the nucleation chamber walls (section VI-3.1), inside the cooling system. The temperature is one of the most important and sensible parameters to estimate S_i. Thus, an accurate calibration of the temperature between the inner wall and the outer wall is strongly recommended.

Conclusion and prospectives

The main goal of this work is to improve the understanding from the theoretical and experimental point of view of the ensemble of processes (atmospheric aging) that convert freshly emitted, hygroscopic soot particles into efficient cloud condensation (CCN) and ice (IN) nuclei in the atmosphere.

In this work, the classical thermodynamic κ-Köhler theory has been applied to describe the activation of aerosol particles in water supersaturated conditions. κ-Köhler theory uses a single parameter (κ) representation to account for the hygroscopicity of dry particle. Based on the κ-Köhler theory, a model has been developed to calculate the activation curves (activated fraction as function of supersaturation, $F_a - SS$) of soot particles by considering the dry particle size distribution and morphology. Lognormal size distributions of ammonium sulfate and soot particles have been considered in this work. The mode (μ_{mode}) and the geometrical standard deviation (σ_{geo}) of the distributions have been used as parameters to convert the mobility diameter (d_m), measured by SMPS, into the volume equivalent diameter (d_{ve}) used in the κ-Köhler theory. The dependence on the morphology uses the primary particle diameter (d_{pp}) and the fractal dimension (D_f) of the aggregates as parameters to be introduced in the theory. These parameters are determined from TEM investigation of ammonium sulfate and soot particles. First, a series of $F_a - SS$ of $(NH_4)_2SO_4$ particles obtained experimentally using a CCNc have been fitted to validate the role of size distribution on $F_a - SS$. Then, $F_a - SS$ of soot particles exposed to OH^- have been fitted to validate the role of soot morphology on $F_a - SS$. The model has been used for fitting $F_a - SS$ curves obtained in this work.

The model demonstrates that the shape of the $F_a - SS$ curve depends on μ_{mode}, σ_{geo} and κ. The increase of μ_{mode} and κ leads to the leftward shift of the $F_a - SS$ curves, thus to the decrease of the SS at which the particles become active. Conversely, the increase of σ_{geo} flattens without shifting the $F_a - SS$ curves. The modification of the morphology of soot particles influences d_{ve}, then changes the shape of $F_a - SS$ curve similarly to μ_{mode}. In the literature, the value of κ is often calculated from the critical supersaturation SS_c defined as the value of SS when $F_a = 0.5$. However, our model shows that for polydisperse aerosols with large σ_{geo}, calculations relying on the direct measurement of SS_c underestimate SS_c and therefore overestimate κ. This difference is significant in the case of $\sigma_{geo} > 1.2$.

The model has been validated with five dry $(NH_4)_2SO_4$ particles with different μ_{mode} and σ_{geo} in the Lille atmospheric simulation chamber LASC, where μ_{mode} is in the range of 57-101 nm and σ_{geo} is in the range of 1.06-1.79. $(NH_4)_2SO_4$ particles have been collected for TEM analyses that show that $(NH_4)_2SO_4$ particles in the LASC have quasi-spherical shape and do not aggregate. The F_a-SS curves calculated including the contribution of the size distribution of the dry particles are found to reproduce well both the shape and the position of the corresponding experimental $F_a - SS$ curves.

The model has been also validated with of kerosene and diesel soot particles. Fresh soot particles are generally hydrophobic, therefore beforehand they have been exposed to OH^- to obtain measurable $F_a - SS$ curves. “Monodisperse” soot particles with 150 nm and 300 nm mobility diameter have been studied in this work. Morphology parameters like the diameter of the primary particle d_{pp} and the fractal dimension D_f have been applied to the diameter conversion from the experimentally measured mobility diameter d_m to obtain d_{ve}. By setting κ and σ_{geo}^{ve} as free parameters, the experimental $F_a - SS$ data are well reproduced. The obtained values of σ_{geo}^{ve} are in the range of 1.19 to 1.22 for all activation curves. κ is estimated as high as 3.6×10^{-2} with the exposure time of 1.87×10^{11} $cm^{-3}s$. The fitting results demonstrate that the $F_a - SS$ curve of soot particles can be explained by only taking into account physically meaningful parameters describing the particle morphology, size distribution and hygroscopicity.

When using the model to find unknown κ, the estimation of κ directly comes from the fitting of $F_a - SS$ curves. An important consequence is therefore that size selection before activation experiments is not mandatory for the study of the hygroscopic properties of aerosols since the size distribution can be accounted for in the calculation of $F_a - SS$ curve, which among other things has the potential to greatly simplify the experimental setups.

The activation of soot particles as cloud condensation nuclei (CCN) is studied in laboratory under conditions that aim to simulate atmospheric processes. Soot particles have been exposed to different reactants in two simulation chambers, the Lille Atmospheric Simulation Chamber (LASC) and the Experimental Multiphasic Atmospheric Simulation Chamber (CESAM), then the activation curves have been measured by using a commercial cloud condensation nucleation counter (CCNc). The aging of both "monodisperse" ($\sigma_{geo}{\sim}1.08$) and polydisperse ($\sigma_{geo}{\sim}1.45$) soot particles with different size distributions have been studied under controlled conditions of temperature, pressure and relative humidity (RH). The role of the common atmospheric oxidizers O_3 and SO_2 on the activation of soot particles have been studied respectively. During the experiments, gas concentration and size distribution of soot particles have been recorded on line. Soot samples have been collected at different reaction times to study the evolution of the particle size and morphology by transmission electron microscopy (TEM), while the chemical composition has been obtained by secondary ions mass spectrometry (SIMS). Mass spectra of soot samples have been analyzed statistically by principle component analysis (PCA) and hierarchical clustering analysis (HCA) to extract information on the particle and gas phase reactivity. The corresponding activation curves $F_a - SS$ have been obtained for SS from 0.2% to 1.8% at room temperature.

The activation of "monodisperse" kerosene soot particles exposed to O_3 has been measured first in the LASC. Soot particles are sampled from four heights above the burner (HABs) in the flame: 70, 100, 130 and 140 mm. Soot particles have been exposed to O_3 (~1.2 ppm) at three different exposure times: 0, 90 and 150 min. In total, twelve tests have been performed in the LASC. All F_a-SS curves have been fitted by applying the κ-Köhler modified model presented previously. Estimated σ_{geo} is in the range of 1.07 to 1.16, which corresponds to the experimental σ_{geo} of 1.08. This work shows the fresh kerosene soot particles are not active at SS as high as 1.8%, which is in good agreement with the literature. Even by increasing the exposure well above atmospheric standards (1.37×10^{17} $cm^{-3}s$, equivalent to 100 ppb for 25.7 hours in standard condition), the hygroscopicity κ of soot does not increase above 1.9×10^{-3} which is still very low compared to hydrophilic aerosols such as $(NH_4)_2SO_4$ ($\kappa=0.61$) and H_2SO_4 ($\kappa=0.9$). The activation results show that soot sampled at 70 mm HAB is more efficient than that from other HABs to be activated by O_3. Soot sampled at 130 mm HAB is the most difficult to be activated. Further studies are required to correlate the propensity to form CCN to the maturity of the soot and presumably to their H/C ratio. In addition this difference in the behavior of soot sampled at different HAB (different maturities) is correlated to the ozone loss ratio due to soot (k_{soot}) as well. k_{soot} is significant larger for soot sampled at 70 mm HAB ($6.4\pm0.1\times10^{-5}$) than 130 mm ($0.15\pm0.07\times10^{-5}$). The analysis of the particle chemical composition by SIMS provides further insights. According to our interpretation of the results of PCA and HCA analysis, differences on the chemical composition of soot particles are found to be related to the flame sampling HAB (first principal component, PC1), and to a minor extent to O_3 exposure time (second principal component, PC2)

The role of SO_2 on the activation of "monodisperse" soot sampled at 130 mm HAB has been studied in the CESAM. O_3, SO_2, H_2O and UV radiation have been used as environmental conditions in these tests. The analysis of TEM images of collected soot particles after the aging processes shows the increase of 1.4 ± 0.3 nm of d_{pp} and a stable value of 1.68 ± 0.03 of D_f. The modification of the morphology of soot particles in the CESAM test is therefore not evident. $F_a - SS$ curves of "monodisperse" particles have been measured and fitted by the modified κ-Köhler model. Estimated σ_{geo} is in the range of 1.06 to 1.17 which corresponds to the experimental σ_{geo} of 1.08. The homogeneous nucleation of secondary aerosols has been observed along with the presence of O_3 (1.2 ppm), SO_2 (100 ppb), H_2O ($RH = 20\%$) and UV radiation. Fitting the $F_a - SS$ curves with the modified κ-Köhler theory and using electrical mobility measurements (40 and 60 nm) to estimate d_{ve} result in $\kappa = 0.55$ that is very close to $\kappa = 0.61$ of $(NH_4)_2SO_4$. Then the role of SO_2 on the activation of activated soot has been studied. A sudden decrease of SS_c has been observed immediately after the injection of SO_2 (100 ppb). κ of "monodisperse" soot particles ($d_m = 164$ nm) exposed to OH^- arrives up to 7×10^{-3} with exposure time of 3.5×10^{10} $cm^{-3}s$. κ increases up to 0.18 with SO_2 exposure time of 4.6×10^{15} $cm^{-3}s$ (equivalent to 100 ppb with 1.1 hours). The sudden decrease of SS_c, i.e. increase of κ is strong evidence that SO_2 is directly involved in the activation of soot particles. In the following experiments, it has been observed that only the presence of O_3 and SO_2 ($RH < 0.2\%$), regardless of the injection order, is mandatory to activate soot particles and convert them into efficient CCN.

According to the results of chemical composition by SIMS, PC1 is strongly related to the presence of compounds containing sulfur in their highest oxidation states (IV and VI). Furthermore, the lack of compounds containing sulfur in the gas phase strongly implies that the reaction occurred on the surface of soot particles and not in the gas phase.

An additional test with polydisperse soot particles sampled at 70 mm HAB has been performed in the LASC to verify the validation of the model on the size distribution with large σ_{geo}. Two $F_a - SS$ curves have been measured by the CCNc at different ozone exposure times. The size distribution of soot particles in this test has μ_{mode} of 138 nm and σ_{geo} of 1.45. The estimated σ_{geo} by the model is 1.47 which well agrees to the experimental value (1.45). κ of polydisperse soot particles increases up to 1.0×10^{-3} with exposure time of 1.13×10^{17} $cm^{-3}s$. The value of κ (1.0×10^{-3}) for polydisperse soot sampled at 70 mm HAB is similar to that (1.9×10^{-3}) for “monodisperse” soot sampled at the same HAB.

In conclusion, both O_3 and SO_2 play an important role on the activation of soot particles during the aging process at room temperature. According to TEM imaging, the morphology of soot during the aging process with O_3 and SO_2 does not change significantly and therefore its effect is considered as negligible. The change of the hygroscopic properties of soot strongly has been related to the presence of sulfates on the particle surface detected by SIMS. In the atmosphere, soot particles can be activated by O_3 over long expositions (days) near the ground where O_3 concentration is high due to the ground level ozone pollution. On the other hand, the participation of SO_2 considerably shortens the aging time even at moderate concentration.

This work demonstrates that the presence of O_3 and SO_2 significantly influences the hygroscopic properties of soot particles and the reaction is strongly believed happening on soot surface. However, from the chemical point of view, what exactly happens on soot surface is not understood yet. It there the coating, oxidizing or catalyzing? The study of this heterogeneous chemistry process is a very interesting perspective. For instance, the constant loss ratio of O_3 in the LASC shows that first order kinetic occurs in the aging process. Loss ratio of O_3 and SO_2 in the CESAM need to be studied to obtain kinetic information. By comparing these kinetic parameters with the literature, for instance chemical mechanism of SO_2 and O_3 on surface of calcium carbonate particles (L. Li et al. 2006), these kinetic parameters could help to propose a chemical mechanism of O_3 and SO_2 on soot surface. Prospectively, the different concentrations of

O_3 and SO_2 will be performed in the future to achieve uptake coefficient of O_3 and SO_2 on soot particles.

With the success of the modified κ-Köhler model on reproducing the activated fraction of soot as function of water supersaturation, more aerosols with polydisperse distribution are expected to verify the wide applicability of the model. For example, well-known inorganic aerosols (sulfate nitrate, sodium chloride and sodium nitrate, etc) and organic aerosols (malonic acid, phthalic acid and glutamic acid, etc). The wide application of the modified model could give more propositions on experimental protocols and on the calibration of supersaturation chambers with considering the size distribution. Fa-SS curves of aged soot are better fitted than that of fresh soot, where the Kelvin limit cannot be satisfactorily applied to fresh soot. With increasing the mobility diameter of fresh soot particles, the Kelvin limit might be reached in supersaturated condition of 0.1-2.0%. This potentially helps to improve the model on inactivated soot particles.

This work demonstrates also that soot particles sampled from different HABs give different behaviors on the activation in the aging process with O_3. Is it due to H/C ratio of soot particles or modifications of certain hydrocarbon species? In the literature, the length of the carbon chain in organic compounds decreases the hygroscopicity κ (S. S. Petters et al. 2017). The link between the majority of soot particles in the flame and the hygroscopicity is interesting to be studied in the future.

The protocol of the deposition nucleation study with $(NH_4)_2SO_4$ aerosols has been developed in the Lille Ice Nucleation Chamber (LINC). Soot particles sampled from laboratory flames are expected to be studied in the LINC or in the Portable Ice Nucleation Chamber (PINC) in the programing collaboration with University of Gothenburg, Sweden.

Annex

Annex A. Scanning Mobility Particle Sizer (SMPS)

SMPS is a device which permits to measure the size mobility distribution of an aerosol, which means the particle concentration number as a function of its size. SMPS used in this work consists of a commercial electrostatic classifier TSI model 3080, a differential mobility analyzer (DMA) TSI model 3081 or 3085, an ultrafine condensation particle counter (CPC) TSI model 3776 (annex 2) and a computer with software AIM showed in Figure A5-1.

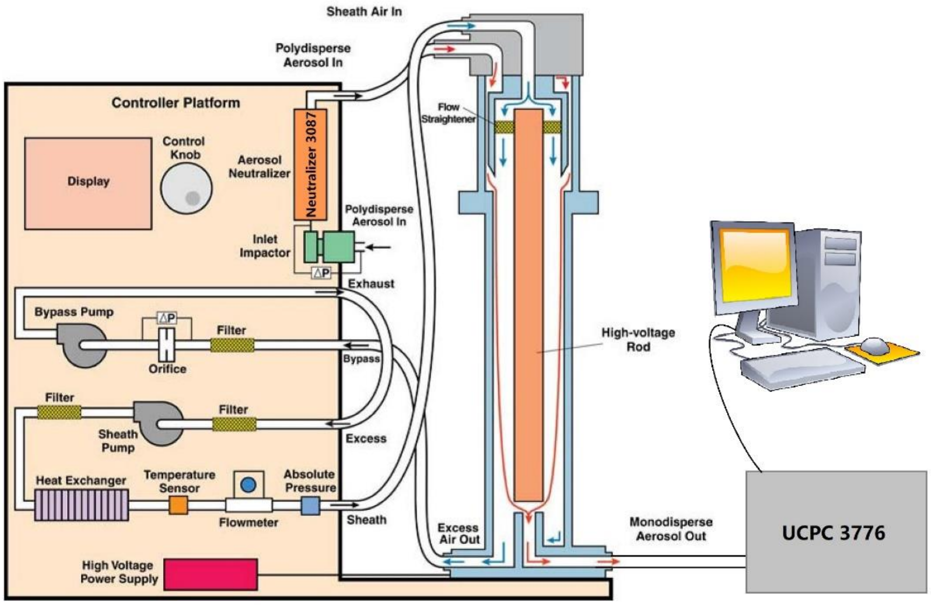

Figure A5-1 SMPS configuration.

Polydisperse aerosol particles are filtered by impaction to remove large particles that potentially carry more than a single charge. Then, they pass through a neutralizer that establishes a bipolar equilibrium charge on the particles. The charged aerosol passes from the neutralizer into the main portion of the DMA as shown in figure A1.1. The DMA contains two concentric metal cylinders. The polydisperse aerosol with a flowrate of Q_a and sheath air with a flowrate of Q_{sh} are introduced at the top of the Classifier and flow down the annular space between the cylinders. The aerosol surrounds the inner core of sheath air, then both flows pass down the annulus with no mixing of the two laminar streams. The inner cylinder, the collector rod, is maintained at a controlled negative voltage, while the outer cylinder is electrically grounded. This creates an electric field between the two cylinders from 0 to 10 kV which is controlled by classifier. Particles are precipitated along the length of the collector rod. The location of the precipitating particles depends on the particle electrical mobility (Z_p), the classifier flowrates, and the classifier geometry. The classifier has 64 channels per scan, these 64 slices are distributed logarithmically. At each voltage step, the concentration of monodisperse particles is measured by CPC 3776. This contribution between CPC and the classifier permits to give the size mobility distribution of the aerosol.

- Impactor

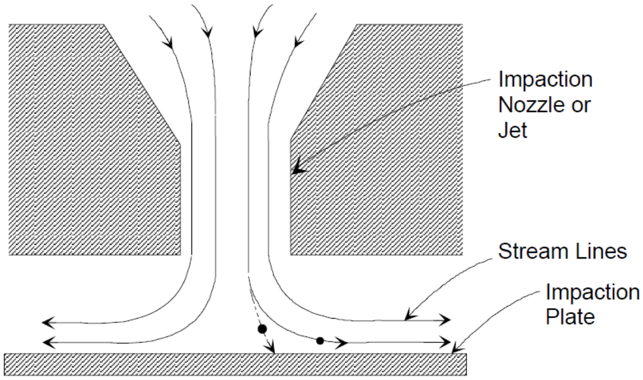

Figure A5-2 Cross-sectional view of an inertial impactor (Hinds 1982)

In Figure A5-2, the impaction plate deflects the flow to form a 90° angle in the streamlines. Particles with sufficient inertia are unable to follow the streamlines and impact on the plate. Smaller particles follow the streamlines, avoid contact with the plate and exit the impactor. The impactor is used in the SMPS system to remove particles larger than a known aerodynamic size due to their contribution to multiply charged aerosols. The aerodynamic particle size at which the particles are separated is called the cut-point diameter. The cut-off diameter is a function of the impactor flow rate and nozzle diameter (Hinds 1982).

$$D_{50} = \sqrt{\frac{9\pi \, Stk \, \mu W^3}{4\rho_p C Q}} \qquad \text{Equation A5-1}$$

Where D_{50} is the particle cut-point diameter in cm; Stk is Stokes number (0.23); ρ_p is the particle density in gcm^{-3}; Q is the volumetric flowrate in cm^{3}s^{-1}; C is the Cunningham Slip Correction; μ is the gas viscosity in gcm^{-1}s^{-1}; W is the nozzle diameter in cm.

In the system of SMPS, there are three nozzle sizes to choose from. The nozzle size and flowrate determine the largest particle size that can be sampled within each SMPS measuring size range. Table A5-1 shows the aerosol flow range and the particle cut-point diameter corresponding to these 3 impactors.

Table A5-1 Typical flow range and particle cut-off diameter for each impactor nozzle.

Nozzle size (cm)	Aerosol inlet flow range (Lmin^{-1})	Cut-off diameter (nm)
0.00457	0.2 to 0.8	850 to 320
0.00508	0.3 to 1.0	812 to 413
0.071	0.6 to 2.1	979 to 491

- The neutralizer

The Model 3087 Advanced Aerosol Neutralizer uses a low energy (<9.5keV) soft X-ray source to generate high concentration of bipolar ions. The soft X-rays ionize air molecules creating equal numbers of positive and negative charges. Aerosol enters the neutralizer from the inlet port, and the air ions are attracted to oppositely charged particles shown as Figure A5-. In the Figure A5-4, the particle charge distribution used in the data reduction for the SMPS is based on a theoretical model developed by Wiedensohler and is an approximation of the Fuchs diffusion theory for particle sizes in the sub-micrometer range (Wiedensohler et al. 1986; Fuchs 1963).

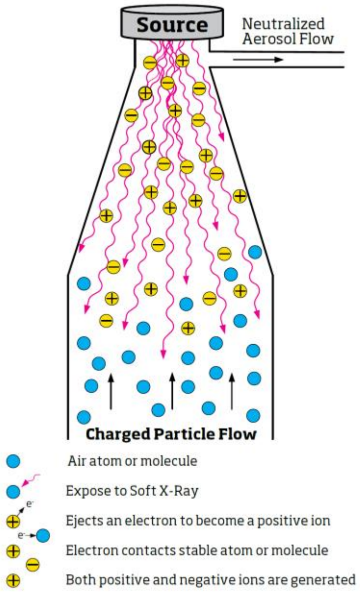

Figure A5-3 Principle of bipolar diffusion charging in the neutralizer model 3087.

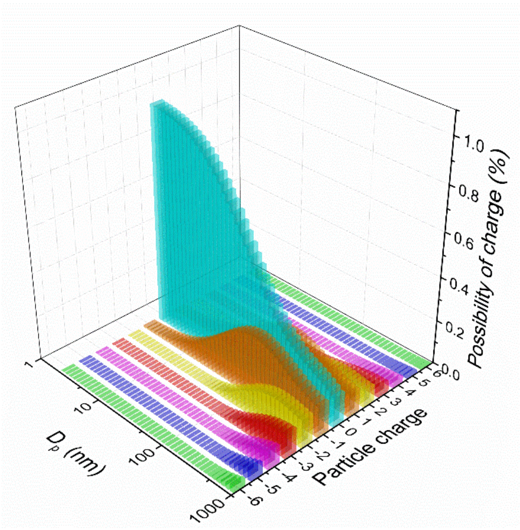

Figure A5-4 Particle charging distribution in the neutralizer model 3087.

- Mobility diameter theory

The electrical mobility is a measure of the particle's ability to move in an electric field. An aerosol particle in an electric field E, carrying n electric charges experiences an electrical force, causing it to move through the gas in which it is suspended. It very quickly reaches its terminal velocity v. The resulting drag force on the particle is given by Stokes law and can be equated to the electrical force to determine the electrical mobility of a particle. The electrical mobility Z_p is defined as:

$$Z_p = \frac{neC}{3\pi\mu D_m} \quad \text{Equation A5-2}$$

Where n is the number of elementary charges on the particle, e is the elementary charge, C is the Cunningham slip correction, μ is the gas viscosity and D_m is the particle diameter. The relationship between the particle electrical mobility and the Classifier parameters is given as (Knutson and Whitby 1975):

$$Z_p = \frac{Q_{sh}}{2\pi \mathrm{v} L} \ln\left(\frac{r_2}{r_1}\right) \quad \text{Equation A5-3}$$

And the mobility bandwidth is:

$$\Delta Z_p = \frac{Q_a}{Q_{sh}} Z_p \qquad \text{Equation A5-4}$$

Where r_2 is the outer radius of annular space in cm, r_1 is the inner radius of annular space in cm, v is the voltage on the inner collector rod in volts and L is the length between exit slit and polydisperse aerosol inlet. Equations A1.2 and A1.3 can be combined to give an equation that relates the particle diameter to collector rod voltage, number of charges on the particle, Classifier flow rate, and geometry for both the Long DMA (3581) and Nano DMA (3585):

$$\frac{D_m}{C} = \frac{2ne\mathrm{v}L}{3\mu Q_{sh} \ln\frac{r_2}{r_1}} \qquad \text{Equation A5-5}$$

Annex B. Ultrafine Condensation Particle Counter 3776

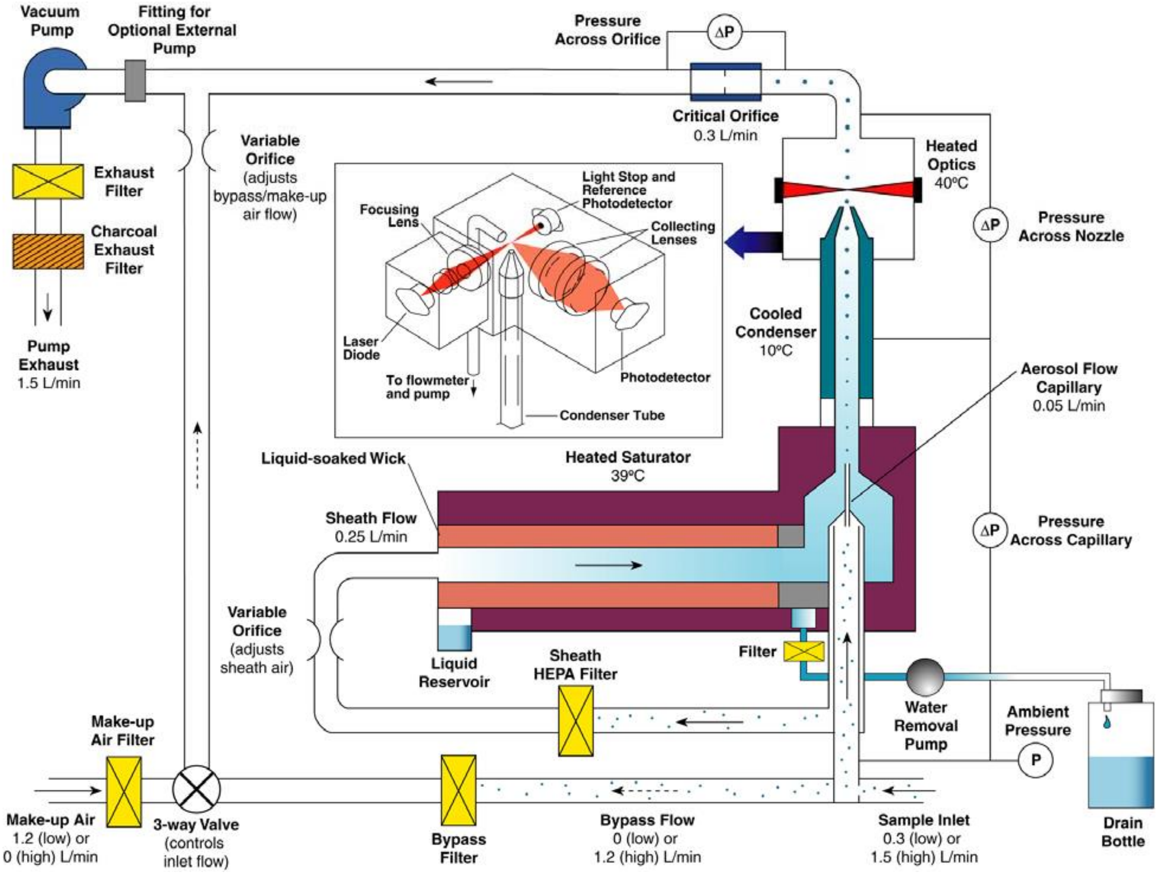

Figure A5-3 Flow Schematic of the Model 3776 CPC.

The CPC TSI 3776 detects particles with a size range of 2.5 nm to 3 μm for concentrations below 10^6 cm^{-3}. According to the operation mode of CPC, the flowrate of aerosol entering to the counter could be either 0.3 $Lmin^{-1}$ or 1.5 $Lmin^{-1}$. In the mode of 0.3 $Lmin^{-1}$, bypass flowrate is 0 and 1.2 $Lmin^{-1}$ flowrate is supplied by make-up air. In the mode of 1.5 $Lmin^{-1}$, this 1.2 $Lmin^{-1}$ flowrate comes from sample flow instead of make-up air. In both modes, the flow passing to the aerosol capillary is 0.05 $Lmin^{-1}$ and another 0.25 $Lmin^{-1}$ pass the saturator filled with 1-butanol. At the working condition, the temperature of the saturator is 39°C and 1-butanol steam follows the flow to meet with aerosol in the condensation chamber where the temperature is 10°C. This rapid temperature drop creates supersaturation conditions for the butanol vapors condensing on the particles to form droplets. The droplets pass through a lighted viewing volume where they scatter light. The scattered-light pulses are collected by a photodetector and converted into electrical pulses. The electrical pulses are then counted and their rate is a measure of particle concentration.

Annex C. Constant Output Atomizer 3076

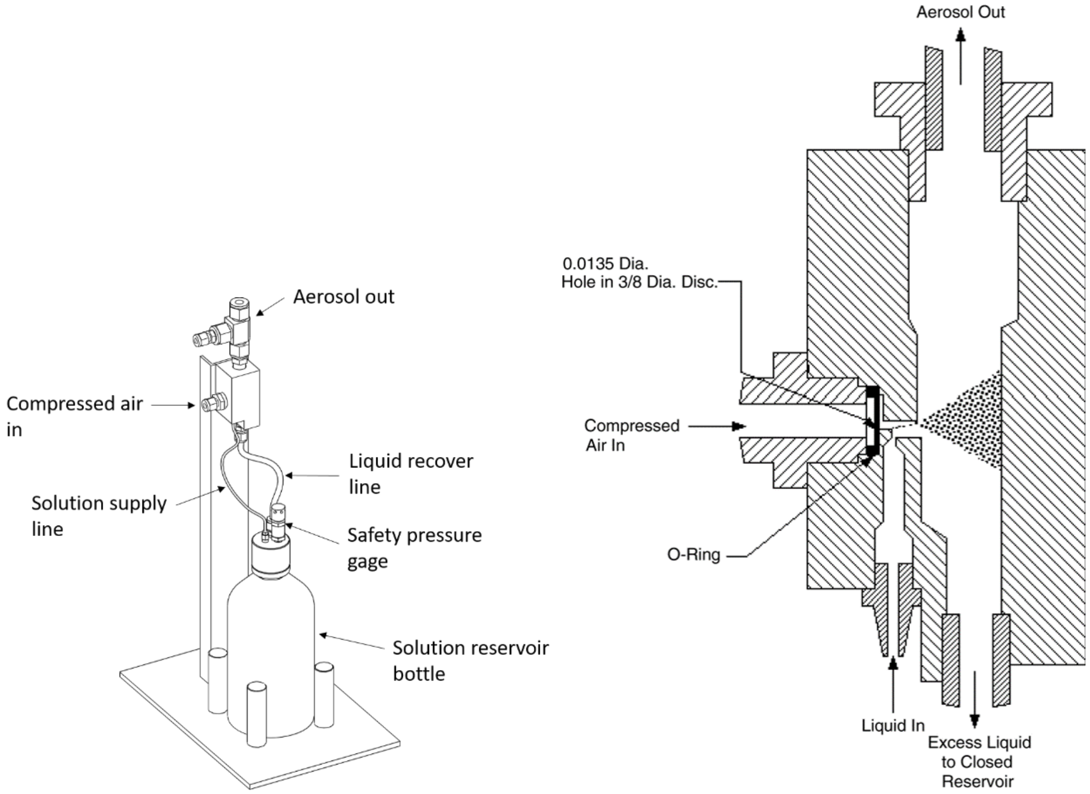

Figure A5-4 Configuration of the atomizer 3076 and the schema of the impactor.

The atomizer is a device that generates submicrometer aerosol by atomizing a solution. The solution is stored in the reservoir bottle. Compressed air expands through an orifice to form a high-velocity jet. Liquid is drawn into the atomizing section through a vertical passage and is then atomized by the jet. Large droplets are removed by impaction on the wall opposite the jet and excess liquid is drained at the bottom of the Atomizer assembly block. Fine spray leaves the Atomizer through a fitting at the top. The atomizer works with up to 3 Lmin^{-1} inlet flow and it can provide total concentration of aerosols as high as 10^7 cm^{-3}.

Annex D. Cloud condensation nuclei counter (CCNc)

The cloud condensation nuclei counter is a commercial device which allows to study the hygroscopic properties of aerosol at the condition of the supersaturation from 0.07% and 0.2%. CCNc contains two parts: the continuous flow diffusion chamber which provides the supersaturation condition; the optical particle counter which counts the water droplets formed by aerosols at the range between 0 to10^4 cm^{-3}. There are two flows working continuously inside the CCNc. Figure A3.1 shows the air and liquid flow.

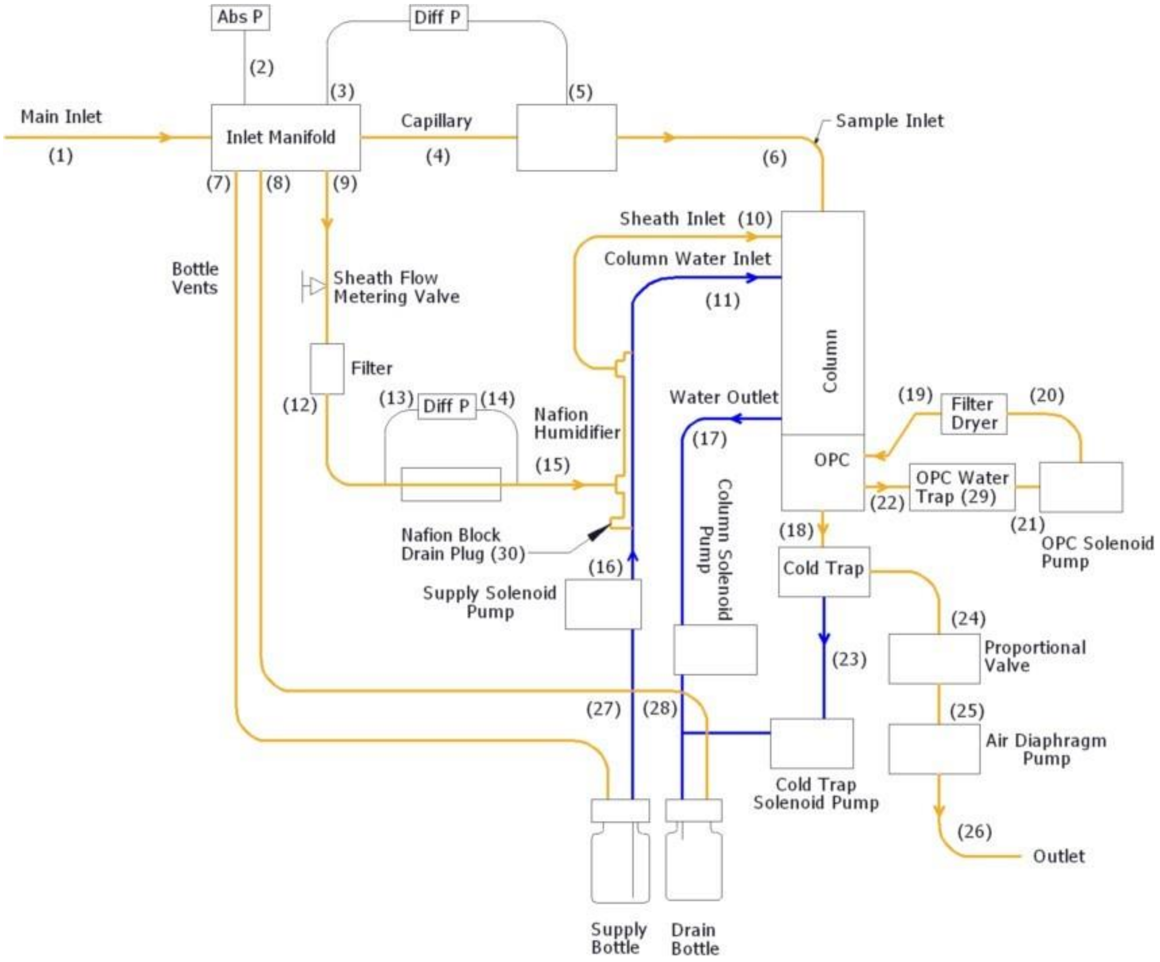

Figure A5-5 Air and Liquid Flow Schematic Diagram.

The sample aerosol arrives to inlet manifold, which serves as the connection point for the sample flow, sheath flow, bottle vents, and the absolute pressure transducer for the sample pressure measurement. Here, the aerosol flow is separated into two pathways. The flowrate of the sample flow passing the sample inlet is 50 $\mathrm{mLmin^{-1}}$ and the flowrate of the sheath flow passing the sheath inlet is 450 $\mathrm{mLmin^{-1}}$. The sample flow and the surrounding sheath flow in the laminar regime pass the optical particle counter and finally are pumped out from the CCNc. At the same time, to ensure the supersaturation condition in the column, water vapor is supplied from the water circulation from the top of the column to the bottom.

- Supersaturation in the column

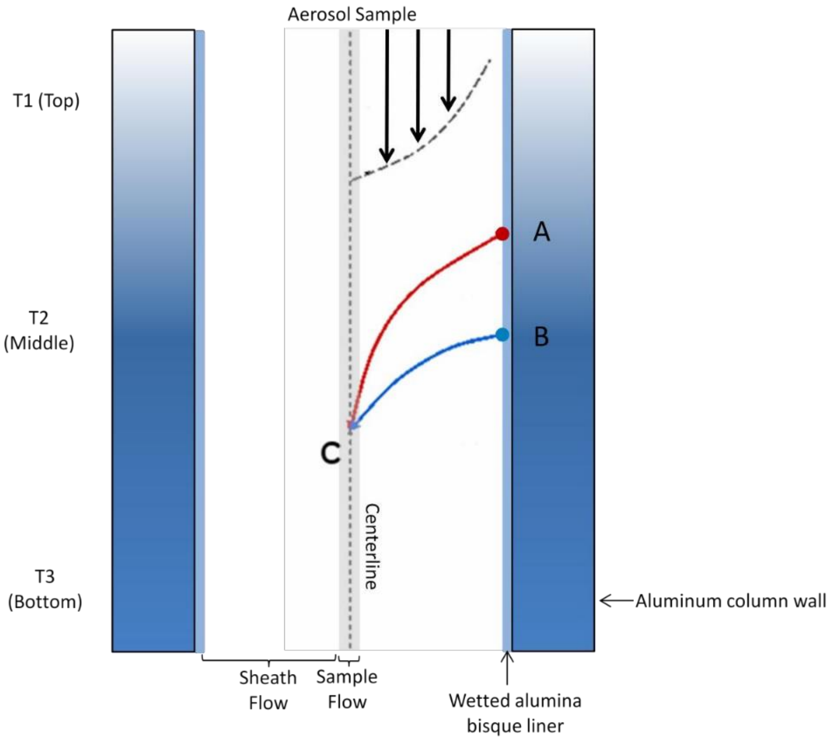

Figure A5-6 Supersaturation being generated in the CCN column.

The CCN counter operates on the principle that diffusion of heat in air is slower than diffusion of water vapor (Roberts and Nenes 2005). Water vapor diffuses from the warm, wet column walls toward the centerline with a mass diffusion of 0.25 $\mathrm{cm^2s^{-1}}$ at 294 K, 1 atm. The heat diffusion is 0.21 $\mathrm{cm^2s^{-1}}$ at 294 K, 1 atm. Figure A5-6 shows a section of the CCN column mounted vertically with a length of 50cm and a radius of 10.9mm. Three thermoelectric control elements (TEC) provide a gradient temperature $\Delta T = T_3 - T_1$ along the column. The inner wall is wetted with water and provides the water vapor. The aerosol sample enters from the top surrounded with sheath flow with a flow rate ratio of 1/10 of the total flow. The point C along the centerline where the diffusing heat originated higher on the column (red-line, point A) than the diffusing mass (blue line, point B). Assuming the water vapor is saturated at the column wall at all points and the temperature at point B is higher than at point A, the water vapor partial pressure is also greater at point B than at point A. The actual partial pressure of water vapor at point C is equal to the partial pressure of water vapor at point B. The temperature at point C is lower than at point B, however, which means that there is more water vapor (corresponding to the saturation vapor pressure at point B) than thermodynamically allowed, thus point C is in the supersaturation condition.

- Calibration of the CCNc

From the manual of CCNc, the CCN temperature must be calibrated regularly with gradients of 3, 4, 6, and 8 K to ensure the supersaturation condition is well calibrated. The monodisperse ammonium sulfate aerosol selected by DMA (annex 1) is used for the CCN temperature calibration. The 50% activation point in Figure A5-7 for that size of ammonium sulfate is considered as $d_{p,c}$ from the Köhler equation (chapter 3), hence SS is estimated by $d_{p,c}$. A linear regression between the measured SS and the temperature gradient is run on the data and that becomes the SS calibration curve for the CCN instrument (Figure A5-7). By comparing the SS curve from calibration procedure and that from CCNc setting, we assume that the difference is negligible. And the CCNc is well calibrated with ammonium sulfate aerosols.

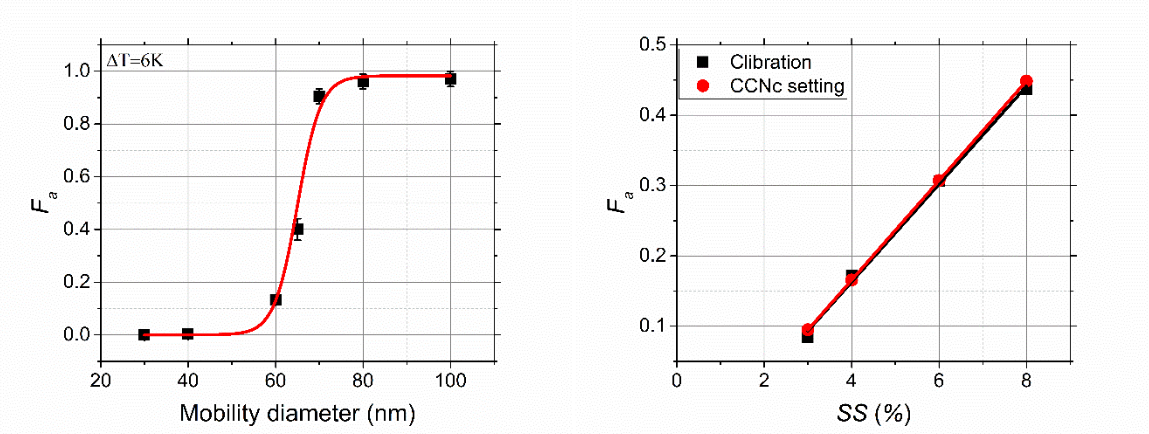

Figure A5-7 Activated fraction of ammonium sulfate against their mobility diameters at gradient temperature of 6K (left figure) and the comparison of the SS vs ΔT between the calibration result and CCNc setting (right figure).

Annex

Bibliography

Abdi, H., and L. J. Williams. 2010. "Principal Component Analysis." *Wiley Interdisciplinary Reviews: Computational Statistics* 2 (4): 433–459.

Alduchov, O. A., and R. E. Eskridge. 1996. "Improved Magnus Form Approximation of Saturation Vapor Pressure." *Journal of Applied Meteorology* 35 (4): 601–9. https://doi.org/10.1175/1520-0450(1996)035<0601:IMFAOS>2.0.CO;2.

Alfè, M., B. Apicella, R. Barbella, J. -N. Rouzaud, A. Tregrossi, and A. Ciajolo. 2009. "Structure–Property Relationship in Nanostructures of Young and Mature Soot in Premixed Flames." *Proceedings of the Combustion Institute* 32 (1): 697–704. https://doi.org/10.1016/j.proci.2008.06.193.

Allen, M. D., and O. G. Raabe. 1985. "Slip Correction Measurements of Spherical Solid Aerosol Particles in an Improved Millikan Apparatus." *Aerosol Science and Technology* 4 (3): 269–86. https://doi.org/10.1080/02786828508959055.

Andreae, M. O., and A. Gelencsér. 2006. "Black Carbon or Brown Carbon? The Nature of Light-Absorbing Carbonaceous Aerosols." *Atmospheric Chemistry and Physics* 6 (10): 3131–3148. https://doi.org/10.5194/acp-6-3131-2006.

Andreae, M. O., and D. Rosenfeld. 2008. "Aerosol–Cloud–Precipitation Interactions. Part 1. The Nature and Sources of Cloud-Active Aerosols." *Earth-Science Reviews* 89 (1): 13–41. https://doi.org/10.1016/j.earscirev.2008.03.001.

Barmet, P., J. Dommen, P. F. DeCarlo, T. Tritscher, A. P. Praplan, S. M. Platt, A. S. H. Prévôt, N. M. Donahue, and U. Baltensperger. 2012. "OH Clock Determination by Proton Transfer Reaction Mass Spectrometry at an Environmental Chamber." *Atmospheric Measurement Techniques* 5 (3): 647–656. https://doi.org/10.5194/amt-5-647-2012.

Baschek, B., F. Lüönd, and U. Lohmann. 2008. "The Zurich Ice Nucleation Chamber (ZINC)-A New Instrument to Investigate Atmospheric Ice Formation AU - Stetzer, Olaf." *Aerosol Science and Technology* 42 (1): 64–74. https://doi.org/10.1080/02786820701787944.

Blake, D. F., and K. Kato. 1995. "Latitudinal Distribution of Black Carbon Soot in the Upper Troposphere and Lower Stratosphere." *Journal of Geophysical Research: Atmospheres* 100 (D4): 7195–7202. https://doi.org/10.1029/94JD03118.

Bloss, C., V. Wagner, M. E. Jenkin, R. Volkamer, W. J. Bloss, J. D. Lee, D. E. Heard, et al. 2005. "Development of a Detailed Chemical Mechanism (MCMv3.1) for the Atmospheric Oxidation of Aromatic Hydrocarbons." *Atmospheric Chemistry and Physics* 5 (3): 641–664. https://doi.org/10.5194/acp-5-641-2005.

Bond, T. C., and R. W. Bergstrom. 2006. "Light Absorption by Carbonaceous Particles: An Investigative Review." *Aerosol Science and Technology* 40 (1): 27–67.

Bond, T. C., S. J. Doherty, D. W. Fahey, P. M. Forster, T. Berntsen, B. J. DeAngelo, M. G. Flanner, et al. 2013. "Bounding the Role of Black Carbon in the Climate System: A Scientific Assessment." *Journal of Geophysical Research: Atmospheres* 118 (11): 5380–5552. https://doi.org/10.1002/jgrd.50171.

Boucher, O, and others. 2013. *Clouds and Aerosols in Climate Change 2013: The Physical Science Basis. Contribution of Working Group I to IPCC AR5, Eds Stocker TF, et Al*. Cambridge Univ Press, Cambridge, UK.

Bro, R., and A. K. Smilde. 2014. "Principal Component Analysis." *Analytical Methods* 6 (9): 2812–2831.

Bundke, U., B. Reimann, B. Nillius, R. Jaenicke, and H. Bingemer. 2010. "Development of a Bioaerosol Single Particle Detector (BIO IN) for the Fast Ice Nucleus CHamber FINCH."

Atmospheric Measurement Techniques 3 (1): 263–71. https://doi.org/10.5194/amt-3-263-2010.

Burkhardt, U., and B. Kärcher. 2011. “Global Radiative Forcing from Contrail Cirrus.” *Nature Climate Change* 1 (1): 54.

Cai, J., N. Lu, and C. M. Sorensen. 1995. “Analysis of Fractal Cluster Morphology Parameters: Structural Coefficient and Density Autocorrelation Function Cutoff.” *Journal of Colloid and Interface Science* 171 (2): 470–73. https://doi.org/10.1006/jcis.1995.1204.

Chapleski, R. C., Y. Zhang, D. Troya, and J. R. Morris. 2016. “Heterogeneous Chemistry and Reaction Dynamics of the Atmospheric Oxidants, O3, NO3, and OH, on Organic Surfaces.” *Chem. Soc. Rev.* 45 (13): 3731–46. https://doi.org/10.1039/C5CS00375J.

Colbeck, I., B. Atkinson, and Y. Johar. 1997. “The Morphology and Optical Properties of Soot Produced by Different Fuels.” *Journal of Aerosol Science* 28 (5): 715–23. https://doi.org/10.1016/S0021-8502(96)00466-1.

Cortez, P., and A. J. R. M. Morais. 2007. “A Data Mining Approach to Predict Forest Fires Using Meteorological Data.”

Crawford, I., O. Möhler, M. Schnaiter, H. Saathoff, D. Liu, G. McMeeking, C. Linke, et al. 2011. “Studies of Propane Flame Soot Acting as Heterogeneous Ice Nuclei in Conjunction with Single Particle Soot Photometer Measurements.” *Atmospheric Chemistry and Physics* 11 (18): 9549–61. https://doi.org/10.5194/acp-11-9549-2011.

D’anna, A, G Mazzotti, and J Kent. 2004. “Modeling of Particulate Formation in a Coflowing Diffusion Flame.” *Combustion Science and Technology* 176 (5–6): 753–767.

DeMott, P. J., A. J. Prenni, X. Liu, S. M. Kreidenweis, M. D. Petters, Cynthia Twohy, M. S. Richardson, T. Eidhammer, and D. C. Rogers. 2010. “Predicting global atmospheric ice nuclei distributions and their impacts on climate.” 2010.

Desgroux, P., A. Faccinetto, X. Mercier, T. Mouton, D. A. Karkar, and A. El Bakali. 2017. “Comparative Study of the Soot Formation Process in a ‘Nucleation’ and a ‘Sooting’ Low Pressure Premixed Methane Flame.” *Combustion and Flame* 184: 153–166.

Dobbins, R. A., R. A. Fletcher, B. A. Benner Jr, and S. Hoeft. 2006. “Polycyclic Aromatic Hydrocarbons in Flames, in Diesel Fuels, and in Diesel Emissions.” *Combustion and Flame* 144 (4): 773–781.

Dufour, L., and R. Defay. 1963. *Thermodynamics of Clouds*.

Durant, A. J., C. Bonadonna, and C. J. Horwell. 2010. “Atmospheric and Environmental Impacts of Volcanic Particulates.” *Elements* 6 (4): 235–40. https://doi.org/10.2113/gselements.6.4.235.

Dymarska, M., B. J. Murray, L. Sun, M. L. Eastwood, D. A. Knopf, and A. K. Bertram. 2006. “Deposition Ice Nucleation on Soot at Temperatures Relevant for the Lower Troposphere.” *Journal of Geophysical Research: Atmospheres* 111 (D4). https://doi.org/10.1029/2005JD006627.

Eggersdorfer, M. L., and S. E. Pratsinis. 2014. “Agglomerates and Aggregates of Nanoparticles Made in the Gas Phase.” *Advanced Powder Technology* 25 (1): 71–90.

Ehhalt, D., M. Prather, F. Dentener, R. Derwent, Edward J. Dlugokencky, E. Holland, I. Isaksen, et al. 2001. “Atmospheric Chemistry and Greenhouse Gases.”

Faccinetto, A., P. Desgroux, M/ Ziskind, E. Therssen, and C. Focsa. 2011. “High-Sensitivity Detection of Polycyclic Aromatic Hydrocarbons Adsorbed onto Soot Particles Using Laser Desorption/Laser Ionization/Time-of-Flight Mass Spectrometry: An Approach to Studying the Soot Inception Process in Low-Pressure Flames.” *Combustion and Flame* 158 (2): 227–39. https://doi.org/10.1016/j.combustflame.2010.08.012.

Fisher, R. A., and W. A. Mackenzie. 1923. “Studies in Crop Variation. II. The Manurial Response of Different Potato Varieties.” *The Journal of Agricultural Science* 13 (3): 311–320.

Frenklach, M., D. W. Clary, W. C. Gardiner, and S. E. Stein. 1985. “Detailed Kinetic Modeling of Soot Formation in Shock-Tube Pyrolysis of Acetylene.” *Symposium (International) on*

Combustion, Twentieth Symposium (International) on Combustion, 20 (1): 887–901. https://doi.org/10.1016/S0082-0784(85)80578-6.

Friedman, B., G. Kulkarni, J. Beránek, A. Zelenyuk, J. A. Thornton, and D. J. Cziczo. 2011. "Ice Nucleation and Droplet Formation by Bare and Coated Soot Particles." *Journal of Geophysical Research: Atmospheres* 116 (D17). https://doi.org/10.1029/2011JD015999.

Fuchs, N. A. 1963. "On the Stationary Charge Distribution on Aerosol Particles in a Bipolar Ionic Atmosphere." *Geofisica Pura e Applicata* 56 (1): 185–93. https://doi.org/10.1007/BF01993343.

Gorbunov, B, A Baklanov, N Kakutkina, H. L Windsor, and R Toumi. 2001. "Ice Nucleation on Soot Particles." *Journal of Aerosol Science* 32 (2): 199–215. https://doi.org/10.1016/S0021-8502(00)00077-X.

Govardhan, G., S. K. Satheesh, R. Nanjundiah, K. K. Moorthy, and S. S. Babu. 2017. "Possible Climatic Implications of High-Altitude Black Carbon Emissions." *Atmospheric Chemistry and Physics* 17 (15): 9623–44. https://doi.org/10.5194/acp-17-9623-2017.

Grimonprez, S. 2016. "PROPRIÉTÉS HYGROSCOPIQUES DE PARTICULES DE SUIE PRÉLEVÉES DANS DES FLAMMES DE KÉROSÈNE ET DE DIESEL : INFLUENCE DE L'EXPOSITION À DES OXYDANTS ATMOSPHÉRIQUES." Villeneuve d'Ascq: Université de Lille.

Grimonprez, S., Faccinetto A., Batut S.., Wu J., Desgroux P., and Petitprez D. 2018. "Cloud Condensation Nuclei from the Activation with Ozone of Soot Particles Sampled from a Kerosene Diffusion Flame." *Aerosol Science and Technology*, 1–41. https://doi.org/10.1080/02786826.2018.1472367.

Haywood, J., and O. Boucher. 2000. "Estimates of the Direct and Indirect Radiative Forcing Due to Tropospheric Aerosols: A Review." *Reviews of Geophysics* 38 (4): 513–543.

He, X., S. Pang, J. Ma, and Y. Zhang. 2017. "Influence of Relative Humidity on Heterogeneous Reactions of O3 and O3/SO2 with Soot Particles: Potential for Environmental and Health Effects." *Atmospheric Environment* 165: 198–206. https://doi.org/10.1016/j.atmosenv.2017.06.049.

Heintzenberg, J. 1994. "Properties of the Log-Normal Particle Size Distribution." *Aerosol Science and Technology* 21 (1): 46–48. https://doi.org/10.1080/02786829408959695.

Hinds, William. C. 1982. *Aerosol Technology: Properties, Behavior, and Measurement of Airborne Particles*. New York: JOHN WILEY & SONS, INC.

Hoose, C, and O Mohler. 2012. "Heterogeneous ice nucleation on atmospheric aerosols: a review of results from laboratory experiments." *Atmos. Chem. Phys. Discuss*, May 16, 2012.

Hu, B., B. Yang, and U. O. Koylu. 2003. "Soot Measurements at the Axis of an Ethylene/Air Non-Premixed Turbulent Jet Flame." *Combustion and Flame* 134 (1): 93–106. https://doi.org/10.1016/S0010-2180(03)00085-3.

Hughey, C. A., C. L. Hendrickson, R. P. Rodgers, A. G. Marshall, and K. Qian. 2001. "Kendrick Mass Defect Spectrum: A Compact Visual Analysis for Ultrahigh-Resolution Broadband Mass Spectra." *Analytical Chemistry* 73 (19): 4676–4681.

Irimiea, C., A. Faccinetto, Y. Carpentier, I. K. Ortega, N. Nuns, E. Therssen, P. Desgroux, and C. Focsa. 2018. "A Comprehensive Protocol for Chemical Analysis of Flame Combustion Emissions by Secondary Ion Mass Spectrometry." *Rapid Communications in Mass Spectrometry* 32 (13): 1015–25. https://doi.org/10.1002/rcm.8133.

Jeffery, C. A., and P. H. Austin. 1997. "Homogeneous Nucleation of Supercooled Water: Results from a New Equation of State." *Journal of Geophysical Research: Atmospheres* 102 (D21): 25269–79. https://doi.org/10.1029/97JD02243.

Jones, H. M., M. J. Flynn, P. J. DeMott, and O. Möhler. 2011. "Manchester Ice Nucleus Counter (MINC) Measurements from the 2007 International Workshop on Comparing Ice Nucleation Measuring Systems (ICIS-2007)." *Atmospheric Chemistry and Physics* 11 (1): 53–65. https://doi.org/10.5194/acp-11-53-2011.

Kanji, Z. A., and J. P. D. Abbatt. 2009. “The University of Toronto Continuous Flow Diffusion Chamber (UT-CFDC): A Simple Design for Ice Nucleation Studies.” *Aerosol Science and Technology* 43 (7): 730–38. https://doi.org/10.1080/02786820902889861.

Kanji, Z. A., O. Florea, and J. P. D. Abbatt. n.d. “Ice formation via deposition nucleation on mineral dust and organics: dependence of onset relative humidity on total particulate surface area.” *IOP Science*.

Kapadia, Zarashpe Z, Dominick V Spracklen, Steve R Arnold, Duncan J Borman, Graham W Mann, Kirsty J Pringle, Sarah A Monks, et al. 2016. “Impacts of Aviation Fuel Sulfur Content on Climate and Human Health.” *Atmospheric Chemistry and Physics* 16 (16): 10521–10541.

Karataş, A. E., and Ö. L. Gülder. 2012. “Soot Formation in High Pressure Laminar Diffusion Flames.” *Progress in Energy and Combustion Science* 38 (6): 818–45. https://doi.org/10.1016/j.pecs.2012.04.003.

Kärcher, B, O Möhler, PJ DeMott, S Pechtl, and F Yu. 2007. “Insights into the Role of Soot Aerosols in Cirrus Cloud Formation.” *Atmospheric Chemistry and Physics* 7 (16): 4203–4227.

Khalizov, Alexei F., Renyi Zhang, Dan Zhang, Huaxin Xue, Joakim Pagels, and Peter H. McMurry. 2009. “Formation of Highly Hygroscopic Soot Aerosols upon Internal Mixing with Sulfuric Acid Vapor.” *Journal of Geophysical Research: Atmospheres* 114 (D5): n/a–n/a. https://doi.org/10.1029/2008JD010595.

King, S. M., T. Rosenoern, J. E. Shilling, Q. Chen, Z. Wang, G. Biskos, K. A. McKinney, U. Pöschl, and S. T. Martin. 2010. “Cloud Droplet Activation of Mixed Organic-Sulfate Particles Produced by the Photooxidation of Isoprene.” *Atmospheric Chemistry and Physics* 10 (8): 3953–3964. https://doi.org/10.5194/acp-10-3953-2010.

Kirkby, J., J. Curtius, J. Almeida, E. Dunne, J. Duplissy, S. Ehrhart, A. Franchin, et al. 2011. “Role of Sulphuric Acid, Ammonia and Galactic Cosmic Rays in Atmospheric Aerosol Nucleation.” *Nature* 476: 429.

Knutson, E. O., and K. T. Whitby. 1975. “Aerosol Classification by Electric Mobility: Apparatus, Theory, and Applications.” *Journal of Aerosol Science* 6 (6): 443–51. https://doi.org/10.1016/0021-8502(75)90060-9.

Koop, T., B. Luo, A. Tsias, and T. Peter. 2000. “Water Activity as the Determinant for Homogeneous Ice Nucleation in Aqueous Solutions.” *Nature* 406: 611.

Kotzick, R., U. Panne, and R. Niessner. 1997. “Changes in Condensation Properties of Ultrafine Carbon Particles Subjected to Oxidation by Ozone.” *Journal of Aerosol Science* 28 (5): 725–35. https://doi.org/10.1016/S0021-8502(96)00471-5.

Köylü, Ü Ö, and G. M. Faeth. 1992. “Structure of Overfire Soot in Buoyant Turbulent Diffusion Flames at Long Residence Times.” *Combustion and Flame* 89 (2): 140–56. https://doi.org/10.1016/0010-2180(92)90024-J.

Köylü, Ü Ö, G. M. Faeth, T. L. Farias, and M. G. Carvalho. 1995. “Fractal and Projected Structure Properties of Soot Aggregates.” *Combustion and Flame* 100 (4): 621–33. https://doi.org/10.1016/0010-2180(94)00147-K.

Kulkarni, G., S. China, S. Liu, M. Nandasiri, N. Sharma, J. Wilson, A. C. Aiken, et al. 2016. “Ice Nucleation Activity of Diesel Soot Particles at Cirrus Relevant Temperature Conditions: Effects of Hydration, Secondary Organics Coating, Soot Morphology, and Coagulation.” *Geophysical Research Letters* 43 (7): 3580–88. https://doi.org/10.1002/2016GL068707.

Kulkarni, G., S. Dobbie, and J. B. McQuaid. 2009. “A New Thermal Gradient Ice Nucleation Diffusion Chamber Instrument: Design, Development and First Results Using Saharan Mineral Dust.” *Atmospheric Measurement Techniques* 2 (1): 221–29. https://doi.org/10.5194/amt-2-221-2009.

Lambe, A. T., A. T. Ahern, J. P. Wright, D. R. Croasdale, P. Davidovits, and T. B. Onasch. 2015. “Oxidative Aging and Cloud Condensation Nuclei Activation of Laboratory Combustion

Soot." *Journal of Aerosol Science* 79 (Supplement C): 31–39. https://doi.org/10.1016/j.jaerosci.2014.10.001.

Lemaire, R., A. Faccinetto, E. Therssen, M. Ziskind, C. Focsa, and P. Desgroux. 2009. "Experimental Comparison of Soot Formation in Turbulent Flames of Diesel and Surrogate Diesel Fuels." *Proceedings of the Combustion Institute* 32 (1): 737–44. https://doi.org/10.1016/j.proci.2008.05.019.

Lemaire, R., M. Maugendre, T. Schuller, E. Therssen, and J. Yon. 2009. "Original Use of a Direct Injection High Efficiency Nebulizer for the Standardization of Liquid Fuels Spray Flames." *Review of Scientific Instruments* 80 (10): 105105. https://doi.org/10.1063/1.3249561.

Li, K., L. Chen, K. Han, B. Lv, K. Bao, X. Wu, X. Gao, and K. Cen. 2017. "Smog Chamber Study on Aging of Combustion Soot in Isoprene/SO2/NOx System: Changes of Mass, Size, Effective Density, Morphology and Mixing State." *Atmospheric Research* 184: 139–48. https://doi.org/10.1016/j.atmosres.2016.10.011.

Li, L., Z. M. Chen, Y. H. Zhang, T. Zhu, J. L. Li, and J. Ding. 2006. "Kinetics and Mechanism of Heterogeneous Oxidation of Sulfur Dioxide by Ozone on Surface of Calcium Carbonate." *Atmospheric Chemistry and Physics* 6 (9): 2453–2464. https://doi.org/10.5194/acp-6-2453-2006.

LIU, B. Y. H., and K. W. LEE. 1975. "An Aerosol Generator of High Stability." *American Industrial Hygiene Association Journal* 36 (12): 861–65. https://doi.org/10.1080/0002889758507357.

Lohmann, U., and J. Feichter. 2005. "Global Indirect Aerosol Effects: A Review." *Atmospheric Chemistry and Physics* 5 (3): 715–737.

Low, R.D. 1969. "A Theoretical Study of Nineteen Condensation Nuclei." *J. Rech. Atmos* 4: 65–78.

Mahrt, F., C. Marcolli, R. O. David, P. Grönquist, E. J. Barthazy Meier, U. Lohmann, and Z. A. Kanji. 2018. "Ice Nucleation Abilities of Soot Particles Determined with the Horizontal Ice Nucleation Chamber." *Atmospheric Chemistry and Physics* 18 (18): 13363–92. https://doi.org/10.5194/acp-18-13363-2018.

Malinowski, E. R. 2002. *Factor Analysis in Chemistry*. Wiley.

Maskey, S., K. Chong, A. Seo, M. Park, K. Lee, and K. Park. 2017. "Cloud Condensation Nuclei Activation of Internally Mixed Black Carbon Particles." *Aerosol and Air Quality Research* 17 (4): 867–877.

Mason, B. 1971. *1971: The Physics of Clouds*. Clarendon Press, Oxford.

McDonald, J. E. 1953. "ERRONEOUS CLOUD-PHY SICS APPLICATIONS OF RAOULT'S LAW." *Journal of Meteorology* 10 (1): 68–70. https://doi.org/10.1175/1520-0469(1953)010<0068:ECPSAO>2.0.CO;2.

Meakin, P., B. Donn, and G. W. Mulholland. 1989. "Collisions between Point Masses and Fractal Aggregates." *Langmuir* 5 (2): 510–18. https://doi.org/10.1021/la00086a038.

Medalia, A. I. 1967. "Morphology of Aggregates: I. Calculation of Shape and Bulkiness Factors; Application to Computer-Simulated Random Flocs." *Journal of Colloid and Interface Science* 24 (3): 393–404. https://doi.org/10.1016/0021-9797(67)90267-6.

Medalia, A. I., and F. A. Heckman. 1971. "Morphology of Aggregates: VII. Comparison Chart Method for Electron Microscopic Determination of Carbon Black Aggregate Morphology." *Journal of Colloid and Interface Science* 36 (2): 173–90. https://doi.org/10.1016/0021-9797(71)90162-7.

Metzger, A., B. Verheggen, J. Dommen, J. Duplissy, A. S. H. Prevot, Ernest Weingartner, Ilona Riipinen, et al. 2010. "Evidence for the Role of Organics in Aerosol Particle Formation under Atmospheric Conditions." *Proceedings of the National Academy of Sciences* 107 (15): 6646–51. https://doi.org/10.1073/pnas.0911330107.

Möhler, O., P. R. Field, P. Connolly, S. Benz, H. Saathoff, M. Schnaiter, R. Wagner, et al. 2006. "Efficiency of the Deposition Mode Ice Nucleation on Mineral Dust Particles." *Atmospheric Chemistry and Physics* 6 (10): 3007–21. https://doi.org/10.5194/acp-6-3007-2006.

Murphy, D. M., D. S. Thomson, and M. J. Mahoney. 1998. "In Situ Measurements of Organics, Meteoritic Material, Mercury, and Other Elements in Aerosols at 5 to 19 Kilometers." *Science* 282 (5394): 1664–1669. https://doi.org/10.1126/science.282.5394.1664.

Murray, K. K., R. K. Boyd, M. N. Eberlin, G. J. Langley, L. Li, and Y. Naito. 2013. "Definitions of Terms Relating to Mass Spectrometry (IUPAC Recommendations 2013)." *Pure and Applied Chemistry* 85 (7): 1515–1609.

Nicolet, M., O. Stetzer, F. Lüönd, O. Möhler, and U. Lohmann. 2010. "Single Ice Crystal Measurements during Nucleation Experiments with the Depolarization Detector IODE." *Atmospheric Chemistry and Physics* 10 (2): 313–25. https://doi.org/10.5194/acp-10-313-2010.

OUF, F-X. 2006. "Caracterisation Des Aerosols Emis Lors d'un Incendie." Rouen.

Paramonov, M., P. P. Aalto, A. Asmi, N. Prisle, V.-M. Kerminen, M. Kulmala, and T. Petäjä. 2013. "The Analysis of Size-Segregated Cloud Condensation Nuclei Counter (CCNC) Data and Its Implications for Cloud Droplet Activation." *Atmospheric Chemistry and Physics* 13 (20): 10285–10301. https://doi.org/10.5194/acp-13-10285-2013.

Pearson, K. 1901. "LIII. On Lines and Planes of Closest Fit to Systems of Points in Space." *The London, Edinburgh, and Dublin Philosophical Magazine and Journal of Science* 2 (11): 559–572.

Pei, L., G. Jiang, B. J. Tyler, L. L. Baxter, and M. R. Linford. 2008. "Time-of-Flight Secondary Ion Mass Spectrometry of a Range of Coal Samples: A Chemometrics (PCA, Cluster, and PLS) Analysis." *Energy & Fuels* 22 (2): 1059–72. https://doi.org/10.1021/ef7003199.

Penner, J. E., C. Zhou, A. Garnier, and D. L. Mitchell. 2018. "Anthropogenic Aerosol Indirect Effects in Cirrus Clouds." *Journal of Geophysical Research: Atmospheres* 123 (20): 11,652-11,677. https://doi.org/10.1029/2018JD029204.

Perraudin, E., H. Budzinski, and E. Villenave. 2007. "Kinetic Study of the Reactions of Ozone with Polycyclic Aromatic Hydrocarbons Adsorbed on Atmospheric Model Particles." *Journal of Atmospheric Chemistry* 56 (1): 57–82. https://doi.org/10.1007/s10874-006-9042-x.

Petters, M. D., and S. M. Kreidenweis. 2007. "A Single Parameter Representation of Hygroscopic Growth and Cloud Condensation Nucleus Activity." *Atmospheric Chemistry and Physics* 7 (8): 1961–1971. https://doi.org/10.5194/acp-7-1961-2007.

Petters, S. S., D. Pagonis, M. S. Claflin, E. J. T. Levin, M. D. Petters, P. J. Ziemann, and S. M. Kreidenweis. 2017. "Hygroscopicity of Organic Compounds as a Function of Carbon Chain Length and Carboxyl, Hydroperoxy, and Carbonyl Functional Groups." *The Journal of Physical Chemistry A* 121 (27): 5164–74. https://doi.org/10.1021/acs.jpca.7b04114.

Petzold, A., M. Gysel, X. Vancassel, R. Hitzenberger, H. Puxbaum, S. Vrochticky, E. Weingartner, U. Baltensperger, and P. Mirabel. 2005. "On the Effects of Organic Matter and Sulphur-Containing Compounds on the CCN Activation of Combustion Particles." *Atmospheric Chemistry and Physics* 5 (12): 3187–3203. https://doi.org/10.5194/acp-5-3187-2005.

Pruppacher, H. R., and J. D. Klett. 2012. *Microphysics of Clouds and Precipitation: Reprinted 1980*. Springer Science & Business Media.

Pruppacher, H.R., and J.D. Klett. 1978. *Microphysics of Clouds and Precipitation*. 2nd ed. Atmospheric and Oceanographic Sciences Library 18. Springer Netherlands. http://gen.lib.rus.ec/book/index.php?md5=15ec9ea758db0a55fc9b4b119cbdddc2.

Richter, H., and J. B. Howard. 2000. "Formation of Polycyclic Aromatic Hydrocarbons and Their Growth to Soot—a Review of Chemical Reaction Pathways." *Progress in Energy and Combustion Science* 26 (4–6): 565–608.

Roberts, G., and A. Nenes. 2005. "A continuous-flow streamwise thermal-gardient CCN chamber for atmospheric measurements." *Aerosol Science and Technology*, 2005.

Rogers, D. C. 1988. "Development of a Continuous Flow Thermal Gradient Diffusion Chamber for Ice Nucleation Studies." *Atmospheric Research* 22 (2): 149–81. https://doi.org/10.1016/0169-8095(88)90005-1.

Rogers, D. C., P. J. DeMott, S. M. Kreidenweis, and Y. Chen. 2001. "A Continuous-Flow Diffusion Chamber for Airborne Measurements of Ice Nuclei." *Journal of Atmospheric and Oceanic Technology* 18 (5): 725–41. https://doi.org/10.1175/1520-0426(2001)018<0725:ACFDCF>2.0.CO;2.

Rose, D., S. S. Gunthe, E. Mikhailov, G. P. Frank, U. Dusek, M. O. Andreae, and U. Pöschl. 2008. "Calibration and Measurement Uncertainties of a Continuous-Flow Cloud Condensation Nuclei Counter (DMT-CCNC): CCN Activation of Ammonium Sulfate and Sodium Chloride Aerosol Particles in Theory and Experiment." *Atmospheric Chemistry and Physics* 8 (5): 1153–1179. https://doi.org/10.5194/acp-8-1153-2008.

Samson, R. J., George W. Mulholland, and J. W. Gentry. 1987. "Structural Analysis of Soot Agglomerates." *Langmuir* 3 (2): 272–81. https://doi.org/10.1021/la00074a022.

Sassen, K., and G. C. Dodd. 1988. "Homogeneous Nucleation Rate for Highly Supercooled Cirrus Cloud Droplets." *Journal of the Atmospheric Sciences* 45 (8): 1357–69. https://doi.org/10.1175/1520-0469(1988)045<1357:HNRFHS>2.0.CO;2.

Sleno, L. 2012. "The Use of Mass Defect in Modern Mass Spectrometry." *Journal of Mass Spectrometry* 47 (2): 226–236. https://doi.org/10.1002/jms.2953.

Sorensen, C. M. 2011. "The Mobility of Fractal Aggregates: A Review." *Aerosol Science and Technology* 45 (7): 765–779.

Sorensen, C. M., J. Cai, and N. Lu. 1992. "Light-Scattering Measurements of Monomer Size, Monomers per Aggregate, and Fractal Dimension for Soot Aggregates in Flames." *Appl. Opt.* 31 (30): 6547–6557. https://doi.org/10.1364/AO.31.006547.

Sorensen, C. M., and GD Feke. 1996. "The Morphology of Macroscopic Soot." *Aerosol Science and Technology* 25 (3): 328–337.

Sorensen, C. M., and G. C. Roberts. 1997. "The Prefactor of Fractal Aggregates." *Journal of Colloid and Interface Science* 186 (2): 447–52. https://doi.org/10.1006/jcis.1996.4664.

Sorjamaa, R., and A. Laaksonen. 2007. "The Effect of H_2O Adsorption on Cloud Drop Activation of Insoluble Particles: A Theoretical Framework." *Atmospheric Chemistry and Physics* 7 (24): 6175–6180. https://doi.org/10.5194/acp-7-6175-2007.

Stocker, T. F., Qin D., Plattner G. K., Tignor M., Allen S. K., Boschung J., Nauels A., Xia Y., Bex V., and Midgley P.M.. 2013. "Contribution of Working Group I to the Fifth Assessment Report of the Intergovernmental Panel on Climate Change." *Climate Change*.

Stokes, R. H., and R. A. Robinson. 1966. "Interactions in Aqueous Nonelectrolyte Solutions. I. Solute-Solvent Equilibria." *The Journal of Physical Chemistry* 70 (7): 2126–31. https://doi.org/10.1021/j100879a010.

Streets, D. G., and S. T. Waldhoff. 2000. "Present and Future Emissions of Air Pollutants in China:: SO2, NOx, and CO." *Atmospheric Environment* 34 (3): 363–74. https://doi.org/10.1016/S1352-2310(99)00167-3.

Stubenrauch, C., and U. Schumann. 2005. "Impact of Air Traffic on Cirrus Coverage." *Geophysical Research Letters* 32 (14). https://doi.org/10.1029/2005GL022707.

Sullivan, R. C., M. J. K. Moore, M. D. Petters, S. M. Kreidenweis, G. C. Roberts, and K. A. Prather. 2009. "Effect of Chemical Mixing State on the Hygroscopicity and Cloud

Nucleation Properties of Calcium Mineral Dust Particles." *Atmos. Chem. Phys.* 9 (10): 3303–16. https://doi.org/10.5194/acp-9-3303-2009.

Tanaka, Y. 1988. "Sensitivity Analysis in Principal Component Analysis: Influence on the Subspace Spanned by Principal Components." *Communications in Statistics-Theory and Methods* 17 (9): 3157–3175.

Tang, M. J., J. Whitehead, N. M. Davidson, F. D. Pope, M. R. Alfarra, G. McFiggans, and M. Kalberer. 2015. "Cloud Condensation Nucleation Activities of Calcium Carbonate and Its Atmospheric Ageing Products." *Phys. Chem. Chem. Phys.* 17 (48): 32194–203. https://doi.org/10.1039/C5CP03795F.

Tian, K., K. A. Thomson, F. Liu, D. R. Snelling, G. J. Smallwood, and D. Wang. 2006. "Determination of the Morphology of Soot Aggregates Using the Relative Optical Density Method for the Analysis of TEM Images." *Combustion and Flame* 144 (4): 782–91. https://doi.org/10.1016/j.combustflame.2005.06.017.

Tomlinson, E. M., and N. Fukuta. 1985. "A New Horizontal Gradient, Continuous Flow, Ice Thermal Diffusion Chamber." *Journal of Atmospheric and Oceanic Technology* 2 (4): 448–67. https://doi.org/10.1175/1520-0426(1985)002<0448:ANHGCF>2.0.CO;2.

Tritscher, T., Z. Jurányi, M. Martin, R. Chirico, M. Gysel, Maarten F. Heringa, Peter F. DeCarlo, et al. 2011. "Changes of Hygroscopicity and Morphology during Ageing of Diesel Soot." *Environmental Research Letters* 6 (3): 034026.

Vali, G. 1985. "Nucleation Terminology." *Bulletin of the American Meteorological Society* 66 (11): 1426–1427.

Wagner, MS, DJ Graham, BD Ratner, and David G Castner. 2004. "Maximizing Information Obtained from Secondary Ion Mass Spectra of Organic Thin Films Using Multivariate Analysis." *Surface Science* 570 (1–2): 78–97.

Wang, H. 2011. "Formation of Nascent Soot and Other Condensed-Phase Materials in Flames." *Proceedings of the Combustion Institute* 33 (1): 41–67. https://doi.org/10.1016/j.proci.2010.09.009.

Wang, H., D. G. Castner, B. D. Ratner, and S. Jiang. 2004. "Probing the Orientation of Surface-Immobilized Immunoglobulin G by Time-of-Flight Secondary Ion Mass Spectrometry." *Langmuir* 20 (5): 1877–1887.

Wang, J., J. F. Doussin, S. Perrier, E. Perraudin, Y. Katrib, E. Pangui, and B. Picquet-Varrault. 2011. "Design of a New Multi-Phase Experimental Simulation Chamber for Atmospheric Photosmog, Aerosol and Cloud Chemistry Research." *Atmospheric Measurement Techniques* 4 (11): 2465–2494. https://doi.org/10.5194/amt-4-2465-2011.

Wiedensohler, A., E. Lütkemeier, M. Feldpausch, and C. Helsper. 1986. "Investigation of the Bipolar Charge Distribution at Various Gas Conditions." *Journal of Aerosol Science* 17 (3): 413–16. https://doi.org/10.1016/0021-8502(86)90118-7.

Wittbom, C., A. C. Eriksson, J. Rissler, J. E. Carlsson, P. Roldin, E. Z. Nordin, P. T. Nilsson, E. Swietlicki, J. H. Pagels, and B. Svenningsson. 2014. "Cloud Droplet Activity Changes of Soot Aerosol upon Smog Chamber Ageing." *Atmospheric Chemistry and Physics* 14 (18): 9831–9854. https://doi.org/10.5194/acp-14-9831-2014.

Wong, H.-W., and R. C. Miake-Lye. 2010. "Parametric Studies of Contrail Ice Particle Formation in Jet Regime Using Microphysical Parcel Modeling." *Atmospheric Chemistry and Physics* 10 (7): 3261–3272. https://doi.org/10.5194/acp-10-3261-2010.

Wu, J., A. Faccinetto, S. Grimonprez, S. Batut, J. Yon, P. Desgroux, and D. Petitprez. 2019. "Influence of the Dry Aerosol Particle Size Distribution and Morphology on the Cloud Condensation Nuclei Activation. An Experimental and Theoretical Investigation." *Atmospheric Chemistry and Physics Discussions*, February, 1–23. https://doi.org/10.5194/acp-2019-172.

Yon, J., A. Bescond, and F.-X. Ouf. 2015. “A Simple Semi-Empirical Model for Effective Density Measurements of Fractal Aggregates.” *Journal of Aerosol Science* 87: 28–37. https://doi.org/10.1016/j.jaerosci.2015.05.003.

Yon, J., R. Lemaire, E. Therssen, P. Desgroux, A. Coppalle, and K. F. Ren. 2011. “Examination of Wavelength Dependent Soot Optical Properties of Diesel and Diesel/Rapeseed Methyl Ester Mixture by Extinction Spectra Analysis and LII Measurements.” *Applied Physics B* 104 (2): 253–271. https://doi.org/10.1007/s00340-011-4416-4.

Yu, H., Y. J. Kaufman, M. Chin, G. Feingold, L. A. Remer, T. L. Anderson, Y. Balkanski, et al. 2006. “A Review of Measurement-Based Assessments of the Aerosol Direct Radiative Effect and Forcing.” *Atmospheric Chemistry and Physics* 6 (3): 613–66. https://doi.org/10.5194/acp-6-613-2006.

Zdanovskii, A. B. 1936. “Regularities in the Property Variations of Mixed Solutions.” *Tr. Solyanoi Lab. Akad. Nauk SSSR* 6: 5–70.

Zhang, R., A. F. Khalizov, J. Pagels, D. Zhang, H. Xue, and P. H. McMurry. 2008. “Variability in Morphology, Hygroscopicity, and Optical Properties of Soot Aerosols during Atmospheric Processing.” *Proceedings of the National Academy of Sciences* 105 (30): 10291–10296. https://doi.org/10.1073/pnas.0804860105.

Zuberi, B., K. S. Johnson, G. K. Aleks, L. T. Molina, M. J. Molina, and A. Laskin. 2005. “Hydrophilic Properties of Aged Soot.” *Geophysical Research Letters* 32 (1). https://doi.org/10.1029/2004GL021496.

List of figures

List of tables

Abstract

Freshly emitted soot particles from combustion processes are hydrophobic. However, the aging process in the atmosphere can modify their size, morphology and surface chemistry and turn them into efficient cloud condensation (CCN) and ice nuclei (IN) that significantly contribute to the indirect radiative forcing of climate. For spherical and monodisperse aerosols, κ-Köhler theory is often used in the literature to quantify the hygroscopic properties of aerosols. In this work, a combined theoretical and experimental approach is proposed to add to the theory the contributions of the particle size distribution and morphology. Hygroscopic properties of the particles are derived by measuring their activated fraction as a function of the water supersaturation using a CCN counter. The model developed in this work is first tested on dry ammonium sulfate particles (quasi spherical and non aggregating). Then, it is applied to soot particles that are complex aggregates of primary particles. Soot particles are generated from a laboratory diffusion jet flame supplied with kerosene, and aged with ozone and sulfur dioxide in controlled conditions of temperature, pressure and relative humidity to simulate their permanence in the atmosphere. The electrical mobility, morphology and chemical composition of fresh and aged soot are measured by scanning mobility particle sizing, electron microscopy and secondary ion mass spectrometry, respectively, before and after the aging and related to the activation process. From the comparison of the experimental activation curves and the model, the values of the hygroscopicity parameter κ could be determined for a large variety of operating conditions.

Key words: soot, hygroscopicity, Köhler theory, aging process, mass spectrometry, supersaturation

Résumé

Les particules de suie émises par les processus de combustion sont hydrophobes. Cependant leurs caractéristiques morphologiques et chimiques sont modifiées lorsqu'elles séjournent dans l'atmosphère. Elles peuvent alors devenir des noyaux de condensation (CCN) ou glaciogènes (IN) et contribuer de manière significative au forçage radiatif indirect affectant le climat. Pour les aérosols sphériques et mono dispersés, la théorie de κ-Köhler est souvent utilisée pour quantifier les propriétés hygroscopiques des aérosols. Dans ce travail une approche théorique et expérimentale est proposée afin d'étendre la théorie à des distributions de tailles et de morphologies d'aérosols plus complexes. Les propriétés hygroscopiques des particules sont déterminées en mesurant leur fraction activée en fonction de la sursaturation en eau au moyen d'un compteur de CCN. Le modèle développé est d'abord testé sur des particules sphériques et isolées de sulfate d'ammonium. Puis il est appliqué aux agrégats complexes de particules de suie. Les suies sont générées dans une flamme de diffusion de kérosène, et ensuite exposées à des concentrations variables d'ozone et de dioxyde de soufre dans des conditions contrôlées de température, pression et humidité relative. La mobilité électrique, la morphologie et la composition chimique de surface sont mesurées par granulométrie, microscopie électronique et spectrométrie de masse par ions secondaires respectivement, avant et après le vieillissement, et reliées au processus d'activation. A partir de la comparaison entre les courbes d'activation et le modèle, les valeurs du paramètre d'hygroscopicité κ ont été déterminées pour une large gamme de conditions opératoires.

Mots clés: suie, hygroscopicité, théorie de Köhler, vieillissement, spectrométrie de masse, sursaturation